

**Magnetic Nanocrystal Clusters: Understanding, Shaping, and
Exploiting their Giant Susceptibility**

By Zhen Xiao

B.S., Chemistry, Beihang University, China, 2017

A DISSERTATION SUBMITTED IN PARTIAL FULFILLMENT OF THE
REQUIREMENTS FOR THE DEGREE OF DOCTOR OF PHILOSOPHY IN THE
DEPARTMENT OF CHEMISTRY AT BROWN UNIVERSITY

Providence, Rhode Island

May 2022

© Copyright 2022 by Zhen Xiao

This dissertation by Zhen Xiao is accepted in its present form by the Department of Chemistry as satisfying the dissertation requirement for the degree of Doctor of Philosophy.

Date _____

Vicki L. Colvin, Advisor

Recommended to the Graduate Council

Date _____

Ou Chen, Reader

Date _____

Jerome R. Robinson, Reader

Approved by the Graduate Council

Date _____

Andrew G. Campbell, Dean of the Graduate School

Curriculum Vitae

Zhen grew up in a remote, mountainous region in China. As close to nature, he has had many interests in natural science since elementary school. Under the guidance of his father, a math teacher in a local junior high school, Zhen gradually developed a strong background in math, physics, and chemistry. At the age of 15, he decided to leave the county where he had lived for 15 years to pursue better education at Ankang High School, the best school in the city. Zhen met the class teacher, Mrs. Lin Qingxia, who had constantly encouraged Zhen to explore more in the natural science world independently. After three years of hard work, he excelled in the Entrance Examination in 2013 and was admitted to Beihang University, where he chose chemistry as his major. Again, he left his hometown Shaanxi Province and traveled a thousand miles to Beijing, the well-known city but a strange place for Zhen.

In Beijing, he realized he was an average student, just like everyone else, who have had excelled in many ways. Without other unique talents, his only gift was modesty and diligence, and he put his mind to chemistry research. He later joined the research group of Professor Zhu Ying to work on carbon nanomaterials for energy conversion devices. It was a new area and rather challenging for a sophomore who knew little about nanomaterials. To catch up in this world, he devoted himself to literature and the lab. In the 4th College Student Chemistry Competition, he and his team won the first prize. His teammates faced this success and joy and left the project for other activities. But he did not stop there. Instead, he wanted to carry on even just by himself. Finally, his hard work paid off, and he turned his projects on carbon nanomaterials into several publications, which not only brought him

recognition by the university as honored the Outstanding Undergraduate student but also encouraged him to pursue a career in research.

Zhen also enjoyed learning English. In his mind, English was not just a foreign language but also a necessary implementation to communicate with the world. He chose English as a second major and got to know many friends who helped him practice speaking. He enjoyed being with one of his best friends, Ouyang Zhihao, and the two always talked in English until they both could fluently and proudly speak. English not only opened his eyes but also granted him a chance to travel abroad. He did not hesitate when he came across the Canadian summer intern project with a high standard of English performance. With his academic capability, fluency in English, and a bit of luck, he earned himself the opportunity to go to Canada in the summer. He joined the research group of Professor David MaGee at the University of New Brunswick and studied organic synthesis for natural compounds. The experience in Canada helped Zhen determine his mind to pursue a graduate education abroad.

In 2017, Zhen finally set foot in the US, the country that has only existed in the books, the movies, and the news. During the chemistry department orientation at Brown, Professor Vicki Colvin's research projects on magnetic nanocrystals really inspired Zhen. Soon after the orientation, Zhen contacted Professor Colvin and expressed his interest in her projects. In the following conversations with Professor Colvin, her expertise in both chemistry and biology, her confidence in these materials in biomedical applications, and her impressive presentations all made Zhen decide to join her lab. Under her guidance in the research and her care of Zhen's everyday life, Zhen was able to explore the world of magnetic nanomaterials and have published several first-authored papers in the area. Now Zhen is

ready to present this thesis for his Ph.D. and continue doing further research using magnetic nanomaterials.

Publications

1. The Giant Susceptibility of Magnetic Nanocrystal Clusters. Zhang, Q.* , Raj, S.* , **Xiao, Z.***, Zhang, L.* , Fellows, B., Saayujya, C., Chandrasekharan, P., Masterson, C.M., Li, J., Guo, W., Conolly, S.M., Bao, G., Král, P. and Colvin, V.L. *Submitted*.

*These authors contributed equally.

2. Magnetic Nanocrystal Chains with Large Magnetic Susceptibilities and Anisotropic Coercivity. **Xiao, Z.**, Villanova, J., Lee, M.J., Stueber, D.D., Zhang, Q., and Colvin, V.L. *In preparation*.

3. Portable Heating and Environmental Remediation Using the Giant Susceptibilities of Manganese-Doped Ferrite Clusters. **Xiao, Z.**, Guo, X., Villanova, J., Bi, Y., Avidan, S., Effman, S., Zhang, Q. and Colvin, V.L. *In preparation*.

4. Magnetically Induced Nanoheaters: from Biomedicine to the Remediation of Emerging Contaminants in Drinking Water. **Xiao, Z.**, Villanova, J., Koval, P., Stueber, D.D. and Colvin, V.L. *In preparation*.

5. Synthesis and Application of Magnetic Nanocrystal Clusters. **Xiao, Z.**, Zhang, L., Colvin, V.L., Zhang, Q. and Bao, G. *Industrial & Engineering Chemistry Research*, 2022, doi.org/10.1021/acs.iecr.1c04879

6. Stable Aqueous Suspensions of Manganese Ferrite Clusters with Tunable Nanoscale Dimension and Composition. Effman, S.* , Avidan, S.* , **Xiao, Z.***, Colvin, V. *Journal of Visualized Experiments*, 2022, 180, e63140, doi:10.3791/63140.

*These authors contributed equally.

7. Sub-second multi-channel magnetic control of select neural circuits in behaving flies. Sebesta, C., Torres, D., Wang, B., Li, Z., Duret, G., Jiang, K., **Xiao, Z.**, Zhang, Q., Colvin, V., Goetz, S. and Peterchev, A. *Nature Materials*, accepted.
8. Controlled oxidation and surface modification increase heating capacity of magnetic iron oxide nanoparticles. Jiang, K., Zhang, Q., Hinojosa, D.T., Zhang, L., **Xiao, Z.**, Yin, Y., Tong, S., Colvin, V.L. and Bao, G. *Applied Physics Reviews*, 2021, 8(3), 031407.
9. 2D Gadolinium Oxide Nanoplates as T1 Magnetic Resonance Imaging Contrast Agents. Stinnett, G., Taheri, N., Villanova, J., Bohloul, A., Guo, X., Esposito, E.P., **Xiao, Z.**, Stueber, D., Avendano, C., Decuzzi, P. Pautler, R.G., and Colvin, V.L. *Advanced Healthcare Materials*, 2021, 10(11), 2001780.
10. Nanoparticle-Catalyzed Green Chemistry Synthesis of Polybenzoxazole. Shen, M., Yu, C., Guan, H., Dong, X., Harris, C., **Xiao, Z.**, Yin, Z., Muzzio, M., Lin, H., Robinson, J.R., Colvin, V.L., and Sun, S. *Journal of the American Chemical Society*, 2021, 143(4), 2115-2122.
11. Magnetic nanoparticles in biology and medicine: Past, present, and future trends. Stueber, D.D., Villanova, J., Aponte, I., **Xiao, Z.** and Colvin, V.L. *Pharmaceutics*, 2021, 13(7), 943.
12. Libraries of Uniform Magnetic Multicore Nanoparticles with Tunable Dimensions for Biomedical and Photonic Applications. **Xiao, Z.***, Zhang, Q.*, Guo, X., Villanova, J., Hu, Y., Külaots, I., Garcia-Rojas, D., Guo, W. and Colvin, V.L. *ACS Applied Materials & Interfaces*, 2020, 12(37), 41932-41941.

*These authors contributed equally.

13. Homogeneously Dispersed Co₉S₈ Anchored on Nitrogen and Sulfur Co-Doped Carbon Derived from Soybean as Bifunctional Oxygen Electrocatalysts and Supercapacitor. **Xiao, Z.**, Xiao, G., Shi, M. and Zhu, Y. ACS applied materials & interfaces, 2018, 10(19), 16436-16448.
14. China rose-derived tri-heteroatom co-doped porous carbon as an efficient electrocatalysts for oxygen reduction reaction. **Xiao, Z.**, Gao, X., Shi, M., Ren, G., Xiao, G., Zhu, Y. and Jiang, L. RSC advances, 2016, 6(89), 86401-86409.
15. Natural tea-leaf-derived, ternary-doped 3D porous carbon as a high-performance electrocatalyst for the oxygen reduction reaction. Guo, Z.*, **Xiao, Z.***, Ren, G., Xiao, G., Zhu, Y., Dai, L. and Jiang, L., 2016. Nano Research, 9(5), 1244-1255.

*These authors contributed equally.

Preface and Acknowledgements

A great doctor in Ancient China of the Tang Dynasty, Sun Simiao, wrote in his book, “Foolish people would brag themselves that they can treat every disease after three years of medical books reading, and would complain no disease can be cured after three years of medical practice.” I always have had the same feeling. When I read literature and books, I felt I almost knew everything about my research; however, when I did do my own experiments in the lab, I got frustrated as not all experiments guarantee my desired outcome. The gap between my envision and the result is the most challenging part to accept. I believe a qualified researcher must be able to confront their failures and walk out of their desperation and look for solutions. And such ability is something that I gradually developed during my five-year research life. I’ve had tears when my painstaking effort failed, had frustrations when my paper writing got stuck, and most importantly, had joy and laughter when my papers finally became published. Taking this opportunity, I would like to thank everyone that has helped prepare my Ph.D. thesis in many ways.

First and foremost, I would appreciate the effort put on me by my advisor, Professor Vicki Colvin. Professor Colvin made a strong impression on me the first time we met. When she invited me for a talk about future research, she showed me the graphs on the blackboard in her office, which is now still proudly exhibited there. It was a simple graph with a curve that increased first and then decreased at the highest point. She told me that was the size-dependent properties of the magnetic nanomaterials first discovered in the Colvin lab. Apart from mechanism study, the lab was also taking advantage of the superior magnetic properties of these materials for biomedical applications, including cancer treatment. If I could join the research group and put my synthesis skills into it, high-quality papers would

be on the way based on these findings. I was so touched at that moment, yes, I wanted papers published, yes, I wanted to learn about biomedical engineering, yes, I was confident in my research skills, and yes, Professor Colvin was the responsible, enthusiastic and compassionate advisor. That day marked the start of all these dreams for the next five years.

Professor Colvin always cared about our physical and mental health. She once asked us what kind of behavior in the lab could really piss her off? The first thing that came to my mind was wasting time on other activities instead of doing research. But she said no. The only thing that could make her angry was seeing us in the lab without goggles and other necessary PPE. She was never the one who would push the students for outcomes, but she would provide useful insights and encourage us to independently think about our research. In the past few years, I could feel that she has put much effort into training our summary, presentation, and writing skills. I have always admired her reading and writing skills as she could scan through hundreds to thousands of papers quickly and get straight to the point that would be useful for our own research and writing. I can never thank Professor Colvin enough for her help and time making me a qualified researcher. Finally, parties in her house were super cool and were especially favorable for us non-native English speakers to learn about American culture. I am grateful for knowing such a noble person as Professor Colvin and appreciate my valuable five-year growth under her guidance. Professor Colvin, I wish you and your family all the best.

Special thanks to Dr. Qingbo Zhang and his wife, Dr. Linlin Zhang. Qingbo was the first Postdoc I made acquaintance with in the Colvin lab. He always had big smiles on his face and was nice to everyone around him. When Professor Colvin told me to learn about the synthesis of magnetic nanomaterials with him for the rotation program, I knew I had the

right guy to turn to. Qingbo was generous to offer everything he had to help me gain knowledge and experience in this new area. For the first few times I shadowed him on the synthesis of nanomaterials in the lab, then as I tried to do it on my own, he was there pointing out my mistakes and explaining to me what could have been wrong. When I prepared my summary slides, he was there to help me improve my presentations patiently. Every time I had struggles with research, he was there to listen and give me advice. I could not have made my experiment successful and have my papers published without him. In retrospect, Qingbo was one reason I joined the Colvin lab, and he was also the one who dedicated himself to the preparation of my Ph.D. In 2019 Qingbo left Brown for Texas and joined his wife at Rice University. I was glad that he could be with his wife but also felt sad about his absence. The distance from Texas to Rhode Island could not hold back our relationship and our collaboration. With his expertise in nanomaterials and his wife's outstanding experience dealing with cells and animals, we together have achieved many fantastic projects, which will be presented in the following content. It has been a privilege to know you, Qingbo, and to collaborate with you is the happiest research experience I've had. I wish you and your wife the best, and may your future career be as smooth as you please.

I would express my gratitude to the current and past members of the Colvin lab, as we have all been part of the "Colvinites". Many thanks to my best lab pals, Xiaoting Guo and Jake Villanova. As we three joined the lab at the same time, we helped each other to become familiar with this lab and the operations of various equipment. I especially appreciate Xiaoting's excellence in chromatography operations. The polymer characterization and emerging contaminants quantification would be a significant burden on me without you.

Dr. Yue Hu, Dr. Caitlin Masterson, Dr. Adriana Mendoza-Garcia, Dr. Hyewon Kim, and Dr. Daniel Garcia-Rojas, thank you all for your diligent maintenance to lab so we could have our research going smoothly. I also appreciate that you all did not hesitate to enlighten us based on your research experience. Yidan Bi, Deanna Stueber, Joshua Dunn, Myung Joo Lee, Phoebe Koval, and Itzel Aponte, it was my pleasure to have worked with you in the lab. I cannot say enough thanks to you all and would only wish you all good luck with your research and your careers. Let's use our wisdom and our hands to push nanotechnology out of the lab!

I greatly appreciate my other two thesis committee members, Professor Ou Chen and Professor Jerome Robinson, for your valuable feedback on my Ph.D. qualifications and your constant encouragement of my research over the years. In my first year as a Ph.D. student, I have had many difficulties in your lectures, Advanced Inorganic Chemistry and Organometallics. I still remember your generous help after classes to make me understand many concepts in the classes. When I finally got an A at the end of the semester, I knew I owed it to you both. I would also like to appreciate the support from the Department of Chemistry and the Department of Engineering, especially from Anthony McCormick, Hector Garces, Joseph Orchard, David Murray, Tun-Li Shen, Russel Hopson, Zachary Saleeba, Rose Barreira, Sheila Quigley, Melissa Shein, Elaine Tucci, Eric Friedfeld, Allen Sylvia, John Geleney, Al Tente, and Robert Wilson. Your service and kind help are what make Brown a famous university and make our research community productive.

Thanks to my friends at Brown, Dr. Min Chen, Dr. Mengqi Shen, Dr. Bo Shen, Dr. Wenyu Bai, Dr. Qizhong Wang, Dr. Chenhui Qian, Dr. Zhenghong Dai, Dr. Kecheng Wei, Zehua Gao, Jordan Yang, Fan Fei, and Xilin Gu. Thank you all for lending a helping hand when

I needed one. Thanks to our collaborators at the University of Illinois Chicago, Dr. Sanoj Raj, and Professor Petr Král. Your expertise in simulation and calculation not only contributed an essential part to our upcoming big papers, but your excellent explanation also helped us understand the mechanism of our magnetic nanomaterials. Thanks to our collaborators at the University of California Berkeley, Dr. Benjamin Fellows, Dr. Prashant Chandrasekharan, Chinmoy Saayujya, and Professor Stephen Conolly. Thank you for your expertise in magnetic particle imaging technology and your warm welcome when I visited the Berkeley campus and your lab.

Finally, I would like to thank my family for their support during my graduate study. I have been making video calls with my parents every weekend since I left them for higher education almost ten years ago. Their constant support was the critical part that sustained my mental health over the years. I am also grateful to have met my girlfriend, Yijie Zhu. Thank you for being with me since 2018. I especially appreciate your love and your constant support. We have encountered many problems and challenges, and we have also dealt with them one by one. Together, we will build our future.

Contents

Curriculum Vitae.....	iv
Publications.....	vi
Preface and Acknowledgements.....	ix
List of Figures	xvii
List of Tables	xvii
Chapter 1 Magnetic Nanocrystal Clusters – A Critical Review on the Synthesis and Applications	1
1.1 Abstract.....	2
1.2 Introduction.....	2
1.3 The formation mechanism of magnetic nanocrystal clusters	5
1.4 Synthesis of the magnetic nanocrystal clusters with controlled dimensions.....	10
1.5 Properties and applications of magnetic nanocrystal clusters	17
1.6 Conclusions and outlook	25
References in Chapter 1	28
Chapter 2 Systematic Synthesis of Iron Oxide Nanocrystal Clusters with Independent Dimensional Control.....	36
2.1 Abstract.....	37
2.2 Introduction.....	38
2.3 Synthesis and dimensional control of the clusters	40

2.4 Surface functionalization of the clusters	49
2.5 Clusters as dynamic photonic crystals.....	52
2.5 Clusters as efficient MRI contrast agent	55
2.6 Conclusion	57
2.7 Experimental Section	58
2.8 Supplemental Figures	71
References in Chapter 2	80
Chapter 3 The Giant Susceptibility of Magnetic Nanocrystal Clusters	86
3.1 Abstract.....	87
3.2 Introduction.....	87
3.3 The structure and magnetic properties of clusters	88
3.4 Micromagnetic simulations on the clusters	97
3.5 The biomedical applications of clusters	102
3.6 Conclusion	106
3.7 Experimental and Simulation.....	107
3.8 Supplemental Figures and Tables	129
References in Chapter 3	150
Chapter 4 Enhanced Susceptibility of Manganese Doped Ferrite Clusters	154
4.1 Abstract.....	155
4.2 Introduction.....	155

4.3 Characterizations of the manganese ferrite clusters	158
4.4 The magnetic and magnetothermal properties of manganese ferrite clusters.....	163
4.5 Applying manganese ferrite clusters for contaminants remediation.....	170
4.6 Conclusion	173
4.7 Experimental section.....	173
4.8 Supplemental figures and tables	180
References in Chapter 4	185
Chapter 5 Tunable Magnetic Cluster Chains and The Enhanced Magnetic Properties	190
5. 1 Abstract.....	191
5.2 Introduction.....	192
5.3 Nanoworm synthesis and characterizations.....	195
5.4 Aqueous-phase Magnetic Characterization	201
5.5 Solid-state Magnetic Characterization	207
5.6 Conclusion	210
5.7 Experimental Section	211
5.8 Supplemental Figures and Tables	218
References in Chapter 5	223

List of Tables

Table 1. 1. Summary of one-step approaches for magnetic cluster synthesis	15
Table 2. 1. The cluster size (D_c), particle size (d_p) and grain size measured by both electron microscopy and x-ray diffraction.....	44
Table S3. 1. Synthesis conditions of iron oxide Clusters with different dimensions.	147
Table S3. 2. Hydrodynamic size of the iron oxide clusters with different dimensions. ...	148
Table S3. 3. Magnetic properties of the iron oxide nanoparticles.	148
Table S3. 4. Magnetic properties of the iron oxide clusters.....	149
Table 4. 1. Comparison of the commercial induction heater and the portable heating device.....	166
Table 4. 1. Comparison of the commercial induction heater and the portable device. ...	166
Table S4. 1. Synthesis and properties of MFCs in Figure 4.4 a.....	183
Table S4. 2. Synthesis and properties of MFCs in Figure 4.4 b.	183
Table S4. 3. Synthesis and properties of MFCs in Figure 4.4 c.....	184
Table 5. 1. Summary of the properties of the nanoworms.....	207

Table S5. 1. The hydrodynamic size and the zeta potential of the 40 nm nanoclusters with different coatings.....	218
--	-----

List of Figures

Figure 1. 1. Synthesis of magnetic nanocrystal clusters.....	4
Figure 1. 2. Limited ligand protection (LLP) mechanism.	6
Figure 1. 3. Illustration of the cluster formation due to conjugative molecules.	7
Figure 1. 4. Effect of Ostwald ripening on the morphology of the clusters.	9
Figure 1. 5. Effect of the ligand concentration on the cluster size.....	10
Figure 1. 6. Effect of the sonication pretreatment on the morphology of clusters.....	12
Figure 1. 7. Synthesis of clusters with independent dimensional control.....	14
Figure 1. 8. Oriented attachment of the primary nanocrystals.....	17
Figure 1. 9. Magnetic properties of clusters.....	18
Figure 1. 10. Cellular localization of clusters.	19
Figure 1. 11. Superior magnetic heating efficiency of clusters.....	20
Figure 1. 12. Application of clusters as heating mediator for magnetic hyperthermia in vitro.....	21
Figure 1. 13. Application of clusters as MRI contrast agent in vivo.....	22
Figure 1. 14. Application of clusters for drug delivery.	23
Figure 1. 15. Clusters for toxic metal removal.....	24
Figure 1. 16. Clusters for reversible photonic crystal.....	25
Figure 2. 1. Synthesis of the iron oxide nanoclusters.....	42
Figure 2. 2. Dimensional control of the cluster synthesis by water.	44

Figure 2. 3. Internal cluster structure.....	48
Figure 2. 4. Surface functionalization of the clusters.	49
Figure 2. 5. Clusters as magnetically controllable photonic crystals.	53
Figure 2. 6. MRI T ₂ contrast highly depends on D _c and weakly on d _p	55
Figure S2. 1. Effect of water on the cluster diameter.	71
Figure S2. 2. High resolution transmission electron microscopy of clusters.....	71
Figure S2. 3. Libraries of uniform magnetic nanoclusters with tunable dimensions.	72
Figure S2. 4. Effect of reaction conditions on the dimensions of clusters.	73
Figure S2. 5. Specific surface area of the clusters.....	73
Figure S2. 6. X-ray diffraction pattern of the clusters.....	74
Figure S2. 7. Raman spectra of the clusters.....	75
Figure S2. 8. Magnetization curves of the clusters.	75
Figure S2. 9. Selected area electron diffraction pattern of the clusters collected over a large area of particles.....	76
Figure S2. 10. FTIR spectra of the clusters.	76
Figure S2. 11. Characterization of the poly(acrylic acid-co-2-acrylamido-2-methyl-1- propane sulfonic acid).....	77
Figure S2. 12. Conjugation of fluorescent molecules onto the clusters.	78
Figure S2. 13. Hydrodynamic sizes and PDIs of the clusters used for photonic crystal...	78
Figure S2. 14. Inverse of T ₂ relaxation time of different cluster samples	79

Figure 3. 1. Tailoring the magnetization of magnetic nanocrystals via changing the level of exchange interaction.....	89
Figure 3. 2. Characterization of Moderately exchange-coupled magnetic nanocrystal clusters.	91
Figure 3. 3. Magnetic properties of both iron oxide nanoparticles and clusters with different dimensions.	95
Figure 3. 4. Monte Carlo simulation on the magnetic properties of iron oxide clusters. ..	97
Figure 3. 5. Clusters are much more effective in applications that use external magnetic fields to heat, move or image.	103
Figure S3. 1. Additional micrograph of the clusters.....	129
Figure S3. 2. TEM and size distributions histograms of the cluster with different cluster sizes.	130
Figure S3. 3. TEM images of the cluster with different primary nanocrystal sizes.	131
Figure S3. 4. The excellent colloidal stability of concentrated clusters in both water and cell growth media (DMEM).....	131
Figure S3. 5. TEM images of the iron oxide nanoparticles with different diameters.	132
Figure S3. 6. The magnetic properties of the nanoparticles and clusters.	133
Figure S3. 7. Dependence of initial susceptibility of iron oxide nanomaterials on their volume.	134
Figure S3. 8. The zero-field-cooled (ZFC) and field-cooled (FC) magnetization curves of the clusters.....	134
Figure S3. 9. The AC susceptibility of the clusters.....	135

Figure S3. 10. The magnetic susceptibility of iron oxide clusters in different forms.	135
Figure S3. 11. The activation volume of the clusters.	136
Figure S3. 12. The magnetic moment and anisotropy energy barrier of clusters and nanoparticles and the effect of magnetic interactions on the magnetic properties of clusters.	137
Figure S3. 13. The magnetic properties simulated using the Monte Carlo methods.	138
Figure S3. 14. Configuration of superspins within the clusters of different exchange constants.....	138
Figure S3. 15. Simulated zero-field-cooled magnetization curve of clusters and their energy barrier.	139
Figure S3. 16. The effect of defects and the orientation of primary nanocrystals on the magnetization curves of the clusters.....	140
Figure S3. 17. Magnetic heating of iron oxide clusters solution above the coil.	141
Figure S3. 18. Cell killing effect of Clusters and nanoparticles in the battery-operated magnetic hyperthermia system.....	142
Figure S3. 19. Magnetic heating efficiency of iron oxide clusters in vivo.....	142
Figure S3. 20. The magnetic hyperthermia treatment of mice.....	143
Figure S3. 21. The histological examination of major organs after different treatments.	144
Figure S3. 22. Results of in vivo magnetic hyperthermia study using iron oxide nanomaterials in the literature and this work.	145
Figure S3. 23. The clusters as MPI contrast agents.....	146

Figure S3. 24. Subcellular localization of the iron oxide clusters and nanoparticles in cells.....	146
Figure S3. 25. The cytotoxicity of clusters.	147
Figure 4. 1. The morphologies, composition, and magnetic properties of the manganese ferrite clusters.....	159
Figure 4. 2. Manganese ferrite clusters with varying dimensions and compositions.....	161
Figure 4. 3. The size-dependent magnetic properties of the manganese ferrite nanoclusters.....	163
Figure 4. 4. The magnetothermal properties of the manganese ferrite nanoclusters.....	165
Figure 4. 5. The magnetic susceptibility and SAR values of the MFC samples.	169
Figure 4. 6. Applying the MFC for the remediation of emerging contaminants.	172
Figure S4. 1. Manganese ferrite clusters as ferrofluid.....	180
Figure S4. 2. The electronic circuit diagram of the portable heating device used in this study.....	181
Figure S4. 3. Reading from the oscilloscope.	181
Figure S4. 4. The magnetic and magnetothermal properties of the isolated nanoparticles.	182
Figure S4. 5. HPLC analysis of streptomycin and its degradation by the MFCs.	182
Figure 5. 1. Forming the magnetic nanochains via magnetic interactions.	196

Figure 5. 2. Synthesis of the nanoworms in different conditions.....	198
Figure 5. 3. SEM of the nanoworm samples with different curvatures.....	199
Figure 5. 4. Effect of magnetic field strength on the average length of the chains.....	201
Figure 5. 5. The magnetic properties of the nanoworms in aqueous solution.	203
Figure 5. 6. Comparison of the initial magnetic susceptibilities of all nanoworm samples and the free nanoclusters.....	205
Figure 5. 7. The anisotropic magnetic properties of the nanoworm (NW3) in the solid state.....	210
Figure S5. 1. The effect of magnetic field uniformity on the curvature of the chains. ...	218
Figure S5. 2. The optical images of the aqueous nanoworms solution show the excellent colloidal stability.	219
Figure S5. 3. The effect of the cluster size and surface coating on the formation of the nanoworms.....	219
Figure S5. 4. The chain length distribution of the nanoworm samples.....	220
Figure S5. 5. The magnetization curves of the non-straight nanoworms in aqueous solution.....	221
Figure S5. 6. Magnetic properties of the solid nanoworms.....	222
Figure S5. 7. Nanoworms as MRI contrast agent.....	222

Chapter 1

Magnetic Nanocrystal Clusters – A Critical Review on the Synthesis and Applications[†]

[†] Reprinted (adapted) with permission from Xiao, Z., Zhang, L., Colvin, V.L., Zhang, Q. and Bao, G. Synthesis and Application of Magnetic Nanocrystal Clusters. Industrial & Engineering Chemistry Research, 2022, doi.org/10.1021/acs.iecr.1c04879. Copyright © 2022, American Chemical Society

1. Magnetic Nanocrystal Clusters – A Critical Review on the Synthesis and Applications

1.1 Abstract

Magnetic nanocrystal clusters exhibit unique properties that differ from the constituent nanocrystals due to the intra-cluster interactions. This review article summarizes the recent advances in the synthesis and application of magnetic nanocrystal clusters. Specifically, we describe the formation mechanism of the clusters, discuss the strategies to control the dimensions of the clusters and primary nanocrystals, and showcase the applications of clusters in magnetic hyperthermia cancer therapy, magnetic resonance imaging, drug delivery, wastewater treatment, and the formation of photonic crystals. The opportunities and challenges in improving magnetic nanocrystal clusters for different applications are also discussed.

1.2 Introduction

When the dimension of magnetic materials is reduced to a specific size, the magnetization of particles can randomly flip direction due to the thermal fluctuation.^[1] This phenomenon is called superparamagnetism. Superparamagnetic nanocrystals can be magnetized quickly in an external magnetic field, and the magnetization disappears when the magnetic field is removed.^[1-3] The superparamagnetism of nanocrystals is usually manifested by the zero remanence and coercivity in the magnetization curve. Due to their interesting properties, superparamagnetic nanocrystals remain a rich source of scientific inquiry and technological exploration. They have found many applications in a wide variety of fields,

such as wastewater treatment, oil reservoir imaging, drug delivery, and hyperthermia for cancer treatment.^[4-9]

Extensive efforts have been made to generate magnetic nanocrystals of different sizes and determine their size-dependent properties.^[10-13] It has been demonstrated that wet chemistry offers a powerful tool to generate uniform nanocrystals dispersed in solutions.^[14-17] Many solution chemistry methods have been developed to synthesize an extensive library of magnetic nanocrystals with different sizes and compositions. These nanocrystals have enabled researchers to establish the relationship between particle size and magnetic properties and explore their uses in a wide variety of applications.^[18-21] It was found that big nanocrystals exhibit better performance than smaller ones in many applications since the big magnetic moments make the particles more susceptible to the external magnetic field.^[22-26] Increase in nanocrystal size, however, will cause an increase in the anisotropy energy of the particles. The increased anisotropy energy will block the thermal fluctuation of the magnetic moment, as manifested by their increased coercivity and remanence.^[27-29] The nanocrystals in the blocked state tend to aggregate in the solution, thus compromising their functionalities in many applications.^[30-33]

Recently, it was found that the properties of magnetic nanomaterials can be further modified by clustering nanocrystals into controlled aggregates.^[34-37] Each aggregate, or cluster, consists of tens to thousands of small single nanocrystals.^[38-43] The magnetic properties of clusters may dramatically differ from those of constituent particles due to the interaction between particles.^[35,44] For example, the cluster can retain superparamagnetism at a much bigger size than isolated nanocrystals.^[45,46] Because of these different properties,

nanocrystal clusters display much better performance in some applications.^[34] Since the properties of clusters depend on the dimensions of both clusters and primary particles, it is crucial to control these two structural parameters for the establishment of structure-property relationship and achievement of optimal performance for a specific application. The synthesis of magnetic nanocrystal clusters has drawn the attention of many researchers, and many methods have been reported to control the size of the cluster and primary particle. The nanocrystal clusters are usually synthesized using either two-step self-assembly or one-step polyol synthesis, as shown in Figure 1.1.^[47, 48]

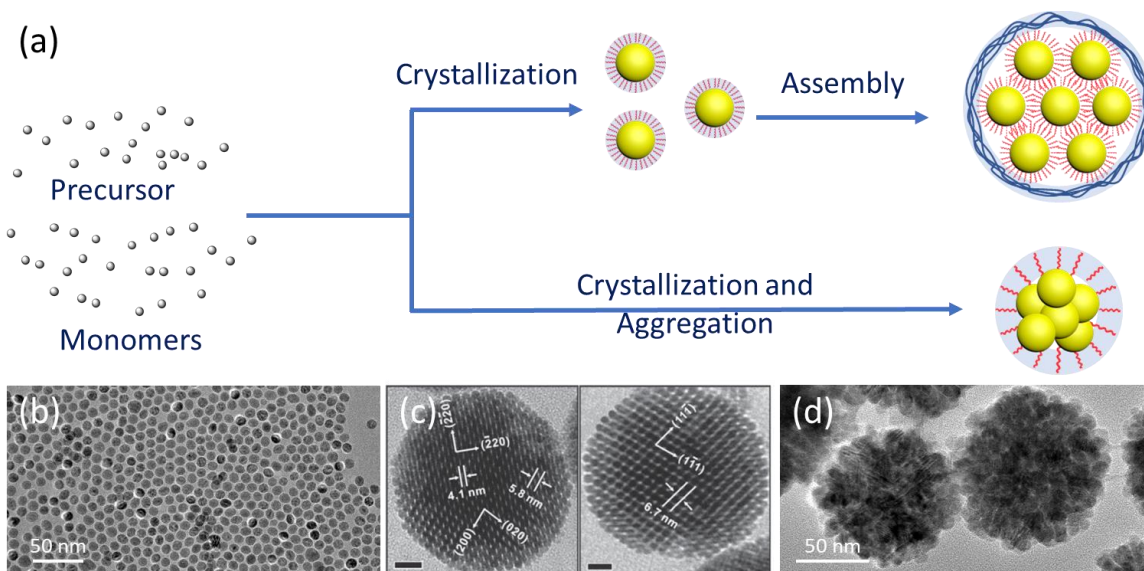


Figure 1. 1. The synthesis of magnetic nanocrystal clusters. (a) Schematic illustration of the one-pot method and two-step method to generate clusters. (b) TEM images of isolated magnetic nanocrystals. (c) Clusters formed via the two-step method. Figure adapted from reference [38] with permission. Copyright 2007 American Chemical Society. (d) Clusters formed via one-pot synthesis.

In this article, we review the recent advances in the synthesis and application of magnetic nanocrystal clusters. We focus our discussion on the clusters synthesized using the one-pot method since this method is efficient to control the dimensions of the cluster. We begin the

discussion with the formation mechanism of magnetic nanocrystal clusters, followed by the summary of the effort to control the cluster size and primary particle size, the unique magnetic properties of the clusters, and the application of magnetic nanocrystal clusters in various fields. We conclude this article with an outlook for the future research directions of magnetic nanocrystal clusters, including the opportunities and challenges.

1.3 The formation mechanism of magnetic nanocrystal clusters

The ferrite magnetic nanocrystal clusters were usually synthesized by the thermodecomposition of the metal salts. In a typical synthesis of clusters, a metal precursor, a capping agent, and an alkaline substance are mixed in a polyol solvent. The metal precursor undergoes forced hydrolysis reactions and reductions at high temperatures and turns into monomers of the nanocrystals (metal oxide), which eventually form the clusters. While iron precursors may undergo self-hydrolysis in many solutions, the forced hydrolysis at very high rate is essential for the formation of uniform magnetic nanocrystal clusters. The most common reactants are summarized in Table 1. By changing the nature and concentration of the reactants, the reaction time, and the reaction temperature, clusters consisting of tens to thousands of nanocrystals could be generated.^[49, 50] The magnetic nanocrystal clusters are generally deemed to follow a two-step formation mechanism. In the first step, primary nanocrystals are formed through nucleation and growth, as indicated by the conventional LaMer mechanism. Then these primary nanocrystals aggregate to form clusters. The aggregation of the primary nanocrystals to form clusters might follow different pathways, depending on the reaction system and conditions. The detailed mechanism of the cluster formation is still unclear.

Metal oxide nanocrystal clusters might be formed through limited ligand protection (LLP), first proposed by Narayanaswamy et al. (Figure 1.2).^[51] They found that isolated In_2O_3 nanocrystals were formed when the amount of ligands was much higher than that of the metal precursor, while clusters (nanoflowers) were formed when the amount of ligand was significantly decreased. The nanocrystals formed in the reaction tend to group together to reduce their surface areas until the desired ligand to surface ratio is achieved if the amount of ligand is insufficient and the primary nanocrystals cannot be fully protected during the nanocrystal formation. The ligand to surface ratio also accounts for the surprisingly high uniformity of the clusters. In principle, the LLP mechanism could account for the formation of clusters composed of other metal oxides, such as iron oxide.

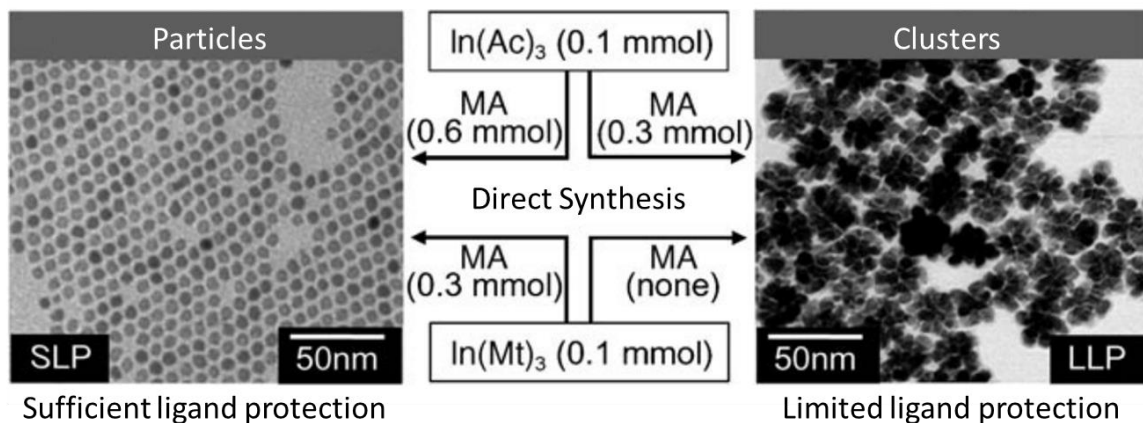


Figure 1. 2. The formation of nanocrystal clusters because of the limited ligand protection (LLP). In sufficient ligand protection (SLP), isolated nanocrystals were formed. In LLP, particles tended to form clusters to minimize the surface energy. Figure adapted from reference [51] with permission. Copyright 2006 John Wiley and Sons.

Many researchers found that clusters could be formed even if there is sufficient amount of capping agents in the reaction solution. The formation of the clusters might be because of the competition between the attractive force and the repulsive force, as suggested by Cheng

et al.^[48] The primary particles assume high surface tension, which makes them tend to aggregate. Meanwhile, the capping agent binds to the particle surface, which provides the electrostatic and/or steric repelling force. The balance between these two opposite driving forces might account for the formation of clusters and determine the cluster dimension.

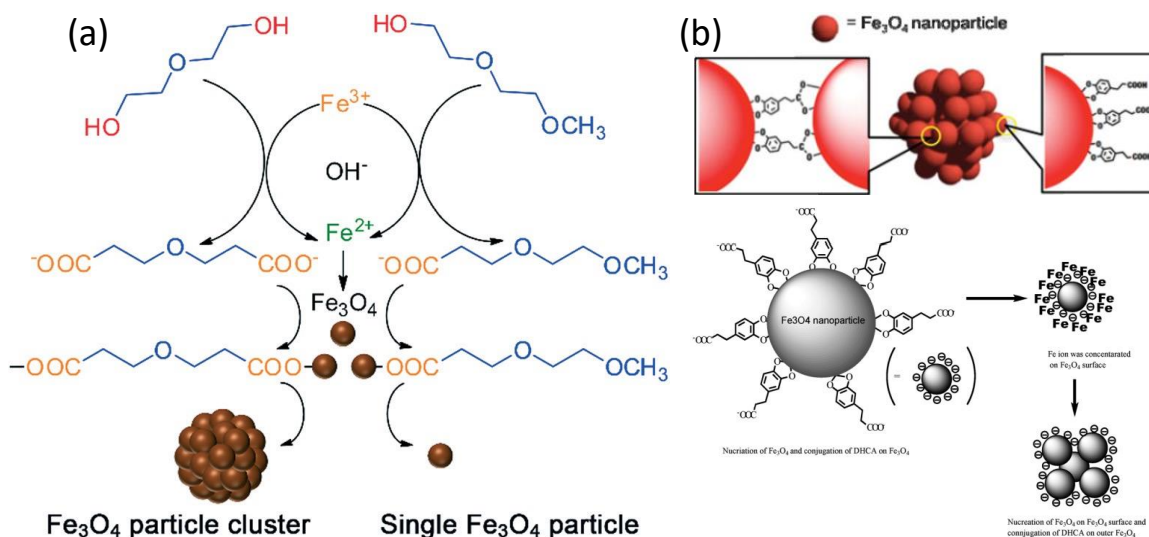


Figure 1.3. Schematic illustration of the cluster formation due to the conjugative molecules in the reaction. (a) The primary nanocrystals were interconnected by dicarboxylic acids. Figure adapted from reference [60] with permission. Copyright 2011 Royal Society of Chemistry. (b) The primary nanocrystals were interconnected by 3,4-dihydroxycinnamic acid (DHCA). Figure adapted from reference [59] with permission. Copyright 2018 Royal Society of Chemistry.

The clusters could be formed via the ligands' crosslinking of the primary nanocrystals. Wei et al. synthesize magnetite nanocrystal clusters using diethylene glycol as the solvent and reducing agent. They attributed the formation of clusters to the dicarboxylic acids, the oxidative product of diethylene glycol (Figure 1.3).^[59] The dicarboxylic acids could crosslink the primary particles to form clusters. If triethylene glycol (TEG) or tetraethylene glycol (TTEG) were used as the solvent and reducing agent instead of diethylene glycol, only particles were observed as the oxidative product of TEG or TTEG cannot interconnect

the primary particles. In another work, Togashi et al. synthesized magnetite nanocrystal clusters using 3,4-dihydroxyhydroxycinnamic acid (DHCA) as the capping agent. Both the phenolic hydroxyl groups and the carboxylic groups in DHCA can form dative bonds with iron, thus interconnecting primary nanocrystal to clusters.^[60]

The clusters might undergo Ostwald ripening once the reaction is complete, which leads to the change of the cluster morphology. In the synthesis of isolated nanocrystals, Ostwald ripening leads to the growth of big particles at the expense of small particles. In the clusters, Ostwald ripening usually causes the increase of the primary particles. Gerber et al. monitored the formation process of magnetite nanocrystal clusters using high resolution TEM (HRTEM) (Figure 1.4a).^[57] They found that the diameter of the primary particles could increase from 5 nm to 25 nm if the reaction time increased from 7 hours to 13 hours while the cluster diameter remained 250 nm. Gavilan et al. found a similar phenomenon in the generation of maghemite nanocrystal clusters (Figure 1.4b). Both TEM images and X-ray diffraction (XRD) spectra clearly show that the primary particles increase dramatically with reaction time.

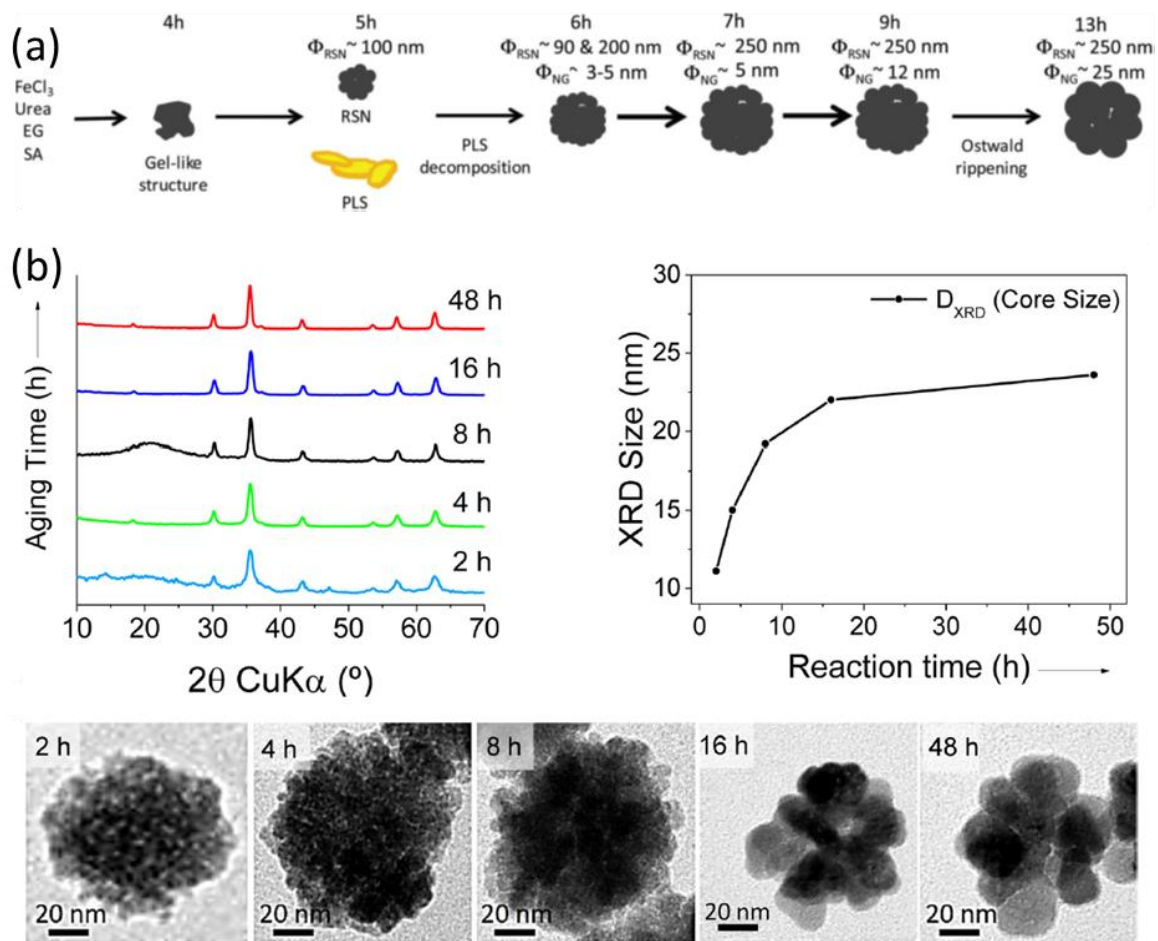


Figure 1. 4. The effect of Ostwald ripening on the morphology of the clusters. (a) Schematic illustration of the formation of the clusters. Figure adapted from reference [57] with permission. Copyright 2017 Royal Society of Chemistry. (b) Time-dependent observation on the formation of the nanoclusters corresponding to the Ostwald ripening. Both TEM and XRD showed the nanocrystals with increasing size over time. Figures adapted from reference [58] with permission. Copyright 2017 American Chemical Society.

1.4 Synthesis of the magnetic nanocrystal clusters with controlled dimensions

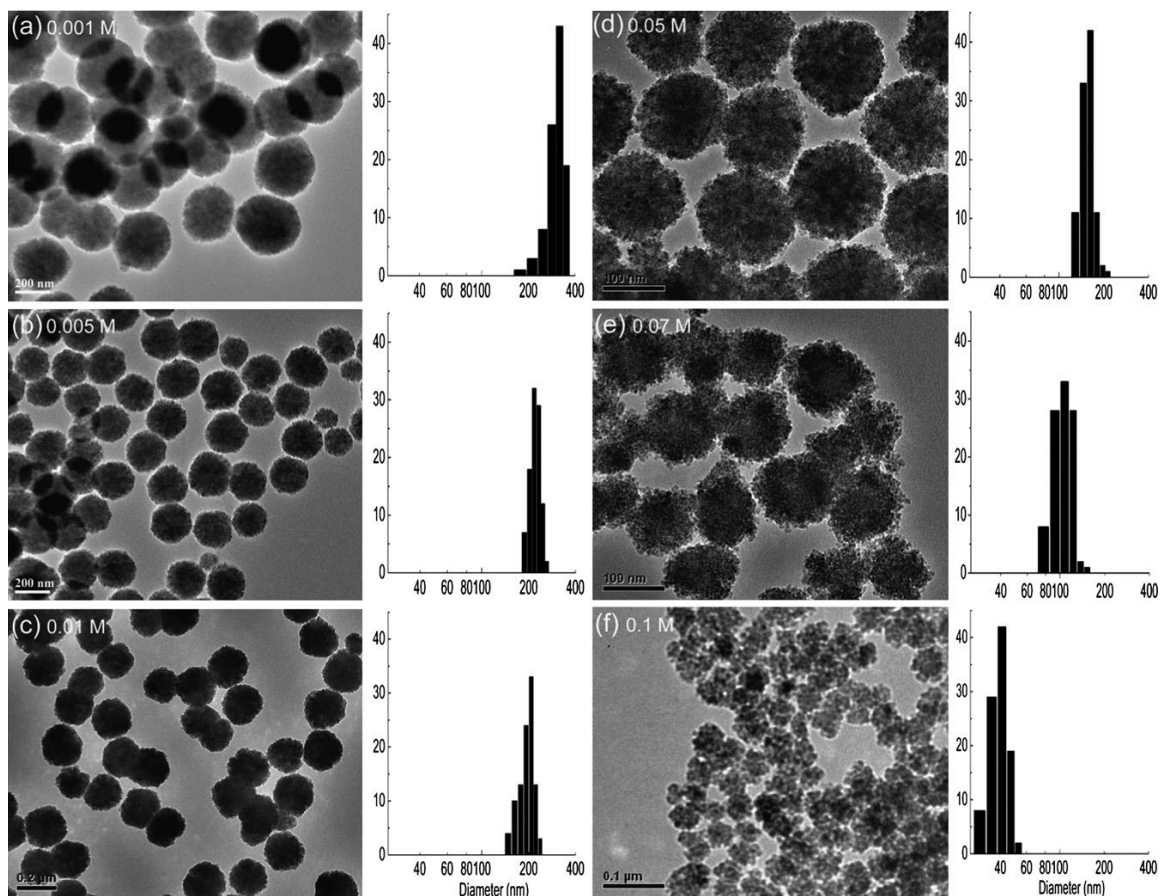


Figure 1. 5. The effect of the ligand concentration on the cluster size. The clusters with decreasing cluster diameter from 300 nm to 40 nm by increasing sodium citrate concentration in the synthesis. The clusters have good uniformity, and the standard deviation of the cluster diameter measured by TEM is less than 20%. Figure adapted from reference [48] with permission. Copyright 2009 Royal Society of Chemistry.

Synthesis of the clusters with controlled dimensions is challenging since there are two parameters to control, cluster size and primary particle size. In principle, the size of the cluster and primary particles can be controlled by varying the nature and concentration of the reactants, the reaction time, and the reaction temperature.^[52-68] The relationship between the reaction conditions and the kinetics of nucleation, growth and aggregation has not been well established. The reaction system and conditions for dimension control were

usually determined through extensive experimentation. Researchers have developed many procedures to generate magnetic nanocrystal clusters with different dimensions. The reaction schemes used are summarized in Table 1.1.

The hydrolysis rate of metal precursors plays a vital role in controlling the size of clusters. It was found that the hydrolysis rate of the precursors is positively correlated to the cluster size. Ge et al. prepared magnetite clusters from 30 nm to 180 nm by simply changing sodium hydroxide concentration.⁴⁵ Hydroxide in the solution can create an alkaline medium that induces the forced hydrolysis of iron precursors at high temperatures. The increase of sodium hydroxide concentration accelerated the hydrolysis rate, thus leading to a high concentration of primary particles. The high concentration of primary particles might result in a larger cluster diameter. Their flexible synthesis with an accurate size control on the clusters was a milestone for discovering the size-dependent properties of the clusters. The hydrolysis rate can also be increased by increasing the amount of metal precursors. Liu et al. synthesized clusters from 80 to 400 nm by simply increasing the concentration of iron chloride from 0.05 to 0.25 mmol L⁻¹.^[70]

The ratio between the ligand and the metal precursor significantly influences the cluster size. Several studies found that the ligand to metal precursor ratio is negatively correlated to the cluster size. Cheng et al. found that the size of the magnetite clusters decreased when concentration of the ligand, sodium citrate was increased. This finding is in agreement with the LLP mechanism.^[48] The authors synthesized uniform magnetite clusters by changing the concentration of the ligands (Figure 1.5). As the ratio of ligand to precursor increased from 1/120 to 100/120, the cluster diameter decreased from 300 nm to 40 nm. Part of the carboxylic groups on the citrate form the dative bond with the iron oxide core, while the

rest can provide electrostatic stabilization against other clusters. Using another reaction system, Wei et al. successfully controlled the cluster diameter from 15 to 70 nm by reducing the amount of polyacrylic acid (PAA) from 8 mmol to 0.^[59] The clusters prepared without PAA were coated with the dicarboxylic acids that originated from the solvent ethylene glycol. In addition to the concentration of the ligands, the ligand to metal precursor ratio can also be varied by changing the concentration of the metal precursor, thus generating clusters of different sizes.^[49, 70, 72]

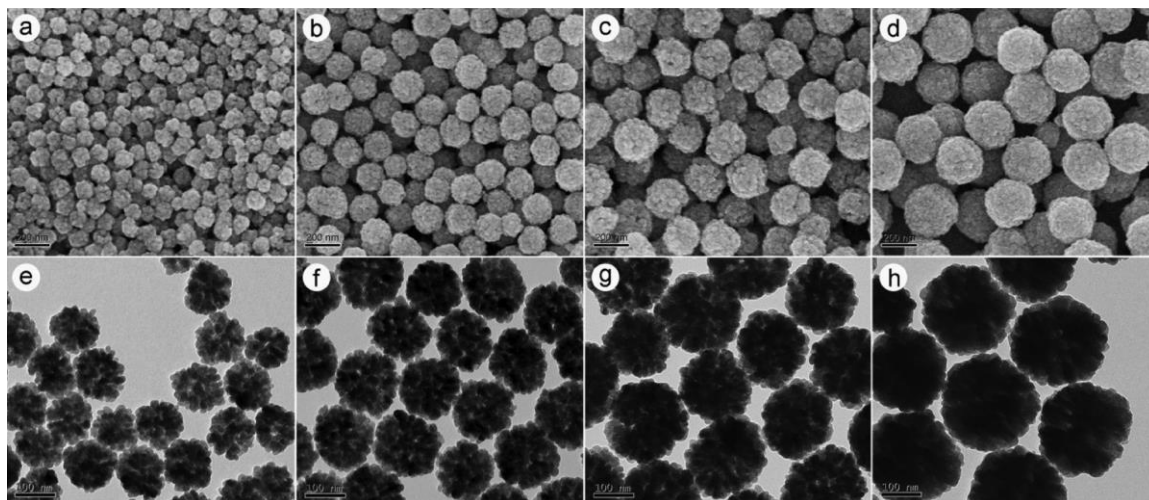


Figure 1. 6. The effect of the sonication pretreatment on the morphology of clusters. SEM (a–d) and TEM (e–h) images of four cluster samples were obtained from different times of sonication pretreatment: 40 min (a, e), 30 min (b, f), 15 min (c, g), and 5 min (d, h), while other parameters were kept unchanged (0.68 g of $\text{FeCl}_3 \cdot 6\text{H}_2\text{O}$, 1.2 g of NaAc, and 0.034 g of EDTA-2Na in 20 mL of ethylene glycol at 200 °C for 10 h). Figure adapted from reference [62] with permission. Copyright 2013 American Chemical Society.

The pretreatment of the reaction mixture also affects the size of clusters. Lin et al. prepared magnetite clusters of different sizes by sonicating the reaction mixture for different periods of time (Figure 1.6).^[62] They found that longer sonication pretreatment on the reaction mixture led to small clusters. This is because the precursors and the ligands were more readily combined to form the primary nanocrystals when the sonication time was longer.

Although such a method is simple and effective, the mixing effect is hard to quantify. This method may not be well reproducible. This study suggests that the reactants should be well mixed in the solvent before increasing temperature to achieve good control over the cluster size in the reaction.

Another factor that influences the size of clusters is the selection of solvent. The polyol solvent also serves as a reducing agent in generating the magnetite nanocrystal clusters. After going through forced hydrolysis, the iron(III) salt will form $\text{Fe}(\text{OH})_3$ that is partially subject to reduction by the polyols to form $\text{Fe}(\text{OH})_2$ and convert to Fe_3O_4 eventually.^[79] The reducing capacity of the polyols determines the rate of the formation of the monomers, thus changing the size of the clusters. Different types of polyols have been used to tune the cluster size.^[47] Using a mixture of two polyols as solvent provides an efficient way to vary the reducing capacity of the solvent. Huang et al. reported the synthesis of magnetite clusters from 50 to 400 nm by changing the ratio of ethylene glycol to diethylene glycol.^[68] With the increase of the diethylene glycol content, the clusters formed in such solvent mixture became smaller. No clusters were formed in a pure diethylene glycol solvent, which could be ascribed to the extremely slow reduction that impeded the growth of the clusters. Similar observations have been reported using other polyols, such as triethylene glycol, 1,2-propanediol, and polyethylene glycol.

The addition of a small amount of water into the reaction mixture could dramatically reduce the size of clusters. The addition of water to the solvent will cause the reduction of the viscosity, thus leading to smaller clusters.^[63, 64] The viscosity of water is around 1 mPa·s at room temperature, whereas the typical value for various glycols is about 15 to 30 times higher.^[75] In a highly viscous medium, the movement of the primary nanocrystals is more

kinetically confined and tends to form larger clusters.^[63, 64] Conversely, when the primary nanocrystals have higher mobility in a less viscous medium, smaller clusters can be formed. Hemery et al. found that the diameter of the maghemite clusters decreased from 50 nm to 16 nm by increasing the amount of water in the solvent.^[63]

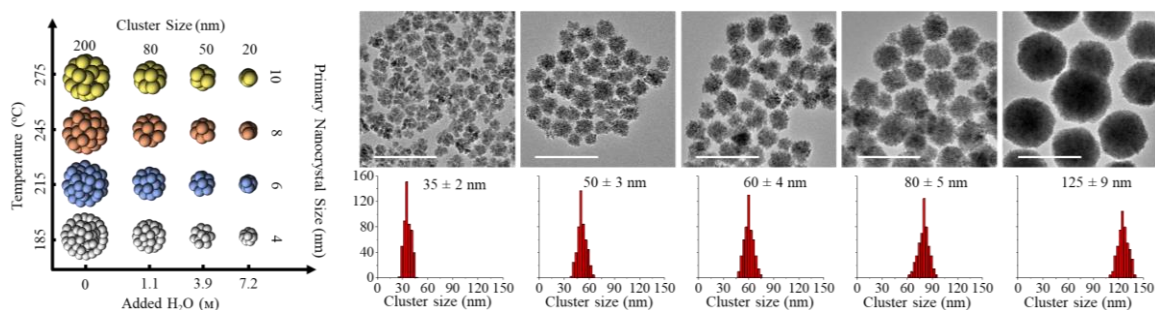


Figure 1. 7. Synthesis of clusters with independent control of cluster size and primary particle size. (a) Proposed scheme for the independent dimensional control of the clusters. The amount of water can only dictate the cluster size, while the reaction temperature can determine the primary nanocrystal size. A library of clusters, with the cluster diameter from 20 to 200 nm and the size of the primary nanocrystals from 4 to 10 nm, can be formed in this synthetic system. (b) TEM images and size distributions of the cluster samples with different cluster sizes. Scale bar: 200 nm. The amount of added water for each cluster sample synthesis was 2.0, 1.5, 1.0, 0.4, and 0.1 mL, from left to right. Figure adapted from reference [80] with permission. Copyright 2020 American Chemical Society.

By varying two or more factors, it is possible to control both the cluster size and nanocrystal size. Xiao et al. successfully developed libraries of clusters with independent dimensional control over the two parameters by changing the amount of water and the reaction temperature (Figure 1.7).^[80] In this work, iron chloride, poly(acrylic acid), urea, and ethylene glycol were used as the iron precursor, the stabilizing agent, the base, and the solvent, respectively. In this reaction system, the amount of water only affected the size of the cluster and had a negligible effect on the primary nanocrystal size. The reaction temperature only influenced the primary nanocrystal size and had a negligible effect on the cluster size. Changing the reaction temperature and amount of water provides an efficient

approach to produce the magnetite nanocrystal cluster library with tunable cluster size and primary particle size. Change of other reaction conditions, such as the concentration of ligands (polyacrylate) and iron precursors, can affect the sizes of both clusters and primary particles. Nevertheless, this method was only applicable when urea was used to provide the alkaline environment for forced hydrolysis of the iron precursors. In some other reaction systems where sodium acetate was used as a base, change in the cluster size was usually accompanied by the change on the primary nanocrystal size, and vice versa, as reported by Xuan et al.^[67] This was ascribed to the fact that the acetate also binds to the nanocrystal surface.^[48]

While most strategies to control the cluster dimensions were exploited using magnetite as an example, these strategies can be used in other metal oxide systems such as maghemite and ferrites. Liu et al. synthesized zinc ferrite ($ZnFe_2O_4$) clusters with a size range of 300 to 600 nm.^[71] They found that increase in the concentration of sodium acetate led to a reduction of cluster size. A library of ferrite clusters, including manganese, cobalt, and nickel, have been reported by Otero-Lorenzo et al. These materials greatly expand the library of magnetic nanocrystal clusters and provide a rich source for scientific exploration and technological development.^[61]

Table 1. 1. Summary of one-step approaches for magnetic cluster synthesis

Reference	Composition	Capping agent	Alkaline	Solvent	Reaction Temp	Reaction method	Size range	Size control
Cheng ^[47] (2011)	Fe_3O_4/Fe_2O_3 mixed phase	Succinic acid	Urea	EG and PG	200 °C	Hydrothermal	Varying Dc 50-300 nm	solvent ratio and reaction time
Gavilan ^[58] (2017)	Fe_3O_4	Polyvinylpyrrolidone (PVP40)	Sodium acetate	EG	200 °C	Hydrothermal	Dc at 60 nm, varying grain size from 11-24 nm (XRD)	reaction time
Ge ^[45] (2007)	Fe_3O_4	polyacrylic acid (PAA)	Sodium hydroxide	Diethylene glycol (DEG)	220 °C	NaOH Injection	Varying Dc 30-180 nm, dp at 6 nm	NaOH concentration
Hemery ^[63] (2017)	$\gamma-Fe_2O_3$ (oxidized by nitrate)	N/A	Sodium hydroxide	EDG and N-methyldiethanolamine (NMDEA)	220 °C	Thermal decomposition	Varying Dc 10-50 nm	water content

Kostopoulou ^[64] (2014)	γ -Fe ₂ O ₃	PAA	Sodium hydroxide	DEG	220 °C	NaOH Injection	Dc 50 and 85 nm	water content in solvent with different grade
Lin ^[62] (2013)	Fe ₃ O ₄	Ethylenediaminetetraacetic acid disodium (EDTA Na ₂)	Sodium acetate	EG	180-200 °C	Hydrothermal	Varying Dc 100-260 nm, dp at 6 nm	different time of sonication pretreatment
Maity ^[65] (2011)	Fe ₃ O ₄	N/A	iron(III) acetylacetonate	tri(ethylene glycol) (TREG) and triethanolamine (TREA)	245-280 °C	Thermal decomposition	Dc 44 nm	TREG and TREA ratio
Nikitin ^[66] (2018)	Fe ₃ O ₄	Series of organic acid	N/A	Benzyl ether and 1,2-hexadecanediol	210-260 °C	Thermal decomposition	Varying Dc 20-40 nm	using different ligand in the synthesis
Otero-Lorenzo ^[61] (2017)	Fe ₃ O ₄ and Mn _x Fe _{3-x} O ₄	Polyethylene glycol	Sodium acetate	EG	185 °C	Hydrothermal	Varying Dc 30-180 nm, dp at 7 nm	reaction time
Xuan ^[67] (2009)	Fe ₃ O ₄	Polyvinylpyrrolidone (PVP, K30)	Sodium acetate, sodium acrylate	EG and DEG	200 °C	Hydrothermal	Varying Dc 6-280 nm, varying dp 6-14 nm	Dc controlled by EG/DEG ratio; dp controlled by acetate/acrylate ratio
Cheng ^[48] (2009)	Fe ₃ O ₄	Sodium citrate	Urea	EG	200 °C	Hydrothermal	Varying Dc 40-300 nm	amount of sodium citrate
Gerber ^[57] (2017)	Fe ₃ O ₄	Succinic acid	Urea	EG	200 °C	Hydrothermal	Varying Dc 100-250 nm, varying dp 3-25 nm	reaction time
Huang ^[68] (2016)	Fe ₃ O ₄	PEG-2000, hexadecyltrimethyl ammonium bromide (CTAB)	Sodium acetate	EG, DEG, PG and triethylene glycol (TEG)	200 °C	Hydrothermal	Varying Dc 55-480 nm	ratio of solvent
Lartigue ^[44] (2012)	γ -Fe ₂ O ₃ (oxidizing Fe ₃ O ₄ by nitrate)	N/A	Sodium hydroxide	EDG and NMDEA	220 °C	Thermal decomposition	Varying Dc 10-30 nm	ratio of solvent
Liang ^[69] (2013)	Fe ₃ O ₄	PAA and sodium dodecyl benzene sulfonic (SDBS)	Sodium acetate	EG	200 °C	Hydrothermal	Varying Dc 200-400 nm	amount of PAA or SDBS
Liu ^[70] (2009)	Fe ₃ O ₄	Sodium citrate	Sodium acetate	EG	200 °C	Hydrothermal	Varying Dc 80-410 nm	amount of iron precursor and ligand
Liu ^[71] (2017)	ZnFe ₂ O ₄	N/A	Sodium acetate	EG	200 °C	Hydrothermal	Varying Dc 330-560 nm	amount of sodium acetate
Lu ^[72] (2016)	Fe ₃ O ₄	PEG diacid (Mn = 600 Da) and oleate	N/A	phenyl ether	260 °C	Thermal decomposition	Dc at 25 and 62 nm	amount of iron precursor and ligand
Luo ^[73] (2009)	Fe ₃ O ₄	N/A	Sodium acetate	EG	200 °C	Hydrothermal	Varying Dc 90-260 nm	reaction time
Pereira ^[74] (2015)	Fe ₃ O ₄ /Fe ₂ O ₃ mixed phase	alkanolamines diethanolamine (DEA), triethanolamine (TEA) and triisopropanolamine (TIPA)	N/A	Hydrochloric acid	100 °C	Thermal decomposition	Varying Dc (DLS) 30-40 nm	using different ligand
Togashi ^[60] (2011)	Fe ₃ O ₄	3,4-dihydroxyhydroxycinnamic acid (DHCA 98%)	Potassium hydroxide	Water	250 °C	Hydrothermal	Varying Dc 50-400 nm	reaction time
Tong ^[75] (2015)	Fe ₃ O ₄ /Fe ₂ O ₃ mixed phase	PEG-2000	sodium carbonate	EG	200 °C	Hydrothermal	Varying Dc 30-290 nm	amount of water
Wang ^[49] (2006)	Fe ₃ O ₄	1,6-hexanediamine	Sodium acetate	EG	190 to 205 °C	Hydrothermal	Varying Dc 100-200nm	amount of iron precursor
Wang ^[76] (2013)	Fe ₃ O ₄	poly (diallyldimethyl ammonium chloride) (PDDA)	Sodium acetate	EG	200 °C	Hydrothermal	Varying Dc 90-350 nm, varying dp 15-35 nm	amount of PDDA

Wang ^[77] (2015)	Fe ₃ O ₄	Sodium citrate	Sodium acetate	EG and DEG	200 °C	Hydrothermal	Varying Dc 60-250 nm, varying dp 6-9 nm	ratio of solvent
Wei ^[59] (2018)	Fe ₃ O ₄	PAA	Sodium hydroxide	DEG	200 °C	Thermal decomposition	Varying Dc 15-70 nm	amount of PAA
Xi ^[46] (2008)	Fe ₃ O ₄	Oleic acid	Sodium acetate	EG	200 °C	Hydrothermal	Varying Dc 100-400 nm	amount of iron precursor
Kim ^[78] (2019)	Fe ₃ O ₄ and Mn _x Fe _{3-x} O ₄	N/A	Sodium acetate	EG	200 °C	Thermal decomposition	Dc 29 and 33 nm	using different metal precursor

1.5 Properties and applications of magnetic nanocrystal clusters

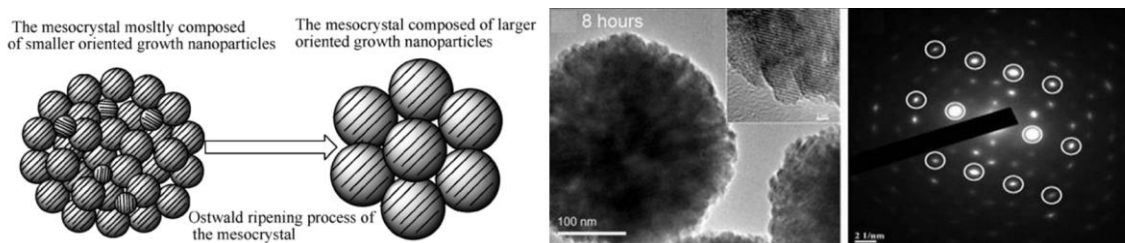


Figure 1. 8. Oriented attachment of the primary nanocrystals. The parallel orientation of the primary nanocrystals was facilitated by Ostwald ripening. Figure adapted from reference [47] with permission. Copyright 2011 Royal Society of Chemistry.

The magnetic nanocrystal clusters display unique magnetic properties that are different from their constituent primary particles due to the unique structure of the clusters. These magnetic properties arise from the interactions between primary nanocrystals within the cluster.^[81-83] Particularly, the clusters might show more attractive properties when the primary particles within a cluster assume the same crystallographic orientation (Figure 1.8). One interesting property is that the clusters may remain superparamagnetic until hundreds of nanometers. These superparamagnetic clusters assume much more magnetic volume than the isolated nanocrystals.^[44, 45, 80] In addition, magnetic nanocrystal clusters show high saturation magnetization (Figure 1.9).^[45] These unique properties are not only interesting for fundamental research but also useful for technological development since these properties make the clusters more efficient in moving, heating, and imaging for many applications. The application of these materials in many different fields has been explored.

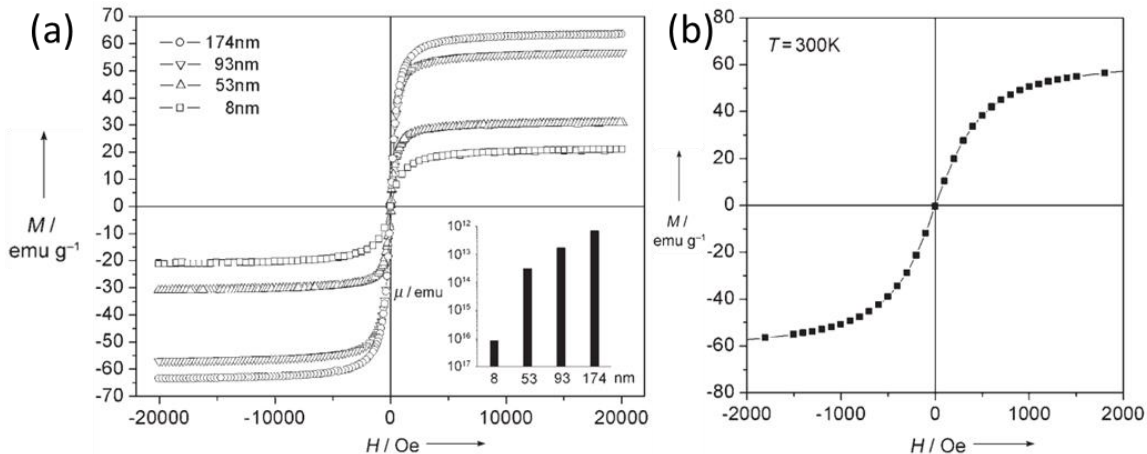


Figure 1. 9. Magnetic properties of clusters. (a) The magnetization curves of the clusters with different sizes. (b) The 93 nm clusters demonstrated superparamagnetic behavior with zero coercivity and remanence at room temperature. Figure adapted from reference [45] with permission. Copyright 2007 John Wiley and Sons.

Another interesting feature of magnetic nanocrystal clusters is their high uptake by various types of cells. Hemery et al. studied the uptake of 30 nm clusters coated with polyethylene glycol (PEG) using U87 glioblastoma cells.^[85] Both the confocal and TEM images show that the clusters were localized in the lysosomes of the cells, suggesting the clusters were taken up through an endocytosis pathway (Figure 1.10). The number of clusters entering the cell was much higher than the isolated iron oxide nanocrystals. Kim et al. investigated the uptake of magnetite and manganese ferrite clusters using Vibrating-sample magnetometer.^[78] After incubating the cancer cells with the clusters, internalization of the clusters was determined by measuring the magnetization of the cells. They found that the uptake of the clusters depends on the type of cells. MCF10A cells had the highest cellular uptake capability among various types of cells. The authors also found the roughness of the cluster surface had significant impact on the cellular uptake, where the clusters covered with protein corona were preferably taken up by the cells. The clusters remain their

morphology in all the *in vivo* applications since they are hard aggregates. While large clusters show higher delivery efficiency in the *in vitro* studies, more work are needed to determine the optimal size for the *in vivo* applications since large clusters will be cleared out by the mononuclear phagocytic system.

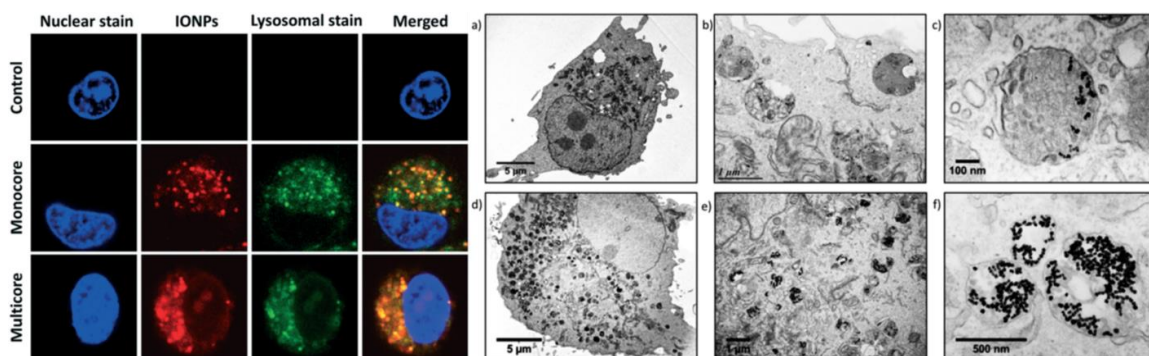


Figure 1. 10. Cellular localization of clusters. The confocal and TEM images showing the localization of clusters (multicore) and particles (monocore) in cells. U87 glioblastoma cells were incubated with 15 nm nanocrystals and 30 nm clusters to load the nanocrystals. Figure adapted from reference [85] with permission. Copyright 2017 Royal Society of Chemistry.

The magnetic clusters are very efficient in generating heat under the alternating magnetic field (AMF), which makes them a good candidate for hyperthermia cancer treatment. Lartigue et al. prepared the maghemite clusters and compared their magnetic heating performance with isolated nanocrystals. They found that clusters outperformed isolated nanocrystals. When placed in the same AMF, the clusters could elevate the temperature of the surrounding solution up to 35 °C in about 30 seconds, which was seven times higher than that of conventional nanocrystals at the same concentration (Figure 1.11a).^[44] They attributed the improved performance of clusters to the cooperative magnetic behavior of primary particles within a cluster. The enhanced magnetic heating of clusters was also reported by Hemery et al.^[63] They found that the magnetic heating performance of clusters

increases with the cluster diameter in the range of 10 to 35 nm. (Figure 1.11b). The improved magnetic heating performance of clusters was used to kill tumor cells by Lartigue et al.^[44] The MCF-7 tumor cells were incubated with the 24 nm clusters to load the clusters into the cells. The TEM images show the clusters were localized in the lysosomes of the cells. (Figure 1.12). A cluster loading of 8 pg per cell could be achieved using the clusters with an iron concentration of 2 mM. When the cells loaded with clusters were placed in an AMF with a field strength of 29 kA/m and a frequency of 520 kHz, the temperature of the cells increased to 50 °C, leading to a cell death rate of 60%.

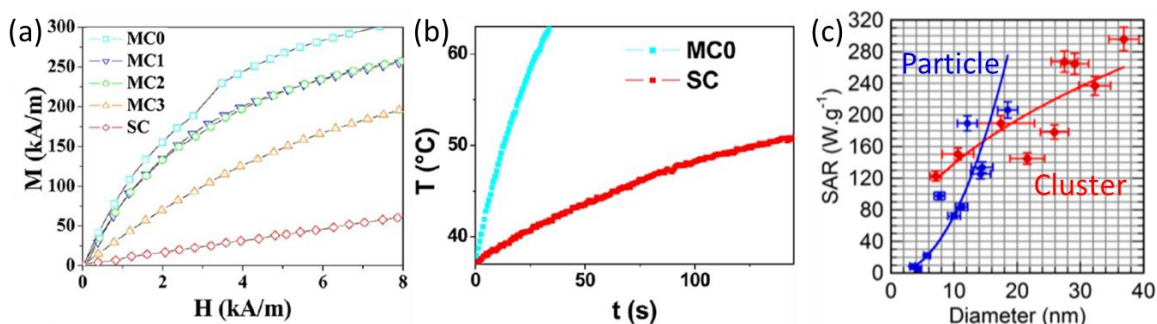


Figure 1. 11. The superior magnetic heating efficiency of iron oxide nanocrystal clusters. (a) The low field magnetization and (b) the heating of the clusters and the particles. Figures adapted from reference [44] with permission. Copyright 2012 American Chemical Society. (c) The SAR of the clusters and particles with different sizes. The clusters outperformed the particles in nearly all size ranges in both cases. Figure adapted from reference [63] with permission. Copyright 2017 American Chemical Society

Clusters have also been used as the magnetic resonance imaging (MRI) contrast agent and showed excellent performance. Maity et al. compared the properties and performance of 44 nm magnetite clusters with 10 nm isolated nanocrystals (Figure 1.13). They found that the clusters display both much higher specific absorption rate (SAR) value and higher T2 relaxivity for MRI, making the clusters an ideal multifunctional platform for both treatment and imaging.^[65] In their *in vivo* experiments, the clusters were injected into the mice with

subcutaneous xenograft tumors of MCF-7 cancer cells. The MRI images show that the intensities in the kidney and the liver were enhanced, which was due to the clearance of the clusters by these organs. However, the intensities decayed over time, and the postcontrast of these sites was not obvious. On the contrary, the clusters retained in the tumor much longer and the signals from the tumor nearly remained the same over the entire operation. This was ascribed to the enhanced permeation and retention mechanism where the clusters passively targeted the tumor sites by penetrating through the leaky vasculature of the tumor.

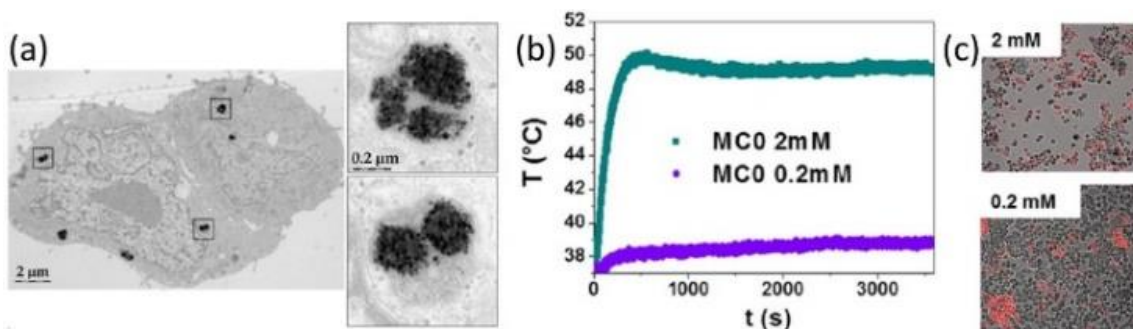


Figure 1. 12. The application of clusters as heating mediator for magnetic hyperthermia *in vitro*. (a) The TEM images of the MCF-7 tumor cells containing the clusters. (b) The magnetic heating of the cells treated with 2 mM and 0.2 mM clusters in the AMF. (c) The death assessment of the cells placed in the AMF. Figure adapted from reference [44] with permission. Copyright 2012 American Chemical Society.

(a)	Samples	Average particle size/nm	$M_s/\text{emu g}^{-1}$	Relaxivity/ $\text{s}^{-1} \text{mM}^{-1}$	
				r_2	r_2^*
	MNC-10	10	63	205.6	309.2
	MNC-14	44	75	294.99	450.05

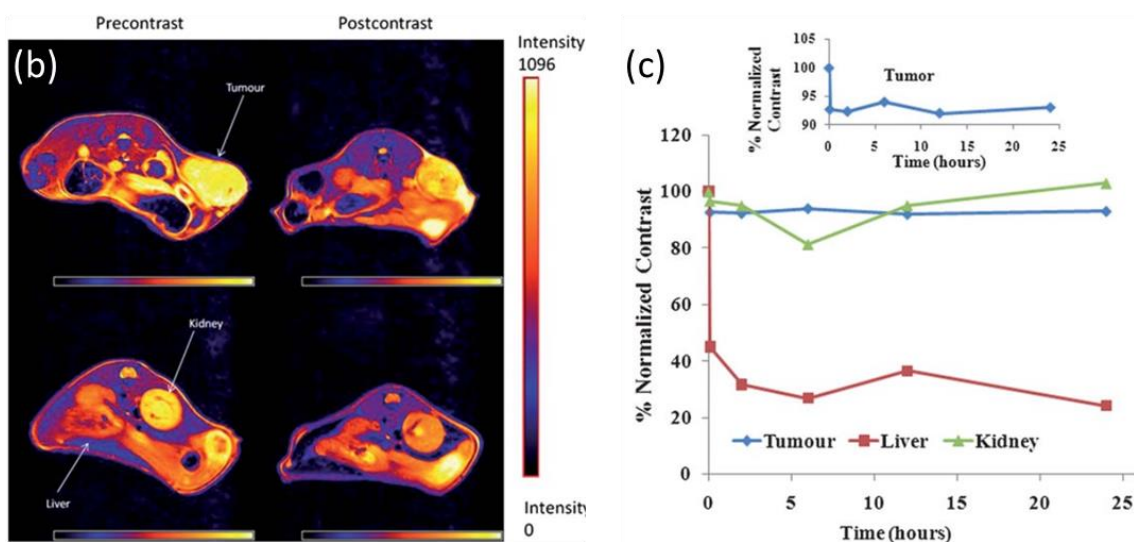


Figure 1. 13. The application of clusters as MRI contrast agent in vivo. (a) The relaxivities of the isolated nanocrystals and clusters. Sample MNC-10 and MNC-14 were 10 nm nanocrystals and 44 nm clusters, respectively. (b) The MRI image of the SCID mice using clusters as contrast agent. (c) The MRI signals in the tumor sites remained nearly the same over 25 hours. Figure adapted from reference [65] with permission. Copyright 2011 Royal Society of Chemistry.

Magnetic nanocrystal clusters can serve as a multifunctional nanoplatform for disease treatment. Wang et al. designed a nanoplatform composed of iron oxide clusters and polypyrrole (PPy) for remotely controlled cancer therapy. (Figure 1.14).^[86] Poly(ethylene glycol) was coated on the surface of the platform to improve its biocompatibility and stability. The iron oxide nanocluster was used for both magnetically controlled drug delivery and T2-weighted MRI. The PPy not only serves as a photothermal agent but also was used for drug loading and release. It allows the clusters to release doxorubicin when irradiated by near-infrared light. Moreover, the cancer cells containing the clusters were

captured by magnets and could increase the selectivity of the near-infrared irradiation. *In vitro* experiment showed that the cell viability was less than 0.15 with the external field, whereas the clusters were nearly harmless to the cells in the control experiment. In the *in vivo* studies, the tumor growth in the mice was clearly inhibited when applying this nanoplatform.

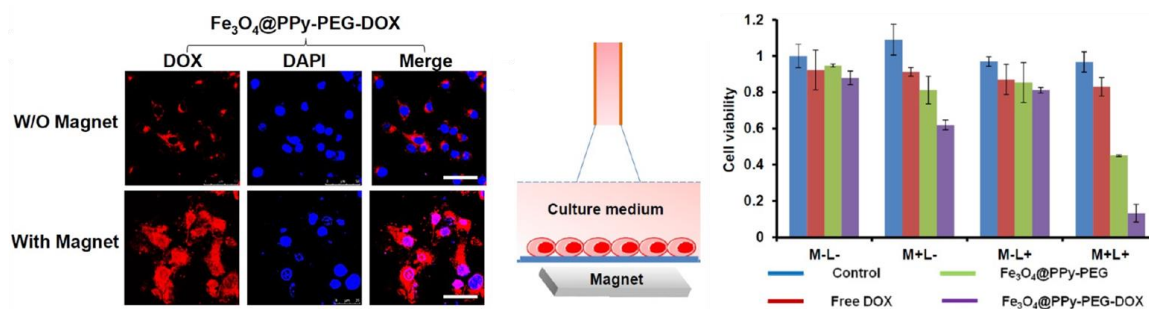


Figure 1. 14. The application of clusters as a multifunctional platform for improved drug delivery. (a) Confocal images of 4T1 cells incubated with $Fe_3O_4@PPy-PEG-DOX$. (b) Schematic illustration of *in vitro* combined therapy. (c) Relative viabilities of 4T1 cells after different treatment. Figure adapted from reference [86] with permission. Copyright 2013 American Chemical Society.

The application of magnetic clusters in environmental remediation has also been explored. Due to the unique structure and magnetic properties of clusters, they are ideal materials to capture pollutants and toxic composites from wastewater. Due to the porous structure of the clusters, they have more specific surface areas than the isolated nanocrystals with similar overall sizes, which give rise to high absorption capacity. The big magnetic moment of clusters makes them easy to be captured by a magnet. Wang et al. synthesized the magnetite clusters with an average size from 95 to 350 nm and studied their performance in removing arsenic pollutants.^[76] The clusters were coated with a positively charged polymer, poly(diallyldimethylammonium chloride), to increase their affinity toward the As(III) and As(V) species, which are negatively charged. They found that in both

experiments for removal, the clusters showed high capacities for the adsorption of the As(III) and As(V). The adsorption capacity depends on the cluster size. The clusters with an average size of 200 nm had the best efficiency for low-level arsenic removal due to their larger magnetization and better colloidal stability (Figure 1.15 a). In another paper from the same group, the authors used clusters coated with poly(m-phenylenediamine) to remove Cr(VI) species in the water. Poly(m-phenylenediamine) can reduce Cr(VI) to Cr(III) and then chelate to Cr(III) species for better adsorption (Figure 1.15 b).^[87] Both studies showed high removal efficiency of the toxic metal from wastewater and satisfactory durability where the clusters can be recycled more than five times with little decrease in performance.

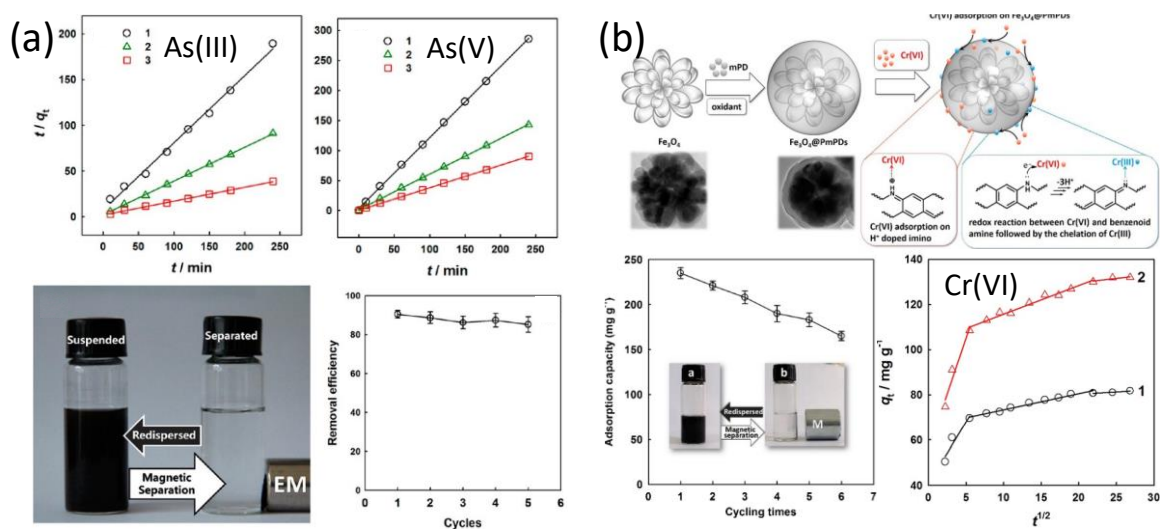


Figure 1. 15. Clusters for toxic metal removal. (a) The adsorption of As (III) and As(V) using magnetite clusters. The clusters were coated with Poly(diallyldimethylammonium chloride) (PDDA). The sizes for 1-3 were 215 nm, 195 nm, and 185 nm, respectively. The adsorption of both As (III) and As(V) followed the pseudo-second-order rate kinetic model, where the equilibrium adsorption capacity was inversely proportional to the slope of the curve. The 185 nm clusters had the highest adsorption performances. Figure adapted from reference [76] with permission. Copyright 2013 American Chemical Society. (b) The adsorption of Cr(VI) using magnetite clusters coated with poly(m-phenylenediamine) (PmPDs). The cluster diameter was around 200 nm, and the coating thickness was about

50 nm. Figure adapted from reference [87] with permission. Copyright 2015 American Chemical Society.

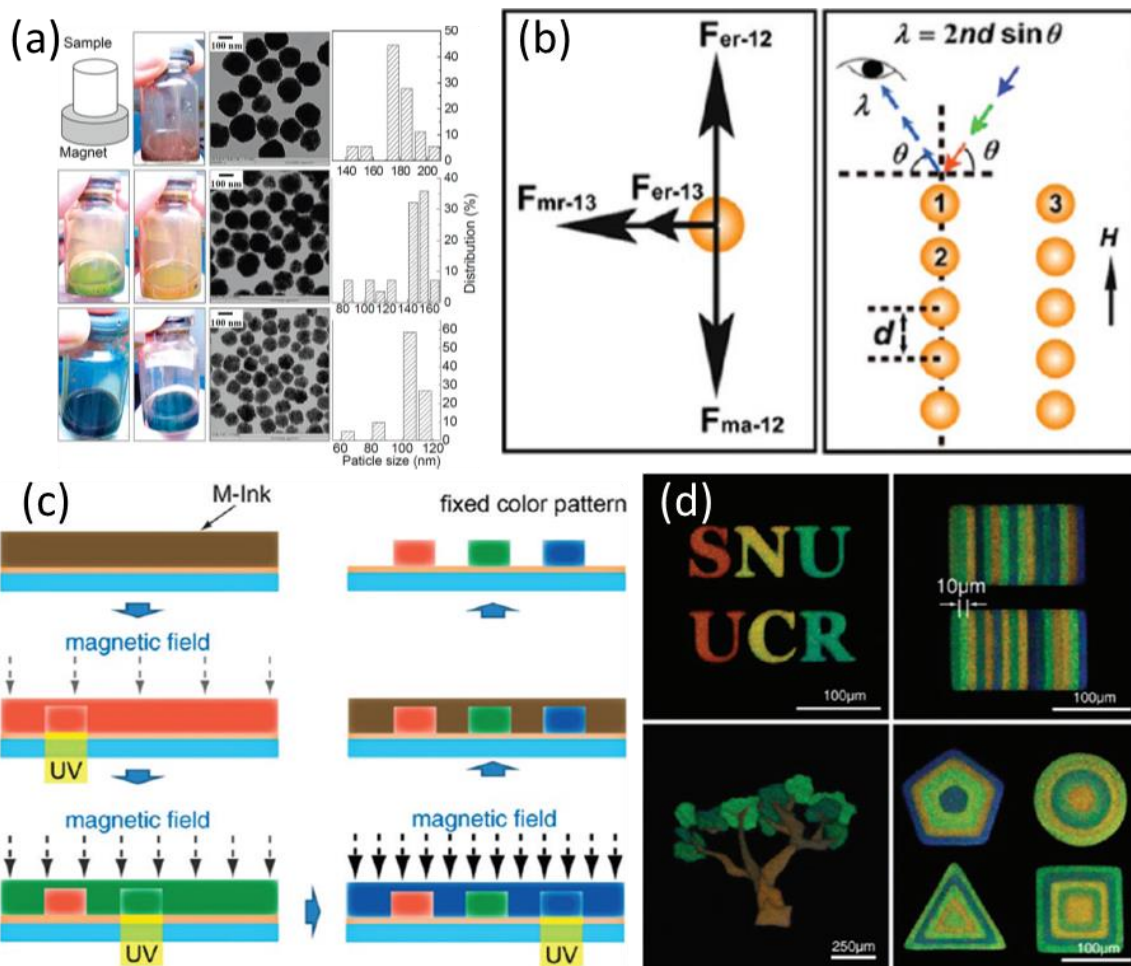


Figure 1.16. Clusters for reversible photonic crystal with magnetically controllable bandgap. (a) The optical images of the clusters placed in a static magnetic field and the TEM images of the clusters with their size distribution. Figure adapted from reference [88] with permission. Copyright 2009 American Chemical Society. (b) Illustration of the clusters forming photonic crystals. (c) Applying clusters for structural color printing. Figure b and c adapted from reference [89] with permission. Copyright 2012 American Chemical Society. (d) Picture of the high-resolution printing using photonic crystals. Figure adapted from references [90] with permission. Copyright 2009 Springer Nature.

Another interesting application of the superparamagnetic clusters is as photonic crystal. Magnetic nanocrystal clusters can form responsive photonic crystals in an external field.

Xia et al. synthesized 100 to 200 nm clusters and observed a clear colored pattern of the aqueous solution when placed on a magnet (Figure 16 a).^[88] The color of the solution was dependent on the cluster size, where smaller clusters showed purple color while larger ones became brown to red. He et al. attributed this color change to the Bragg diffraction of the cluster chains (Figure 16 b).^[89] The clusters form chains along the direction of the field in a static magnetic field because of the balance between the attractive magnetic dipolar force and the repulsive steric or electrostatic force of the clusters. The distance between clusters in the chain is influenced by the size and coating of the cluster as well as the magnetic field strength.^[69] When this distance is within the optical wavelength range, the light with a specific wavelength can be reflected due to Bragg diffraction, therefore presenting the unique color of the cluster solution.

The magnetic nanocrystal clusters have been applied to color production since the bandgap of the photonic crystal can be controlled by varying the strength of the magnetic field. Kim et al. proposed structural color printing using the clusters (Figure 16 c).^[90, 91] The authors invented a material called M-ink, which was composed of magnetic nanocrystal clusters, solvation liquid, and photocurable resin. The external field was used to reversibly control the color of the photonic crystal. When exposed to UV light, the photocurable resin would polymerize and fix the colored pattern of the clusters in the field. The sequential steps of “tuning and fixing” finally lead to multicolor printing with high resolution and quality. This proposed structural color printing scheme significantly impacted color production since it may replace conventional dyes that cause severe environmental pollution.

1.6 Conclusions and outlook

In this article we review the recent advances in the synthesis and applications of magnetic nanocrystal clusters. Solution chemistry has been demonstrated to be an efficient method to synthesize clusters with controlled dimensions. The clusters might be formed through different mechanisms in various reaction systems such as limited ligand protection, ligand crosslinking, and so on. The size of clusters and primary particles can be varied by selecting different reactants and changing reaction conditions. A large library of clusters with different compositions, cluster sizes, and primary particle sizes has been generated. Compared to the conventional isolated nanocrystals, the clusters exhibit superior magnetic properties due to the intra-cluster interactions. The superior magnetic properties of clusters make them useful in various industrial and biomedical applications.

While magnetic nanocrystal clusters are promising for many applications, there are still substantial challenges to address before making full use of these interesting materials. The physics underlying their interesting magnetic properties have not been well understood. Micromagnetics simulation will provide a powerful tool to understand the physics and predict the dependence of the magnetic properties on the cluster size and primary particle size. Although many methods have been reported to synthesize clusters, the reproducibility and scalability of these synthesis methods remain a challenge due to the lack of understanding of the formation process of clusters. More mechanistic studies are needed to elucidate this complicated process. Another challenge for applying clusters is to improve the colloidal stability of clusters in various media. Most cluster samples synthesized using current methods are only stable in pure water, and they tend to aggregate in many biological and environmental media, limiting their extensive applications.^[47, 49, 67, 80] New surface

coating chemistry is needed to stabilize the clusters in various media. The safety of the clusters needs to be evaluated before applying these materials in clinical setting.⁹³⁻⁹⁷ With the excellent magnetic properties, magnetic nanocrystal clusters are expected to find applications in many fields such as magnetic particle imaging, biosensing, etc.^[98-103]

References in Chapter 1

- [1] Bean, C.; Livingston, u. D., Superparamagnetism. *Journal of Applied Physics* **1959**, *30* (4), S120-S129.
- [2] Knobel, M.; Nunes, W.; Socolovsky, L.; De Biasi, E.; Vargas, J.; Denardin, J., Superparamagnetism and other magnetic features in granular materials: a review on ideal and real systems. *Journal of nanoscience and nanotechnology* **2008**, *8* (6), 2836-2857.
- [3] Mikhaylova, M.; Kim, D. K.; Bobrysheva, N.; Osmolowsky, M.; Semenov, V.; Tsakalakos, T.; Muhammed, M., Superparamagnetism of magnetite nanoparticles: dependence on surface modification. *Langmuir* **2004**, *20* (6), 2472-2477.
- [4] Cardoso, V. F.; Francesko, A.; Ribeiro, C.; Bañobre-López, M.; Martins, P.; Lanceros-Mendez, S., Advances in magnetic nanoparticles for biomedical applications. *Advanced healthcare materials* **2018**, *7* (5), 1700845.
- [5] Mohammed, L.; Gomaa, H. G.; Ragab, D.; Zhu, J., Magnetic nanoparticles for environmental and biomedical applications: A review. *Particuology* **2017**, *30*, 1-14.
- [6] Mou, X.; Ali, Z.; Li, S.; He, N., Applications of magnetic nanoparticles in targeted drug delivery system. *Journal of nanoscience and nanotechnology* **2015**, *15* (1), 54-62.
- [7] Vaghari, H.; Jafarizadeh-Malmiri, H.; Mohammadlou, M.; Berenjian, A.; Anarjan, N.; Jafari, N.; Nasiri, S., Application of magnetic nanoparticles in smart enzyme immobilization. *Biotechnology letters* **2016**, *38* (2), 223-233.
- [8] Zhou, Z.; Yang, L.; Gao, J.; Chen, X., Structure–relaxivity relationships of magnetic nanoparticles for magnetic resonance imaging. *Advanced Materials* **2019**, *31* (8), 1804567.
- [9] Wei, H.; Bruns, O. T.; Kaul, M. G.; Hansen, E. C.; Barch, M.; Wiśniowska, A.; Chen, O.; Chen, Y.; Li, N.; Okada, S., Exceedingly small iron oxide nanoparticles as positive MRI contrast agents. *Proceedings of the national academy of sciences* **2017**, *114* (9), 2325-2330.
- [10] Li, Q.; Kartikowati, C. W.; Horie, S.; Ogi, T.; Iwaki, T.; Okuyama, K., Correlation between particle size/domain structure and magnetic properties of highly crystalline Fe₃O₄ nanoparticles. *Scientific Reports* **2017**, *7*.
- [11] Mohapatra, J.; Zeng, F. H.; Elkins, K.; Xing, M. Y.; Ghimire, M.; Yoon, S.; Mishra, S. R.; Liu, J. P., Size-dependent magnetic and inductive heating properties of Fe₃O₄ nanoparticles: scaling laws across the superparamagnetic size. *Physical Chemistry Chemical Physics* **2018**, *20* (18), 12879-12887.

- [12] Patsula, V.; Moskvina, M.; Dutz, S.; Horak, D., Size-dependent magnetic properties of iron oxide nanoparticles. *Journal of Physics and Chemistry of Solids* **2016**, *88*, 24-30.
- [13] Yoo, K.; Jeon, B. G.; Chun, S. H.; Patil, D. R.; Lim, Y. J.; Noh, S. H.; Gil, J.; Cheon, J.; Kim, K. H., Quantitative Measurements of Size-Dependent Magnetoelectric Coupling in Fe₃O₄ Nanoparticles. *Nano Letters* **2016**, *16* (12), 7408-7413.
- [14] Wu, L.; Mendoza-Garcia, A.; Li, Q.; Sun, S., Organic phase syntheses of magnetic nanoparticles and their applications. *Chemical reviews* **2016**, *116* (18), 10473-10512.
- [15] Kudr, J.; Haddad, Y.; Richtera, L.; Heger, Z.; Cernak, M.; Adam, V.; Zitka, O., Magnetic nanoparticles: From design and synthesis to real world applications. *Nanomaterials* **2017**, *7* (9), 243.
- [16] Majidi, S.; Zeinali Sehgig, F.; Farkhani, S. M.; Soleymani Goloujeh, M.; Akbarzadeh, A., Current methods for synthesis of magnetic nanoparticles. *Artificial cells, nanomedicine, and biotechnology* **2016**, *44* (2), 722-734.
- [17] Sun, S.; Zeng, H., Size-controlled synthesis of magnetite nanoparticles. *Journal of the American Chemical Society* **2002**, *124* (28), 8204-8205.
- [18] Lisjak, D.; Mertelj, A., Anisotropic magnetic nanoparticles: A review of their properties, syntheses and potential applications. *Progress in Materials Science* **2018**, *95*, 286-328.
- [19] Obaidat, I. M.; Issa, B.; Haik, Y., Magnetic properties of magnetic nanoparticles for efficient hyperthermia. *Nanomaterials* **2015**, *5* (1), 63-89.
- [20] Caruntu, D.; Caruntu, G.; O'Connor, C. J., Magnetic properties of variable-sized Fe₃O₄ nanoparticles synthesized from non-aqueous homogeneous solutions of polyols. *Journal of Physics D-Applied Physics* **2007**, *40* (19), 5801-5809.
- [21] Koseoglu, Y.; Kavas, H., Size and surface effects on magnetic properties of Fe₃O₄ nanoparticles. *Journal of Nanoscience and Nanotechnology* **2008**, *8* (2), 584-590.
- [22] Darbandi, M.; Stromberg, F.; Landers, J.; Reckers, N.; Sanyal, B.; Keune, W.; Wende, H., Nanoscale size effect on surface spin canting in iron oxide nanoparticles synthesized by the microemulsion method. *Journal of Physics D-Applied Physics* **2012**, *45* (19).
- [23] Schaller, V.; Wahnstrom, G.; Sanz-Velasco, A.; Gustafsson, S.; Olsson, E.; Enoksson, P.; Johansson, C., Effective magnetic moment of magnetic multicore nanoparticles. *Physical Review B* **2009**, *80* (9).
- [24] Tadic, M.; Kralj, S.; Jagodic, M.; Hanzel, D.; Makovec, D., Magnetic properties of novel superparamagnetic iron oxide nanoclusters and their peculiarity under annealing treatment. *Applied Surface Science* **2014**, *322*, 255-264.
- [25] Jun, Y. W.; Seo, J. W.; Cheon, A., Nanoscaling laws of magnetic nanoparticles and their applicabilities in biomedical sciences. *Accounts of Chemical Research* **2008**, *41* (2), 179-189.
- [26] Vreeland, E. C.; Watt, J.; Schober, G. B.; Hance, B. G.; Austin, M. J.; Price, A. D.; Fellows, B. D.; Monson, T. C.; Hudak, N. S.; Maldonado-Camargo, L., Enhanced nanoparticle size control by extending LaMer's mechanism. *Chemistry of Materials* **2015**, *27* (17), 6059-6066.

- [27] Moya, C.; Iglesias-Freire, Ó.; Batlle, X.; Labarta, A.; Asenjo, A., Superparamagnetic versus blocked states in aggregates of Fe_{3-x}O₄ nanoparticles studied by MFM. *Nanoscale* **2015**, *7* (42), 17764-17770.
- [28] Mourdikoudis, S.; Pallares, R. M.; Thanh, N. T., Characterization techniques for nanoparticles: comparison and complementarity upon studying nanoparticle properties. *Nanoscale* **2018**, *10* (27), 12871-12934.
- [29] Ivanov, A. O.; Kantorovich, S. S.; Zverev, V. S.; Elfimova, E. A.; Lebedev, A. V.; Pshenichnikov, A. F., Temperature-dependent dynamic correlations in suspensions of magnetic nanoparticles in a broad range of concentrations: a combined experimental and theoretical study. *Physical Chemistry Chemical Physics* **2016**, *18* (27), 18342-18352.
- [30] Yeap, S. P.; Lim, J.; Ooi, B. S.; Ahmad, A. L., Agglomeration, colloidal stability, and magnetic separation of magnetic nanoparticles: collective influences on environmental engineering applications. *Journal of Nanoparticle Research* **2017**, *19* (11), 1-15.
- [31] Lim, J.; Yeap, S. P.; Che, H. X.; Low, S. C., Characterization of magnetic nanoparticle by dynamic light scattering. *Nanoscale research letters* **2013**, *8* (1), 1-14.
- [32] Eberbeck, D.; Wiekhorst, F.; Steinhoff, U.; Trahms, L., Aggregation behaviour of magnetic nanoparticle suspensions investigated by magnetorelaxometry. *Journal of Physics: Condensed Matter* **2006**, *18* (38), S2829.
- [33] Moore, T. L.; Rodriguez-Lorenzo, L.; Hirsch, V.; Balog, S.; Urban, D.; Jud, C.; Rothen-Rutishauser, B.; Lattuada, M.; Petri-Fink, A., Nanoparticle colloidal stability in cell culture media and impact on cellular interactions. *Chemical Society Reviews* **2015**, *44* (17), 6287-6305.
- [34] Lu, Z.; Yin, Y., Colloidal nanoparticle clusters: functional materials by design. *Chemical Society Reviews* **2012**, *41* (21), 6874-6887.
- [35] Li, Z.; Fan, Q.; Yin, Y., Colloidal Self-Assembly Approaches to Smart Nanostructured Materials. *Chemical Reviews* **2021**.
- [36] Bender, P.; Fock, J.; Frandsen, C.; Hansen, M. F.; Balceris, C.; Ludwig, F.; Posth, O.; Wetterskog, E.; Bogart, L. K.; Southern, P.; Szczerba, W.; Zeng, L. J.; Witte, K.; Gruttner, C.; Westphal, F.; Honecker, D.; Gonzalez-Alonso, D.; Barquin, L. F.; Johansson, C., Relating Magnetic Properties and High Hyperthermia Performance of Iron Oxide Nanoflowers. *Journal of Physical Chemistry C* **2018**, *122* (5), 3068-3077.
- [37] Bender, P.; Fock, J.; Hansen, M. F.; Bogart, K.; Southern, P.; Ludwig, F.; Wiekhorst, F.; Szczerba, W.; Zeng, L. J.; Heinke, D.; Gehrke, N.; Diaz, M. T. F.; Gonzalez-Alonso, D.; Espeso, J. I.; Rodriguez Fernandez, J.; Johansson, C., Influence of clustering on the magnetic properties and hyperthermia performance of iron oxide nanoparticles. *Nanotechnology* **2018**, *29* (42), 425705.
- [38] Zhuang, J. Q.; Wu, H. M.; Yang, Y. A.; Cao, Y. C., Supercrystalline colloidal particles from artificial atoms. *Journal of the American Chemical Society* **2007**, *129* (46), 14166.
- [39] Wang, T.; Wang, X. R.; LaMontagne, D.; Wang, Z. L.; Wang, Z. W.; Cao, Y. C., Shape-Controlled Synthesis of Colloidal Superparticles from Nanocubes. *Journal of the American Chemical Society* **2012**, *134* (44), 18225-18228.

- [40] Bunge, A.; Porav, A. S.; Borodi, G.; Radu, T.; Pîrnău, A.; Berghian-Grosan, C.; Turcu, R., Correlation between synthesis parameters and properties of magnetite clusters prepared by solvothermal polyol method. *Journal of Materials Science* **2019**, *54* (4), 2853-2875.
- [41] Matijevic, E.; Scheiner, P., FERRIC HYDROUS OXIDE SOLS .3. PREPARATION OF UNIFORM PARTICLES BY HYDROLYSIS OF FE(III)-CHLORIDE, FE(III)-NITRATE, AND FE(III)-PERCHLORATE SOLUTIONS. *Journal of Colloid and Interface Science* **1978**, *63* (3), 509-524.
- [42] Zhang, J.; Song, Y.-F.; Cronin, L.; Liu, T., Self-assembly of organic– inorganic hybrid amphiphilic surfactants with large polyoxometalates as polar head groups. *Journal of the American Chemical Society* **2008**, *130* (44), 14408-14409.
- [43] Chen, O.; Riedemann, L.; Etoc, F.; Herrmann, H.; Coppey, M.; Barch, M.; Farrar, C. T.; Zhao, J.; Bruns, O. T.; Wei, H., Magneto-fluorescent core-shell supernanoparticles. *Nature communications* **2014**, *5* (1), 1-8.
- [44] Lartigue, L.; Hugounenq, P.; Alloyeau, D.; Clarke, S. P.; Levy, M.; Bacri, J.-C.; Bazzi, R.; Brougham, D. F.; Wilhelm, C.; Gazeau, F., Cooperative organization in iron oxide multi-core nanoparticles potentiates their efficiency as heating mediators and MRI contrast agents. *ACS nano* **2012**, *6* (12), 10935-10949.
- [45] Ge, J.; Hu, Y.; Biasini, M.; Beyermann, W. P.; Yin, Y., Superparamagnetic magnetite colloidal nanocrystal clusters. *Angewandte Chemie International Edition* **2007**, *46* (23), 4342-4345.
- [46] Xi, G.; Wang, C.; Wang, X., The Oriented Self-Assembly of Magnetic Fe₃O₄ Nanoparticles into Monodisperse Microspheres and Their Use as Substrates in the Formation of Fe₃O₄ Nanorods. *European Journal of Inorganic Chemistry* **2008**, *2008* (3), 425-431.
- [47] Cheng, C.; Xu, F.; Gu, H., Facile synthesis and morphology evolution of magnetic iron oxide nanoparticles in different polyol processes. *New Journal of Chemistry* **2011**, *35* (5), 1072-1079.
- [48] Cheng, C.; Wen, Y.; Xu, X.; Gu, H., Tunable synthesis of carboxyl-functionalized magnetite nanocrystal clusters with uniform size. *Journal of Materials Chemistry* **2009**, *19* (46), 8782-8788.
- [49] Wang, L.; Bao, J.; Wang, L.; Zhang, F.; Li, Y., One-pot synthesis and bioapplication of amine-functionalized magnetite nanoparticles and hollow nanospheres. *Chemistry—A European Journal* **2006**, *12* (24), 6341-6347.
- [50] Deng, H.; Li, X.; Peng, Q.; Wang, X.; Chen, J.; Li, Y., Monodisperse magnetic single-crystal ferrite microspheres. *Angewandte Chemie* **2005**, *117* (18), 2842-2845.
- [51] Narayanaswamy, A.; Xu, H.; Pradhan, N.; Peng, X., Crystalline nanoflowers with different chemical compositions and physical properties grown by limited ligand protection. *Angewandte Chemie International Edition* **2006**, *45* (32), 5361-5364.
- [52] Wang, F.; Richards, V. N.; Shields, S. P.; Buhro, W. E., Kinetics and mechanisms of aggregative nanocrystal growth. *Chemistry of Materials* **2014**, *26* (1), 5-21.
- [53] Zaiser, E. M.; La Mer, V. K., The kinetics of the formation and growth of monodispersed sulfur hydrosols. *Journal of colloid science* **1948**, *3* (6), 571-598.
- [54] You, H.; Fang, J., Particle-mediated nucleation and growth of solution-synthesized metal nanocrystals: A new story beyond the LaMer curve. *Nano Today* **2016**, *11* (2), 145-167.

- [55] Voorhees, P. W., The theory of Ostwald ripening. *Journal of Statistical Physics* **1985**, *38* (1), 231-252.
- [56] Kabalnov, A., Ostwald ripening and related phenomena. *Journal of Dispersion Science and Technology* **2001**, *22* (1), 1-12.
- [57] Gerber, O.; Pichon, B.; Ihiawakrim, D.; Florea, I.; Moldovan, S.; Ersen, O.; Begin, D.; Grenèche, J.-M.; Lemonnier, S.; Barraud, E., Synthesis engineering of iron oxide raspberry-shaped nanostructures. *Nanoscale* **2017**, *9* (1), 305-313.
- [58] Gavilán, H.; Sánchez, E. H.; Brollo, M. E.; Asín, L.; Moerner, K. K.; Frandsen, C.; Lázaro, F. J.; Serna, C. J.; Veintemillas-Verdaguer, S.; Morales, M. P., Formation mechanism of maghemite nanoflowers synthesized by a polyol-mediated process. *Acs Omega* **2017**, *2* (10), 7172-7184.
- [59] Wei, X.; Jing, L.; Liu, C.; Hou, Y.; Jiao, M.; Gao, M., Molecular mechanisms for delicately tuning the morphology and properties of Fe₃O₄ nanoparticle clusters. *CrystEngComm* **2018**, *20* (17), 2421-2429.
- [60] Togashi, T.; Naka, T.; Asahina, S.; Sato, K.; Takami, S.; Adschiri, T., Surfactant-assisted one-pot synthesis of superparamagnetic magnetite nanoparticle clusters with tunable cluster size and magnetic field sensitivity. *Dalton Transactions* **2011**, *40* (5), 1073-1078.
- [61] Otero-Lorenzo, R.; Ramos-Docampo, M. A.; Rodríguez-González, B.; Comesaña-Hermo, M.; Salgueiriño, V. n., Solvothermal clustering of magnetic spinel ferrite nanocrystals: a Raman perspective. *Chemistry of Materials* **2017**, *29* (20), 8729-8736.
- [62] Lin, M.; Huang, H.; Liu, Z.; Liu, Y.; Ge, J.; Fang, Y., Growth–dissolution–regrowth transitions of Fe₃O₄ nanoparticles as building blocks for 3D magnetic nanoparticle clusters under hydrothermal conditions. *Langmuir* **2013**, *29* (49), 15433-15441.
- [63] Hemery, G.; Keyes Jr, A. C.; Garaio, E.; Rodrigo, I.; Garcia, J. A.; Plazaola, F.; Garanger, E.; Sandre, O., Tuning sizes, morphologies, and magnetic properties of mononucleus versus multicore iron oxide nanoparticles through the controlled addition of water in the polyol synthesis. *Inorganic chemistry* **2017**, *56* (14), 8232-8243.
- [64] Kostopoulou, A.; Velu, S. K.; Thangavel, K.; Orsini, F.; Brintakis, K.; Psycharakis, S.; Ranella, A.; Bordonali, L.; Lappas, A.; Lascialfari, A., Colloidal assemblies of oriented maghemite nanocrystals and their NMR relaxometric properties. *Dalton Transactions* **2014**, *43* (22), 8395-8404.
- [65] Maity, D.; Chandrasekharan, P.; Pradhan, P.; Chuang, K.-H.; Xue, J.-M.; Feng, S.-S.; Ding, J., Novel synthesis of superparamagnetic magnetite nanoclusters for biomedical applications. *Journal of Materials Chemistry* **2011**, *21* (38), 14717-14724.
- [66] Nikitin, A. A.; Shchetinin, I. V.; Tabachkova, N. Y.; Soldatov, M. A.; Soldatov, A. V.; Sviridenkova, N. V.; Beloglazkina, E. K.; Savchenko, A. G.; Fedorova, N. D.; Abakumov, M. A., Synthesis of iron oxide nanoclusters by thermal decomposition. *Langmuir* **2018**, *34* (15), 4640-4650.
- [67] Xuan, S.; Wang, Y.-X. J.; Yu, J. C.; Cham-Fai Leung, K., Tuning the grain size and particle size of superparamagnetic Fe₃O₄ microparticles. *Chemistry of Materials* **2009**, *21* (21), 5079-5087.

- [68] Huang, Z.; Wu, K.; Yu, Q.-H.; Wang, Y.-Y.; Xing, J.; Xia, T.-L., Facile synthesis of size tunable Fe₃O₄ nanoparticles in bisolvent system. *Chemical Physics Letters* **2016**, *664*, 219-225.
- [69] Liang, J.; Ma, H.; Luo, W.; Wang, S., Synthesis of magnetite submicrospheres with tunable size and superparamagnetism by a facile polyol process. *Materials Chemistry and Physics* **2013**, *139* (2-3), 383-388.
- [70] Liu, J.; Sun, Z., Yonghui; Zou, Y.; Li, C.; Guo, X.; Xiong, L.; Gao, Y.; Li, F.; Zhao, D., Highly water-dispersible biocompatible magnetite particles with low cytotoxicity stabilized by citrate groups. *Angewandte Chemie International Edition* **2009**, *48* (32), 5875-5879.
- [71] Liu, R.; Lv, M.; Wang, Q.; Li, H.; Guo, P.; Zhao, X., Solvothermal synthesis of size-tunable ZnFe₂O₄ colloidal nanocrystal assemblies and their electrocatalytic activity towards hydrogen peroxide. *Journal of Magnetism and Magnetic Materials* **2017**, *424*, 155-160.
- [72] Lu, C.; Wang, H.; Ma, J.; Yuan, H.; Liang, H.; Wu, L.; Chai, K. Y.; Li, S., Facile synthesis of superparamagnetic magnetite nanoflowers and their applications in cellular imaging. *RSC advances* **2016**, *6* (48), 42649-42655.
- [73] Luo, B.; Song, X.-J.; Zhang, F.; Xia, A.; Yang, W.-L.; Hu, J.-H.; Wang, C.-C., Multi-functional thermosensitive composite microspheres with high magnetic susceptibility based on magnetite colloidal nanoparticle clusters. *Langmuir* **2009**, *26* (3), 1674-1679.
- [74] Pereira, C.; Pereira, A. M.; Rocha, M.; Freire, C.; Geraldes, C. F., Architected design of superparamagnetic Fe₃O₄ nanoparticles for application as MRI contrast agents: mastering size and magnetism for enhanced relaxivity. *Journal of Materials Chemistry B* **2015**, *3* (30), 6261-6273.
- [75] Tong, G.; Liu, Y.; Wu, T.; Tong, C.; Du, F., H₂O-steered size/phase evolution and magnetic properties of large-scale, monodisperse Fe_xO_y nanomaterials. *Journal of Materials Chemistry C* **2015**, *3* (21), 5506-5515.
- [76] Wang, T.; Zhang, L.; Wang, H.; Yang, W.; Fu, Y.; Zhou, W.; Yu, W.; Xiang, K.; Su, Z.; Dai, S., Controllable synthesis of hierarchical porous Fe₃O₄ particles mediated by poly (diallyldimethylammonium chloride) and their application in arsenic removal. *ACS applied materials & interfaces* **2013**, *5* (23), 12449-12459.
- [77] Wang, W.; Tang, B.; Ju, B.; Zhang, S., Size-controlled synthesis of water-dispersible superparamagnetic Fe₃O₄ nanoclusters and their magnetic responsiveness. *RSC Advances* **2015**, *5* (92), 75292-75299.
- [78] Kim, Y. J.; Park, B. C.; Choi, Y. S.; Ko, M. J.; Kim, Y. K., Quantitative analysis on cellular uptake of clustered ferrite magnetic nanoparticles. *Electronic Materials Letters* **2019**, *15* (4), 471-480.
- [79] Zhu, Y.; Zhao, W.; Chen, H.; Shi, J., A simple one-pot self-assembly route to nanoporous and monodispersed Fe₃O₄ particles with oriented attachment structure and magnetic property. *The Journal of Physical Chemistry C* **2007**, *111* (14), 5281-5285.
- [80] Xiao, Z.; Zhang, Q.; Guo, X.; Villanova, J.; Hu, Y.; Kulaots, I.; Garcia-Rojas, D.; Guo, W.; Colvin, V. L., Libraries of Uniform Magnetic Multicore Nanoparticles with Tunable Dimensions for Biomedical and Photonic Applications. *ACS Applied Materials & Interfaces* **2020**, *12* (37), 41932-41941.

- [81] Mørup, S.; Hansen, M. F.; Frandsen, C., Magnetic interactions between nanoparticles. *Beilstein journal of nanotechnology* **2010**, *1* (1), 182-190.
- [82] Sánchez, F. H.; Zélis, P. M.; Arciniegas, M.; Pasquevich, G. A.; Van Raap, M. F., Dipolar interaction and demagnetizing effects in magnetic nanoparticle dispersions: Introducing the mean-field interacting superparamagnet model. *Physical Review B* **2017**, *95* (13), 134421.
- [83] Landeros, P.; Escrig, J.; Altbir, D.; Laroze, D.; e Castro, J. d. A.; Vargas, P., Scaling relations for magnetic nanoparticles. *Physical Review B* **2005**, *71* (9), 094435.
- [84] Kostopoulou, A.; Brintakis, K.; Vasilakaki, M.; Trohidou, K.; Douvalis, A.; Lascialfari, A.; Manna, L.; Lappas, A., Assembly-mediated interplay of dipolar interactions and surface spin disorder in colloidal maghemite nanoclusters. *Nanoscale* **2014**, *6* (7), 3764-3776.
- [85] Hemery, G.; Genevois, C.; Couillaud, F.; Lacomme, S.; Gontier, E.; Ibarboure, E.; Lecommandoux, S.; Garanger, E.; Sandre, O., Monocore vs. multicore magnetic iron oxide nanoparticles: Uptake by glioblastoma cells and efficiency for magnetic hyperthermia. *Molecular Systems Design & Engineering* **2017**, *2* (5), 629-639.
- [86] Wang, C.; Xu, H.; Liang, C.; Liu, Y. M.; Li, Z. W.; Yang, G. B.; Cheng, H.; Li, Y. G.; Liu, Z., Iron Oxide @ Polypyrrole Nanoparticles as a Multifunctional Drug Carrier for Remotely Controlled Cancer Therapy with Synergistic Antitumor Effect. *Acs Nano* **2013**, *7* (8), 6782-6795.
- [87] Wang, T.; Zhang, L.; Li, C.; Yang, W.; Song, T.; Tang, C.; Meng, Y.; Dai, S.; Wang, H.; Chai, L., Synthesis of core-shell magnetic Fe₃O₄@ poly (m-phenylenediamine) particles for chromium reduction and adsorption. *Environmental science & technology* **2015**, *49* (9), 5654-5662.
- [88] Xia, H.; Zhang, L.; Chen, Q. D.; Guo, L.; Fang, H. H.; Li, X. B.; Song, J. F.; Huang, X. R.; Sun, H. B., Band-Gap-Controllable Photonic Crystals Consisting of Magnetic Nanocrystal Clusters in a Solidified Polymer Matrix. *Journal of Physical Chemistry C* **2009**, *113* (43), 18542-18545.
- [89] He, L.; Wang, M. S.; Ge, J. P.; Yin, Y. D., Magnetic Assembly Route to Colloidal Responsive Photonic Nanostructures. *Accounts of Chemical Research* **2012**, *45* (9), 1431-1440.
- [90] Kim, H.; Ge, J.; Kim, J.; Choi, S.-e.; Lee, H.; Lee, H.; Park, W.; Yin, Y.; Kwon, S., Structural colour printing using a magnetically tunable and lithographically fixable photonic crystal. *Nature Photonics* **2009**, *3* (9), 534-540.
- [91] Ge, J. P.; Yin, Y. D., Responsive Photonic Crystals. *Angew. Chem.-Int. Edit.* **2011**, *50* (7), 1492-1522.
- [92] Bagaria, H. G.; Yoon, K. Y.; Neilson, B. M.; Cheng, V.; Lee, J. H.; Worthen, A. J.; Xue, Z.; Huh, C.; Bryant, S. L.; Bielawski, C. W., Stabilization of iron oxide nanoparticles in high sodium and calcium brine at high temperatures with adsorbed sulfonated copolymers. *Langmuir* **2013**, *29* (10), 3195-3206.
- [93] Bixner, O.; Lassenberger, A.; Baurecht, D.; Reimhult, E., Complete Exchange of the Hydrophobic Dispersant Shell on Monodisperse Superparamagnetic Iron Oxide Nanoparticles. *Langmuir* **2015**, *31* (33), 9198-9204.

- [94] Ding, X.; Vegesna, G. K.; Meng, H.; Winter, A.; Lee, B. P., Nitro-Group Functionalization of Dopamine and its Contribution to the Viscoelastic Properties of Catechol-Containing Nanocomposite Hydrogels. *Macromolecular chemistry and physics* **2015**, *216* (10), 1109-1119.
- [95] Thomas, G.; Demoisson, F.; Chassagnon, R.; Popova, E.; Millot, N., One-step continuous synthesis of functionalized magnetite nanoflowers. *Nanotechnology* **2016**, *27* (13), 135604.
- [96] Yu, W. W.; Chang, E.; Sayes, C. M.; Drezek, R.; Colvin, V. L., Aqueous dispersion of monodisperse magnetic iron oxide nanocrystals through phase transfer. *Nanotechnology* **2006**, *17* (17), 4483-4487.
- [97] Zirbs, R.; Lassenberger, A.; Vonderhaid, I.; Kurzhals, S.; Reimhult, E., Melt-grafting for the synthesis of core-shell nanoparticles with ultra-high dispersant density. *Nanoscale* **2015**, *7* (25), 11216-11225.
- [98] Gleich, B.; Weizenecker, J., Tomographic imaging using the nonlinear response of magnetic particles. *Nature* **2005**, *435* (7046), 1214-1217.
- [99] Bauer, L. M.; Situ, S. F.; Griswold, M. A.; Samia, A. C., Magnetic Particle Imaging Tracers: State-of-the-Art and Future Directions. *J Phys Chem Lett* **2015**, *6* (13), 2509-17.
- [100] Panagiotopoulos, N.; Duschka, R. L.; Ahlborg, M.; Bringout, G.; Debbeler, C.; Graeser, M.; Kaethner, C.; Ludtke-Buzug, K.; Medimagh, H.; Stelzner, J.; Buzug, T. M.; Barkhausen, J.; Vogt, F. M.; Haegele, J., Magnetic particle imaging: current developments and future directions. *Int J Nanomedicine* **2015**, *10*, 3097-114.
- [101] Chandrasekharan P, T. Z., Zhou XY, et al. , A perspective on a rapid and radiation-free tracer imaging modality, magnetic particle imaging, with promise for clinical translation. . *Br J Radiol.* **2018**, *91*, 1091.
- [102] Tay, Z. W.; Hensley, D. W.; Vreeland, E. C.; Zheng, B.; Conolly, S. M., The Relaxation Wall: Experimental Limits to Improving MPI Spatial Resolution by Increasing Nanoparticle Core size. *Biomed Phys Eng Express* **2017**, *3* (3), 035003.
- [103] Wu, L. C.; Zhang, Y.; Steinberg, G.; Qu, H.; Huang, S.; Cheng, M.; Bliss, T.; Du, F.; Rao, J.; Song, G.; Pisani, L.; Doyle, T.; Conolly, S.; Krishnan, K.; Grant, G.; Wintermark, M., A Review of Magnetic Particle Imaging and Perspectives on Neuroimaging. *AJNR Am J Neuroradiol* **2019**, *40* (2), 206-212.

Chapter 2

Systematic Synthesis of Iron Oxide Nanocrystal Clusters with Independent Dimensional Control[†]

[†] Reprinted (adapted) with permission from Xiao, Z.*, Zhang, Q.*, Guo, X., Villanova, J., Hu, Y., Külaots, I., Garcia-Rojas, D., Guo, W. and Colvin, V.L. Libraries of Uniform Magnetic Multicore Nanoparticles with Tunable Dimensions for Biomedical and Photonic Applications. *ACS Applied Materials & Interfaces*, 2020, 12(37), 41932-41941. Copyright © 2020, American Chemical Society

*These authors contributed equally.

2. Systematic Synthesis of Iron Oxide Clusters with Independent Dimensional Control

2.1 Abstract

Multicore iron oxide nanoparticles, also known as colloidal nanocrystal clusters, are magnetic materials with diverse applications in biomedicine and photonics. Here we examine how both of their characteristic dimensional features, the primary particle and sub-micron colloid diameters, influence their magnetic properties and performance in two different applications. The characterization of these basic size-dependent properties is enabled by a synthetic strategy that provides independent control over both the primary nanocrystal and cluster dimensions. Over a wide range of conditions, electron microscopies and x-ray diffraction reveal that oriented attachment of smaller nanocrystals results in their crystallographic alignment throughout the entire superstructure. We apply a sulfonated polymer with high charge density to prevent cluster aggregation and conjugate molecular dyes to particle surfaces so as to visualize their collection by handheld magnets. These libraries of colloidal clusters, indexed both by the primary nanocrystal dimension (d_p) and the overall cluster diameter (D_c), form magnetic photonic crystals with relatively weak size-dependent properties. In contrast their performance as MRI T_2 contrast agents is highly sensitive to cluster diameter, not primary particle size, and is optimized for materials of 50 nm diameter ($r_2 = 364 \text{ mM}^{-1} \text{ s}^{-1}$). These results exemplify the relevance of dimensional control in developing applications for these versatile materials.

2.2 Introduction

Magnetic multicore particles are an important class of nanomaterials whose unique properties are relevant to both medical and optical technologies.^[1-3] Also referred to as nanoclusters or colloidal nanocrystal clusters, these systems are comprised of tens to hundreds of sub-10 nm iron oxide crystallites hard aggregated into larger, porous clusters.^[4-7] In the absence of a magnetic field these materials exhibit superparamagnetic behavior characteristic of their nanocrystalline composition.^[8] As an external magnetic field is applied, however, the individual crystallites collectively magnetize ultimately forming magnetic domains encompassing the entire cluster.^[8-11] It is this combination of superparamagnetism, large magnetic volume and small dimension that underlie their value as materials for drug delivery, magnetic hyperthermia, magnetic resonance imaging and responsive photonic crystals.^[2, 11-13]

Their magnetic behavior and technological performance should be critically dependent on both the cluster diameter, D_c , and the primary nanocrystal diameter, d_p .^[14, 15, 19] Exploring these trends has been of interest, but systematic studies over a broad range of material dimensions has remained an elusive goal.^[5, 16-18] The challenge is largely synthetic as these nanomaterials have two distinct structural dimensions of interest and the conventional “polyol” synthesis of the materials does not easily yield wide ranging tunability or independent control over either feature.^[19-22] Researchers have manipulated cluster diameter by varying the concentration of iron precursor and surfactant,^[18, 23-28] as well as altering the solvent;^[29, 30] however, such conditions also affect the dimensions of the primary nanocrystals thus confounding any independent evaluation of each critical dimension.^[26-32] Insightful strategies for decoupling these two features are available for

materials with diameters in excess of 100 nm, but they do not extend to smaller nanoclusters most relevant in medical applications.^[24, 27]

Any consideration of size control must also confront the challenge of forming multicore particles that remain non-aggregating in water and relevant biological media.^[3, 11-13] Magnetic dipolar interactions drive interparticle aggregation and this problem is especially acute for larger particles.^[9] To combat this, multicore materials can be charge-stabilized using polyacrylic acid (PAA) or citrate.^[23-26] While these coatings provide substantial charge repulsion and less particle aggregation in pure water, they fail at lower pH and in the presence of divalent cations common in biological media such as Ca^{2+} .^[35] Neutral coatings, such as polyethylene glycol (PEG) or silica, have been widely used for the stabilization of these and other nanoparticles.^[12] Nevertheless, for magnetic nanoparticles, material aggregation hard to avoid in biological media and large external magnetic fields. Such conditions increase the attractive magnetic dipolar forces between particles and diminish electrostatic repulsive interactions.^[35-38, 53] The difficulty in preventing particle aggregation in biological media may be one reason there are relatively few in-vivo studies of magnetic multicore particles in spite of their promise in MRI imaging, drug delivery and magnetic particle imaging.^[13, 39-41]

Here we present a method to generate libraries of non-aggregating magnetic multicore particles with cluster diameters and primary nanocrystal sizes that are independently controlled. The work takes advantage of the proposed two-step mechanism for cluster formation so as to achieve dimensional control.^[44-46] The resulting materials have tunable particle diameters from 20 to 200 nm with less than 10% polydispersity; the primary nanocrystals can be tuned from 4 to 10 nm in diameter thus forming a library of materials

that span relevant dimensional ranges. Electron microscopy and x-ray diffraction confirm that the sub-10 nm particles share grain boundaries with aligned crystallographic axes. We graft a sulfonated polyelectrolyte to the multicore particles to impart colloidal stability over a wide range of solution conditions, including low pH, and further derivatize the materials with molecular dyes relevant for biological imaging. The larger multicores, with cluster diameters greater than 100 nm, form reversible and magnetically responsive photonic crystals whose properties are relatively independent of size. Their performance as T₂ MRI contrast agents reveals a striking dependence on cluster diameter and a conversely weak dependence on primary nanocrystal diameter. Smaller clusters, with diameters near 50 nm, provide the best T₂ contrast with a notably high relaxivity at clinically relevant field strengths (3.4 T, r₂ = 364 mM⁻¹ s⁻¹).

2.3 Synthesis and dimensional control of the clusters

Studies of the reaction mechanism of this classic ‘polyol’ synthesis have found that forced hydrolysis of iron salts leads to the formation of condensed iron oxide phases that gradually ripen into multicore particles (Figure 2.1 a).^[26, 41] Our strategy for size control of these materials is based on the expectation that material formation follows a two-step process as suggested by several mechanistic studies.^[41-46] The first step depends critically on the small amount of water either present in hydrous polar solvents and precursors or intentionally added as a reactant; this water hydrolyzes iron salts leading to the formation of iron hydroxides that at elevated temperature ripen into very small particles of iron oxide phases such as magnetite (Figure 2.1 b). The diameter of these primary nanocrystals is fixed during this first stage. The second process drives aggregation of these crystallites into larger clusters (Figure 2.1 c) which determines the overall cluster diameter and its uniformity.

The end-products contain tens to hundreds of crystallites in each cluster and are characterized both by the size of their primary nanocrystal (d_p) and by the physical diameter of the cluster (D_c) as indicated in Figure 2.1 c.

Methods that allow independent and wide-ranging control over both of these dimensional features have been elusive. For example to form larger primary nanocrystals investigators can extend the reaction time, but this also yields broader size distributions.^[6, 27, 37, 40, 41] Moreover cluster dimensions from prolonged reactions typically yield larger clusters with dimensions in excess of 100 nm. The formation of smaller products, with cluster diameters well below 50 nm, generally requires a different strategy. Researchers have faced this challenge by changing the solvent composition, typically mixing ethylene glycol with diethylene glycol, triethylene glycol or other glycol derivatives;^[30] alternatively adding water can accelerate hydrolysis and change the viscosity of the reaction media both of which are thought to favor smaller cluster diameters.^[16, 61, 62] Studies of the product evolution suggest that primary nanocrystal formation occurs early in the reaction as the result of the forced hydrolysis of iron salts;^[6, 41-44] acceleration of this reaction at higher temperatures can lead to the formation of larger primary nanocrystals but also faster cluster growth.^[45, 46] Conversely, the addition of water can limit primary nanocrystal aggregation and yield smaller cluster dimensions.^[16, 43, 46] These observations suggest that by limiting the hydrolysis reaction and primary nanocrystal aggregation, through both manipulation of temperature and water, it may be possible to achieve independent control over both dimensional variables.

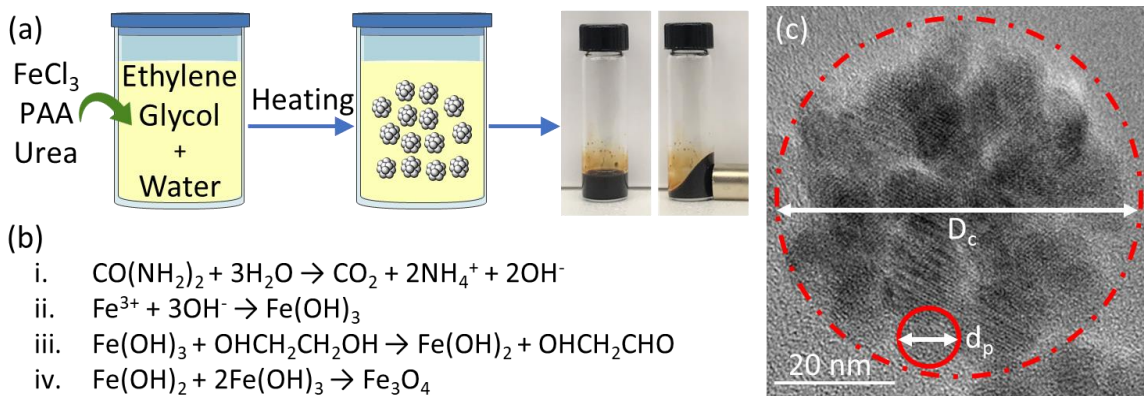


Figure 2. 1. Synthesis of the iron oxide nanoclusters. (a) Synthetic scheme for the reaction. Water and temperature are used to tune the cluster dimension. PAA stands for polyacrylate. (b) Reaction pathway for the formation of Fe₃O₄. (c) The internal structure characterized by electron microscopy shows the clusters are composed of many primary nanocrystals. In this example, the cluster size (D_c) is 50 nm and the primary nanocrystal (d_p) diameter is 10 nm.

Using the insights provided from this prior work, we manipulated the water content and temperature of the reaction in systematic ways to produce uniform and size-tunable cluster diameters. Shown in Figure 2.2 and Figure S2.1 are products ranging in cluster diameter (D_c) from 20 to 200 nm. Water is an essential reactant in this synthesis as it hydrolyzes the iron salt and ultimately contributes to the aggregative growth of clusters. Prior studies, in agreement with our own observations, have demonstrated when water is stringently removed from the reactants, clusters in excess of several microns will form (Figure S2.1 c). As water content is increased smaller diameter multicore particles are formed. Water apparently accelerates the cluster formation process leading to more growing clusters competing for individual crystallites.^[7] For example, at 185 °C and iron concentrations of 100 mM, clusters over 120 nm in diameter form with relatively low water concentrations (0.3 M water). When the amount of water is increased to 6.2 M the cluster dimensions fall to 35 nm for the same conditions (Figure 2.2 a-e). Over this range the primary nanocrystal

size remains unchanged at 4 nm. Water places multiple roles in the reaction, both influencing the forced hydrolysis of the iron salt as well as the kinetics of aggregation through the solution viscosity.^[16] When there is more water available, there is faster hydrolysis and primary nanocrystal formation, leading to more rapid aggregation and thus smaller clusters.^[42, 43] We also found that cluster uniformity generally improved with increasing water content, presumably as the initial cluster nucleation even occurred over a narrower time window (Figure S2.4 d).

Reaction temperature provides the best avenue for manipulating primary nanocrystal dimension. Higher temperatures speed up nucleation, promote Ostwald ripening, and encourage the non-aggregative growth of crystals.^[41] We find that for the same reaction conditions we form larger primary nanocrystal sizes at higher temperatures.^[43-46] At the maximum temperature, which is 275 °C for our reactor, we measure primary nanocrystal sizes up to 10 nm (Figure 2.1 c) via electron microscopy. By gradually decreasing the temperature to the lowest level that permits crystallization of the iron oxides within six hours, or 185 °C, we can reduce the primary nanocrystal dimensions from 10 to 4 nm (Figure S2.2 a-f). While manipulating reaction time yields similar trends, it comes at the expense of particle uniformity (Figure S2.4 e). Notably, the cluster diameter of samples prepared at different temperatures are all near 50 nm for the same fixed concentration of water. As a result, it is possible to independently control both of the characteristic dimensions of multicore magnetic particles.

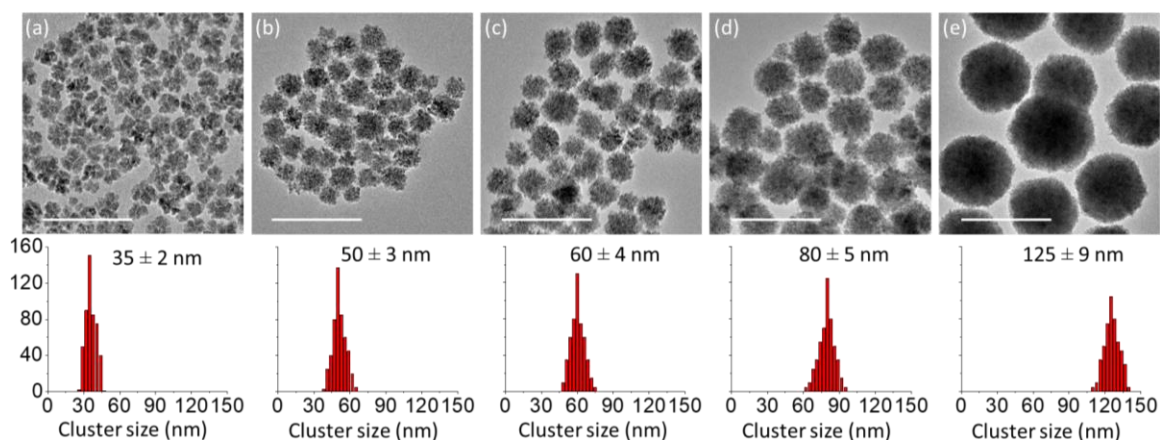


Figure 2. 2. Dimensional control of the cluster synthesis by water. (a-e) Transmission electron microscopy images (top) and size distribution histograms (bottom) of the cluster samples with different cluster sizes. Scale bar: 200 nm. The molar concentration of water for each synthesis is 6.2, 3.9, 2.6, 1.1 and 0.3 M, respectively. The y axis represents the number of clusters counted. For each sample, a total of 500 clusters were measured for overall cluster diameter. The reported spread in diameter is the standard deviation from the measured diameters of the 500 clusters.

Through control over temperature and water content we can generate libraries of uniform iron oxide nanoclusters (Figure S2.3) with tunable cluster diameters (D_c), from 20 to 200 nm, and primary nanocrystal sizes (d_p), from 4 to 10 nm. The cluster uniformity is notably consistent across the varying samples ranging from 6 to 10% on the overall cluster diameter. The size distributions of these samples are equivalent or in some cases better than those reported by other researchers.^[41-47]

While microscopy can be used to visualize the smaller nanocrystals present in these materials, the presence of overlapping crystallites in the field of view makes quantitative assessment of their uniformity problematic.^[12] X-ray diffraction linewidths (Figure S2.6) can be used to confirm that the average crystallite dimensions are consistent with those observed by electron microscopy. As anticipated, the materials for which we measured smaller primary nanocrystal diameters via electron microscopy also had broader diffraction

linewidths (Table 2.1). However, quantitative agreement between the methods was not observed. Instead we found primary nanocrystal dimensions measured from microscopy to be smaller than the grain size calculated from the diffraction linewidths. This has been observed by others and is attributed to the oriented attachment of primary nanocrystals during the formation of the clusters.^[9, 16, 67]

Table 2. 1. The cluster size (D_c), particle size (d_p) and grain size measured by both electron microscopy and x-ray diffraction. The samples are denoted as D_c - d_p . The molar concentration of water for the synthesis of sample 6-25 to 6-90 (left part) is 6.2, 5.4, 4.2, 3.9, 1.7 and 0.84 M, respectively, with a reaction temperature of 215 °C. The reaction temperature for the synthesis of sample 5-45 to 10-45 (right part) is 200, 215, 230, 245, 260, 275 °C, respectively, with a molar concentration of water of 4.2 M.

Sample	D_c /nm (TEM)	d_p /nm (TEM)	Grain size/nm (XRD)	Sample	D_c /nm (TEM)	d_p /nm (TEM)	Grain size/nm (XRD)
6-25	25	6.0	10.6	5-45	45	5.0	9.9
6-35	35	6.0	10.5	6-45	45	6.0	10.6
6-45	45	6.0	10.6	7-45	45	7.0	11.6
6-50	50	6.0	10.6	8-45	45	8.0	12.8
6-70	70	6.0	10.5	9-45	45	9.0	14.3
6-90	90	6.0	10.6	10-45	45	10.0	16.6

We also explored the effect of other reaction conditions, including the concentrations of polyacrylate (PAA), urea and iron salts and compiled our results in Figure S2.4. PAA provides a surface coating for the nanoclusters,^[24, 28] while urea ensures a basic reaction environment that promotes forced hydrolysis and ripening of iron oxides.^[26] Neither of these agents exert substantial control over cluster dimensions although they do impact sample uniformity (Figure S2.4 b and c). The iron salt concentration contributes to the

overall number of primary nanoparticles, and thus can impact cluster size as well as the dimensional distributions. Others have noted the concentration of iron has the most impact on the primary nanocrystal aggregation process, with comparatively little effect on the ripening and crystallization of the materials.^[27,28] We observed that iron concentration was an important variable to control with respect to both cluster diameter as well as uniformity; we selected an optimal value (100 mM) which is much less than our estimated concentration of water (3900 mM). Excess water is necessary in order to force the hydrolysis of the iron salts in polar solvents and ultimately form the iron hydroxides that ripen into primary nanocrystals. At very low levels of iron precursor (18 mM) nucleation is likely to occur over long periods of time leading to small and ill-formed materials. With increasing precursor concentration (56 mM), nucleation of the primary nanocrystal will proceed quickly and separately from the slower aggregation of clusters leading to larger materials with poor uniformity. Finally, at the highest iron concentrations we found more uniform clusters but with very small diameters. Our speculation is that for these conditions the surfaces of the primary nanocrystals are iron-rich which may alter their propensity to aggregate (Figure S2.4 a).^[68]

Our examination of the morphology of these clusters largely confirms what others have reported for these multicore materials: namely, that these particles are superstructures which consist of aggregates of primary nanocrystals. We describe these aggregates as ‘hard’ because the small crystallites of iron oxide share common interfaces with no intervening surfactant.^[18,69] While microscopy from these samples are consistent with this structural model, further confirmation comes from an analysis of the surface area of the bulk multicore powders. These samples possess surface areas that range from 55 to 110

$\text{m}^2 \text{g}^{-1}$ (Figure S2.5). Samples with larger primary nanocrystals had lower surface areas as would be expected. Also as anticipated the cluster diameter had little impact on overall surface area; even though a 20 nm cluster would have nominally more surface area than a 200 nm cluster, this difference is negligible given the surface area contributed by the much smaller primary nanocrystals. We calculated the expected surface areas of these materials assuming isolated, non-aggregated, primary nanocrystals and generally found these values to be twice as large as the measured surface areas. Thus, roughly half of the surface area of the smaller nanocrystals is in contact with neighbors in ways that limit the access of those interfaces to molecular gases, in this case nitrogen, during surface area analysis.

High resolution TEM and electron diffraction reveal a cluster morphology with densely packed primary nanocrystals. Shown in Figure 2.3 are representative data from two samples with smaller (Figure 2.3 a) and larger (Figure 2.3 c) cluster dimensions. In both instances the primary nanocrystals are evident as are shared interfaces between neighboring primary nanocrystals. These data are consistent with the surface area analysis (Figure S5) which indicates that some shared interfaces are inaccessible for surface adsorption. Electron diffraction from these materials reveals that the primary nanocrystals possess some degree of crystallographic alignment in agreement with prior studies of these multicore structures.^[12, 45] Figure 2.3 b and d show the electron diffraction patterns from an individual cluster. In each example the bright areas at specific angles, as opposed to rings, are more consistent with diffraction from a single crystal as opposed to randomly oriented crystallites.^[48] When electron diffraction is collected from many clusters, the diffraction spots merge together to form rings consistent with polycrystalline, randomly oriented material (Figure S2.9). For a single nanocluster the specific reflections in electron

diffraction are not perfect spots as would be expected for a single crystal, but rather narrow arcs (Figure 2.3 b, d).^[6, 49] This indicates some level of misalignment between closely aligned domains.^[45] Further evidence for this structure can be seen in the widths of the x-ray diffraction peaks; an application of the Debye-Scherrer formula yields scattering domain sizes significantly larger than the measured microscopy would suggest (Table 2.1).^[18] These data suggest the particles undergo an oriented attachment process as they aggregate, and that in the final multicore cluster this alignment is nearly perfect over the entire particle.^[47, 48]

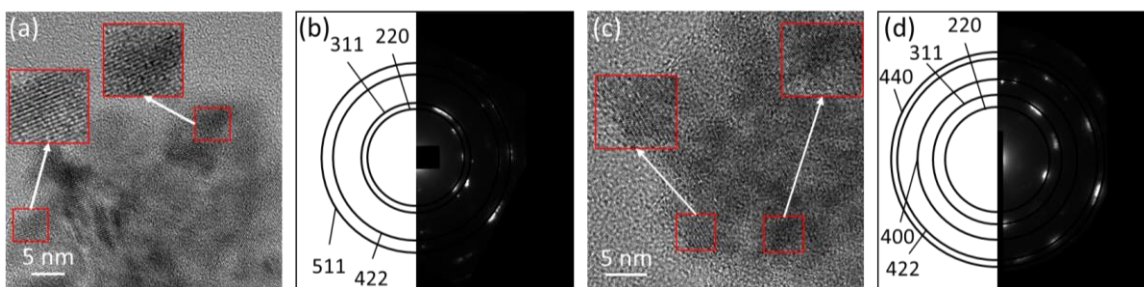


Figure 2. 3. Internal cluster structure. (a, c) High-resolution TEM (HRTEM) and (b, d) the selected area electron diffraction (SAED) pattern of the sample in a and c, respectively, with diffraction rings identified according to magnetite.

These electron microscopy observations are consistent with x-ray diffraction of the purified powders, as shown in Figure S2.6 a and b. Reflections consistent with iron oxide crystal phases are present; magnetite (Fe_3O_4) and maghemite (Fe_2O_3) are notoriously difficult to distinguish using x-ray diffraction although the separation of higher order peaks is consistent with magnetite (Figure S2.6 c and d).^[6, 18] Raman spectroscopy (Figure S2.7) finds peaks consistent with both Fe(II) and Fe(III). This data, along with the materials' black appearance (Figure 2.1 a), are strong evidence that as-synthesized the slightly more reduced form of iron oxide (Fe_3O_4) is dominant.^[50] These isolated magnetite nanocrystals

can undergo a slow oxidation process,^[16] and over two months samples gradually become reddish-brown, likely corresponding to Fe₃O₄, if not stored under nitrogen. This observation is consistent with their magnetic properties. The saturation magnetization values range from 74 to 86 emu/g Fe₃O₄; these values are very close to that seen for bulk magnetite ($M_{\text{sat}} \sim 90$ emu/g Fe₃O₄),^[9] which indicates these are high quality-crystals with well-formed surfaces.^[51] The materials are superparamagnetic at smaller dimensions with a small remanence (~ 13 Oe) at larger dimensions (Figure S2.8). For the smaller cluster sizes (below 50 nm in diameter) there is no observable hysteresis in the dependence of sample magnetization on applied magnetic field at room temperature.

2.4 Surface functionalization of the clusters

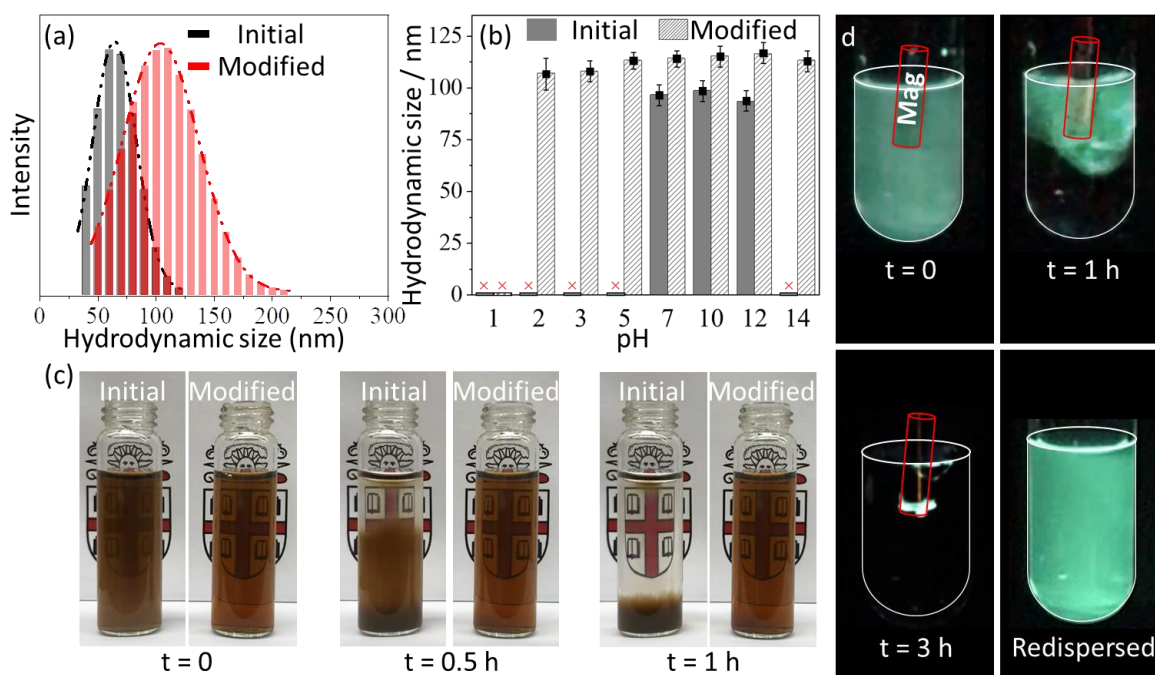


Figure 2. 4. Surface functionalization of the clusters. (a) The DLS size distribution of a typical as-synthesized cluster sample and further modified by P(AA-co-AMPS), with a polydispersity index (PDI) of 0.12 and 0.11, respectively. (b) The hydrodynamic size of the cluster sample and P(AA-co-AMPS) modified sample at different pH where × indicates the visible aggregation of the cluster in aqueous solution. (c) Stability in phosphate-buffered saline (PBS, 1X) of the as-synthesized cluster sample (right) and P(AA-co-AMPS) modified

sample (left). (d) The images of the EDANS dye labeled cluster sample under UV radiation with a magnet (contoured in red) on top of the solution for 3 hours and finally redispersed in the solution with the magnet removed and rinsed by water. The cluster sample used in the above tests has a D_c of 45 nm and d_p of 4 nm.

A conventional polyacrylate additive (PAA, Mw = 6,000) is included in these reactions as others have shown that this surface coating yields non-aggregating materials in pure water (Figure 2.1 a);^[23, 24] the products are dark brown or black stable suspensions depending on the concentration. Infrared spectroscopy (Figure S2.10) of the native materials shows features consistent with polyacrylic acid.^[52] PAA both binds to the cluster surface and promotes colloidal stability. Figure 2.4 a shows that the hydrodynamic diameter of a 45 nm cluster (TEM dimension) is larger ($D_H = 65$ nm) due to the polymer coating. These clusters are not stable in the ionic media relevant for biological applications as demonstrated by their sedimentation (Figure 2.4 b and c) in acidic solution or phosphate buffered saline (PBS). They must undergo modification with a more robust and functional polymer coating in order to remain non-aggregating under conditions that shield their charge-repulsive interactions.^[32, 37, 49]

We applied a sulfonated polyelectrolyte used to stabilize surfactants in the high brine water of underground aquifers to generate stable suspensions;^[35, 53] we reasoned that the increased charge of the polymer, along with the sulfonic acid moieties, would contribute to a strong steric and charge-repulsive interface able to reduce aggregation between particles. Briefly, a sulfonic acid polyelectrolyte [P(AA-co-AMPS)] was anchored to the surface of iron oxide cluster by a catechol-iron bond. Figure 2.4 a shows the hydrodynamic sizes increase to 100 nm after polyelectrolyte grafting; in contrast to polyacrylate this surface coating provides materials resistant to aggregation under a wide range of conditions.

Surface coatings containing sulfonic acids have not yet been applied to biologically relevant nanoparticles, but they are known to be robust and the charge-stabilized coatings for applications in oil and gas recovery. To tether the coating to the iron oxide surface, we relied on a catechol head group (nitro-dopamine) to form a bidentate bond with iron.^[47, 54] The inclusion of a nitro functionality in this structure further strengthens the iron-catechol bond and makes the polymer coating that much more stable.^[55] We characterized the polymer by HPLC and NMR (Figure S2.11) prior to conjugation: the average molecular weight was 87,000 g/mol, and the AA to AMPS ratio was nearly 1 to 1. Other investigators have found that in the case of polyethylene glycol (PEG) polymer chains terminated in single catechols can be gradually removed from nanoparticle surfaces after washing.^[56] Because of this, the polymer (cat-PAMPS) geometry includes many catechols so as to strengthen the attachment of the coating to the multicore particle. The resulting samples are larger in hydrodynamic diameter as expected given the larger chain length of the cat-PAMPS. We optimized the ratio of the catechol along the PAMPS backbone: generally better stability is observed when there are 20 catechols distributed among the 300 units in each polymer chain. If polymer chains contained higher ratios of grafting sites then coated clusters could become cross-linked into larger aggregates.

These clusters are easily modified as we retain some free acrylic acids as well as amines at the particle interfaces allowing for conjugation of fluorescent dyes (Figure S2.12). In some cases the amine groups were used as conjugation points for organic acids available on common dyes; alternatively, other dyes were conjugated first to the catechol grafting agent, and then incorporated onto the polyelectrolyte as seen in Figure S2.12 c and e. In the case of a hydrophobic dye, DiI, we altered our surface modification strategy by using an

amphiphilic polymaleimide-octadecene that functionally wrapped the multicore particle. The hydrophobic character of this surface allowed us to tether DiI to the water-soluble clusters (Figure S2.12 g).^[57] In each example, the emission characteristics of the dye-labeled particles was equivalent to the original dye behavior (Figure S2.12 b, d, f, h). We note that the dye conjugation schemes are efficient enough to permit the visualization of labeled clusters using a handheld ultraviolet light (Figure 2.4 d).

2.5 Clusters as dynamic photonic crystals

Magnetic multicore materials can form a dynamic photonic crystal superstructure under the application of a weak magnetic field.^[2] Figure 2.5 a shows the changing colors that result as a small handheld magnet is brought close to a vial of the initially dark brown clusters. As compared to Figure 2.4, these clusters are not functionalized by any fluorescent dyes and their colors arise from the diffraction of visible light. Reflection spectroscopy (Figure 2.5 c) confirmed what is apparent to the naked eye: under even weak external fields these suspensions develop a strong reflection peak that shifts from the red to the blue with increasing magnetic field. Moreover, the peak intensity is very sensitive to the angle between the applied field and the optical detector as would be expected for a photonic crystal (Figure 2.5 b, d).

This behavior is consistent with prior studies which term these materials “magnetic photonic crystals”.^[58, 59] Their optical diffraction is thought to arise not from a three-dimensional arrangement of particles but from scattering from particles assembled into one-dimensional chains. To visualize these superstructures we applied for the first time cryogenic SEM to the aqueous suspensions (Figure 2.5 e). The observed interchain distances are on the order of microns and thus too large to account for the observed

scattering of visible light seen here. In contrast, intrachain particles are closely spaced, though not touching, and become more densely packed with increasing magnetic field. The particle-particle packing within each chain, larger than the diameter of the particles as they are not touching, accounts for the optical diffraction.^[34, 60-62] The particle-particle separation here is governed by an interplay between attractive magnetic dipole-dipole and Van der Waal interactions and surface charge repulsion; we note this is in contrast to hard sphere photonic crystals in which this separation is solely dependent on particle diameter as the particles physically contact each other.^[58, 59] Notably, the clusters coated with the sulfonic acid polyelectrolytes are quite stable against field-induced aggregation and can be cycled on and off into a diffractive state multiple times.

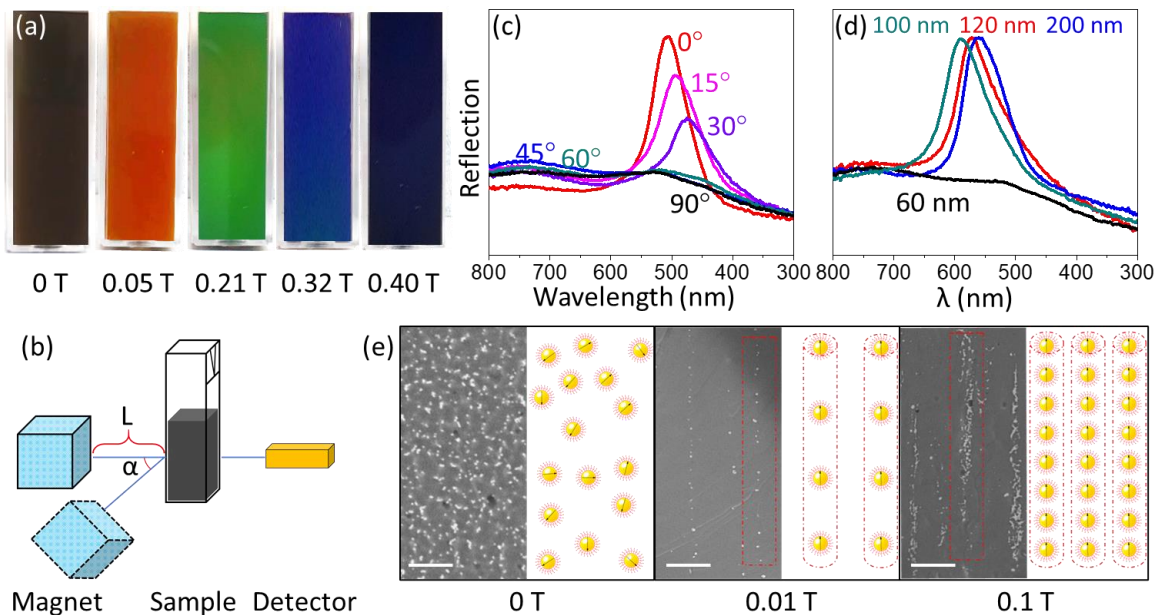


Figure 2. 5. Clusters as magnetically controllable photonic crystals. (a) Images of the cluster solution showing different colors at different external magnetic field strength, (b) the reflection spectra of the clusters solution at different external magnetic field strength, (c) the intensities of the reflection spectra at different detector angles, (d) the setup of the reflection spectrometer where the distance (L) and angle (α) between the magnet and the sample can be adjusted, and (e) the cryo-SEM images and the proposed magnetically induced photonic crystal structures of the cluster solution at different magnetic field strength. Scale bar: $5 \mu\text{m}$. The clusters presented in Figure 2.5 a, c and e have a D_c of 120

nm and a d_p of 4 nm. In Figure 2.5 d, the cluster sizes are 60 nm, 100 nm, 120 nm and 200 nm, respectively, with the same d_p of 4 nm. All cluster samples been coated with polyelectrolyte to prevent irreversible aggregation.

For the same external field conditions we can also observe how the optical properties depend on cluster dimensions (Figure 2.5 c). We found no significant visible diffraction for suspensions containing cluster dimensions below 100 nm. In smaller particles the magnetic dipole-dipole interaction is much less pronounced and not large enough to overcome the particles' electrostatic repulsion. As cluster diameters exceeded 100 nm diffractive phenomena became apparent; we noted for the exact same applied field and solution concentrations, with increasing diameters there was a small blue shift in the diffractive peak from 560 to 590 nm (Figure 2.5 c). We speculate that as clusters increase in dimension they experience more magnetic dipole-dipole attraction which draws the particles closer together leading to the observed blue shift. This simple explanation presumes that the repulsive interaction between our highly charged particles is large and relatively independent of cluster diameter (Figure S2.13). This assumption may not be true for magnetic particles with less charged surfaces and indeed another study of this phenomenon reported the opposite trend in conditions of varying magnetic field.^[59] In describing the optical properties of magnetic photonic crystal cluster dimension is one of several material parameters that can be related to the color and stability of the diffraction.

2.5 Clusters as efficient MRI contrast agent

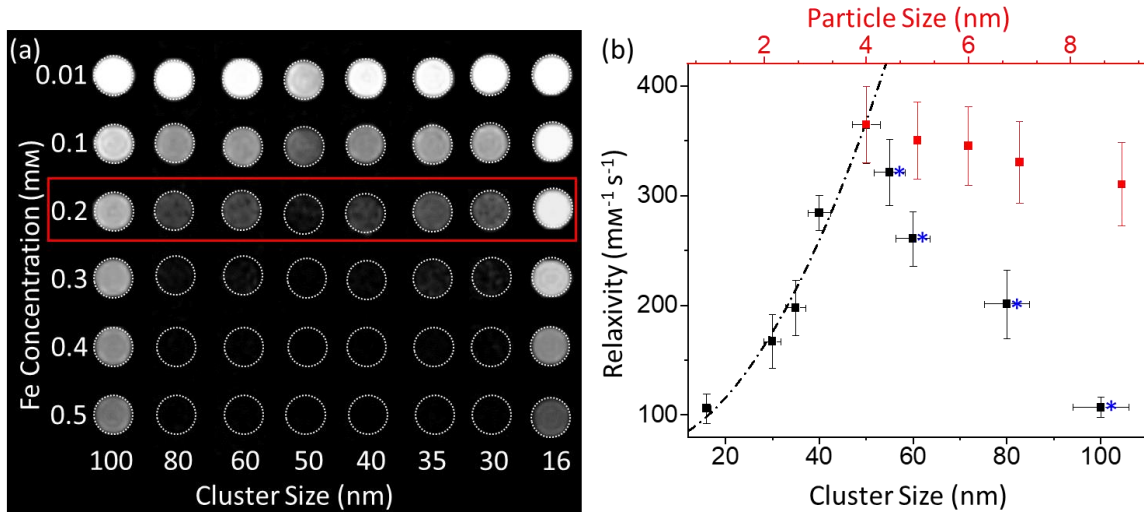


Figure 2. 6. MRI T_2 contrast highly depends on D_c and weakly on d_p . (a) The phantom images of the clusters of different cluster sizes at different atomic iron concentrations. All sample positions are marked by a dotted ring, and the black color signifies the contrast. The red box highlights that at 0.2 mM only those particles with dimensions of 50 nm appear dark in phantom images. (b) The T_2 relaxivity of the cluster samples with different D_c (black, same d_p at 4 nm) and d_p (red, same D_c at 50 nm). The error bars in the cluster size represent the standard deviation of the cluster diameters found from TEM imaging and that of r_2 was based on the regression coefficients from the linear fitting of the concentration-dependent contrast (see Figure S2.14). The blue dash line fits the Universal Scaling Law model proposed by Sandre et. al^[14] where r_2 is linear increasing to the square of D_c . The four points ($D_c > 50$ nm) accompanied by blue stars indicate the relaxivity as measured by MRI contrast. However, we consider these data obscured by the propensity of larger particles to aggregate in large external fields. This aggregation is severe enough at these dimensions to lead to rapid sedimentation and inhomogeneous solutions of contrast agent; we include them to illustrate the problematic nature of measuring the relaxivity of rapidly aggregating contrast solutions.

Particle dimensions and surface chemistry are also important factors in the design of nanoparticle MRI contrast agents.^[17, 64, 65] Figure 2.6 a shows the phantom images in a MRI scanner of a range of different cluster diameters, where the contrast changes very rapidly with the variation of cluster concentration among all samples. Consistent with this observation in phantom images is the quantitative analysis of the relaxivity shown in Figure 2.6 b. These values are found from the slope of the contrast versus particle concentration

(Figure S2.14) and demonstrate that at intermediate cluster dimensions (50 nm), the MRI T₂ contrast is optimized. Since there is only a negligible difference in the saturation magnetization of these cluster samples (Figure S2.8), we can conclude that the physical size of the clusters is the major contributing factor to the size-dependent relaxivity. The optimized size-dependent relaxivity, $r_2 = 364 \text{ mM}^{-1} \text{ s}^{-1}$, is modestly higher than the best values reported for similar multicore materials even at this very high and clinically relevant magnetic field (e.g. 3.4 T).^[64, 65] Interestingly, primary nanocrystal size has only a slight impact on relaxivity (Figure 2.6 b, red). Others who have studied size dependence for very small clusters have also reported an increase in relaxivity with increasing size.^[66, 67]

Once cluster dimensions exceed 50 nm, however, their contrast decline with increasing diameter (Figure 2.6). This observation is consistent with studies of larger clusters which reported a decline in relaxivity with cluster dimension.^[17] Conceptual models for T₂ nanoparticle contrast generally predict monotonically increasing T₂ relaxivity with increasing particle diameter. Briefly, the magnetic gradients of larger particles will influence a larger volume of water simply by virtue of their increased surface area; this in turn will lead to more influence on the relaxation of proton spins and consequently greater contrast (Figure 2.6b, dashed line).^[14] We find that as the cluster dimensions increase beyond 50 nm the relaxivity begins to fall. This behavior arises from the inevitable aggregation of clusters induced by the large applied field of the MRI scanner, more than 3 T in these experiments. While we have successfully formed colloiddally stable materials (Figure 2.3), even weak magnetic fields can induce limited aggregation as observed in the formation of magnetic photonic crystals (Figure 2.5). Larger magnetic particles are driven to aggregate more when they are magnetized due to increased dipole-dipole interactions,

and such magnetization is likely in the large fields present in an MRI scanner.^[10] This leads to interparticle aggregation, significantly lowering cluster concentration resulting in an underestimate of contrast relaxivity. For any in-vivo application such behavior is not acceptable and for all practical purposes these larger materials are limited in their applications as MRI contrast agents.^[69] For smaller clusters at all field strengths, or for larger clusters that never experience the high fields of MRI scanners, our current coatings are sufficient to preclude cluster aggregation. Further improvements in MRI contrast especially in high field scanners will require particle surface coatings that are better able to impose both electrostatic and steric barriers to magnetic-field induced aggregation.

2.6 Conclusion

It is possible to systematically generate uniform libraries of multicore iron oxide nanoparticles whose two critical dimensions can be tuned over ranges relevant to both photonic and biomedical applications. Independent control over the cluster and particle dimensions is possible through rational choice of the reaction water content and temperature, respectively. While these nanoclusters are not as monodisperse as isolated nanocrystals, their polydispersity is sufficient ($\sigma < 10\%$) to examine size-dependent properties with some precision. Surface control is critical for these materials as most applications require non-aggregating and stable suspensions, often in water. We applied a sulfonated polyelectrolyte to this problem and demonstrated how it could be further derivatized with molecular dyes for visualizing clusters. To demonstrate the relevance of dimensional control, we formed visible magnetic photonic crystals from these materials. The optical phenomena were readily observed for cluster diameters greater than 100 nm and exhibited only a weak dependence on material dimensions. Conversely, cluster

diameter played a significant role in the effectiveness of these materials as T₂ contrast agents for MRI. For both applications the propensity of the materials to aggregate played a central role but in very different ways. In the case of the photonic crystals, limited and ordered aggregation is necessary in the presence of weak applied fields; for clusters that are too small, interparticle attractive forces are not sufficient to drive their assembly into 1D chains. In contrast for MRI applications interparticle interactions between larger clusters can limit performance especially as large-scale aggregates sediment out of solution. This synthetic approach now makes it possible to examine size-dependent properties in these materials with far more control, and optimize their behavior for different applications.

2.7 Experimental Section

Materials and Reagents: Ethylene glycol (anhydrous, 99.8%), Iron(III) Chloride Hexahydrate (FeCl₃·6H₂O, ACS reagent, 97%), Urea (ACS reagent, 99.0%), Azobisisobutyronitrile (AIBN, 98%), Acrylic acid (anhydrous, contains 200 ppm MEHQ as inhibitor, 99%), 2-Acrylamido-2-methylpropane sulfonic acid (AMPS, 99%), dimethylformamide (DMF, anhydrous, 99.8%), dimethyl sulfoxide (DMSO, anhydrous, ≥99.9%), 3,4-dihydroxyphenethylamine hydrochloride (Dopamine), Rhodamine B (≥95%), 5-((2-Aminoethyl)amino)naphthalene-1-sulfonic acid (EDANS), methoxypolyethylene glycol amine (PEG-NH₂, Mw = 5,000), Poly(maleic anhydride-alt-1-octadecene) (PMAO, Mw = 30,000), triethylamine, iron standard solution (Fe(NO₃)₃ in HNO₃ 0.5 mol/L, 1000 mg/L Fe) Certipur®, 3-(2-Pyridyl)-5,6-diphenyl-1,2,4-triazine-*p,p'*-disulfonic acid monosodium salt hydrate (FerroZine™ Iron Reagent), ammonium acetate (for molecular biology, ≥98%), hydroxylamine hydrochloride (99.995% trace metals basis), and sodium nitrite (ACS reagent, ≥97.0%) were purchased from Sigma-Aldrich. Polyacrylic acid

sodium salt (PAA, $M_w \sim 6,000$) was from Polyscience Inc. 1-ethyl-3-(3-dimethylaminopropyl)carbodiimide hydrochloride (EDC), 6-carboxyfluorescein (FAM), sulfuric acid (ACS grade, 98%), hydrochloric acid (ACS grade, 37%) and hydrogen peroxide (30%) were purchased from Fisher Scientific.

Synthesis of Fe₃O₄ clustered nanoparticles: The clusters were synthesized using a hydrothermal method also referred to as the “polyol” synthesis. In a standardized reaction, FeCl₃·6H₂O (540 mg, 2. mmol) was first dissolved in ethylene glycol (20 mL) using a magnetic stirrer. Then PAA (250 mg, 0.042 mmol) was then added into the solution, followed by urea (1,200 mg, 20 mmol) and ultra-high purity deionized water (1.5 mL, specific resistance less than 18 mΩ). The mixture was vigorously stirred for 30 min, yielding a transparent and bright yellow solution. A Teflon-lined reactor with a total volume of 40 mL was immersed in 37% HCl for 30 min, and then washed by water several times and dried in oven at 60 °C. The suspension was subsequently transferred to the Teflon-lined stainless steel autoclave, tightly sealed and then heated at 185 °C for 6 hours with a temperature ramp of 20 °C/min. After the reactant cooling to room temperature, a black solution was recovered; for such reaction conditions electron microscopy revealed the presence of multicore nanoparticle clusters with an average cluster diameter of 50 nm. The clusters were precipitated by placing a rare earth cubic magnet under the container and then washed by a mixture of acetone and Milli-Q water several times to remove impurities. The product was finally redispersed in water and could be concentrated by using a magnet. Clusters were then attracted to the bottom of the vial near the magnet and the nearly colorless supernatant was decanted slowly. The amount of water added to the synthesis (0

to 4 mL) controls the overall cluster dimension (D_c), and the reaction temperature (185 to 275 °C) controls the primary nanocrystal diameter (d_p) as described in the main text.

Synthesis condition for Figure 2.2: The molar concentration of water for the synthesis of a-e is 6.2, 3.9, 2.6, 1.1 and 0.3 M, respectively. Other reaction conditions are fixed at: 100 mM $\text{FeCl}_3 \cdot 6\text{H}_2\text{O}$, 2.1 mM PAA, 1 M urea and 20 mL ethylene glycol and heated at 185 °C for 6 hours.

Synthesis condition for Table 2.1: The molar concentration of water for the synthesis of sample 6-25 to 6-90 (left part) is 6.2, 5.4, 4.2, 3.9, 1.7 and 0.84 M, respectively, with a reaction temperature of 215 °C. The reaction temperature for the synthesis of sample 5-45 to 10-45 (right part) is 200, 215, 230, 245, 260, 275 °C, respectively, with a molar concentration of water of 4.2 M. Other reaction conditions are fixed at: 100 mM $\text{FeCl}_3 \cdot 6\text{H}_2\text{O}$, 2.1 mM PAA, 1 M urea and 20 mL ethylene glycol and heated for 6 hours.

Synthesis condition for Figure S2.1: (a-c): 100 mM $\text{FeCl}_3 \cdot 6\text{H}_2\text{O}$ + 7.2 M H_2O , 100 mM $\text{FeCl}_3 \cdot 6\text{H}_2\text{O}$ + 0 M H_2O and 100 mM anhydrous FeCl_3 + 0 M H_2O , as iron precursors, respectively. The synthesis conditions are standardized except for added water and iron salt: 2.1 mM polyacrylate and 1 M urea in 20 mL ethylene glycol heated at 185 °C for 6 hours.

Synthesis condition for Figure S2.2: These samples were synthesized at 185, 200, 215, 230, 245 and 260 °C, respectively. Other reaction conditions are fixed at: 100 mM $\text{FeCl}_3 \cdot 6\text{H}_2\text{O}$, 3.9 M H_2O , 2.1 mM PAA, 1 M urea and 20 mL ethylene glycol and heated for 6 hours.

Synthesis condition for Figure S2.4: The amount of $\text{FeCl}_3 \cdot 6\text{H}_2\text{O}$, polyacrylic acid (PAA), urea, water, and reaction time and temperature is shown in a-f. Unless stated in the figure,

other reaction conditions are standardized at: 100 mM $\text{FeCl}_3 \cdot 6\text{H}_2\text{O}$ 3.9 M H_2O , 2.1 mM PAA, 1 M urea and 20 mL ethylene glycol and heated at heated at 185 °C for 6 hours.

Poly(AA-co-AMPS) modified nanoparticles: The as-synthesized clusters were further modified by a co-polymer prepared as described below. Poly(Acrylic acid-co-2-acrylamido-2-methyl-1-propane sulfonic acid), or Poly(AA-co-AMPS), improves the colloidal stability of the materials in biological media.

Synthesis of Poly(AA-co-AMPS): Poly(AA-co-AMPS) was synthesized by free radical polymerization. In a typical synthesis, AMPS (1.5 g), acrylic acid (0.50 g) and AIBN (50 mg) were added to DMF (10 mL) and stirred for 30 min. The mixture was then transferred to an oven equipped with an ultraviolet illumination lamp (LZC-4Xb photoreactor, UVA 350 nm, 36 W) and polymerized under ultraviolet radiation for 1 h; while the solution remained colorless it did become more viscous. The resultant copolymer was purified by using a dialysis bag (Cellulose Membrane, MWCO 3,000 Da, Sigma-Aldrich) and then freeze-dried (LABCONCO FreeZone 6 Liter Freeze Dry Systems) for 2 days. The freeze-dried polymer powder was dissolved as described below and analyzed by NMR. The molecular weight of the product, around 87,000 g/mol, was determined by size exclusion chromatography also as described below.

Functionalization of Poly(AA-co-AMPS) by nitrodopamine to make dopa-Poly(AA-co-AMPS): Nitrodopamine was synthesized following an existing protocol. Five grams dopamine was first dissolved in 150 mL H_2O and vigorously stirred in an ice bath, followed by the addition of sodium nitrate (6.5 g). Fifty milliliters of 20% sulfuric acid was added to the mixture at a rate of 1 drop (0.05 ml) per second. Note that the reaction must be fully

vented as NO_2 is generated as a by-product. The ice bath was then removed, and the reaction was allowed to sit at room temperature for at least 12 h. Nitrodopamine hydrogensulfate (nitrodopa) was obtained by filtering this mixture and washing the residue with cold water several times, after which it was freeze dried into a powder. Two hundred milligrams of Poly(AA-co-AMPS) was dissolved in 0.1 M MES buffer (10 mL) and then EDC (12 mg) and (20 Mg) dried nitrodopa were added. The mixture was stirred at room temperature for 2 h and was then purified by dialysis (Cellulose Membrane, MWCO: 3,000 Da, Sigma-Aldrich). After this purification, the functionalized polymer solution was 10 mg/mL (± 1 mg/ml) based on the final volume of the solution. On average there were twenty molecules of nitrodopa conjugated to each polymer chain.

Grafting functionalized Poly(AA-co-AMPS) onto the clusters: Ten milliliters of 500 ppm (in terms of Fe_3O_4) clusters ($D_c = 45$ nm, $d_p = 4$ nm) solution was added to 2 mL of the previously prepared dopa-Poly(AA-co-AMPS) solution (~ 10 mg/mL) with a rate of 1 drop per second. The mixture was stirred for 30 min during which time the polyacrylate native to the clusters was replaced by dopa-Poly(AA-co-AMPS). The excessive dopa-Poly(AA-co-AMPS) was removed by collecting the clusters using a magnet followed by resuspension in water several times. The dopa-Poly(AA-co-AMPS) coating was confirmed by FTIR and DLS.

Fluorescent nanoparticles: the nanoparticles could be further treated with fluorescent molecules, including EDANS, Rhodamine B, FAM and DiI, to make them visible in biological settings.

EDANS labeled clusters: Five milliliters of dopa-Poly(AA-co-AMPS) coated cluster ($D_c = 45$ nm, $d_p = 4$ nm) solution with a concentration of 1000 ppm was first mixed with 0.2 M MES buffer (5. mL), followed by EDC (10. mg) and EDANS (1 mg). This solution was stirred at room temperature for 2 h. The EDANS labeled clusters were washed by water several times to remove unbounded dye.

FAM or Rhodamine B labeled clusters: FAM (4 mg) or Rhodamine B (5 mg) was dissolved in 0.1 M MES buffer (10 mL), followed by the addition of EDC (10 mg) and nitrodopa (3 mg). The mixture was stirred at room temperature for 2 h, after which it can be stored in the fridge at 4 °C as a bulk solution. One milliliter of the nitrodopa conjugated FAM or Rhodamine solution was added into dopa-Poly(AA-co-AMPS) coated cluster solution (10 mL) previously prepared with a concentration of 500 ppm, and was then stirred at room temperature for 30 min. The FAM or Rhodamine B labeled clusters were washed and collected magnetically as described above.

DiI labeled clusters: DiI is a lipophilic dye widely used for staining in cell culture. To attach such dye onto the clusters, the materials were first modified by the amphiphilic polymer PMAO-PEG-Dopa. This polymer was formed using standard methods: PEG-NH₂ (50 mg) and PMAO (7.5 mg, Mw = 20,000) were dissolved in chloroform (5 mL). Then nitrodopa (2 mg) was dissolved in DMF (1 mL). The two solutions were subsequently mixed by vigorously stirring together forming a bright yellow solution. Triethylamine (25 µL) was then added. The reaction proceeded at 25 °C for 24 hours, and then H₂O (5 mL) was added to hydrolyze the unreacted anhydride and the solution became turbid instantly. The mixture was heated to 60 °C to evaporate chloroform until the solution became clear again. The resultant polymer was purified by dialysis and finally dissolved in H₂O (10 mL).

The stock solution should be stored at 4 °C. Ten milliliter as-synthesized cluster ($D_c = 45$ nm, $d_p = 4$ nm) solution with a concentration of 500 ppm was added in the previously prepared PMAO-PEG-Dopa solution (2 mL) with a rate of 1 drop per second. The mixture was stirred for 30 min. Excess polymer was removed magnetically as described above.

DiI (2 mg) was dissolved in 1 mL DMSO and then added to H₂O (200 mL) to form DiI aqueous solution (10 mg/L). The PMAO-PEG-Dopa attached cluster solution with a concentration of 200 ppm was mixed with the DiI aqueous solution with a volume ratio of 1:1. The mixture was shaken for 24 hours and protected by aluminum foil to prevent photodecomposition of DiI. Again, the unattached DiI was removed by washing the cluster magnetically and finally redispersed in water. The DiI labeled cluster solution had a pale pink color when the concentration was around 100 ppm.

Materials Characterization

Transmission Electron Microscopy (TEM): TEM, high-resolution TEM (HRTEM) and selected area diffraction (SAED) of the as-synthesized clusters were acquired by JEOL 2100 Field Emission Gun Transmission Electron Microscope at an acceleration voltage of 200 kV. Three microliters of the cluster solution with a concentration of 300 ppm was dropped on a 200-mesh carbon-coated copper grid. After complete evaporation of water, the clusters were deposited on the copper grid and were ready for TEM measurement. The cluster dimension and primary nanocrystal diameter were analyzed by ImageJ; average dimension and size distribution were determined from measurement of at least five hundred clusters.

X-ray diffraction (XRD): XRD patterns of the cluster samples were obtained by Bruker D8 Discovery 2D X-ray Diffractometer (Cu K α , $\lambda = 1.54056 \text{ \AA}$). One milliliter of a cluster solution with a concentration of 3,000 ppm was dropped on the center of a microscope slides with single depression concave (AmScope BS-C12) with a small magnet placed beneath. After complete evaporation of water, XRD was performed on the residue and the diffraction pattern was collected from 10 to 95 $^\circ$. The grain size of each sample was calculated based on the full width at half maximum (FWHM) of the (311) peak centered at 35.4 $^\circ$ by using Origin peak analysis function, and was calculated as the following Debye Scherrer equation:

$$\text{Grain size} = \frac{\lambda}{FWHM \cos(\theta)}$$

In most cases, the XRD data was collected within a day of the sample evaporation in order to minimize oxidation by air.

Dynamic light scattering (DLS): The hydrodynamic size of the clusters was measured using a Zetasizer Nano S90. One and a half milliliters of a cluster solution with a concentration of 100 ppm was placed in a plastic cuvette; after a 2-minute equilibrium period at 25 $^\circ\text{C}$, DLS data was collected. Each sample was measured three times over a period of 12 min. The hydrodynamic size was derived from Z average. The error bar reported for hydrodynamic size corresponds to the standard deviation of the three measurements.

Fluorescence spectra: The fluorescence of the dye-labeled clusters was measured on a FluoroMax-4 spectrofluorometer with a xenon arc lamp. The excitation wavelength for

EDANS, Rhodamine B, FAM and DiI was 380 nm, 466 nm, 492 nm and 549 nm, respectively. The fluorescence of the dye-labeled cluster solution was measured by a fluorometer. Prior to measurement, the cluster solution was diluted to a 50 ppm cluster concentration to minimize light scattering by the nanoparticles.

Raman spectra: The Raman spectra of the cluster samples were obtained using a Witec Alpha 300 Confocal Raman Microscope. The sample preparation was the same as for XRD. Two laser source, 532 and 785 nm, were used to obtain the Raman spectra. The spectra were collected from 100 to 1500 cm^{-1} .

Magnetic resonance imaging (MRI): The T2 relaxivity (r_2) of the cluster samples was obtained on the 3.4 Tesla Tim Trio MRI scanner. The repetition time (TR) was 2280.0 ms, echo time (TE) was from 9 to 150 ms, the reference Voxel size was $0.5 \times 0.5 \times 10.0$ mm, the slice thickness was 3.0 mm, the slice number was 7, and the slice used for the data was the second from the top. The cluster samples were first diluted to 38.6 ppm, which was equivalent to an iron concentration of 0.5 mM. These samples were then diluted to 0.4 mM, 0.3 mM, 0.2 mM, 0.1 mM and 0.01 mM, respectively, and transferred to a 100-well plate for measurement. The error bar of r_2 was based on the regression coefficients from the linear fitting of the $1/T_2$ versus sample concentration.

Surface area analysis: Quantachrome Instruments *Autosorb-1* was applied to obtain N_2 isotherms at 77 K from which the surface areas of the cluster samples based on the Brunauer–Emmett–Teller (BET) theory were obtained. The cluster solution was dried at 60 °C to generate a powdered sample. Prior to the measurement, the samples were outgassed overnight under vacuum at 200 °C.

Nuclear magnetic resonance spectroscopy (NMR): The ¹H NMR spectrum of the as-synthesized Poly(AA-co-PAMPS) was collected on a Bruker Ascend™ 600. Ten milligram powdered Poly(AA-co-AMPS) was dissolved in 0.7 mL D₂O and shaken well to form a homogeneous solution. The solution was then transferred to an NMR tube and scanned 128 times seconds to yield a spectrum.

Size Exclusion Chromatography: The molecular weight of the as-synthesized Poly(AA-co-AMPS) was measured by size exclusion chromatography (SEC). This data was collected using an Agilent HPLC 1100 series (Agilent, Santa Clara, CA) chromatography instrument equipped with a pL-aquagel-OH 40 and a pL-aquagel-OH 60 (25.0 x 300 mm, 15 μm, HPLC column) designed for hydrophilic polymers with molecular weights between 10,000-200,000 and 200,000-10,000,000, respectively. A refractive index detector (RID) was connected to the end of the column by a 3000 x 0.17 mm, SS capillary tube. Dead volumes during each test were shortened as much as possible and a constant temperature of 30°C was maintained during experiments. A series of polystyrene sulfonates with molecular weights of 1 k, 2 k, 4.2 k, 10 k, 30 k, 80 k, 140 k, 280 k, and 450 k (American Polymer Standards Corporation, Mentor, OH) were dissolved in phosphate buffers with a pH of 10 and run through the column to obtain the calibration curve. The Poly(AA-co-AMPS) sample was allowed to run through the HPLC with the same parameters and compared to the standard curve for its own molecular weight. The following conditions were kept the same for each sample: Flow rate: 1ml/min; Pressure: 40 bar; Injection volume: 25.0 μl; Column thermostat temperature: 30 °C; RID unit temperature: 30 °C.

Fourier-transform infrared spectroscopy (FTIR): The IR spectra of the as-synthesized clusters ($D_c = 45$ nm, $d_p = 4$ nm) and polymer modified clusters were obtained on an

IRAffinity-1S FTIR Spectrometer (Shimadzu). One milliliter of a cluster solution with a concentration of 500 ppm was dropped onto the center of a glass slide. The slide was dried at 60 °C to form a thin layer of residue. The spectra were collected from 4000 to 400 cm^{-1} at room temperature.

Cluster concentration measurement: The concentration of the cluster solution was determined using ultraviolet-visible (UV-vis) absorption spectroscopy.⁴ A calibration curve for spectrophotometric analysis of iron was first obtained from iron standards. The standard curve was obtained by mixing iron $[\text{Fe}(\text{NO}_3)_3]$ standard solutions (0.2 mL, 1, 5, 10, 25 and 50 ppm, respectively, in terms of Fe), 7.5 M ammonium acetate solution (0.15 mL), 5% hydroxylamine hydrochloride solution (0.25 mL), 0.1% ferrozine solution (0.4 mL) and H_2O (1 mL) and placed in a 4 mL quartz cuvette. The absorption peak of Fe(III)-ferrozine composite was at 590 nm in agreement with existing literature, and the peak intensity is linear with the concentration of iron. To measure the concentration of a cluster solution, 0.1 mL of the solution was first dissolved in 37% hydrochloric acid (0.89 mL) with the addition of H_2O_2 (0.01 mL); the solution quickly became clear and pale yellow. Then the above solution (0.1 mL) was diluted with H_2O (0.9 mL). Finally, the diluted solution (0.2 mL) was added in 7.5 M ammonium acetate solution (0.15 mL), 5% hydroxylamine hydrochloride solution (0.25 mL), 0.1% ferrozine solution (0.4 mL) and H_2O (1 mL) and placed in a 4 mL quartz cuvette. The absorption spectrum was collected and compared to the standard curve. The measured concentration, in terms of ppm iron, was multiplied by a factor of 1.38 (molar mass ratio between Fe and $1/3 \text{Fe}_3\text{O}_4$) to express the concentration in terms of ppm Fe_3O_4 for the original cluster solution.

Magnetic measurements: The magnetization curves of dried cluster samples were obtained from a vibrating-sample magnetometer (Lake Shore 7400 Series VSM). A tenth of one milliliter of the cluster solution with a concentration of 1000 ppm was mixed with 10 mg gypsum and then dried at 60 °C prior to measurement. The hysteresis loop was recorded from 10,000 to -10,000 oersted (Oe) at room temperature.

Photonic crystal characterization: The optical behavior of the sample was observed by placing 3 mL of a 500 ppm cluster solution ($D_c = 120$ nm, $d_p = 4$ nm) in a 4 mL plastic cuvette. A cube magnet (NdFeB, Grade N42, Supermagnetman) was placed on the rear of the cuvette while a camera was trained on the front. By moving the magnet away from the cuvette, different colors on the cuvette front surface were recorded and the distance between the cuvette and magnet recorded. The magnetic field strength at the cuvette surface was obtained according to a model reported previously:

$$B = \frac{B_r}{\pi} \left[\arctan \left(\frac{a^2}{2z\sqrt{4z^2 + 2a^2}} \right) - \arctan \left(\frac{a^2}{2(a+z)\sqrt{4(a+z)^2 + 2a^2}} \right) \right]$$

Where B_r (1.32 T) is remanence field of the magnet, a (3 cm) is edge length of the cube magnet and z (from 0.5 to 10 cm) is the distance of the cuvette to the magnet.

Reflection spectra: The reflection spectra of the magnetic photonic crystals were recorded on a SP-UV1000 spectrophotometer (DLAB Scientific) equipped with a tungsten Lamp over the range of 200 to 800 nm. The same sample and magnet relationship described above was used for these data. 3 mL of a 500 ppm cluster solution ($D_c = 120$ nm, $d_p = 4$ nm) was placed in a quartz cuvette and a cube magnet was placed on the rear of the cuvette. We

recorded the reflection spectra of the cluster solution by changing the distance and the angle between the magnet and the cuvette as seen in Figure 2.6.

Cryo-SEM: The cryo-SEM images of the clusters as photonic crystals were obtained on the SIGMA VP Field Emission-Scanning Electron Microscope (FE-SEM) with cryogenic capability. Twenty microliters of a 500 ppm cluster solution ($D_c = 120$ nm, $d_p = 4$ nm) was dropped on the sample holder and then transferred to the cryogenic chamber with a cube magnet placed beneath. The distance between the magnet and the chamber was adjusted to acquire different magnetic field strength.

2.8 Supplemental Figures

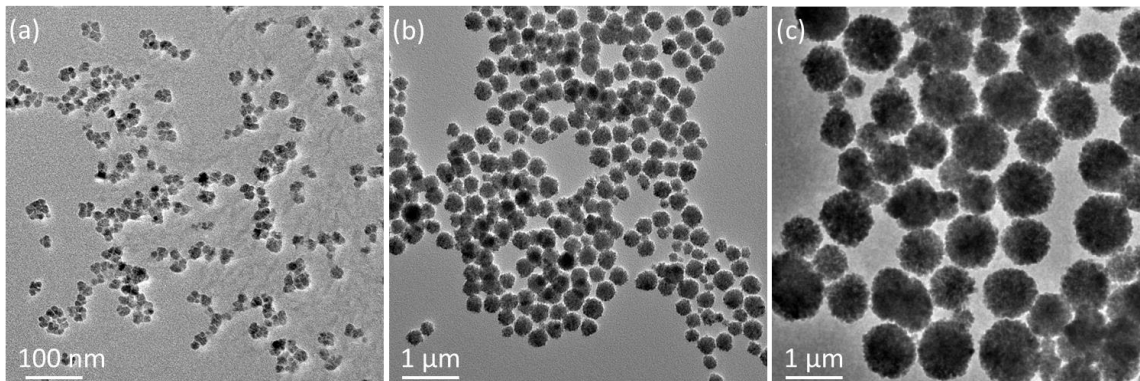


Figure S2. 1. The effect of water on the cluster diameter. (a-c): TEM micrographs of the iron oxide nanocrystal clusters synthesized using 100 mM $\text{FeCl}_3 \cdot 6\text{H}_2\text{O}$ + 7.2 M H_2O , 100 mM $\text{FeCl}_3 \cdot 6\text{H}_2\text{O}$ + 0 M H_2O and 100 mM anhydrous FeCl_3 + 0 M H_2O , as iron precursors, respectively. The cluster sizes are 20 ± 1 nm, 200 ± 20 nm and 800 ± 100 nm, respectively. The results show that the removal of the waters of hydration in iron chloride leads to a much larger cluster size.

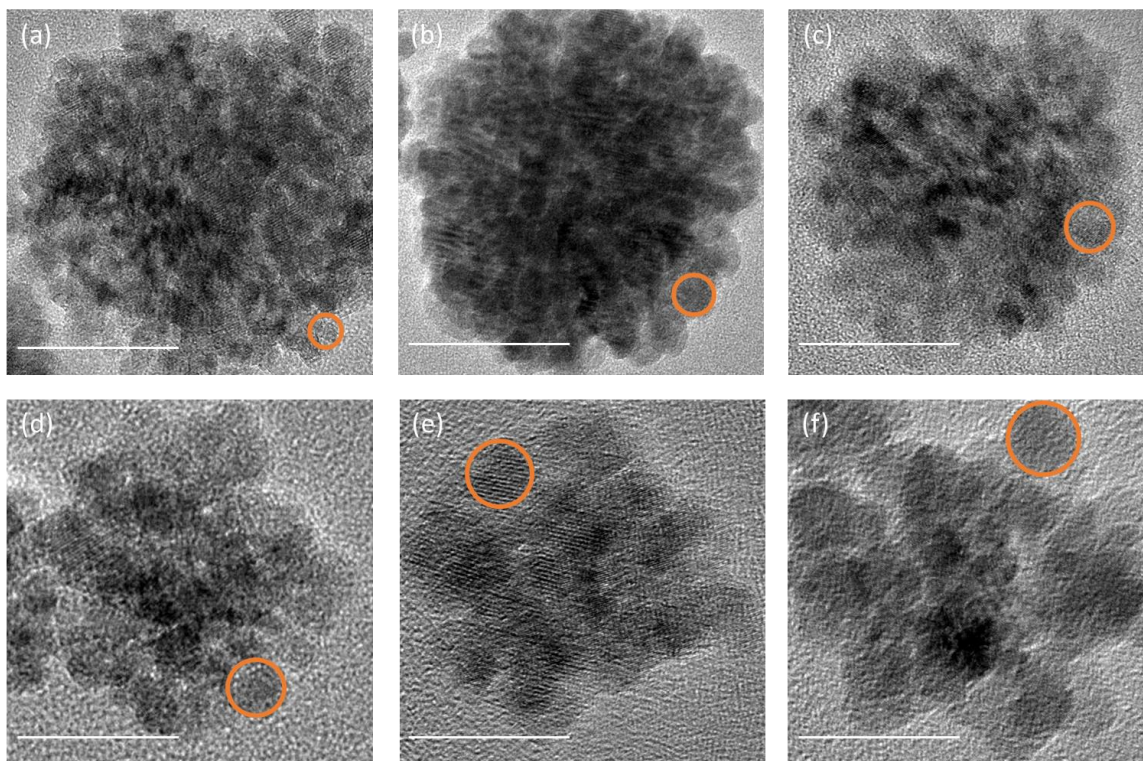


Figure S2. 2. High resolution transmission electron microscopy graphs of clusters with different primary nanocrystal diameters. Scale bar: 20 nm. (a-f): Clusters with primary

nanocrystal diameter of 4 nm, 5 nm, 6 nm, 7 nm, 8 nm, and 9 nm, respectively. The cluster diameter of all these samples were around 50 nm. The primary nanocrystal diameter was varied by changing the reaction temperature while other conditions remaining the same. These samples were synthesized at 185, 200, 215, 230, 245 and 260 °C, respectively.

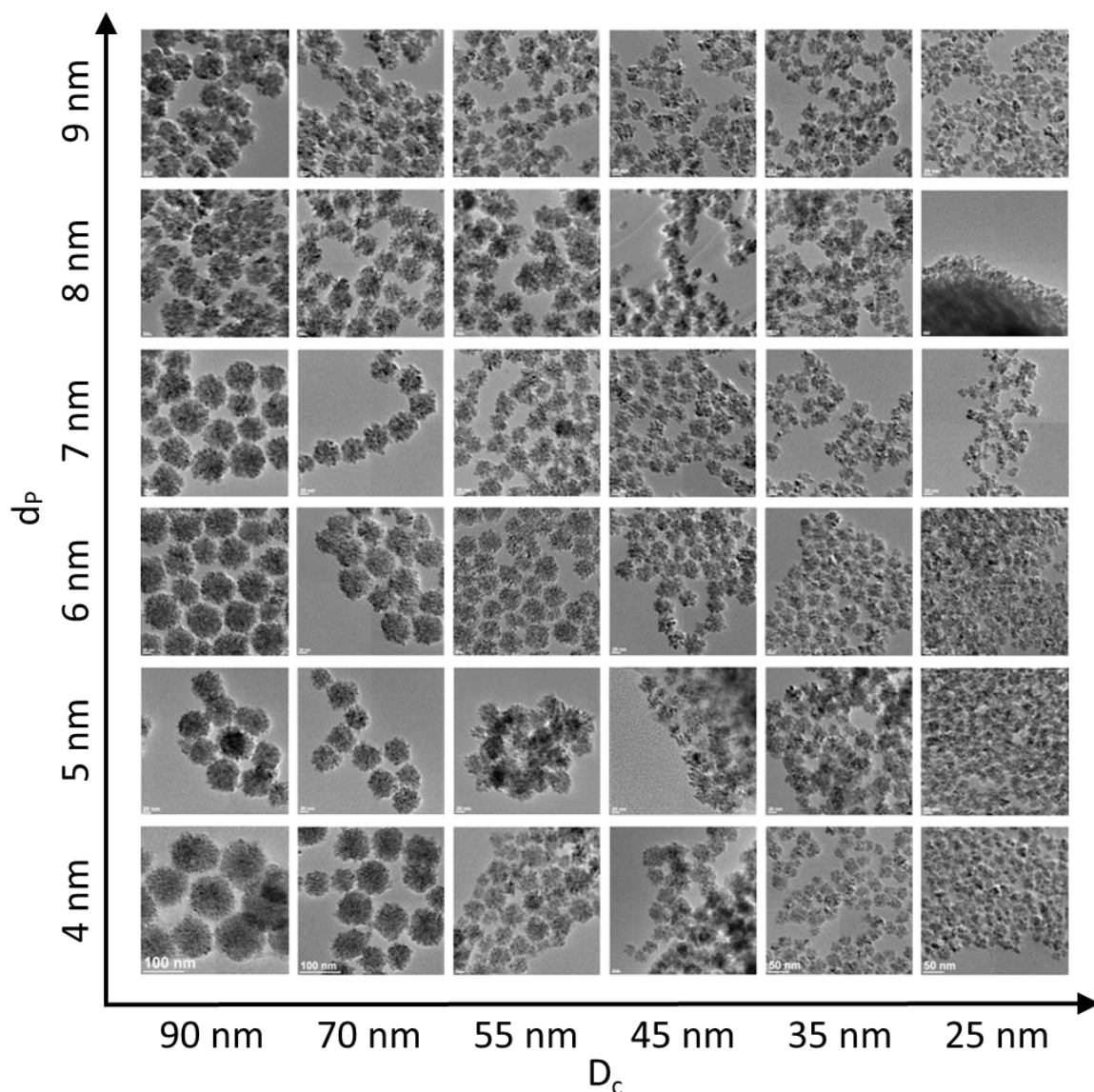


Figure S2. 3. Libraries of uniform magnetic nanoclusters with tunable dimensions. Representative TEM micrographs of the library of multicore iron oxide nanoparticle clusters with different cluster diameters (D_c) and primary nanocrystal diameters (d_p).

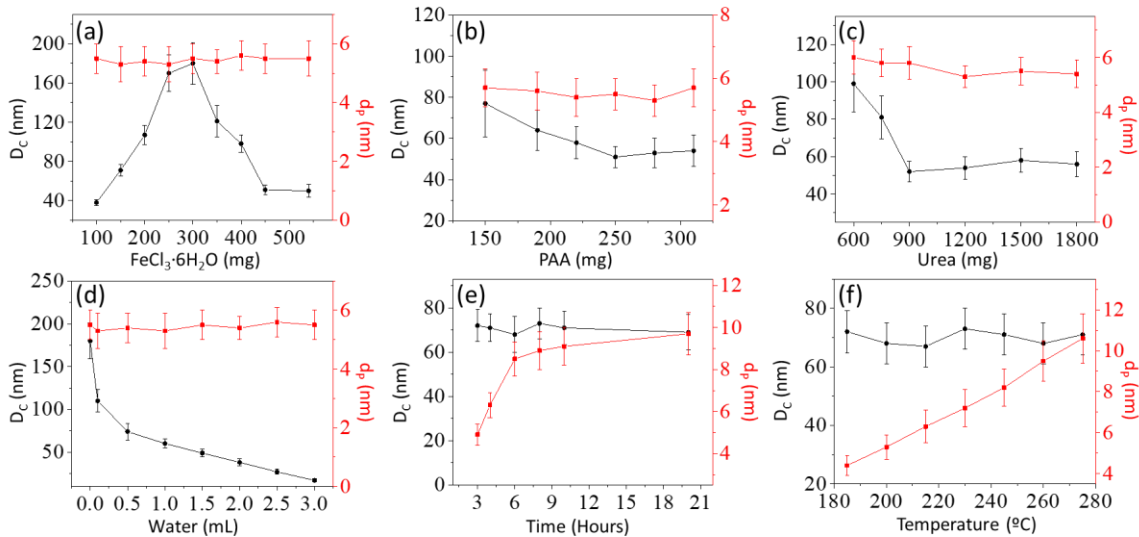


Figure S2. 4. The effect of reaction conditions on the dimensions of clusters (D_c) and primary nanocrystals (d_p). (a): the amount of $\text{FeCl}_3 \cdot 6\text{H}_2\text{O}$; (b): polyacrylic acid (PAA); (c): urea; (d): water; (e): reaction time; (f): temperature. Unless stated in the figure, other reaction conditions are fixed at: 540 $\text{FeCl}_3 \cdot 6\text{H}_2\text{O}$, 0.6 mL H_2O , 250 mg PAA, 1,200 mg urea and 20 mL ethylene glycol and heated at heated at 185 $^{\circ}\text{C}$ for 6 hours.

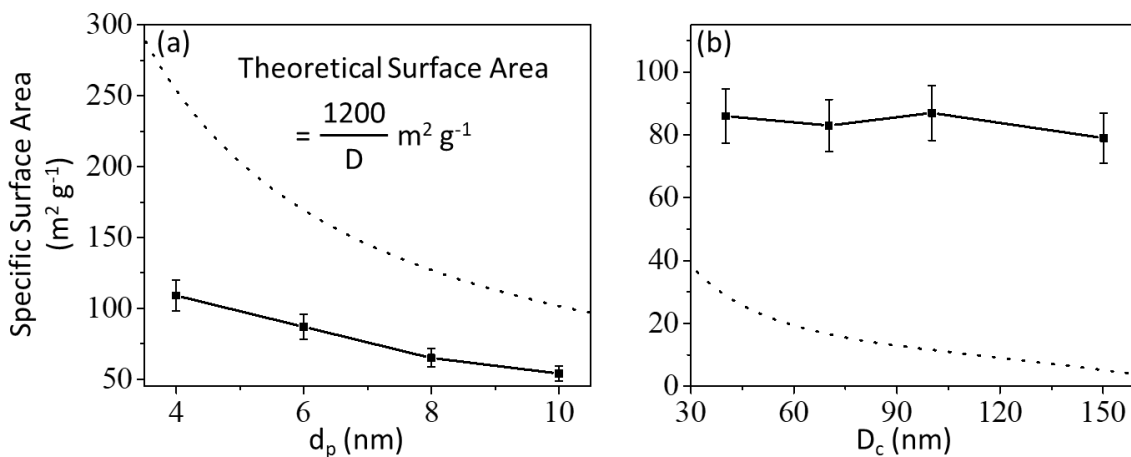


Figure S2. 5. The specific surface area of the clusters with different cluster diameters (D_c) and primary nanocrystal diameters (d_p). (a): The clusters with different primary nanocrystal diameters. The cluster diameters of these samples are around 70 nm; (b): The clusters with different cluster diameters. The primary nanocrystal diameters of these samples are around 6 nm. The dots represent surface area measured using the Brunauer-Emmett-Teller adsorption method. The dotted line represents the theoretical surface area of a solid, non-clustered iron oxide nanoparticle with no internal porosity.

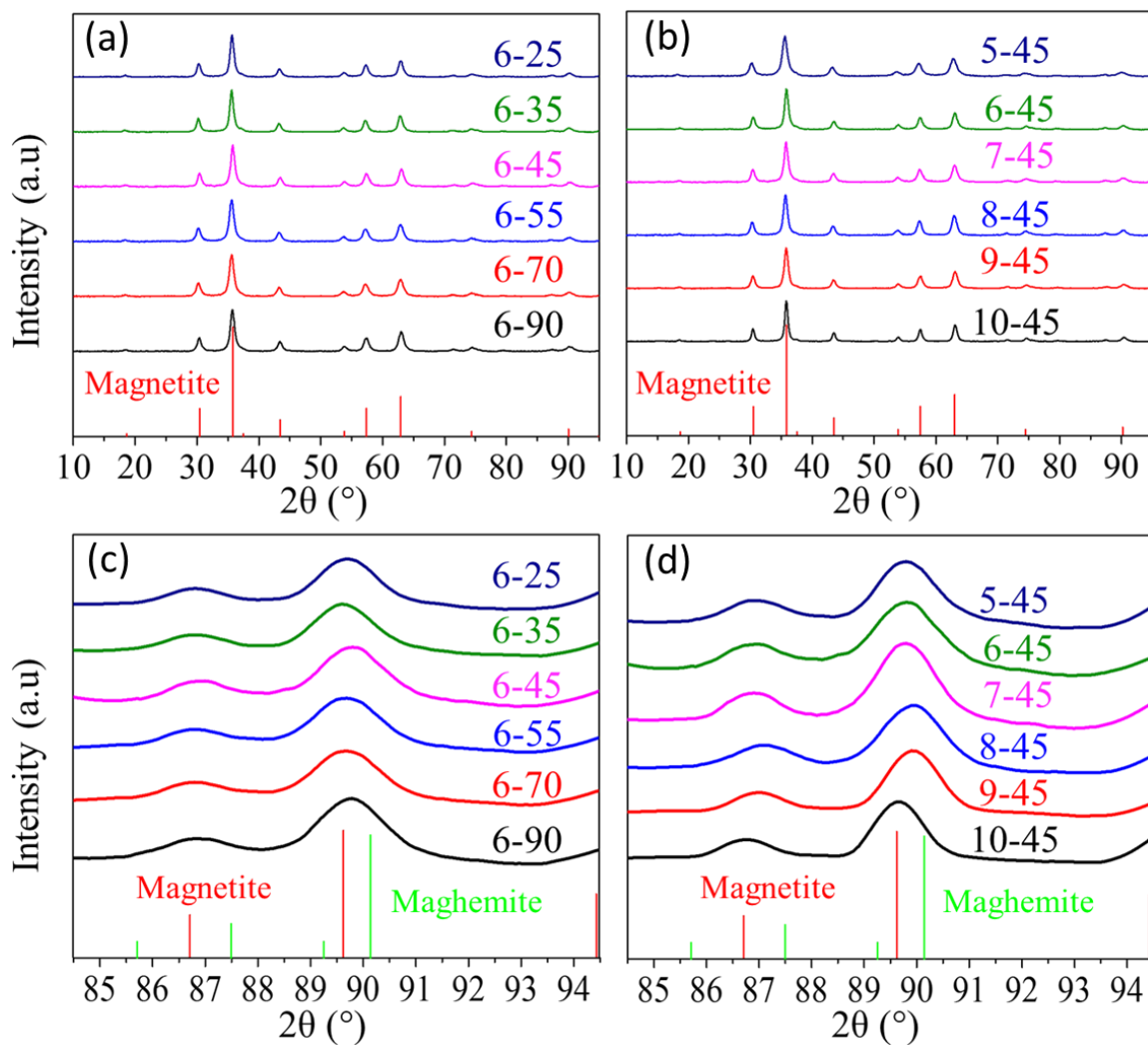


Figure S2. 6. The X-ray diffraction pattern of the iron oxide clusters. (a & c): Clusters with different cluster diameters (D_c); (b and d): Clusters with different primary nanocrystal diameters (d_p). These samples are denoted as d_p - D_c according to their cluster sizes and primary nanocrystal sizes measured from TEM micrographs. The red and green vertical bars indicate the peak positions and intensities of bulk magnetite (PDF#19-0629) and maghemite (PDF#39-1346), respectively.

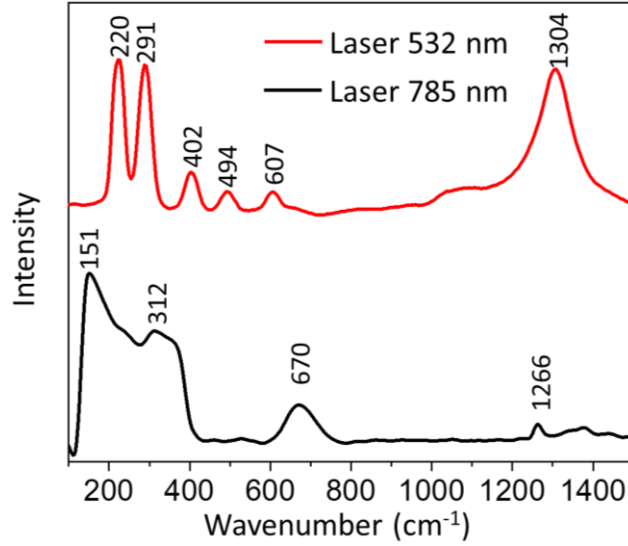


Figure S2. 7. The Raman spectra of a typical sample of iron oxide clusters. The average cluster diameter and primary nanocrystal diameter of the sample are 45 nm and 4 nm, respectively. The peaks located at 607, 402, 291 cm^{-1} obtained using laser 532 nm and those at 670 and 312 cm^{-1} obtained using laser 785 nm are the characteristic bands for Fe_3O_4 . The higher peaks at 1304 and 1266 cm^{-1} indicate the presence of defects at the surface of the clusters.

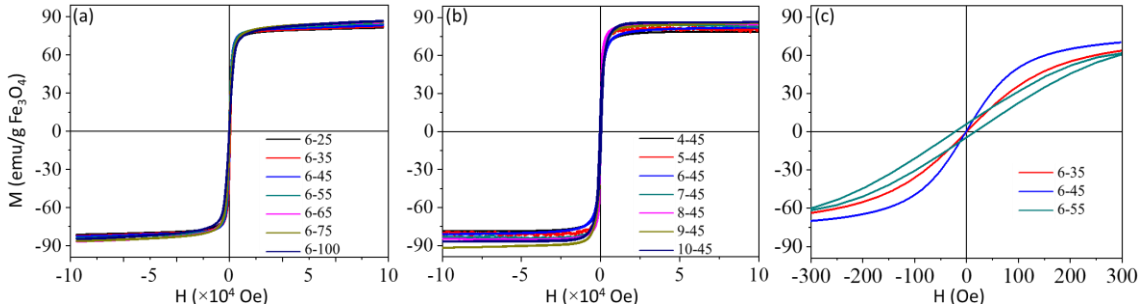


Figure S2. 8. Magnetization curves of the iron oxide clusters. (a) The clusters with different cluster diameters (D_c); (b) The clusters different primary nanocrystal diameters (d_p). These samples are denoted as d_p - D_c according to their cluster diameters and primary nanocrystal diameters based on TEM measurement. The hysteresis loop was recorded from 10,000 to -10,000 oersted (Oe) at room temperature. The saturation magnetizations ranged in (a) from 81.2 to 86.7 $\text{emu/g Fe}_3\text{O}_4$, and in (b) from 78.7 to 86.7 $\text{emu/g Fe}_3\text{O}_4$. (c) The zoom panel recorded at low field from -300 to 300 Oe for sample 6-35, 6-45 and 6-55, with an initial susceptibility of 30, 50 and 25, respectively. Only a negligible coercivity (13 Oe) was observed for sample 6-55, indicating the superparamagnetic nature of these samples.

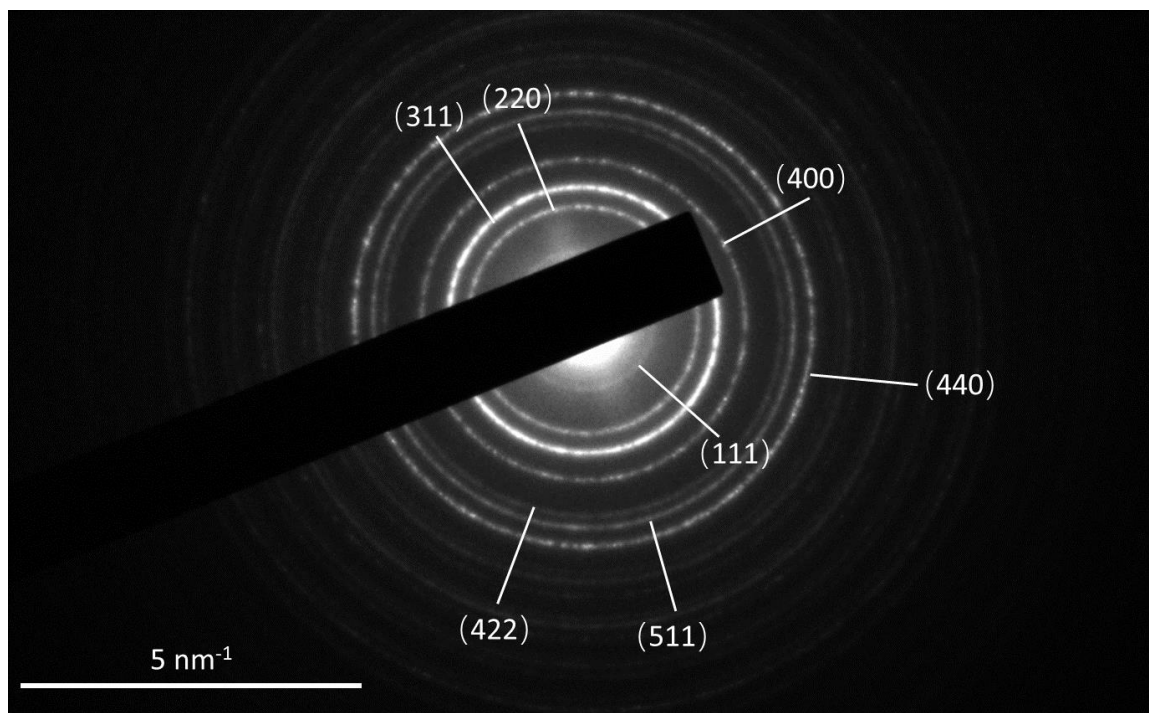


Figure S2. 9. The selected area electron diffraction pattern of the iron oxide clusters collected over a large area of particles. The cluster sample has an average cluster diameter of 45 nm and primary nanocrystal diameter of 4 nm. The nearly continuous diffraction rings suggest that the clusters assume random orientations in the TEM grid.

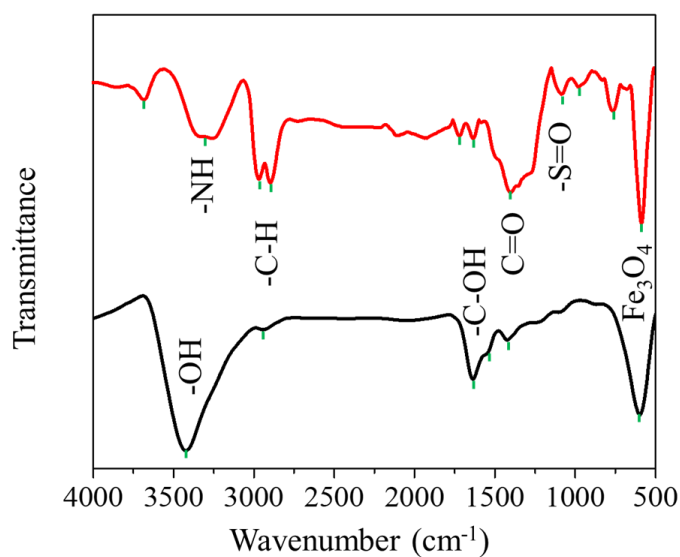


Figure S2. 10. FTIR spectra of the clusters before (black) and after (red) surface modification. The average diameters of clusters and primary nanocrystals are 45 nm and 4 nm, respectively. The FTIR spectrum demonstrates that clusters after modification with

poly(acrylic acid-co-2-acrylamido-2-methyl-1-propane sulfonic acid) possess the expected features. The FTIR spectrum of as-synthesized clusters is similar to that of poly(acrylic acid), suggesting the clusters are coated with poly(acrylic acid). The FTIR spectra of clusters after surface modification shows a peak assigned to sulfonated groups, indicating the presence of Poly(AA-co-AMPS) on cluster surface.

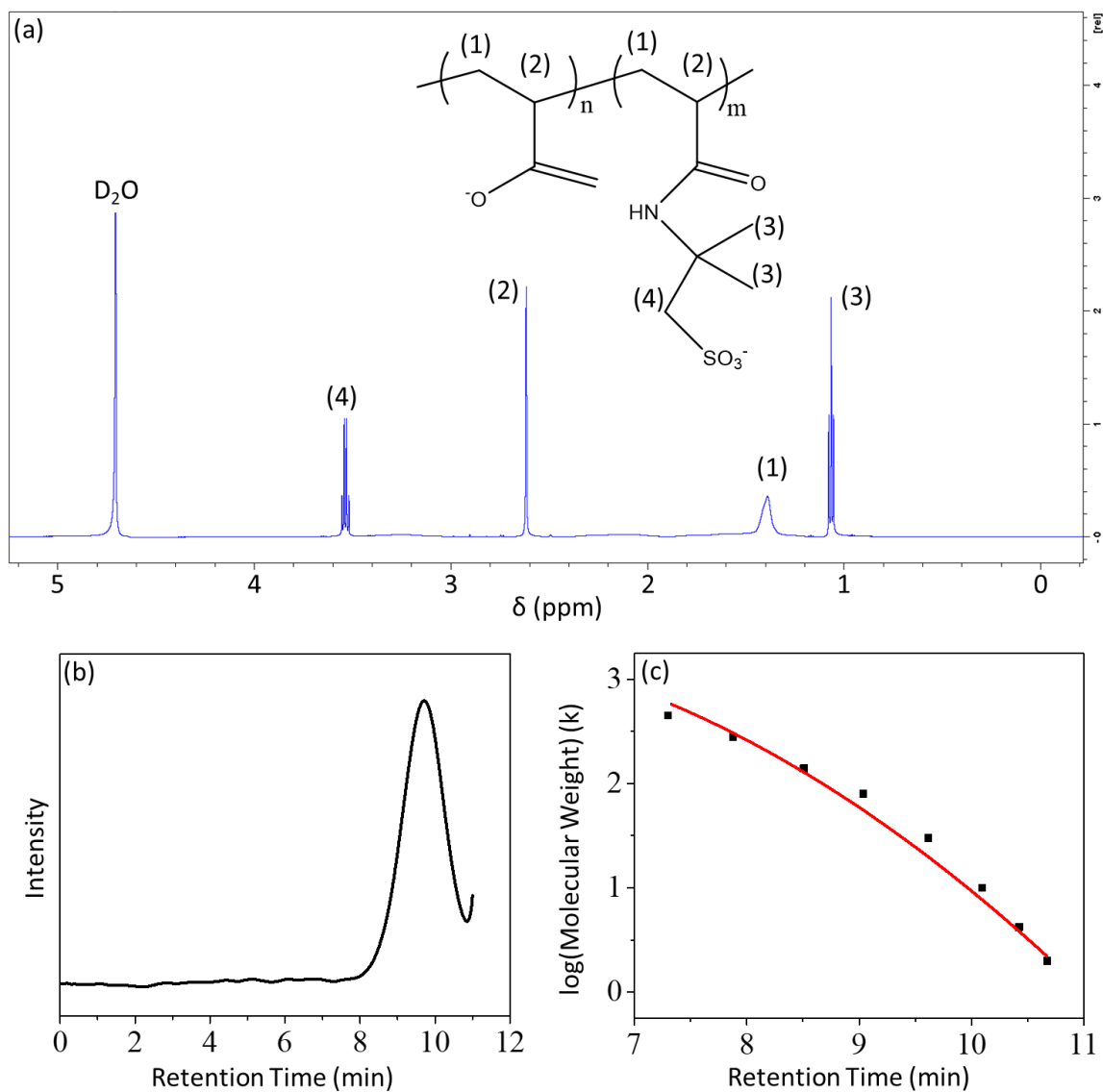


Figure S2. 11. Characterization of the poly(acrylic acid-co-2-acrylamido-2-methyl-1-propane sulfonic acid). (a): The NMR spectrum of the as-synthesized Poly(AA-co-AMPS). The result suggests the molar ratio between AA and AMPS is 1:1; (b): Refractive intensity response of Poly(AA-co-AMPS) in HPLC, where the recorded value corresponding to the vertex of the first visible peak between 7-12 min was taken as the retention time; (c): Polystyrene sulfonates standard curve line with a 5th degree exponential curve fitting. The

retention time of the as-synthesized Poly(AA-co-AMPS) shows a weight average molecular weight of 87,000 g/mol.

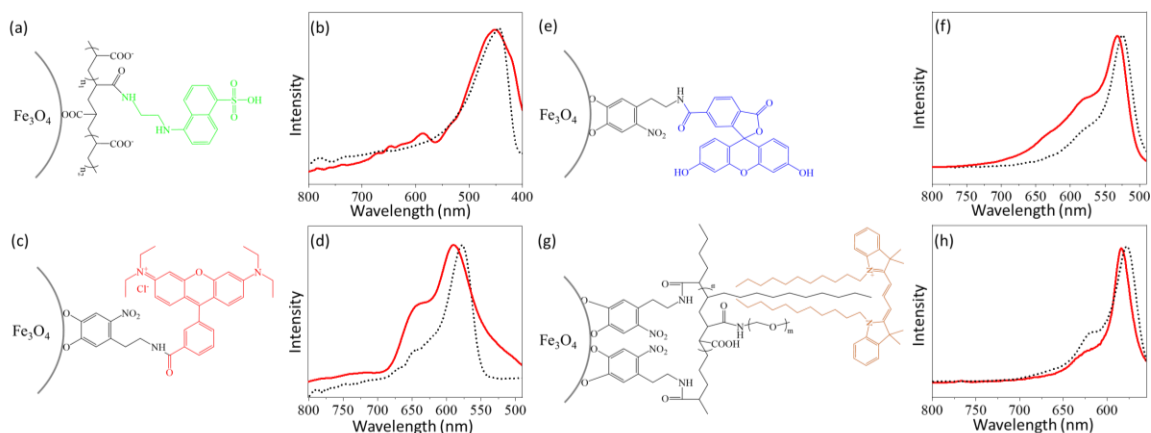


Figure S2. 12. Conjugation of fluorescent molecules onto the clusters. (a, c, e & g): The schematics description of the conjugation chemistry between clusters and EDANS, Rhodamine B, FAM and DiI, respectively; (b, d, f, h): the fluorescence spectra of the various fluorescent dyes. The dotted lines in the spectra represent the emission spectra of the pure fluorescent dyes in water; the solid lines represent the emission spectra of the dyes labeled cluster samples.

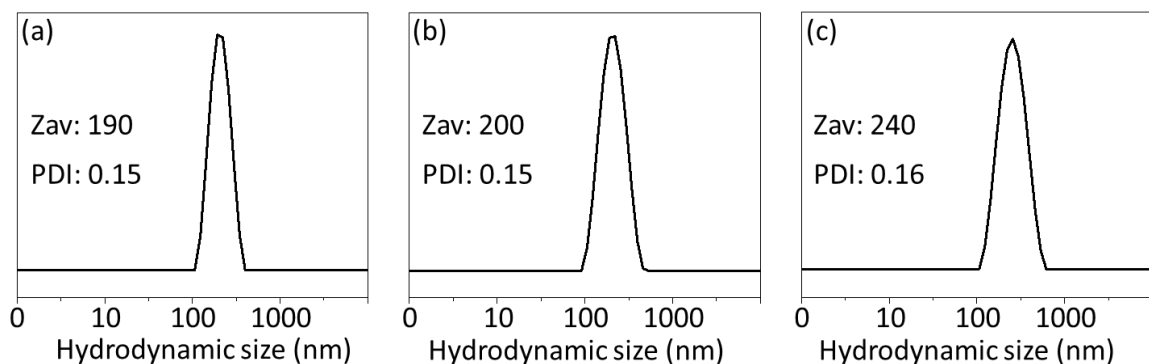


Figure S2. 13. (a-c) The hydrodynamic sizes and PDIs of the clusters used for photonic crystal in Figure 5d, with a cluster size of 100 nm, 120 nm, and 200 nm, respectively.

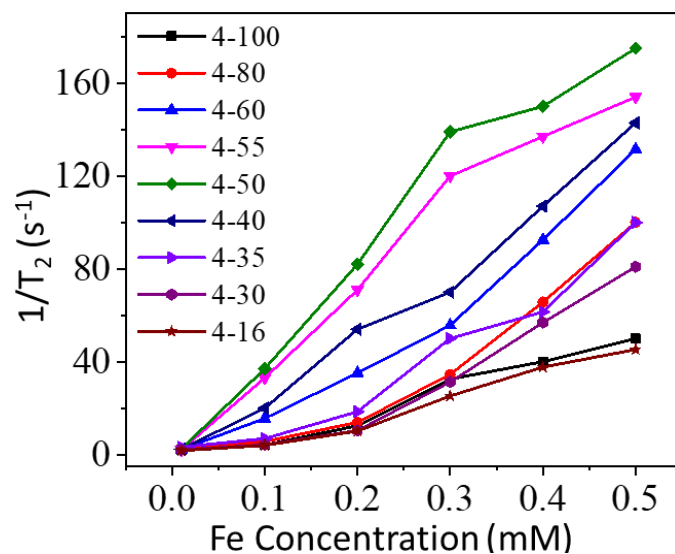


Figure S2. 14. The inverse of T_2 relaxation time of different cluster samples at various concentration, consistent with the observation in phantom images (Figure 2.6 a). The relaxivities are found from the slope of these curves and demonstrate that at intermediate cluster dimensions the MRI T_2 contrast is optimized.

References in Chapter 2

- [1] Ge, J. P.; Yin, Y. D., Responsive Photonic Crystals. *Angew. Chem.-Int. Edit.* **2011**, *50* (7), 1492-1522.
- [2] He, L.; Wang, M. S.; Ge, J. P.; Yin, Y. D., Magnetic Assembly Route to Colloidal Responsive Photonic Nanostructures. *Accounts Chem. Res.* **2012**, *45* (9), 1431-1440.
- [3] Mandriota, G.; Di Corato, R.; Benedetti, M.; De Castro, F.; Fanizzi, F. P.; Rinaldi, R., Design and Application of Cisplatin-Loaded Magnetic Nanoparticle Clusters for Smart Chemotherapy. *ACS Applied Materials & Interfaces* **2019**, *11* (2), 1864-1875.
- [4] Deng, H.; Li, X.; Peng, Q.; Wang, X.; Chen, J.; Li, Y., Monodisperse magnetic single-crystal ferrite microspheres. *Angewandte Chemie* **2005**, *117* (18), 2842-2845.
- [5] Ge, J.; Hu, Y.; Biasini, M.; Beyermann, W. P.; Yin, Y., Superparamagnetic magnetite colloidal nanocrystal clusters. *Angewandte Chemie International Edition* **2007**, *46* (23), 4342-4345.
- [6] Cheng, C.; Xu, F.; Gu, H., Facile synthesis and morphology evolution of magnetic iron oxide nanoparticles in different polyol processes. *New Journal of Chemistry* **2011**, *35* (5), 1072-1079.
- [7] Kostopoulou, A.; Brintakis, K.; Vasilakaki, M.; Trohidou, K.; Douvalis, A.; Lascialfari, A.; Manna, L.; Lappas, A., Assembly-mediated interplay of dipolar interactions and surface spin disorder in colloidal maghemite nanoclusters. *Nanoscale* **2014**, *6* (7), 3764-3776.
- [8] Kuznetsov, A. A., Zero-Field and Field-Induced Interactions between Multicore Magnetic Nanoparticles. *Nanomaterials* **2019**, *9* (5), 16.
- [9] Schaller, V.; Wahnstrom, G.; Sanz-Velasco, A.; Gustafsson, S.; Olsson, E.; Enoksson, P.; Johansson, C., Effective magnetic moment of magnetic multicore nanoparticles. *Physical Review B* **2009**, *80* (9).
- [10] Tadic, M.; Kralj, S.; Jagodic, M.; Hanzel, D.; Makovec, D., Magnetic properties of novel superparamagnetic iron oxide nanoclusters and their peculiarity under annealing treatment. *Applied Surface Science* **2014**, *322*, 255-264.
- [11] Coral, D. F.; Soto, P. A.; Blank, V.; Veiga, A.; Spinelli, E.; Gonzalez, S.; Saracco, G. P.; Bab, M. A.; Muraca, D.; Setton-Avruij, P. C.; Roig, A.; Roguin, L.; van Raap, M. B., Nanoclusters of crystallographically aligned nanoparticles for magnetic thermotherapy: aqueous ferrofluid, agarose phantoms and ex vivo melanoma tumour assessment. *Nanoscale* **2018**, *10* (45), 21262-21274.
- [12] Lartigue, L.; Hugounenq, P.; Alloyeau, D.; Clarke, S. P.; Levy, M.; Bacri, J.-C.; Bazzi, R.; Brougham, D. F.; Wilhelm, C.; Gazeau, F., Cooperative organization in iron oxide multi-core nanoparticles potentiates their efficiency as heating mediators and MRI contrast agents. *ACS nano* **2012**, *6* (12), 10935-10949.
- [13] Wang, C.; Xu, H.; Liang, C.; Liu, Y. M.; Li, Z. W.; Yang, G. B.; Cheng, H.; Li, Y. G.; Liu, Z., Iron Oxide @ Polypyrrole Nanoparticles as a Multifunctional Drug Carrier for Remotely Controlled Cancer Therapy with Synergistic Antitumor Effect. *Acs Nano* **2013**, *7* (8), 6782-6795.

- [14] Vuong, Q. L.; Berret, J. F.; Fresnais, J.; Gossuin, Y.; Sandre, O., A Universal Scaling Law to Predict the Efficiency of Magnetic Nanoparticles as MRI T2-Contrast Agents. *Advanced Healthcare Materials* **2012**, *1* (4), 502-512.
- [15] Dutz, S., Are Magnetic Multicore Nanoparticles Promising Candidates for Biomedical Applications? *IEEE Trans. Magn.* **2016**, *52* (9), 3.
- [16] Hemery, G.; Keyes Jr, A. C.; Garaio, E.; Rodrigo, I.; Garcia, J. A.; Plazaola, F.; Garanger, E.; Sandre, O., Tuning sizes, morphologies, and magnetic properties of monocoresh versus multicore iron oxide nanoparticles through the controlled addition of water in the polyol synthesis. *Inorganic chemistry* **2017**, *56* (14), 8232-8243.
- [17] Xiao, J. M.; Zhang, G. L.; Qian, J. C.; Sun, X.; Tian, J.; Zhong, K.; Cai, D. Q.; Wu, Z. Y., Fabricating High-Performance T2-Weighted Contrast Agents via Adjusting Composition and Size of Nanomagnetic Iron Oxide. *ACS Applied Materials & Interfaces* **2018**, *10* (8), 7003-7011.
- [18] Wang, T.; Zhang, L.; Wang, H.; Yang, W.; Fu, Y.; Zhou, W.; Yu, W.; Xiang, K.; Su, Z.; Dai, S., Controllable synthesis of hierarchical porous Fe₃O₄ particles mediated by poly (diallyldimethylammonium chloride) and their application in arsenic removal. *ACS applied materials & interfaces* **2013**, *5* (23), 12449-12459.
- [19] Chatterjee, J.; Haik, Y.; Chen, C. J., Size dependent magnetic properties of iron oxide nanoparticles. *Journal of Magnetism and Magnetic Materials* **2003**, *257* (1), 113-118.
- [20] Koseoglu, Y.; Kavas, H., Size and surface effects on magnetic properties of Fe₃O₄ nanoparticles. *Journal of Nanoscience and Nanotechnology* **2008**, *8* (2), 584-590.
- [21] Patsula, V.; Moskvina, M.; Dutz, S.; Horak, D., Size-dependent magnetic properties of iron oxide nanoparticles. *Journal of Physics and Chemistry of Solids* **2016**, *88*, 24-30.
- [22] Li, Q.; Kartikowati, C. W.; Horie, S.; Ogi, T.; Iwaki, T.; Okuyama, K., Correlation between particle size/domain structure and magnetic properties of highly crystalline Fe₃O₄ nanoparticles. *Scientific Reports* **2017**, *7*.
- [23] Liu, J.; Sun, Z., Yonghui; Zou, Y.; Li, C.; Guo, X.; Xiong, L.; Gao, Y.; Li, F.; Zhao, D., Highly water-dispersible biocompatible magnetite particles with low cytotoxicity stabilized by citrate groups. *Angewandte Chemie International Edition* **2009**, *48* (32), 5875-5879.
- [24] Xuan, S.; Wang, Y.-X. J.; Yu, J. C.; Cham-Fai Leung, K., Tuning the grain size and particle size of superparamagnetic Fe₃O₄ microparticles. *Chemistry of Materials* **2009**, *21* (21), 5079-5087.
- [25] Wang, L.; Bao, J.; Wang, L.; Zhang, F.; Li, Y., One-pot synthesis and bioapplication of amine-functionalized magnetite nanoparticles and hollow nanospheres. *Chemistry—A European Journal* **2006**, *12* (24), 6341-6347.
- [26] Cheng, C.; Wen, Y.; Xu, X.; Gu, H., Tunable synthesis of carboxyl-functionalized magnetite nanocrystal clusters with uniform size. *Journal of Materials Chemistry* **2009**, *19* (46), 8782-8788.
- [27] Zhu, M.; Diao, G., Synthesis of Porous Fe₃O₄ Nanospheres and Its Application for the Catalytic Degradation of Xylenol Orange. *Journal of Physical Chemistry C* **2011**, *115* (39), 18923-18934.

- [28] Liang, J.; Ma, H.; Luo, W.; Wang, S., Synthesis of magnetite submicrospheres with tunable size and superparamagnetism by a facile polyol process. *Materials Chemistry and Physics* **2013**, *139* (2-3), 383-388.
- [29] Wei, X.; Jing, L.; Liu, C.; Hou, Y.; Jiao, M.; Gao, M., Molecular mechanisms for delicately tuning the morphology and properties of Fe₃O₄ nanoparticle clusters. *CrystEngComm* **2018**, *20* (17), 2421-2429.
- [30] Matijevic, E.; Scheiner, P., FERRIC HYDROUS OXIDE SOLS .3. PREPARATION OF UNIFORM PARTICLES BY HYDROLYSIS OF FE(III)-CHLORIDE, FE(III)-NITRATE, AND FE(III)-PERCHLORATE SOLUTIONS. *Journal of Colloid and Interface Science* **1978**, *63* (3), 509-524.
- [31] Togashi, T.; Naka, T.; Asahina, S.; Sato, K.; Takami, S.; Adschiri, T., Surfactant-assisted one-pot synthesis of superparamagnetic magnetite nanoparticle clusters with tunable cluster size and magnetic field sensitivity. *Dalton Transactions* **2011**, *40* (5), 1073-1078.
- [32] Luo, B.; Song, X.-J.; Zhang, F.; Xia, A.; Yang, W.-L.; Hu, J.-H.; Wang, C.-C., Multi-functional thermosensitive composite microspheres with high magnetic susceptibility based on magnetite colloidal nanoparticle clusters. *Langmuir* **2009**, *26* (3), 1674-1679.
- [33] Lu, Z.; Yin, Y., Colloidal nanoparticle clusters: functional materials by design. *Chemical Society Reviews* **2012**, *41* (21), 6874-6887.
- [34] Ohno, K.; Sakaue, M.; Mori, C., Magnetically Responsive Assemblies of Polymer-Brush-Decorated Nanoparticle Clusters That Exhibit Structural Color. *Langmuir* **2018**, *34* (32), 9532-9539.
- [35] Bagaria, H. G.; Yoon, K. Y.; Neilson, B. M.; Cheng, V.; Lee, J. H.; Worthen, A. J.; Xue, Z.; Huh, C.; Bryant, S. L.; Bielawski, C. W., Stabilization of iron oxide nanoparticles in high sodium and calcium brine at high temperatures with adsorbed sulfonated copolymers. *Langmuir* **2013**, *29* (10), 3195-3206.
- [36] Linot, C.; Poly, J.; Boucard, J.; Pouliquen, D.; Nedellec, S.; Hulin, P.; Marec, N.; Arosio, P.; Lascialfari, A.; Guerrini, A., PEGylated Anionic Magnetofluorescent Nanoassemblies: Impact of Their Interface Structure on Magnetic Resonance Imaging Contrast and Cellular Uptake. *ACS applied materials & interfaces* **2017**, *9* (16), 14242-14257.
- [37] Hemery, G.; Genevois, C.; Couillaud, F.; Lacomme, S.; Gontier, E.; Ibarboure, E.; Lecommandoux, S.; Garanger, E.; Sandre, O., Monocore vs. multicore magnetic iron oxide nanoparticles: Uptake by glioblastoma cells and efficiency for magnetic hyperthermia. *Molecular Systems Design & Engineering* **2017**, *2* (5), 629-639.
- [38] Kostopoulou, A.; Brintakis, K.; Fragogeorgi, E.; Anthousi, A.; Manna, L.; Begin-Colin, S.; Billotey, C.; Ranella, A.; Loudos, G.; Athanassakis, I.; Lappas, A., Iron Oxide Colloidal Nanoclusters as Theranostic Vehicles and Their Interactions at the Cellular Level. *Nanomaterials* **2018**, *8* (5).
- [39] Wu, M.; Wang, Q. T.; Zhang, D.; Liao, N. S.; Wu, L. J.; Huang, A. M.; Liu, X. L., Magnetite nanocluster@poly(dopamine)-PEG@ indocyanine green nanobead with magnetic field-targeting enhanced MR imaging and photothermal therapy in vivo. *Colloids and Surfaces B-Biointerfaces* **2016**, *141*, 467-475.

- [40] Lim, S.; Park, J.; Shim, M. K.; Um, W.; Yoon, H. Y.; Ryu, J. H.; Lim, D. K.; Kim, K., Recent advances and challenges of repurposing nanoparticle-based drug delivery systems to enhance cancer immunotherapy. *Theranostics* **2019**, *9* (25), 7906-7923.
- [41] Gerber, O.; Pichon, B.; Ihiawakrim, D.; Florea, I.; Moldovan, S.; Ersen, O.; Begin, D.; Grenèche, J.-M.; Lemonnier, S.; Barraud, E., Synthesis engineering of iron oxide raspberry-shaped nanostructures. *Nanoscale* **2017**, *9* (1), 305-313.
- [42] Tong, G.; Liu, Y.; Wu, T.; Tong, C.; Du, F., H₂O-steered size/phase evolution and magnetic properties of large-scale, monodisperse Fe_xO_y nanomaterials. *Journal of Materials Chemistry C* **2015**, *3* (21), 5506-5515.
- [43] Dong, Y. X.; Wen, B.; Chen, Y. J.; Cao, P. Q.; Zhang, C. C., Autoclave-free facile approach to the synthesis of highly tunable nanocrystal clusters for magnetic responsive photonic crystals. *Rsc Advances* **2016**, *6* (69), 64434-64440.
- [44] Gavilán, H.; Sánchez, E. H.; Brollo, M. E.; Asín, L.; Moerner, K. K.; Frandsen, C.; Lázaro, F. J.; Serna, C. J.; Veintemillas-Verdaguer, S.; Morales, M. P., Formation mechanism of maghemite nanoflowers synthesized by a polyol-mediated process. *Acs Omega* **2017**, *2* (10), 7172-7184.
- [45] Zhu, Y.; Zhao, W.; Chen, H.; Shi, J., A simple one-pot self-assembly route to nanoporous and monodispersed Fe₃O₄ particles with oriented attachment structure and magnetic property. *The Journal of Physical Chemistry C* **2007**, *111* (14), 5281-5285.
- [46] Bunge, A.; Porav, A. S.; Borodi, G.; Radu, T.; Pîrnău, A.; Berghian-Grosan, C.; Turcu, R., Correlation between synthesis parameters and properties of magnetite clusters prepared by solvothermal polyol method. *Journal of Materials Science* **2019**, *54* (4), 2853-2875.
- [47] Thomas, G.; Demoisson, F.; Chassagnon, R.; Popova, E.; Millot, N., One-step continuous synthesis of functionalized magnetite nanoflowers. *Nanotechnology* **2016**, *27* (13), 135604.
- [48] Kostopoulou, A.; Velu, S. K.; Thangavel, K.; Orsini, F.; Brintakis, K.; Psycharakis, S.; Ranella, A.; Bordonali, L.; Lappas, A.; Lascialfari, A., Colloidal assemblies of oriented maghemite nanocrystals and their NMR relaxometric properties. *Dalton Transactions* **2014**, *43* (22), 8395-8404.
- [49] Lu, C.; Wang, H.; Ma, J.; Yuan, H.; Liang, H.; Wu, L.; Chai, K. Y.; Li, S., Facile synthesis of superparamagnetic magnetite nanoflowers and their applications in cellular imaging. *RSC advances* **2016**, *6* (48), 42649-42655.
- [50] Otero-Lorenzo, R.; Ramos-Docampo, M. A.; Rodríguez-González, B.; Comesaña-Hermo, M.; Salgueiriño, V. n., Solvothermal clustering of magnetic spinel ferrite nanocrystals: a Raman perspective. *Chemistry of Materials* **2017**, *29* (20), 8729-8736.
- [51] Gavilán, H.; Kowalski, A.; Heinke, D.; Sugunan, A.; Sommertune, J.; Varón, M.; Bogart, L. K.; Posth, O.; Zeng, L.; González-Alonso, D., Colloidal Flower-Shaped Iron Oxide Nanoparticles: Synthesis Strategies and Coatings. *Particle & particle systems characterization* **2017**, *34* (7), 1700094.
- [52] Sanchez, L. M.; Martin, D. A.; Alvarez, V. A.; Gonzalez, J. S., Polyacrylic acid-coated iron oxide magnetic nanoparticles: The polymer molecular weight influence. *Colloid Surf. A-Physicochem. Eng. Asp.* **2018**, *543*, 28-37.

- [53] Bagaria, H. G.; Xue, Z.; Neilson, B. M.; Worthen, A. J.; Yoon, K. Y.; Nayak, S.; Cheng, V.; Lee, J. H.; Bielawski, C. W.; Johnston, K. P., Iron Oxide Nanoparticles Grafted with Sulfonated Copolymers are Stable in Concentrated Brine at Elevated Temperatures and Weakly Adsorb on Silica. *Acs Applied Materials & Interfaces* **2013**, *5* (8), 3329-3339.
- [54] Amstad, E.; Gillich, T.; Bilecka, I.; Textor, M.; Reimhult, E., Ultrastable iron oxide nanoparticle colloidal suspensions using dispersants with catechol-derived anchor groups. *Nano letters* **2009**, *9* (12), 4042-4048.
- [55] Ding, X.; Vegesna, G. K.; Meng, H.; Winter, A.; Lee, B. P., Nitro-Group Functionalization of Dopamine and its Contribution to the Viscoelastic Properties of Catechol-Containing Nanocomposite Hydrogels. *Macromolecular chemistry and physics* **2015**, *216* (10), 1109-1119.
- [56] Bixner, O.; Lassenberger, A.; Baurecht, D.; Reimhult, E., Complete Exchange of the Hydrophobic Dispersant Shell on Monodisperse Superparamagnetic Iron Oxide Nanoparticles. *Langmuir* **2015**, *31* (33), 9198-9204.
- [57] Yu, W. W.; Chang, E.; Sayes, C. M.; Drezek, R.; Colvin, V. L., Aqueous dispersion of monodisperse magnetic iron oxide nanocrystals through phase transfer. *Nanotechnology* **2006**, *17* (17), 4483-4487.
- [58] Xu, X. L.; Friedman, G.; Humfeld, K. D.; Majetich, S. A.; Asher, S. A., Superparamagnetic photonic crystals. *Adv. Mater.* **2001**, *13* (22), 1681-1684.
- [59] Ge, J. P.; Hu, Y. X.; Zhang, T. R.; Huynh, T.; Yin, Y. D., Self-assembly and field-responsive optical diffractions of superparamagnetic colloids. *Langmuir* **2008**, *24* (7), 3671-3680.
- [60] Xia, H.; Zhang, L.; Chen, Q. D.; Guo, L.; Fang, H. H.; Li, X. B.; Song, J. F.; Huang, X. R.; Sun, H. B., Band-Gap-Controllable Photonic Crystals Consisting of Magnetic Nanocrystal Clusters in a Solidified Polymer Matrix. *Journal of Physical Chemistry C* **2009**, *113* (43), 18542-18545.
- [61] He, L.; Malik, V.; Wang, M. S.; Hu, Y. X.; Anson, F. E.; Yin, Y. D., Self-assembly and magnetically induced phase transition of three-dimensional colloidal photonic crystals. *Nanoscale* **2012**, *4* (15), 4438-4442.
- [62] Cai, Z. Y.; Sasmal, A.; Liu, X. Y.; Asher, S. A., Responsive Photonic Crystal Carbohydrate Hydrogel Sensor Materials for Selective and Sensitive Lectin Protein Detection. *Acs Sensors* **2017**, *2* (10), 1474-1481.
- [63] Kralj, S.; Makovec, D., Magnetic Assembly of Superparamagnetic Iron Oxide Nanoparticle Clusters into Nano chains and Nanobundles. *Acs Nano* **2015**, *9* (10), 9700-9707.
- [64] Yang, F.; Skripka, A.; Tabatabaei, M. S.; Hong, S. H.; Ren, F.; Benayas, A.; Oh, J. K.; Martel, S.; Liu, X.; Vetrone, F.; Ma, D., Multifunctional Self-Assembled Supernanoparticles for Deep-Tissue Bimodal Imaging and Amplified Dual-Mode Heating Treatment. *Acs Nano* **2019**, *13* (1), 408-420.
- [65] Bu, L. L.; Rao, L.; Yu, G. T.; Chen, L.; Deng, W. W.; Liu, J. F.; Wu, H.; Meng, Q. F.; Guo, S. S.; Zhao, X. Z., Cancer Stem Cell-Platelet Hybrid Membrane-Coated Magnetic Nanoparticles for Enhanced Photothermal Therapy of Head and Neck Squamous Cell Carcinoma. *Advanced Functional Materials* **2019**, *29* (10), 1807733.

- [66] Joos, A.; Lova, N.; Wiekhorst, F.; Gleich, B.; Haase, A., Size-dependent MR relaxivities of magnetic nanoparticles. *Journal of Magnetism and Magnetic Materials* **2017**, *427*, 122-126.
- [67] Mues, B.; Buhl, E. M.; Schmitz-Rode, T.; Slabu, I., Towards optimized MRI contrast agents for implant engineering: Clustering and immobilization effects of magnetic nanoparticles. *Journal of Magnetism and Magnetic Materials* **2019**, *471*, 432-438.
- [68] Larsen, B. A.; Haag, M. A.; Serkova, N. J.; Shroyer, K. R.; Stoldt, C. R., Controlled aggregation of superparamagnetic iron oxide nanoparticles for the development of molecular magnetic resonance imaging probes. *Nanotechnology* **2008**, *19* (26).
- [69] Fayol, D.; Luciani, N.; Lartigue, L.; Gazeau, F.; Wilhelm, C., Managing Magnetic Nanoparticle Aggregation and Cellular Uptake: a Precondition for Efficient Stem-Cell Differentiation and MRI Tracking. *Advanced Healthcare Materials* **2013**, *2* (2), 313-325.

Chapter 3

The Giant Susceptibility of Magnetic Nanocrystal Clusters[†]

[†] Reprinted (adapted) with permission from Zhang, Q.* , Raj, S.* , Xiao, Z.* , Zhang, L.* , Fellows, B., Saayujya, C., Chandrasekharan, P., Masterson, C.M., Li, J., Guo, W., Conolly, S.M., Bao, G., Král, P. and Colvin, V.L. The Giant Susceptibility of Magnetic Nanocrystal Clusters. In preparation.

*These authors contributed equally.

3. The Giant Susceptibility of Magnetic Nanocrystal Clusters

3.1 Abstract

The ability to image, move, and heat superparamagnetic nanomaterials at a distance using magnetic fields has extraordinary value in biology and medicine. These opportunities would be vastly expanded by materials with very large magnetic susceptibilities made from safe constituents like iron oxide. Here we show how moderate exchange interactions between oriented nanocrystals can lead to more sensitive superparamagnets, a phenomenon we term giant susceptibility. Micromagnetic simulations illustrate how the fluctuations of the magnetic moments of the nanocrystal clusters minimizes the energetic cost of magnetization. The extraordinary sensitivity of these systems to magnetic fields enables portable magnetic heating and rapid stem cell capture using toy magnetic letters. The particles can also be applied in-vivo to eradicate solid tumors as well as improve the spatial resolution of magnetic particle imaging.

3.2 Introduction

When crystalline iron oxide particles are sufficiently small, they are not magnetized unless a strong enough external field is applied to overcome the thermal fluctuations of their magnetic moments.^[1] This reversible and switchable magnetic behavior, known as superparamagnetism, underpins diverse applications that move, image, and heat these materials often in biological settings.^[2-6] Translation of these remarkable properties into practical technology, however, is limited by the large external magnetic fields needed to manipulate a particle's magnetization.^[7] This barrier could be overcome if the initial magnetic susceptibility of these materials could be increased. Classic models for

superparamagnetism describe how thermal energy and crystallographic anisotropy present intrinsic barriers to the orientation of magnetic moments of nanoscale crystallites.^[8] This framework leaves experimentalists with few options for creating more magnetically susceptible iron oxide particles. Substituents such as manganese and zinc can be mixed with iron oxide to form ferrites, and for a narrow range of compositions this strategy can lower crystal anisotropy offering gains in magnetic heating and imaging performance.^[9, 10] However, ferrites are complex to manufacture and their toxicity profiles present challenges for many biological applications.^[11, 12] New strategies for increasing the magnetic sensitivity of superparamagnets made from earth-abundant, FDA-approved iron oxides would thus be of great interest.

3.3 The structure and magnetic properties of clusters

Here we demonstrate how moderate exchange interactions between the magnetic moments, or superpins, of iron oxide nanocrystals interacting in clusters can lead to substantial enhancement of initial magnetic susceptibility. This work originated in our effort to prepare diameter-controlled clusters consisting of oriented assemblies of tens to hundreds of superparamagnetic nanocrystals.^[13] We expected some level of exchange interaction between the individual, sub-10 nm elements of these clusters given their shared crystallographic interfaces. Exchange interactions between magnetic materials can exert a powerful influence on their magnetic properties leading to a plethora of interesting magnetic phenomena.^[14-20] Exchange-coupled core-shell particles, for example, containing soft magnetic cores and hard magnetic shells exhibit tunable remanence quite different from each individual component.^[21] We reasoned that if superparamagnetic nanocrystals were coupled through exchange interactions, as might be expected in our oriented

assemblies, then superspin alignment would be promoted with a resulting increase in their magnetic susceptibility (Figure 3.1). This approach is tricky to implement as it requires moderate interparticle exchange energies. If the individual nanocrystal's exchange interactions are too large, then nanocrystal assemblies could revert to blocked single domain states. If the nanocrystal exchange interactions are too weak, then systems would behave as non-interacting magnetic superparamagnets well described by the classical model referenced above.

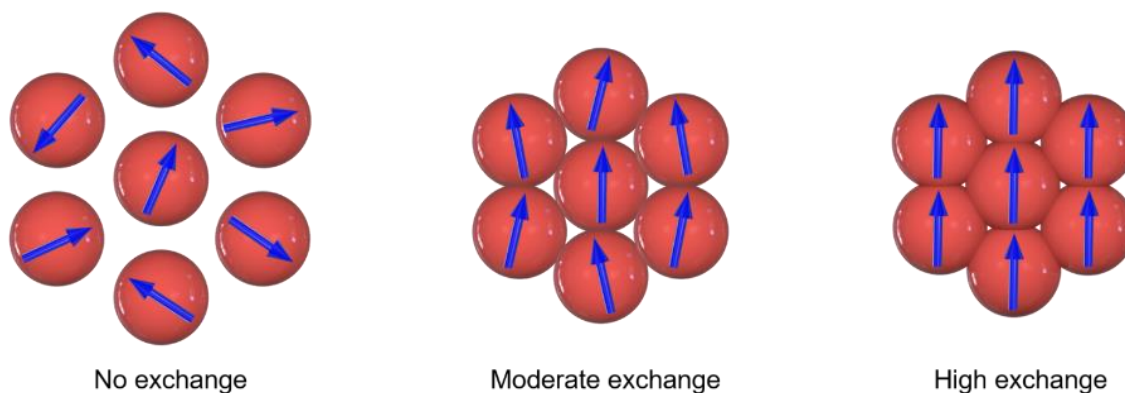


Figure 3. 1. Tailoring the magnetization of magnetic nanocrystals via changing the level of exchange interaction. Magnetic nanocrystals (red) possess magnetic moments (blue) reflecting the contributions from the underlying atomic magnetic moments in the crystalline iron oxide lattice. Isolated particles behave independently (left) and their magnetic moments, arising from their superspins, are not aligned. With moderate exchange interactions (middle) brought about by shared interfaces, adjacent superspins are aligned but not perfectly. Under conditions of high exchange coupling (right), crystallites are effectively joined into one lattice and act as a single monocrystalline material.

To realize an intermediate level of particle-particle interaction, we rely on the shared interfaces of nanocrystals bound together in what we term moderately exchange-coupled magnetic clusters (MECMags). We limited our study here to pure iron oxide as it is relatively inexpensive, approved by the FDA in particle forms for clinical applications, and amenable to large scale manufacturing.^[21] Clusters can be conceptualized as incomplete

single crystals formed from the oriented aggregation of nanocrystals that, because of imperfect packing, have some porosity (Figure 3.2 a and Figure S3.1). They are described dimensionally by both an overall cluster diameter (D_c) and a primary nanocrystal size (d_p). Such assemblies, sometimes referred to as magnetic multicores or nanoflowers, can be generated through hydrolysis of iron salts in solvothermal reactors.^[13, 22, 23] We adapted this synthesis to form gram-quantities of products that are colloidally stable, with reasonable uniformity in cluster diameter ($\sigma < 10\%$), containing tens to thousands of primary nanocrystals in clusters ranging from 20 to 200 nm in diameter (Figure S3.2).^[13] Their compact structure and porous morphology can be resolved by electron microscopy, and quantified by surface area measurements (Figure 3.2 c, d, g and h). For comparison we also generated isolated nanocrystals of iron oxide that are not assembled through the high temperature thermal decomposition of iron carboxylates. These reactions yield very uniform ($\sigma < 5\%$) and non-aggregating crystallites (Figure 3.2 b and Figure S3.5).^[24]

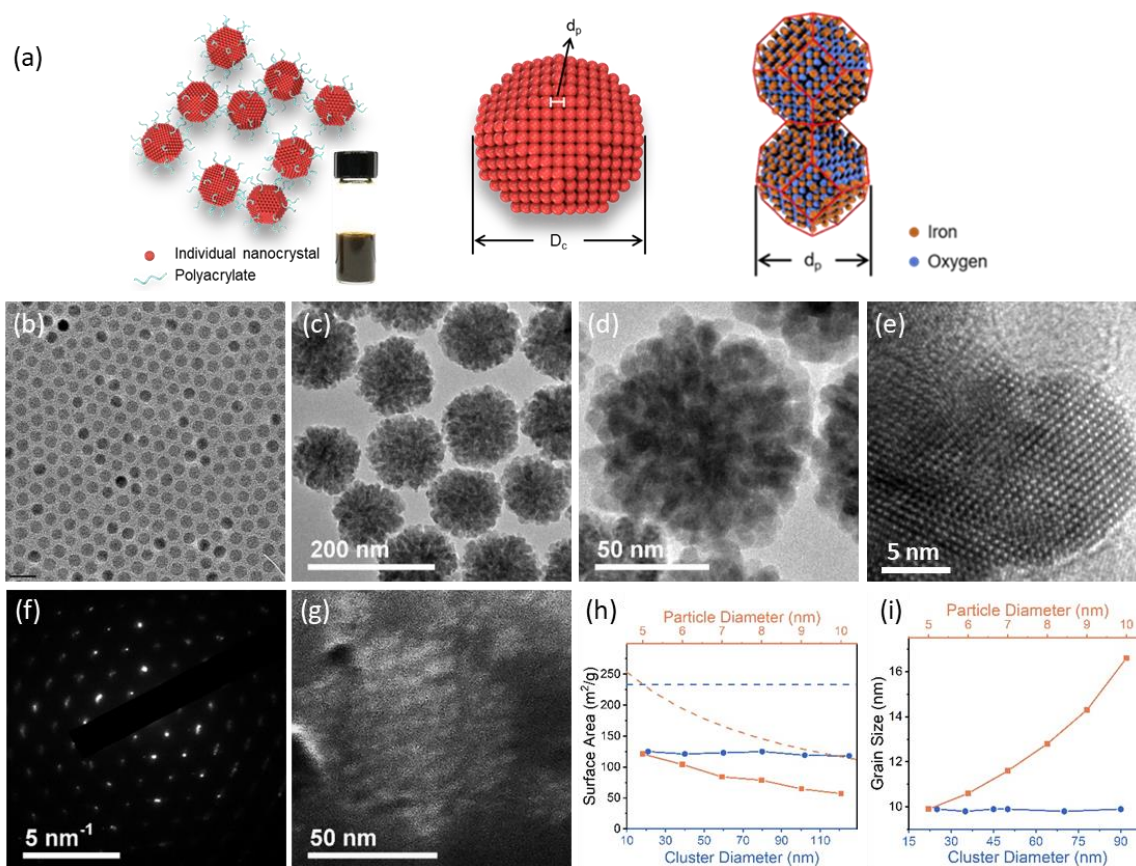


Figure 3. 2. Characterization of Moderately exchange-coupled magnetic nanocrystal clusters. (a) Nanocrystal clusters (Red) are coated with polyacrylate (green) and colloidally stable in aqueous solution. The inset shows an aqueous solution of clusters. (Middle) A cluster is composed of hundreds of smaller nanocrystals that share crystallographic boundaries. The nanocrystals are not close-packed and the sample overall diffracts much like a single crystal. (Right) Two neighboring primary nanocrystal within a cluster. The primary nanocrystals within a cluster assume the same crystallographic orientation and share boundaries, giving rising to exchange interactions. (b) Transmission electron micrograph of isolated iron oxide nanocrystals which serve as controls in much of this work. Scale bar = 20 nm. (c) An example transmission electron micrograph of clusters of diameter $90 \text{ nm} \pm 8.1 \text{ nm}$. (d) High magnification TEM micrograph shows each cluster is composed of many primary particles. (e) High resolution TEM image shows the crystalline lattice of a cluster. Its crystallites, here roughly 9 nm in dimension, possess aligned crystallographic axes. (f) Electron diffraction from a single cluster reveals well defined spots illustrating the crystallographic orientation of neighboring primary nanocrystals extends through the entire cluster. (g) Focused ion beam milling followed by scanning electron microscopy reveals that the internal structure of the clusters is not a dense compact but has some porosity. (h) Nitrogen isotherm measurements of the surface areas of dried cluster powders shows that the overall surface area depends not on cluster diameter (blue, $d_p = 5 \text{ nm}$) but rather on primary particle diameter (red, $D_c = 60 \text{ nm}$). The dashed lines are calculated surface areas assuming no contact between

primary particles (orange) or a completely consolidated monocrystal (blue). (i) The dimensions of clusters calculated from powder X-ray diffraction patterns as a function of both primary nanocrystals and cluster dimension.

Electron diffraction of the clusters illustrates that the individual crystallites have aligned crystallographic axes (Figure 3.2 f) well described by the magnetite (Fe_3O_4) phase of iron oxide. The clusters can under some circumstance form through the oriented attachment of primary magnetite yielding well-defined and uniform assemblies.^[13, 22, 23] Most important for this work is the crystallographic alignment of the tens to hundreds of nanocrystals within the clusters. This is most apparent in the spot-like electron diffraction from one nanocluster (Figure 3.2 f) which demonstrates the materials are well approximated by a nearly perfect single crystal of magnetite. Our observation of single-crystal like structure in this class of materials is not new and has been noted by a few others.^[25] These assemblies are single crystals, but they are not perfect crystals. The diffraction spots from individual clusters show some degree of smearing indicating that the registry of the primary nanocrystals may not be perfect within individual clusters. The clusters appear as relatively compact aggregates with irregular surfaces (Figure 3.2 c and d). The FIB-SEM (Figure 3.2 g) suggests an internal structure with some porosity as would be expected from packed primary particles.

Even though the clusters are single crystals, they possess large surface areas reflecting the substantial internal porosity present within each cluster. Figure 3.2 h shows the surface area of dried cluster powders as a function of cluster diameter (D_c) for a fixed primary nanocrystal size (d_p). Over many samples the surface area is greater than that expected from fully densified nanocrystal aggregate. Moreover, the external diameter of the cluster

has no impact on the measured surface areas illustrating that some of the internal interfaces of the primary nanocrystals are not shared with neighboring particles (Figure 3.2 h). Notably as the primary nanocrystal dimension decreases in different samples, the surface area increases (Figure 3.2 h) further illustrating the accessibility of the internal interfaces of primary particles. Not all interfaces are available, however, as measured surface areas are roughly half what would be expected for isolated particles. Electron microscopy reveals that the primary particles contact their neighbors through hard interfaces (Figure 3.2 d and e and Figure S3.3) lowering the available internal surface for gas adsorption. Aggregative growth of clusters in this solvothermal reaction is self-limiting yielding uniform assemblies that themselves are non-aggregating in various suspensions. These materials have polyacrylate coatings which can be further modified yielding suspensions in water or in other biologically relevant media that remain uniform with no nanocluster-nanocluster aggregation or sedimentation (Figure S3.4).^[13] Solid samples can be recovered from these suspensions and dispersed into a non-magnetic matrix. This format that allows their magnetic properties to be evaluated in the absence of cluster rotation and inter-assembly interactions.^[26]

At room temperature the clusters with cluster diameters under 45 nm are superparamagnets with a magnetization that increases with increasing field strength until the samples are completely magnetized (Figure 3.3 a and Figure S3.6). The saturation magnetizations of clusters larger than 40 nm are within 20% of that expected for bulk magnetite (92 emu/g) confirming their excellent crystallinity.^[27] In this work we are concerned with the behavior at very low applied fields (inset of Figure 3.3 a). For smaller cluster assemblies, the absence of remanent magnetization is consistent with superparamagnetic behavior; we confirmed

this classification with temperature-dependent field cooling studies (Figure 3.3 c). Room temperature remanent magnetization for this morphology was observed only for clusters larger than 45 nm followed by increasing coercivity (H_c) with increasing cluster diameter (Figure 3.3 b and Table S3.4). This observation, along with ZFC-FC curves (Figure 3.3 c), identifies the transition from superparamagnetic to blocked single domain magnetic behavior occurs between 40 and 45 nm cluster diameter with little dependence on the primary nanocrystal dimensions. We also characterized isolated nanocrystals and found superparamagnetic behavior under these experimental conditions only for nanocrystals under 18 nm in diameter (Table S3.3). As compared to isolated nanoparticles, the clusters retain their superparamagnetic behavior up to much larger cluster dimensions. While this may be the first report of systematic size-dependent trends in magnetic assemblies of this type, others have commented that aggregated nanocrystals may exhibit superparamagnetic characteristics up to dimensions much larger than that expected from studies of isolated nanoparticles (Figure 3.3 b).^[22, 23, 25]

The behavior of these materials at large applied magnetic fields varies only slightly with sample morphology and dimension, but at the small magnetic fields of interest here there are profound differences in the initial magnetic susceptibility of the different samples. Here we define the initial magnetic susceptibility (χ) as the slope of the magnetization versus applied field (Figure 3.3 d) near zero applied field. The behavior of the magnetization curve in this low field limit is linear, as expected, and susceptibility could be easily extracted. We observe that the initial magnetic susceptibility is larger for assemblies of nanocrystals than for isolated nanocrystals. Within each morphology, though, susceptibility increases and then decreases with dimension (Figure S3.10). This is shown clearly in Figure 3.3 e

which compares the initial magnetic susceptibility across sample morphologies and diameters. Interestingly for both isolated nanoparticles and clusters, once samples are large enough to exhibit measurable coercivity (Figure 3.3 b and e, 20 nm for isolated nanoparticles or 45 nm for clusters) their initial susceptibility falls substantially as their dimensions increase.

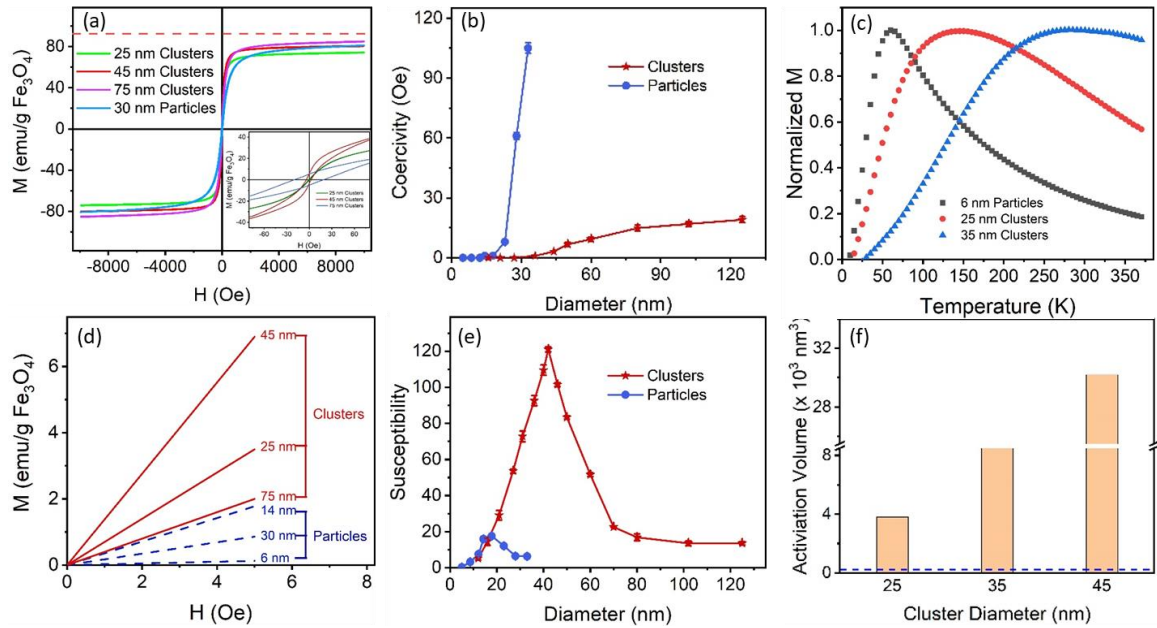


Figure 3.3. Magnetic properties of both iron oxide nanoparticles and clusters with different dimensions. (a) Hysteresis loop of isolated nanoparticles and clusters with different dimensions. The primary nanocrystal size for the clusters is 5 nm. (b) Coercivity of isolated nanoparticles and clusters with different dimensions measured at room temperature. The isolated nanoparticles and clusters exhibit coercivities when they are larger than 18 nm and 45 nm, respectively. The coercivity of isolated nanocrystals and clusters increases with their dimensions. Isolated nanoparticles show much higher coercivities than clusters. (c) Zero-field-cooled magnetization curves of isolated nanoparticles and clusters with different dimensions. The curves were scanned from 5 to 375 K with a magnetic field of 50 Oe. Full FC-ZFC data can be found in supplemental Figure S3.8. (d) Initial magnetization curve of isolated nanoparticles and clusters with different dimensions. (e) Initial susceptibility of isolated nanoparticles and clusters with different dimensions. (f) Activation volume of clusters with different diameters by magnetic relaxation measurement. All the nanomaterials are dispersed in a matrix of calcium sulfate at 0.5% w/w% for magnetic characterizations. The concentration of iron oxide is determined using ICP-AES.

A striking feature of Figure 3.2 e is that the susceptibility of these assemblies is optimized for 45 nm clusters containing roughly four hundred individual nanocrystals. We term this behavior *giant susceptibility* defined here as an initial susceptibility an order of magnitude higher than average iron oxide bulk materials. This phenomenon was in part anticipated, but not named, decades ago by Bean *et al* who postulated that the susceptibility of perfect superparamagnets should increase with their volume; today the Langevin equation used to describe the magnetization of superparamagnets explicitly captures this relationship.^[28] This is the first time to our knowledge that this trend has been confirmed over a wide range of dimensions although Lartigue *et al* used the relationship to calculate effective magnetic moments in multicore clusters similar to these.^[23] Our results show that the magnetic susceptibility of these materials is roughly proportional to particle volume for both isolated superparamagnetic nanoparticles and assembled clusters (Figure 3.3 e). The unexpected finding in these results is that clustered materials retain their superparamagnetic properties up to larger cluster dimensions, and with greater susceptibilities, than the isolated nanocrystals. Because clusters are comprised of tens to hundreds of smaller crystallites with many shared boundaries, exchange interactions between them will be an important contribution to their magnetic behavior.^[29] We confirmed that nanocrystal-nanocrystal exchange interactions exist in these samples using a magnetic relaxation measurement technique (Figure 3.3 f and Figure S3.7). This measurement allows for the measure of the activation volume of a sample which for a 35 nm diameter assembly was 11,000 nm³. This activation volume increases with assembly dimension confirming some degree of exchange coupling exists between the primary nanocrystals in the clusters.^[30, 31]

3.4 Micromagnetic simulations on the clusters

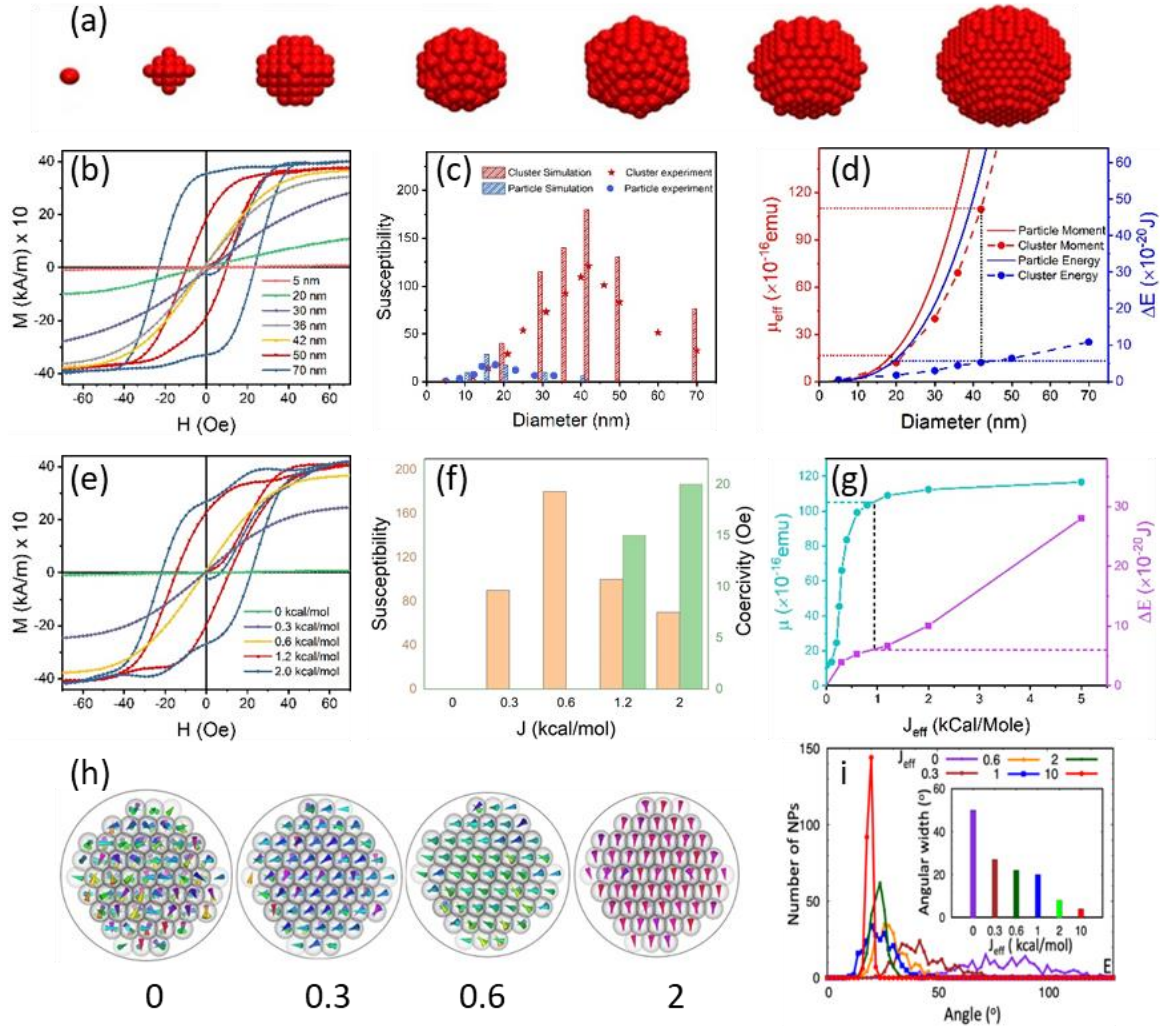


Figure 3. 4. Monte Carlo simulation on the magnetic properties of iron oxide clusters. (a) The schematic illustration of clusters of different diameters. (b) The magnetization curves of iron oxide clusters with different diameters. $J_{\text{eff}}=0.6$ kcal/mole. (c) The susceptibility of iron oxide clusters and isolated nanoparticles with different dimensions. (d) The effective magnetic moment and anisotropy energy barrier of iron oxide Clusters and nanocrystals with different diameters. (e) The magnetization curves of iron oxide clusters with different exchange constant. $D_c = 42$ nm. (F) The susceptibility of iron oxide clusters with different exchange constant. (g) The effective magnetic moment and anisotropy energy barrier of iron oxide clusters with different exchange constants. (h) Spin configuration of the iron oxide clusters with different exchange constants. (i) Angular distributions of the spins within the clusters of different exchange constants. $D_c = 42$ nm.

To gain insight into these experimental observations, we have performed micromagnetic simulations of the systems using a Monte Carlo method that adjusts sampling to capture kinetically trapped blocked states. The simulated assemblies consist of tens to hundreds of individual nanocrystals organized into closely packed spherical clusters (Figure 3.4 a). A local spin approximation is used for each nanocrystal and it sets the magnetic dipole moment, or superspin of each nanocrystal, to a magnitude defined by the collective atomic spins contained in the entire assembly, or global superspin.^[32] Each superspin interacts with the crystal lattice of iron oxide through magnetic anisotropy, with the external field through the Zeeman coupling, and with other superspins through dipolar and exchange couplings between neighboring nanocrystals.^[32] Exchange interactions can only exist between neighboring particles whose atomic orbitals are within a few angstroms of each other.^[29, 33] As is clear in Figure 3.2, some portion of the nanocrystal surfaces within the assemblies are bound to their neighbors creating a possibility for exchange interactions, and this was confirmed by the relaxation measurement of the activation volume (Figure 3.3 f and Figure S3.11).

To explore how exchange interactions between neighboring primary particles may affect the initial magnetic susceptibility of the cluster, the particle-particle exchange interactions are parametrized by an effective exchange constant, J_{eff} . We conceptually relate this parameter to the extent of hard aggregation in a cluster. Isolated nanocrystals with no shared boundaries would have a $J_{\text{eff}} = 0$ while a cluster consisting of completely fused nanocrystals and no internal porosity is assigned a $J_{\text{eff}} = 2$ kcal/mole. At this limit we should recover the behavior of a larger, isolated single crystal given that each solid nanocrystal is completely exchange coupled to its neighbors. We expect that the clusters studied here

would fall in between these two limits and achieve the best agreement with experimental data for a moderate exchange coupling of $J_{\text{eff}} = 0.6$ kcal/mole. Figure 3.4 b shows the simulation of magnetization in these systems. It increases with the applied field and saturates at a value equivalent to the bulk material. These moderately exchange-coupled smaller clusters are superparamagnetic with no notable remanence for diameters less than 45 nm. As we increase the number of interacting nanocrystals, however, the materials develop large magnetic moments unable to spontaneously reorient, leading to blocked single domain states. The size-dependence of the initial susceptibility for clusters is in good agreement with experimental results (Figure 3. 4 c and e). This is also true for micromagnetic simulations of isolated nanoparticles, which transition from superparamagnetic to blocked single-domain states at around 18 nm diameter (Figure S3.13). This limits their maximum susceptibility compared to aggregated nanocrystals.

To understand better the superparamagnetic behavior of larger clusters, we simulate how the magnetic properties of fixed-size (42 nm) clusters depends on the exchange coupling, J_{eff} between the individual subunits. When J_{eff} is small, the magnetic superspins of neighboring nanocrystals do not align (Figure 3.4 e and f). The cluster doesn't develop global particle superspins, and therefore has a low susceptibility. As J_{eff} is increased, primary nanocrystals have a greater tendency to align their moments into a global superspin that remains in a superparamagnetic state (Figure S3.12). Accordingly, the susceptibility increases with J_{eff} and peaks at what we term to be 'moderate' exchange coupling. Further increasing J_{eff} , however, makes the global superspin rigid in orientation, leading to lower magnetic susceptibilities. In this blocked state, the individual superspins within the cluster are strongly correlated. Their reorientation requires that they pass coherently over a large

energetic barrier defined by the crystalline anisotropy of the particle lattices, creating a significant obstacle to magnetic dipole alignment at low applied fields.

Our simulations can illustrate the dynamics of spin reorientation in these assemblies which help us understand how moderate exchange coupling lowers the barriers to global superspin reorientation. With no exchange coupling, or $J_{\text{eff}} = 0$, the nanocrystal superspins are not aligned (zero net magnetic moment), as shown in Figure 3.4 h and i, and the system has a small susceptibility. At moderate exchange coupling, $J_{\text{eff}} = 0.6$ kcal/mole, the superspins become partially correlated, leading to coherence in the dynamics of the global superspin. This global superspin can relatively easily overcome the anisotropy energy barrier because its constituent superspins do not reorient at the same time. This minimizes the energetic barriers and results in a large initial susceptibility. For the increased exchange coupling, $J_{\text{eff}} = 2$ kcal/mole, the superspins are nearly aligned and move coherently in response to applied fields (Figure S3.14). Now the global superspin is locked, or rather blocked, and unable at low applied fields to reorient its large magnetic moment against the magnetic anisotropy barrier of the crystal lattice. The mutual coherence of individual nanocrystal superspins persists in the presence of external fields and the dynamics illustrate the relative coherence of reorienting spins in these assemblies. Moderate exchange coupling provides some coherence to the overall alignment of superspins, but when they are reorienting, it allows for less coherence among their dynamic changes, and as a result a smaller initial magnetic susceptibility.

We can extract the effective energetic barriers for rotation of the global superspin in the clusters (Figure S3.15) by simulating the zero-field cooling curves (ZFC) of our model systems. This analysis gives us the ability to calculate the energetic barriers and the net

effective magnetic moment of the global superspin as assemblies are reorienting. Figures 3.4 d and g illustrate how the effective crystal anisotropy energy barriers and the global dipole moments depend on the diameters of clusters and the degree of their exchange coupling. Figure 3.4 d shows that as the cluster sizes increase, for moderate exchange coupling of $J_{\text{eff}} = 0.6$ kcal/mole, the global moment μ_{eff} increases with the cluster volume. It remains smaller than in solid particles of similar sizes because of a partial misalignment of particle superspins in the clusters (Figure 3.4 h). Figure 3.4 g reveals the formation of global superspins with moments μ as the effective exchange coupling in the clusters (42 nm) is changed within J_{eff} between 0 to 5 kcal/mole. At moderate exchange coupling of J_{eff} between 0.5 to 1 kcal/mole, the global superspin is developed and its magnitude is only slightly reduced from what would be expected in a bulk particle of similar diameter, as shown in Figure 3.4 d. These results underline that tuning the exchange coupling between nanocrystals can trade off against the physical dimensions of their assemblies: both features can be used to optimize the overall susceptibility (Figure S3.16). While the simulations can help explain the qualitative trends observed in the susceptibility results, they predict an initial magnetic susceptibility two times larger than what we measured in our 45 nm diameter Clusters. These results suggest that imperfections in the experimental materials are present. We may be able to further increase assembly susceptibility through manipulation of their exchange constants, or alternatively improvement in the crystallographic alignment of the individual nanocrystals across the entire cluster.

Even though we may not have reached the theoretical limit of giant susceptibility, we anticipate that the gains we have realized would still be valuable to technologies that seek to heat, image, and move magnetic materials. We first confirm the size- and morphology-

dependent susceptibility trends found in solid samples are also present, and larger, in the dilute aqueous suspensions relevant for applications (Figure S3.10). The initial DC susceptibilities of clusters in liquids are over 400, compared to 90 in the solid state. This is not surprising as cluster rotation and field-induced aggregation can both lead to enhancements in DC susceptibility.^[26] Also important is that our prior analysis centered on DC susceptibility, yet for applications in heating and imaging the applied magnetic field is alternating up to about a kilohertz. We elected not to present a full characterization of the frequency dependent behavior as DC and AC susceptibilities are well known to be related. At frequencies below a MHz in water, for example, we expect a linear relationship between DC and the relevant AC susceptibility.^[34]

3.5 The biomedical applications of clusters

We find that gains in the initial DC magnetic susceptibility of these materials translates into improved magnetic nanoparticle heating. Magnetothermal heating can be applied to problems as diverse as cancer treatment and brain stimulation as magnetically labelled tissues, cells, or sub-cellular structures can be heated selectively in a non-invasive manner.^[4, 6, 20, 35] This efficiency of this process is frequently quantified by the specific absorption rate (SAR) and we show in Figure 3.5 c that the SAR of these assemblies tracks their initial DC susceptibility.^[36] Magnetic heating is not a simple technology to implement as the production of magnetic fields large enough to ensure meaningful heating requires high wattage power sources, cumbersome metal coils, and efficient cooling systems.^[37] We reason the magnetic field application would be greatly simplified using highly susceptible clusters and permit new approaches to applying magnetic fields. As an example, these highly susceptible nanomaterials could be readily heated by fringe fields located on top of

electromagnetic coils obviating the need to place samples inside of narrow bore coils (Figure S3.17). We have also designed and applied a compact, portable, battery-operated device capable of heating a solution of highly susceptible clusters by 6 degrees with exceedingly low fields (Figure 3.5 a and b, $H = 3.2 \text{ kA/m}$ or 40 Oe , $f = 130 \text{ kHz}$). We have applied these portable devices inside of tissue culture incubators, demonstrating magnetothermal destruction of HeLa cells only when highly susceptible clusters are present (Figure 3.5 d and Figure S3.18). Clusters of other sizes as well as isolated magnetic nanoparticles have no measurable biological effects under portable magnetothermal heating conditions.

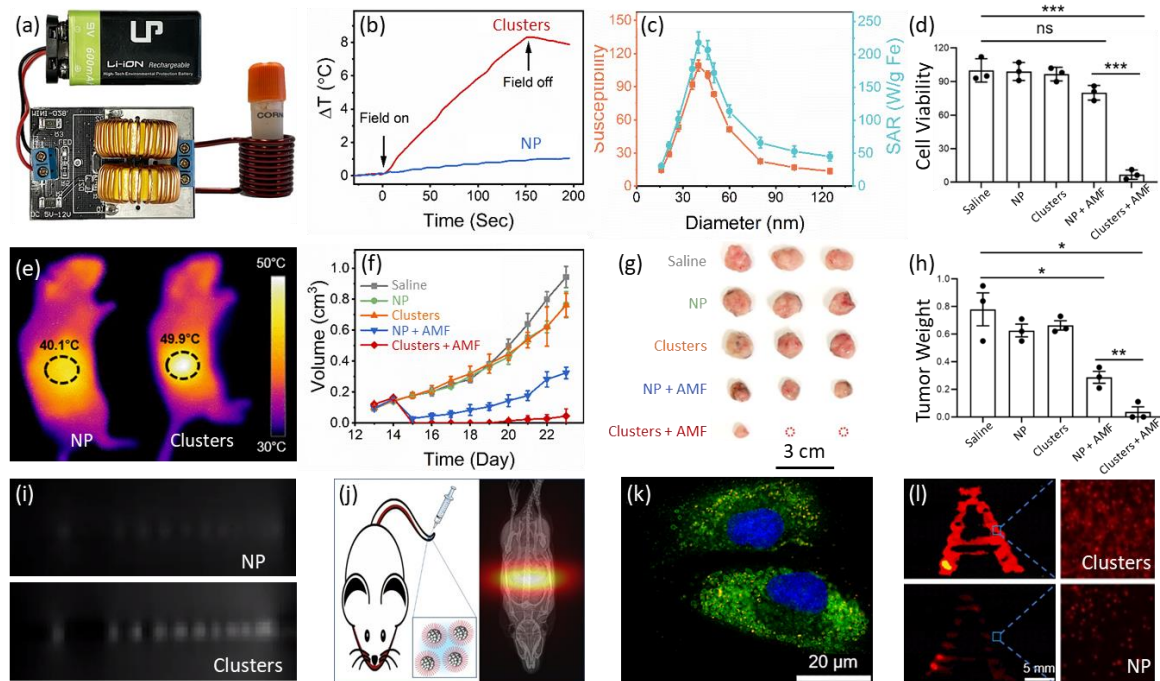


Figure 3. 5. Clusters are much more effective in applications that use external magnetic fields to heat, move or image. (a-d) Clusters make wearable/portable magnetic heating device possible. (a) Photograph of the of the battery-operated magnetic hyperthermia system portable magnetic heating device powered by batteries. (b) Heating profile of iron oxide clusters or nanoparticles solutions in the battery-operated magnetic hyperthermia system ($H = 3.2 \text{ kA/m}$, $f = 130 \text{ kHz}$). The concentration of iron in the solution is 4 mg/mL . (c) SAR and initial susceptibility of the clusters as the functions of the cluster diameters. The change of SAR and initial susceptibility of the clusters with diameter show similar

trends, suggesting the SAR of clusters is related to their initial susceptibility. (d) Cell killing effect of the clusters and nanoparticles in the battery-operated magnetic hyperthermia system. Results show that clusters are much more efficient than nanoparticles in killing tumor cells. HeLa cells were used as an example. (e-h) Clusters enables the elimination of tumors in mice using iron oxide nanomaterials under clinically relevant alternating magnetic field. (e) Infrared thermal images of tumor-bearing mice after treatments with clusters and nanoparticles. (f) The change of tumor volume with time after intratumoral injection of 60 μ L of iron oxide nanoparticles or clusters solution (7.5 mg Fe/mL) and treatment for 1 hour under AMF (9.35 kA/m, 325 kHz). (g) Photographs of excised tumors at the end point for different treatment groups. (h) Weights of excised tumors at the end point for different treatment groups. (i-j) Clusters as the tracer of magnetic particle imaging (MPI). (i) MPI projection images using iron oxide clusters or nanoparticles. (j) The MPI graph of a mouse using iron oxide clusters as the tracer. (k-l) Magnetic targeting of cells. (k) Fluorescent image of human mesenchymal stem cells loaded with clusters; blue, nuclei; green, lysosome; red, DiI-clusters. The image shows that the clusters were localized in the lysosome of cells. (l) Fluorescent images of MSCs loaded with iron oxide nanoparticles or clusters attracted by a magnetic letter. The magnetic field strength is smaller than 5 mT. The cells were labeled with diI. Top, MSCs loaded with clusters (38 nm) Bottom, MSCs loaded with isolated nanocrystals (15 nm). The results show that clusters are much more efficient than nanocrystals in magnetic targeting of cells.

The robust colloidal stability of the clusters makes them suitable for many biomedical applications. Figure 3.5 illustrates how a clinically safe alternating magnetic field could be used to completely eradicate tumors in mice treated with highly susceptible clusters. Magnetic hyperthermia is difficult to achieve in-vivo given the larger working distances, and subsequently lower external field strengths, available to interact with magnetic nanoparticles. As a result, magnetothermal ablation of tumors in rodent models has required either that researchers use ferrite nanomaterials or apply clinically unsafe fields.^[20, 38, 39] We determined the anti-tumor efficacy of clusters using C57BL/6N mice with subcutaneous MC-38 tumors as a model. When the tumor volume reached $\sim 200 \text{ mm}^3$, the mice received an intratumoral injection of isolated nanoparticles or clusters suspended in saline. The mice were then treated for one hour under an alternating magnetic field of $H=9.35 \text{ kA/m}$ (117 Oe) and $f=325 \text{ kHz}$. The tumor temperature was increased to $50 \text{ }^\circ\text{C}$ and

40 °C by clusters and nanoparticles, respectively (Figure 3.5 e and Figure S3.19). The hematoxylin and eosin (H&E) stained tumor sections show clusters exhibited much more significant tumor tissue damage than isolated nanoparticles (Figure S3.20 a). Mice treated with highly susceptible clusters had complete eradication of their tumors compared to a sham control and those treated with isolated nanoparticles (Figure 3.5, f-h). The body weight and the major organs of the mice did not show noticeable change after treatment, suggesting the safety of the treatment (Figure S3.20 b and Figure S3.21). While more expansive toxicology work would of course be required for further development, we note that the FDA currently approves nine different formulations of iron oxide particles as MRI imaging agents several of which have morphologies comparable to those of the clusters.^[21]

Supersusceptible magnetic clusters are also effective as tracers in magnetic particle imaging (MPI). MPI is a background-free method for detecting magnetic material in bulk samples through local changes in material magnetization induced by applied fields typically operating in the kilohertz range.^[3, 40] One obstacle for the clinical application of MPI is its low spatial resolution. Linear response models for the MPI imaging process predict that tracers with greater magnetic susceptibility should be more detectable, and this advantage can be used to improve the spatial imaging of biological samples.^[40, 41] Our experimental results qualitatively confirmed this prediction (Figure S3.23) and show the FWHM of the MPI point spread function is optimized for clusters with dimensions between 35 and 45 nm. Shown in Figure S3.23 is the MPI point spread function (PSF) and the spatial resolution as found from the PSF. Resolution improves with particle susceptibility and samples with the largest susceptibility offer spatial resolution two times better than that found with the commercial MPI tracer VivotraxTM (Figure 3.5 i). The improved

performance of the highly susceptible particles was also observed in-vivo (Figure 3.5 j) where bolus injections resulted in rapid liver clearance in rodent models.

Finally, we explore how the giant susceptibility of the clusters could enable the magnetic capture of cells using very low magnetic fields. Capture of various cells with magnetic nanomaterials is important for many *in vitro* and *in vivo* applications and the purification of stem cells has received recent attention in this regard.^[2, 42, 43] These separations are limited by the need to generate large magnetic fields in order to affect rapid separations.^[5, 44] Stem cells incubated with clusters could readily take up these materials within 2 hours (Figure 3.5 k and Figure S3.24). Once labelled, the cells can be captured using extremely low magnetic fields (< 5 mT or 4 kA/m) such as those found in the inexpensive magnetic composites used in toy magnet letters. Clusters or isolated nanoparticles were loaded into human mesenchymal stem cells with 1 pg Fe/cell by co-incubation with the materials (Figure 3.5 k). Notably no cytotoxicity was observed for the clusters (Figure S3.25). Cell culture plates were then placed on top of a 1 cm “A” magnetic letter. Within 15 minutes red fluorescence from the labelled stem cells was apparent on the outline of the letter for samples preincubated with highly susceptible clusters whereas virtually no cells were observed for samples exposed to isolated nanoparticles (Figure 3.5 l).

3.6 Conclusion

Magnetic susceptibility exhibits a striking size-dependence in both isolated nanoparticles and clustered assemblies of iron oxide nanocrystals; it is optimized in the largest volume superparamagnetic materials and falls dramatically once blocked single domain behavior develops. For cluster dimensions of approximately 40 nm, the initial magnetic susceptibility is an order of magnitude larger than smaller clusters and isolated nanocrystals.

We term these systems “giant susceptibility”. A similar size-dependence was observed for isolated iron oxide nanoparticles although the optimized susceptibility was much lower and peaked at smaller dimensions. Micromagnetic simulations of these aggregates illustrate the importance of moderate exchange coupling between primary particles in clustered materials; because of this interaction these aggregates remain superparamagnetic up to a larger volume than isolated nanocrystals yielding larger susceptibilities. These highly susceptible clusters have superior properties in both magnetic capture, magnetic particle imaging as well as for magnetic heating applications. Their exquisite sensitivity to applied fields makes it possible to apply portable, battery-operated devices to the inductive heating of biological materials as well as inexpensive refrigerator magnets to the capture of live cells containing the particles.

3.7 Experimental and Simulation

The in vitro and vivo studies of the clusters were performed by Dr. Qingbo Zhang and Dr. Linlin Zhang from Rice University. The Monte Carlo (MC) simulations of our materials were performed by Dr. Sanoj Raj and Prof. Petr Král from University of Illinois, Chicago. The magnetic particle imaging studies were performed by Dr. Benjamin Fellows, Chinmoy Saayujya, Dr. Prashant Chandrasekharan and Prof. Steven Conolly from University of California, Berkeley.

3.7.1. Nanomaterial preparation

Materials and Reagents. Iron acetylacetonate ($\text{Fe}(\text{acac})_3$ 99%), oleic acid (technical grade, 90%), benzyl ether (98%), triethylenetetramine (>97%), hydroxylamine HCl, sodium hydroxide, calcium sulfate hemihydrate (>97%), Ethylene glycol (anhydrous, 99.8%),

Iron(III) Chloride Hexahydrate ($\text{FeCl}_3 \cdot 6\text{H}_2\text{O}$, ACS reagent, 97%), Urea (ACS reagent, 99.0%), Azobisisobutyronitrile (AIBN, 98%), Acrylic acid (anhydrous, contains 200 ppm MEHQ as inhibitor, 99%), 2-Acrylamido-2-methylpropane sulfonic acid (AMPS, 99%), dimethylformamide (DMF, anhydrous, 99.8%), dimethyl sulfoxide (DMSO, anhydrous, $\geq 99.9\%$), 3,4-dihydroxyphenethylamine hydrochloride (Dopamine), methoxypolyethylene glycol amine (PEG-NH₂, M_w = 5,000), Poly(maleic anhydride-alt-1-octadecene) (PMAO, M_w = 30,000), triethylamine, iron standard solution ($\text{Fe}(\text{NO}_3)_3$ in HNO_3 0.5 mol/L, 1000 mg/L Fe) Certipur®, 3-(2-Pyridyl)-5,6-diphenyl-1,2,4-triazine-*p,p'*-disulfonic acid monosodium salt hydrate (FerroZine™ Iron Reagent), ammonium acetate (for molecular biology, $\geq 98\%$), hydroxylamine hydrochloride (99.995% trace metals basis), poly(ethylene glycol) methyl ether methacrylate (M_w = 500), and sodium nitrite (ACS reagent, $\geq 97.0\%$) were purchased from Sigma-Aldrich. Polyacrylic acid sodium salt (PAA, M_w = ~6,000) was from Polyscience Inc. 1-ethyl-3-(3-dimethylaminopropyl)carbodiimide hydrochloride (EDC), sulfuric acid (ACS grade, 98%), hydrochloric acid (ACS grade, 37%) and hydrogen peroxide (30%) were purchased from Fisher Scientific. 1,2-Distearoyl-sn-glycero-3-phosphoethanolamine-N [methoxy(polyethylene glycol)-2000] (ammonium salt) (DSPE-PEG2000) were purchased from Avanti Polar Lipids. All the chemicals were used as received.

The synthesis of the clusters with various cluster diameters and primary nanocrystal diameters and their surface functionalization with polysulfonate can be found in Chapter 2.

Synthesis of Isolated iron oxide nanoparticles. Isolated iron oxide nanoparticles are prepared by thermal decomposition of iron precursor. In a typical synthesis of 5 nm nanoparticles in diameter, iron acetylacetonate (12 mmol), 1,2-tetradecanediol (60 mmol),

oleic acid (72 mmol), oleylamine (72 mmol), and benzyl ether (60 mL) are mixed in a round-bottom flask and heated at 100 °C for 1 hour under vacuum. Then, the temperature of the solution is increased to 200 °C and maintained for 2 hours with argon flow. Finally, the temperature of the reaction mixture is increased to 300 °C and maintained for 1 hour. The temperature ramping rate is set at 5°C/min. The synthesized nanocrystals are purified by repeated precipitation with ethanol and dispersion with toluene. Larger iron oxide nanocrystals could be synthesized by seeded growth from the 5 nm nanocrystals or varying the concentration of the reactants and temperature of the synthesis. The as-synthesized iron oxide nanoparticles are coated with oleic acid and are dispersed in toluene.

Phase transfer of iron oxide nanoparticles to water. The isolated iron oxide nanoparticles are transferred into water by coating the nanocrystals with poly(ethylene glycol). In brief, toluene solution of iron oxide nanocrystals (2 mg/mL, 10 mL) and chloroform solution of DSPE-PEG (4 mg/mL, 10 mL) are mixed in a round bottom flask under magnetic stirring. 40 mL DMSO is added to the mixture at a rate of 1 mL/min using a syringe pump. Then the toluene and chloroform are removed using a rotvap. 32 mL deionized water is then slowly added to the solution using a syringe pump. DMSO is removed through using a centrifugal filter (Vivaspin 20, 100 kDa). Free DSPE-PEG in the solution is further removed through ultracentrifugation. The product is washed 3 times using water. Finally, the solution is passed through a 0.2 µm syringe filter to remove the aggregates. The iron oxide nanoparticles are finally coated with PEG and dispersed in water.

3.7.2. Structural characterizations

Transmission Electron Microscopy (TEM). TEM micrographs, high resolution TEM (HRTEM) micrographs, and selected area electron diffraction (SAED) patterns of the

samples are acquired using a JEOL 2100 Field Emission Gun Transmission Electron Microscope at an acceleration voltage of 200 kV. The samples are prepared by evaporating 3 μ L of nanocrystal solution with a concentration of around 0.3 mg/mL on a 300-mesh carbon-coated copper grid. The diameters of clusters and primary particles are obtained by counting more than 500 clusters using the software of ImageJ.

Scanning Electron Microscopy (SEM). The SEM images of the clusters are acquired on a LEO 1530 SEM operating at an acceleration voltage of 20 kV. To prepare the SEM sample, 0.1 mL 5 mg/mL cluster solution is dropped on the SEM sample holder with a carbon conductive tab (9 mm) on top. The solution is dried overnight at room temperature.

Focused Ion Beam- Scanning Electron Microscopy (FIB-SEM). The FIB-SEM images of the clusters are acquired on a Helios 5 DualBeam Focused Ion Beam- Scanning Electron Microscopy. The sample is prepared using the same method as the SEM samples. The operating voltage of the primary beam of electrons is 15 kV.

Dynamic light scattering (DLS). The hydrodynamic diameter of the iron oxide nanocrystals is measured using a Malvern ZEN-3600 Zetasizer Equipped with a HeNe 633 nm laser (Malvern, UK) at 25 °C. To perform the measurement, 1.5 mL of the nanocrystal solution with a concentration of 0.1 mg/mL is placed in a plastic cuvette. The average size is obtained over three measurements for each sample.

Surface area analysis. The surface area of the clusters is measured using a Quantachrome Autosorb-iQ3-MP/Kr Brunauer–Emmett–Teller (BET) surface analyzer. N₂ isotherms is measured at 77K. The clusters are magnetically collected from the solution and dried at

60°C overnight. Prior to the measurement, the clusters powder is outgassed overnight under vacuum at 200°C.

Inductively coupled plasma atomic emission spectroscopy (ICP-AES). The concentration of iron in the solution is measured using an inductively coupled plasma atomic emission spectroscopy (ICP-AES) equipped with an auto sampler (Perkin-Elmer). The samples are prepared by digestion of iron oxide nanocrystals using hydrochloric acid and H₂O₂. 0.1 mL of sample is mixed with 0.89 mL of HCl and 0.01 mL of H₂O₂. The solution gradually becomes clear and turns yellow with the digestion of iron oxide. The resulting solution is then transferred to a 10 mL volumetric flask and diluted to 10 mL using pure water.

3.7.3. Magnetic characterizations

The initial magnetization curve and hysteresis loop of the iron oxide nanocrystals are measured using a vibrating-sample magnetometer (Lake Shore 7400 Series VSM). The magnetic properties of the samples in the form of solid are measured in a capsule. The nanocrystals are dispersed in a solid matrix of calcium sulfate with the volume ratio of 1:300 to prevent the movement of nanocrystals and minimize the dipole-dipole interactions between nanocrystals. To measure the magnetic properties of the iron oxide nanocrystals in solutions, 80 µL solution is loaded in a liquid sample holder. The concentration of the iron oxide is measured using ICP-AES. The initial susceptibilities of the samples were determined from the magnetization of the samples at 1 gauss using linear regression analysis.

A superconducting quantum interference device (Quantum Design MPMS) is used to measure the zero-field-cooled (ZFC) - field-cooled (FC) magnetization curve, AC

susceptibility, direct current demagnetization (DCD) curve, and the relaxation curve of the samples. The nanocrystals are dispersed in a solid matrix of gypsum to prevent movement of nanocrystals and minimize the dipole-dipole interactions between nanocrystals. The ZFC-FC measurements are performed with a magnetic field of 10 Oe. AC susceptibility is measured within a temperature range from 10 to 370 K and with a magnetic field of 4 Oe. The DCD curve is measured by saturating the sample and then measuring the remanence after applying reverse fields of different field strength. To perform the magnetization relaxation measurements, the sample is first saturated in a positive field (50 kOe). Then a negative reverse field is applied to bring the sample into the switching region and the magnetization decay is recorded as a function of time for 75 minutes.

The magnetic viscosity coefficient of the iron oxide nanocrystals is determined by fitting the magnetization relaxation data to the following equation:

$$M(t) = Cons \pm S\left(\frac{t}{t_0}\right)$$

where M is the magnetization, S is the magnetic viscosity coefficient, t is the time, t_0 is the reference time, and the plus or minus sign describes whether M is increasing or decreasing with time. The irreversible susceptibility of the sample is obtained by differentiating the measured DCD curve. The activation volume of the samples is calculated using the following equation.

$$V_{act} = 12 \frac{k_B T \chi_{irr}}{M_s S}$$

where k is the Boltzmann constant, T is the temperature, χ_{irr} is the irreversible susceptibility, M_s is the saturation magnetization of nanomaterials, and S is the magnetic viscosity coefficient.

3.7.4. Monte Carlo simulations

The Monte Carlo (MC) code was used and added to the pool of standard interactions of nanoparticle (NP) superspins (magnetic anisotropy, dipole-dipole, and Zeeman coupling), as well as the exchange interactions between different-NP superspins to describe the magnetic properties of moderately exchange-coupled magnetic magnetite clusters.

In a local-dipole approximation, the global spins in each (single-domain) nanoparticle are represented by a superspin located in the NP center. The magnetic interactions include the Zeeman coupling of the NP-superspins with the external magnetic field, the magnetocrystalline anisotropy (MA) of superspins within NPs, the dipole-dipole (d-d) coupling between NP-superspins and the exchange interactions between superspins of individual NPs. The total energy of an ensemble of NPs is given by

$$E_T = \sum_{i=1}^{N_p} (E_i^Z + E_i^A) + \sum_{i=1}^{N_p} \sum_{j=i+1}^{N_p} (E_{ij}^{dd} + E_{ij}^{ex})$$

where E_i^Z is the Zeeman energy and E_i^A is the MA energy of an isolated NP in a given orientation with respect to the external magnetic field. The Zeeman energy is given by

$$E_i^Z = -K_z(\vec{H} \cdot \vec{M}_i)$$

where $K_z = 4.33 \cdot 10^{-4} \text{ kcal/mol}$, $\vec{H} = (0,0,H_0)$ is the external magnetic field vector in Gauss units and \vec{M}_i is the magnetic dipole unit vector. The magnetocrystalline anisotropy

of NPs is approximated by a quartic term of the bulk magnetite (Fe₃O₄) with a Fd3m crystal structure

$$E_i^A = K_{A1} \left[(M'_{ix} M'_{iy})^2 + (M'_{ix} M'_{iz})^2 + (M'_{iy} M'_{iz})^2 \right]$$

where $K_{A1} = 0.117 \text{ kcal/mol}$ is the quartic-order anisotropy constant and $M'_{ix}, M'_{iy}, M'_{iz}$ are the $\hat{x}, \hat{y}, \hat{z}$ components of the magnetic dipole unit vector in the reference NP coordinates. Here, higher orders of the bulk MA energy and its NPs-shape corrections are neglected. In iron oxide, the quartic term has a cubic symmetry with easy and hard magnetization axes oriented along the cube body diagonals and edges, respectively. The simulations give the same results for cubic and spherical NPs of the same volume, since their magnetic anisotropy dependences are the same (shape anisotropy isn't considered).

Then, dipole-dipole coupling energy between pairs of NP-superdipoles is given by

$$E_{ii}^{dd} = K_d \left[\frac{\vec{M}_i \cdot \vec{M}_j}{|\vec{r}_{ij}|^3} - \frac{3(\vec{M}_i \cdot \vec{r}_{ij})(\vec{M}_j \cdot \vec{r}_{ij})}{|\vec{r}_{ij}|^5} \right]$$

Where $K_d = \frac{\mu_0 m_s^2}{4\pi} = 0.208 \text{ kcal/mol} * a^3$ and the distance between superdipoles ($|\vec{r}_{ij}|$) is measured in units of a (cuboid edge length), $m_s = M_s \cdot V = 3.0 \cdot 10^{-20} \text{ A} \cdot \text{m}^2$ is the intrinsic magnetic moment of a homogeneously magnetized NP (5 nm NC), $M_s = 480 \text{ kA/m}$ is the saturated magnetization of a bulk magnetite, and V is the NP volume. The saturation magnetization in magnetite SPM NPs can be smaller than in bulk magnetite due to the presence of non-collinear (canted) spins showing a spin-glass-like behavior. We assume that the saturation magnetization of the modeled NPs is ~40-50% smaller than in bulk magnetite because of spin canting within a ~1 nm thick surface layer.

Magnetic structures of materials are largely controlled by the exchange interactions between spins sitting on neighboring atoms. When NPs recrystallize, the exchange interactions between groups of atoms in neighboring NPs are reestablished and need to be considered. This effective coupling between neighboring NPs can be approximately evaluated from the formula,

$$E^{ex} = -J_{atomic} \sum_{ij} \vec{s}_i \cdot \vec{s}_j \cong -J_{eff} \vec{S}_i \cdot \vec{S}_j$$

where J_{atomic} is the atomic exchange constant and \vec{s}_i, \vec{s}_j are spins of neighboring atoms present at a boundary layer between the sintered neighboring NPs. Since the atomic spins within each NPs can be assumed to be parallel and oriented as the superspins \vec{S}_i, \vec{S}_j of the neighboring NPs, the exchange energy can be approximately evaluated from the second formula, where J_{eff} is an effective exchange constant for the neighboring NPs. The exchange energy is larger for larger for NPs having more atomic spins at their shared boundary.

The MC algorithm computes the energy difference, ΔE_T , between two superspin configurations of all NPs within the clusters before and after the proposed local motion of NP-superdipoles. Using the Metropolis criterion, the new configuration is accepted when $\Delta E_T \leq 0$ or when a random number in the interval $[0, 1]$ is smaller than $e^{-\frac{\Delta E_T}{kT}}$, otherwise, the old configuration is counted and the algorithm proceeds. In a MC cycle, the algorithm is run 10 times over all the NP superdipoles (looped in randomized order), and a new configuration is accepted based on the Metropolis criterion.

Note that MC codes can efficiently search microstates (along MC trajectories) which are very likely populated within the equilibrium ensembles representing the systems. In contrast, periodically re/magnetized systems can occupy kinetically trapped states, which characterize their non-equilibrium magnetic properties. Since MC methods drive systems towards equilibrium, irrespective of the barrier sizes, to find such trapped states by MC methods, we need to somewhat limit the sampling to prevent the system to easily pass non-thermal barriers, as in experiments. When we tested the MC sampling in the present systems with BS (hysteresis), we found that the coercivity was gradually disappearing with the number of MC sampling steps. To clearly distinguish between SPM and BS states, we have limited the superdipole angle search within 20° . Moreover, we used 300 MC cycles for the equilibration of the systems and the next 200 MC cycles for averaging of the configurations of all the NPs local superdipoles and to plot the magnetization (other approaches were also tested). In the simulations, the magnetic field was changed by 2 Gauss steps.

Effect of dipole-dipole and exchange interactions on the magnetic properties of Clusters

To understand the effect of different interactions on the susceptibility of clusters, the magnetization of 42 nm clusters of 5 nm NPs with separately turned on/off exchange and d-d interactions was simulated. It turns out that the exchange interactions ($J_{\text{eff}} = 0.6$ kcal/mol) can affect the magnetic susceptibility much more than the relatively weak d-d interactions. When the exchange interactions are turned on, the susceptibility is large, when they are turned off (NPs do not overlap), the d-d interactions dominate, and the susceptibility is small.

To examine the effect of d-d interactions on the susceptibility of clusters in matrices, we have simulated systems composed of separated 13 nm large NPs, each representing one fictive cluster. The simulated systems 1 and 2 have randomly oriented NPs, while system 3 has NPs with their easy axis aligned parallel to the external magnetic field. The unfavorable d-d interactions between close NPs (system 1) give a smaller susceptibility than favorable or negligible d-d interactions between separated NPs (systems 2 and 3); every NP is meant to be one cluster. These results can explain the experimental observations for clusters embedded in solids, silica, and liquids. When clusters are in the solid matrix, they are randomly arranged at distances of $D < 5$ nm and fixed, so that unfavorable d-d interactions between them reduce their susceptibility (system 1). In contrast, randomly arranged but fixed clusters in silica ($D > 200$) have a larger susceptibility (system 2). Finally, free clusters can get arranged in an energetically favorable manner (system 3) by rotation, translation, and chain formation (in the magnetic field), so that d-d interactions can enhance their susceptibility.

Angular distributions of superspins at different effective exchange constants

Figure 3.4 i shows the angular distributions of superspins in 42 nm clusters with different J_{eff} . The easy axis of NPs was parallel to the external magnetic field and superspins were initially aligned along it with the help of a short simulation done under extreme conditions of $J_{\text{eff}} = 10$ kcal/mol and $H = 100$ Gauss. Then, we ran separate simulations for different J_{eff} ($H=0$) and obtained (after 50 MC steps) the distributions shown in Figure 3.4 i. As expected, the distributions are narrower for larger J_{eff} and wider for smaller J_{eff} . These distribution widths, which correspond to partly equilibrated superspin orientations, provide

some guidance in our estimation of the freedom and entropy of superspins contributing to the free energy barrier.

Calculation of energy barriers and magnetic moments

To understand the SPM-BS transitions in the studied systems, we have calculated the remagnetization free energy barriers for clusters and solid particles of different sizes. According to the Neel's relaxation theory, a free energy barrier of $E_b \sim 20-25 k_B T$ can still be overcome in reasonable timescales, where k_B is the Boltzmann constant, and T is the room temperature. Therefore, we have assumed that a given system is in an SPM state if $E_b < 20 k_B T$, and in a BS state if $E_b > 20 k_B T$. In solid particles, we have calculated the energy barriers (just enthalpy) directly from $E_b = KV$, where $K = 1.04 \times 10^4 \text{ J/m}^3$ is the magnetic anisotropy constant of magnetite, V is the volume of the magnetic material. However, it is not easy to calculate these energy barriers in clusters. Therefore, we have first simulated in clusters their Zero-field cooling (ZFC) curves (see below), giving their blocking temperatures T_B at the curve maxima, which could then be related to the energy barriers by $E_b = 25 k_B T_B$.

The theoretical energy barriers, E_b , and magnetic momenta, μ_{eff} , of cubic solid particles and clusters of different sizes are simulated. In solid particles, these parameters are calculated from $E_b = KV$ and $\mu_{\text{eff}} = M_s V$, where M_s (480 kA/m) is the saturation magnetization. To calculate the effective energy barrier in clusters, E_b , we have simulated their zero-field cooling (ZFC) curves. The temperature-dependent simulations are performed in two steps. In the first step, a simulated annealing is performed starting from a temperature, T_{max} , which higher than T_B , so that the particles are initially in SPM states.

The system is cooled down to a very low temperature at zero magnetic field ($H = 0$ Oe). In the second step, a small cooling field ($H = 10$ Oe) is applied to the system, which is slowly heated up to T_{\max} while the magnetization is recorded with temperature. In these processes, we have changed the temperature 5 K increments, used 300 MC cycles for the equilibration of the system at a given temperature, and the next 200 MC cycles for averaging the configurations of the NPs dipoles (averaged over 9-ROC). From the T_B maxima in ZFC, obtained for clusters of different sizes, we have calculated the energy barriers, $E_b = 25 k_B T_B$ for different sizes of clusters with $J_{\text{eff}} = 0.6$ kcal/mol. To obtain the effective magnetic momenta (μ_{eff}) for clusters of different sizes, as shown in Figure 3.4 a, we have equilibrated the systems for 300 MC steps at $H = 0$ Gauss and calculated the average vector sum of the superdipoles in the next 200 MC steps.

To also understand the effect of J_{eff} on the barrier E_b , we have simulated ZFC (averaged over 100-ROC) for 42 nm clusters with different J_{eff} for a fixed size of clusters. We can see that E_b monotonously increases with J_{eff} with an average slope of 10 ($E_b \sim 20$ kcal/mol for $J_{\text{eff}} \sim 2$ kcal/mol).

It is important to note that, J_{eff} dictates whether a given cluster will in a paramagnetic, superparamagnetic, or ferromagnetic state at a fixed temperature. Within the cluster, we have two level of superparamagnetic behavior. First, on the level of NPs superspin, and the other on the level of cluster superspin due to the correlation (J_{eff}) of NPs superspin. This phenomenon is like what is observed in SPM NPs (atomic spins coupled together which moves like one big spin). At the given J_{eff} for a given cluster, there exists a maximum temperature after which the cluster will go from SPM to paramagnetic state. This temperature is analogous to the Curie temperature on the level of superspins.

Estimation of the magnetization entropy

The contribution of a magnetic entropy to the free energy barriers, E_b , is dependent on J_{eff} (restriction of superspin angles). The magnetic entropy of a single (magnetic) dipole moment is given by

$$S = k_B \int_0^{2\pi} d\varphi \int_0^\pi d\theta \sin(\theta) p_i(\theta, \varphi) \ln p_i(\theta, \varphi)$$

where k_B is the Boltzmann constant, $p_i(\theta, \varphi)$ is the probability density of the dipole moment M_i having the angle θ relative to the z-axis and the angle φ with respect to the x-axis. In equilibrium, the probability density is given by

$$p_i(\theta, \varphi) = \frac{e^{-E/k_B T}}{\int_0^{2\pi} d\varphi \int_0^\pi d\theta \sin(\theta) e^{-E/k_B T}}$$

Here, E is the total energy of the dipole moment (sum of magnetic anisotropy energy and Zeeman coupling). The integrals can be easily evaluated by Monte Carlo integration schemes.¹⁹

In our entropy estimation, we have considered isotropic systems (without magnetic anisotropy and in the absence of the external magnetic field), where the 2D (angular) probability density of unit vectors is $1/4\pi$. Then, the entropy is $S = -k_B \int_0^{2\pi} d\varphi \int_0^\pi d\theta \sin(\theta) \cdot \frac{1}{4\pi} \cdot \ln\left(\frac{1}{4\pi}\right)$. When the angles of the distribution are unrestricted, we obtain a maximum entropy of $S_{\text{max}} \sim 2.53 k_B$.

When the angles of the distribution are restricted, as in the case of their J_{eff} -coupling within the magnetic clusters, then the entropy can be estimated from $S = -k_B \int_0^\pi d\theta \sin(\theta) \cdot 2\pi \cdot$

$\frac{1}{4\pi} \cdot \ln\left(\frac{1}{4\pi}\right)$, where the angular restrictions are used in the integral limits. The entropy grows as a function of the restricted angle θ from $S = 0$ to a maximum entropy of $S_{\max} \sim 2.53 k_B$. It is important to note here that the J_{eff} is acting like a strong magnetic field. Increasing the J_{eff} will have similar effect on the entropy like increasing the external magnetic field.

We can estimate the magnetic entropy contribution to the free energy barriers in solid particles and clusters. In principle, loosely misaligned superspins can have a relatively large entropy contribution to the free energy ($G=H-TS$), which can be reduced when the superspins are more constrained during their crossing over the barrier. A 40 nm solid particle has a free energy barrier of $\Delta G = E_b \sim 95$ kcal/mol, while a 42 nm cluster formed by 249 NPs of a 5 nm diameter has $\Delta G = E_b \sim 12$ kcal/mol. We can estimate the entropy of superspins crossing the barriers. If the rotation of NP superspins is unrestricted ($\theta = 0 - 180^\circ$), then every superspin in a cluster (300 K) contributes by $TS \sim 1.50$ kcal/mol; in contrast, when the rotation is restricted ($\theta = 0 - 30^\circ$), we obtain $TS \sim 0.1$ kcal/mol. Thus, the entropy contributions are very small in solid particles, but they can be relatively large in clusters, depending on the restrictions of its superspins. A cluster with superspins having no angle restrictions ($\theta = 0 - 180^\circ$) has $TS \sim 374$ kcal/mol ($249 \times 2.53 k_B T$), while if the angles of individual superspins are restricted ($\theta = 0 - 20^\circ$) $TS \sim 11$ kcal/mol ($249 \times 0.076 k_B T$). During the crossing of the barrier, some superspins become *further* restricted, so their entropy becomes reduced (TS drops), which effectively increases the barrier height. Given the relatively small barriers present in clusters, the variation of magnetic entropy during their crossing can significantly contribute to the barrier heights.

Effect of primary particle losing contacts or being missed

In the experiments, clusters of different sizes are composed of 5 nm NPs, which are assumed to be in contact with their neighbors. However, during the self-assembly and recrystallization processes, some NPs might lose contacts or be missing (smaller overlap reduces J_{eff} within neighboring NPs). This can reduce the correlations of NP-superspines within the clusters and affect their magnetization. To understand these effects, we have simulated a 36 nm cluster (177 NPs of 5 nm size with $J_{\text{eff}} = 0.6$ kcal/mol) where randomly chosen NPs had a smaller coupling ($J_{\text{eff}} = 0.1$ kcal/mol) with neighboring NPs, missed connections ($J_{\text{eff}} = 0$ kcal/mol) with neighboring NPs, or were entirely removed. As NPs loose contacts with their neighbors or become removed, the cluster susceptibility is reduced. Interestingly, when NPs are removed the cluster, susceptibility is less affected than when they just lose their contacts.

Effect of rotated primary particles

In the above modeling, we have assumed that recrystallized NPs have their [111] easy axis (crystal structure) aligned parallel to the Clusters [111] axis. However, the crystal and supercrystal structures could be deliberately rotated with respect to each other, while recrystallization should still be possible. Such mutual rotation could provide a broad spectrum of possible clusters and porous metamaterials. We have simulated the magnetization of 42 nm clusters of 5 nm NPs simultaneously rotated with respect to the supercrystal. The [111] crystal axis (parallel to the external magnetic field) had different angles (0° , 23° and 45°) with respect to the Clusters [111] axis. We observe significant changes in the magnetization of 9-ROC, where the coercivity is decreased from 8 (0°) to 3 Gauss (45°). These results could be more pronounced at lower temperatures or in clusters formed of larger NPs.

We have also studied the effect of random NPs rotations. We simulated a 42 nm cluster of 5 nm NPs each of which was separately and randomly rotated ($J_{\text{eff}} = 1.2$ kcal/mol), and recorded magnetization of 9-ROC. The obtained results were compared with the non-random system (a 42 nm cluster of 5 nm NPs with $J_{\text{eff}} = 1.2$ kcal/mol), as described in Figure 3.4 e. BS became less pronounced (coercivity is decreased from 18 to 5 Gauss, red vs blue curve) because the anisotropic energy barrier was effectively reduced due to random orientations of NPs. In clusters with randomly orientated NPs, the total effective superspin is smaller because the superspins in individual NPs are oriented randomly, due to the random orientation of the NPs easy axis. This system behaves somewhat like a metallic glass where the structure is not crystalline, but rather it is disordered with a negligible anisotropic energy barrier.

Magnetization of isolated iron oxide nanoparticles

The MC model is used to calculate magnetization of solid magnetite nanoparticles of different sizes made from 5 nm NPs. The result shows that the solid particles are in SPM state when their sizes are below 15 nm and in BS beyond 15 nm. The MC steps used here are the same as in the porous clusters studied above and J_{eff} was chosen in such a way that we get solid particles in SPM state below 15 nm and in BS state above 15 nm.

3.7.5. Magnetic hyperthermia

Measurement of specific absorption rate of clusters

For the specific absorption rate (SAR) measurement, 1.0 mL of aqueous solution of iron oxide clusters was added to a 2 mL cryovial insulated with Styrofoam. The cryovial was placed in the center of the inductive coil, and the induction heating system was turned on

for 90 s. The temperature increase in the solution was recorded in real time with a fiber optic temperature sensor (Photon Control). The experiment was carried out under close to adiabatic conditions. The average slope of the temperature versus time plot during the first 20 s of heating was calculated by forward linear fitting for each sample and subtracted by that of water alone to compensate for the heat exchange with the environment. SAR was calculated with the following equation

$$SAR = \frac{1}{m_{Fe}} C_{sol} m_{sol} \frac{dT}{dt}$$

where m_{Fe} is the mass of iron (Fe) in the aqueous solution as determined by ICP, m_{sol} is the mass of the solvent, C_{sol} is the specific heat of the solvent ($4.184 \text{ J K}^{-1} \text{ g}^{-1}$).

In vitro magnetic hyperthermia using the portable device

HeLa cells were purchased from the American Type Culture Collection (ATCC) and maintained in Dulbecco's Modified Eagle Medium (DMEM) supplemented with 10% fetal bovine serum (FBS) at 37°C with 5% CO_2 . Around 1×10^4 HeLa cells were seeded into 96-well stripwell microplates (Corning) and allowed to attach overnight. A single well of cells was taken from the strips and placed into a 1.5 mL microcentrifuge tube. Iron oxide nanoparticles or clusters were diluted to 2 mg/mL with culture medium and added to the well. The tube was placed in a homemade inductive coil. The portable device is powered by batteries. The magnetic field strength and frequency are 3.2 kA/m (40 Oe) and 130 kHz, respectively. The cells were exposed to the alternating magnetic field for one hour followed by live/dead staining with Calcein-AM and propidium iodide (PI). Cells were imaged using ZOE Fluorescent Cell Imager (Bio-Rad Laboratories). The cell killing efficiency was

quantified immediately after the hyperthermia treatment using MTT Cell Viability Assay (ThermoFisher Scientific).

In vivo magnetic hyperthermia

All animal procedures were approved by the Institutional Animal Care and Use Committee (IACUC) at Rice University. Female C57BL/6N mice (6 weeks old) were purchased from Charles River. MC-38 cells were purchased from Kerfast and cultured in DMEM with 10% FBS. Xenograft tumors were induced by subcutaneous injection of 5×10^5 MC-38 cells into the right flank of the mice. Tumors were monitored until reaching $\sim 200 \text{ mm}^3$ in volume. The mice were anesthetized with 2% isoflurane and injected with 60 μL of either iron oxide Clusters or nanoparticles (7.5 mg Fe/mL in 5% dextrose) or saline intratumorally at 3 $\mu\text{L}/\text{min}$ using a syringe pump. The mice were placed on a polycarbonate mouse cradle inside an inductive coil (5 turns, 5.00 cm inner diameter) with the tumor centered with the coil in the axial direction. The mice was exposed to an alternating magnetic field (9.35 kA/m, 325 kHz) for one hour. The temperature of the tumor was monitored using an infrared camera (FLIR E95).

The data represent mean \pm s.d. or mean \pm s.e.m. Statistical analysis was performed using GraphPad Prism (v8.0). One-way analysis of variance (ANOVA) with post hoc Dunnett's test was used to analyze difference between groups. *P* values are indicated by asterisks in the figures. *P* value of 0.05 or less was considered statistically significant.

3.7.6. Magnetic particle imaging

Full width at half maximum measurement

Point spread function (PSF) were obtained using the arbitrary waveform relaxometer. A 40 μL test sample was excited using a 20 mT (peak-to-peak) sinusoidal excitation field at 20 kHz while under a slow-shift field moving from -100 mT to 100 mT to recreate the PSF of the tracer. The full width at half maximum (FWHM) of the tracer PSF was extracted as an indicator of tracer resolution.

Projection image

MPI projection image of a linear resolution phantom containing 35 nm clusters was imaged in the Berkeley FFL projection scanner. Aliquots of undiluted tracer were spaced between 700 μm and 3.4 mm apart, increasing at intervals of 300 μm . Acquisition was performed using a 20 kHz, 40 mT (peak-to-peak) sinusoidal excitation field under a 6.3 T/m gradient. Mild deconvolution and thresholding were performed to reduce hazing effects and present improved viewing contrast. The phantom demonstrated an in-scanner resolution of approximately 1.6 mm perpendicular to the projection axis.

Magnetic particle imaging *in vivo*

All animal procedures were approved by the Animal Care and Use Committee (ACUC) at the University of California, Berkeley. Full-body MPI projection scans were obtained on laboratory mice injected in a tail vein with 20 μL of tracer solution (5 mg/mL) and imaged 20 minutes post-injection. Images were taken in the Berkeley field-free line (FFL) projection MPI scanner by projecting along the dorsoventral axis. Acquisition was performed using a 20 kHz, 40 mT (peak-to-peak) sinusoidal excitation field under a 6.3 T/m gradient with 6 cm x 10 cm field-of-view. The MPI image was superimposed on an

X-ray projection image (kubtec XPERT 40) of the mouse for co-localization and anatomical reference.

3.7.7. Magnetic targeting of human mesenchymal stem cells

Cellular uptake of clusters

Human mesenchymal stem cells (hMSCs) were purchased from Lonza and maintained in Mesenchymal Stem Cell Growth Medium (Lonza) at 37°C with 5% CO₂. The cells were cultured in a 1-well glass chamber until confluence. The clusters or isolated nanoparticles were diluted to 100 µg/mL with culture medium and added to the chamber. The chamber was placed on a magnetic plate to increase cellular uptake. The Clusters and nanoparticles were incubated with cells for 0.5 hour and 4 hours, respectively. Then, the cells were washed twice with PBS to remove extracellular nanocrystals and detached with trypsin-EDTA for magnetic targeting. The average amount of nanocrystal uptake is ~ 1pg Fe/Cell for both Clusters and nanoparticles.

Magnetic targeting of stem cells *in vitro*

The hMSCs loaded with clusters or isolated nanoparticles were suspended in growth medium and added to a 1-well glass chamber. The chamber was placed on an A-shape fridge magnet and incubated for 30 min at 80 rpm on a digital shaker (Southwest Science). Then, the floating cells were removed. The cells that were attracted by the fridge magnet were stained with cell membrane dye DiI (ThermoFisher Scientific) and imaged using IVIS Imager (Perkin Elmer).

Subcellular localization of clusters

The subcellular localization of iron oxide nanocrystals in hMSCs were examined using both fluorescence microscope and transmission electron microscope (TEM). hMSCs were seeded in a 2-well glass chamber and allowed to attach overnight. For fluorescence microscopy, the iron oxide nanocrystals were labeled with DiI. The lysosomes were labeled with green fluorescent protein (GFP) by incubating the cells with CellLight Lysosomes-GFP (ThermoFisher Scientific) for 16 h. The cells were incubated with DiI-labeled nanocrystals (100 $\mu\text{g Fe/mL}$) for 2 h on a magnetic plate. The extracellular nanocrystals were removed by washing the cells twice with PBS. The nuclei were stained with Hoechst 33342 (ThermoFisher Scientific). The cells were imaged using DeltaVision fluorescence microscope (Applied Precision). For TEM examination, the cells were loaded with unlabeled nanocrystals, fixed with glutaraldehyde and osmium tetroxide, dehydrated, embedded in resin, cut into ultrathin sections (70 nm), counter-stained with aqueous uranyl acetate and lead citrate, and imaged using JEOL 1230 High Contrast Transmission Electron Microscope.

3.7.8. Cytotoxicity studies

Around 5×10^3 hMSCs were seeded in 96-well plates and allowed to attach overnight. Cells were incubated with 0, 10, 20, 50, and 100 $\mu\text{g Fe /mL}$ of clusters for 2 hours at 37 °C. The nanocrystals were then replaced with fresh culture medium. The cytotoxicity of nanocrystals was evaluated by measuring cell viability at 24 h and 48 h time points using MTT Cell Viability Assay (ThermoFisher Scientific).

3.8 Supplemental Figures and Tables

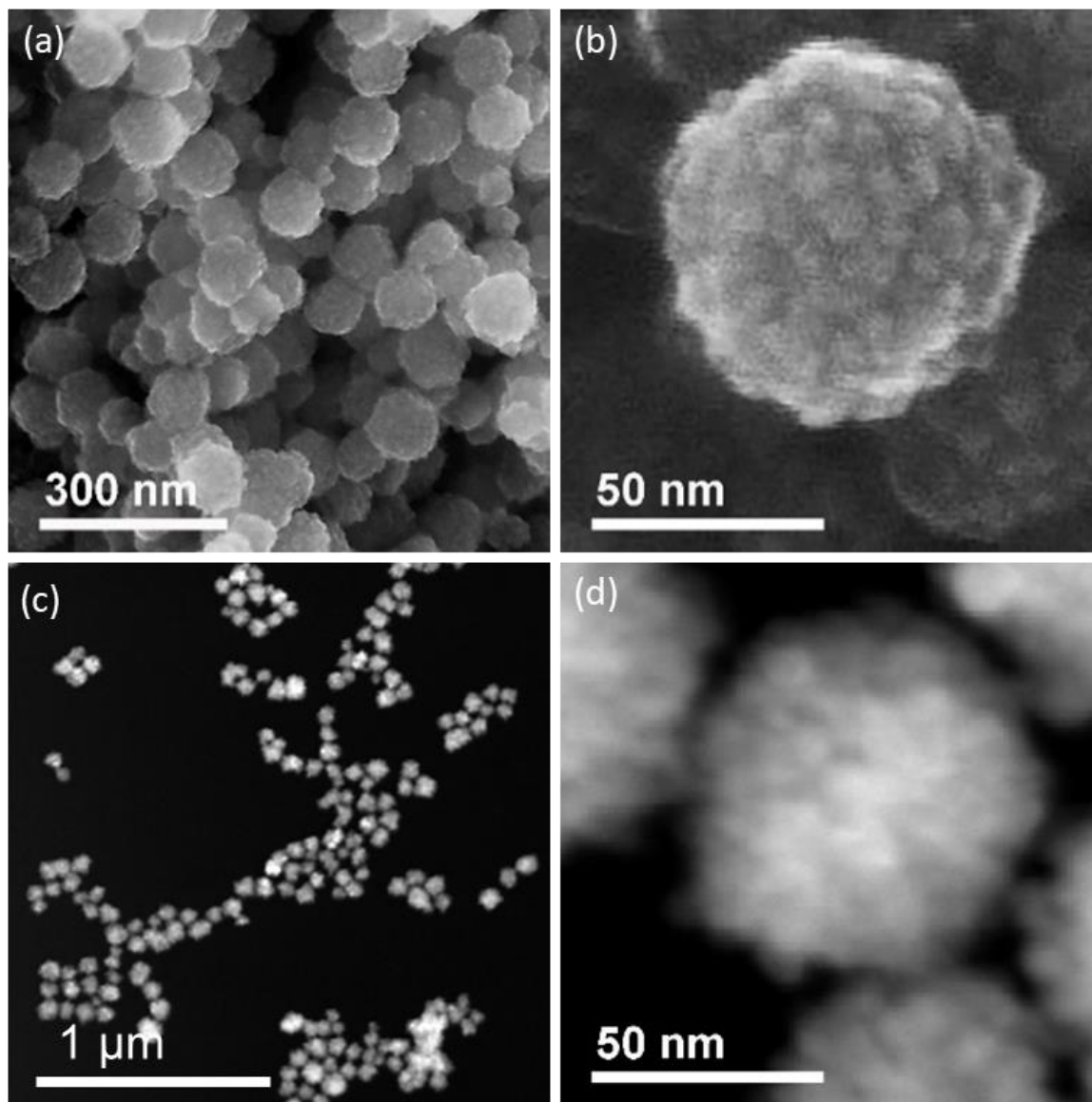


Figure S3. 1. Additional micrograph of the clusters. (a-b) SEM of the clusters with a diameter of $90 \text{ nm} \pm 8.1 \text{ nm}$. (c-d) High-angle annular dark-field scanning transmission electron microscopy (HAADF-STEM) of the clusters.

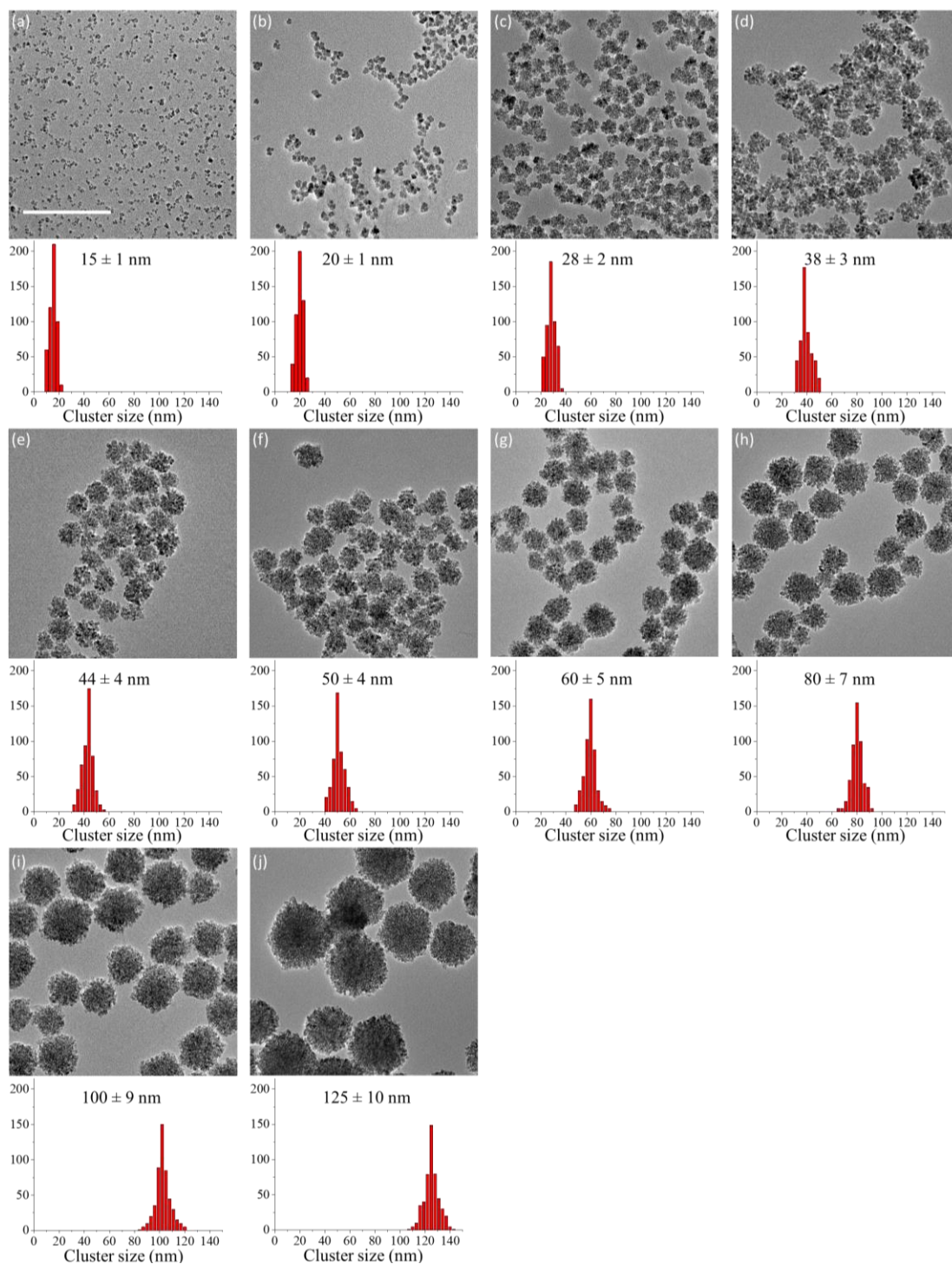


Figure S3. 2. TEM and size distributions histograms of the cluster with different cluster sizes. The primary particle size is 4 nm. For each sample, a total of 500 clusters are measured. The cluster sizes are presented as the average diameters \pm standard deviation.

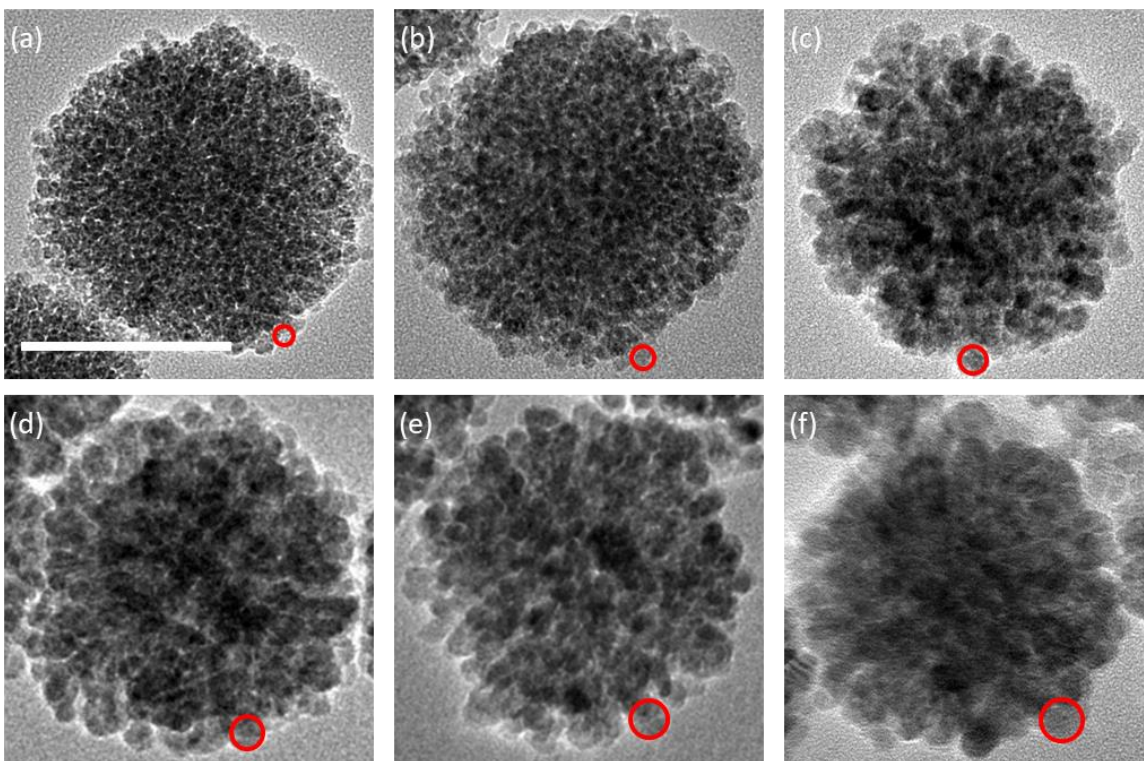


Figure S3. 3. TEM images of the cluster with different primary nanocrystal sizes. (a-f) The primary nanocrystal size is 4 nm, 5 nm, 6 nm, 7 nm, 8 nm, 9 nm, respectively. Scale bar: 50 nm. These samples have similar cluster diameter of around 80 nm.

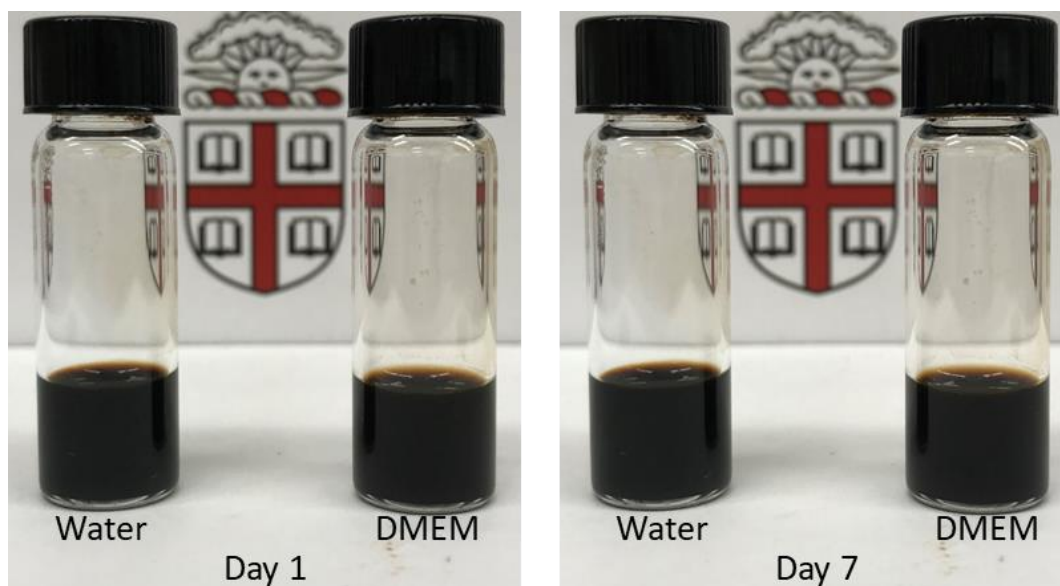


Figure S3. 4. The excellent colloidal stability of concentrated clusters in both water and cell growth media (DMEM). After one week, there was no visible aggregation of the clusters in both settings. The cluster sample has a D_c of 40 nm and d_p of 4 nm and was

coated with dopa-PAA-PAMPS-PEG. The concentration of the clusters were both 10,000 ppm in water (left) and media (right).

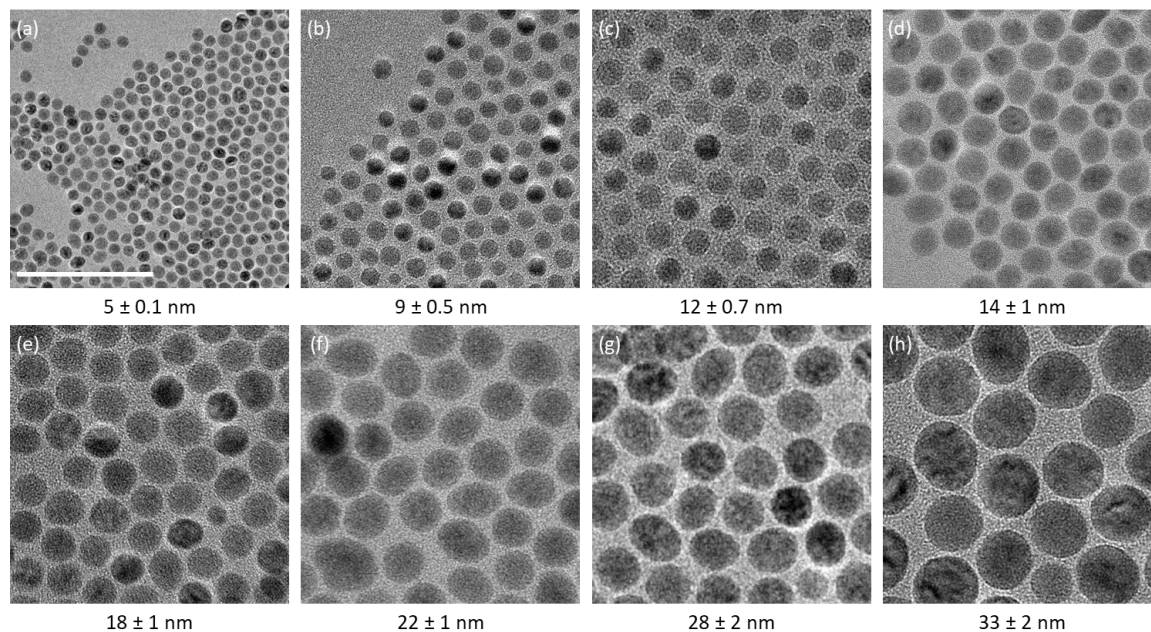


Figure S3. 5. TEM images of the iron oxide nanoparticles with different diameters. Scale bar: 50 nm.

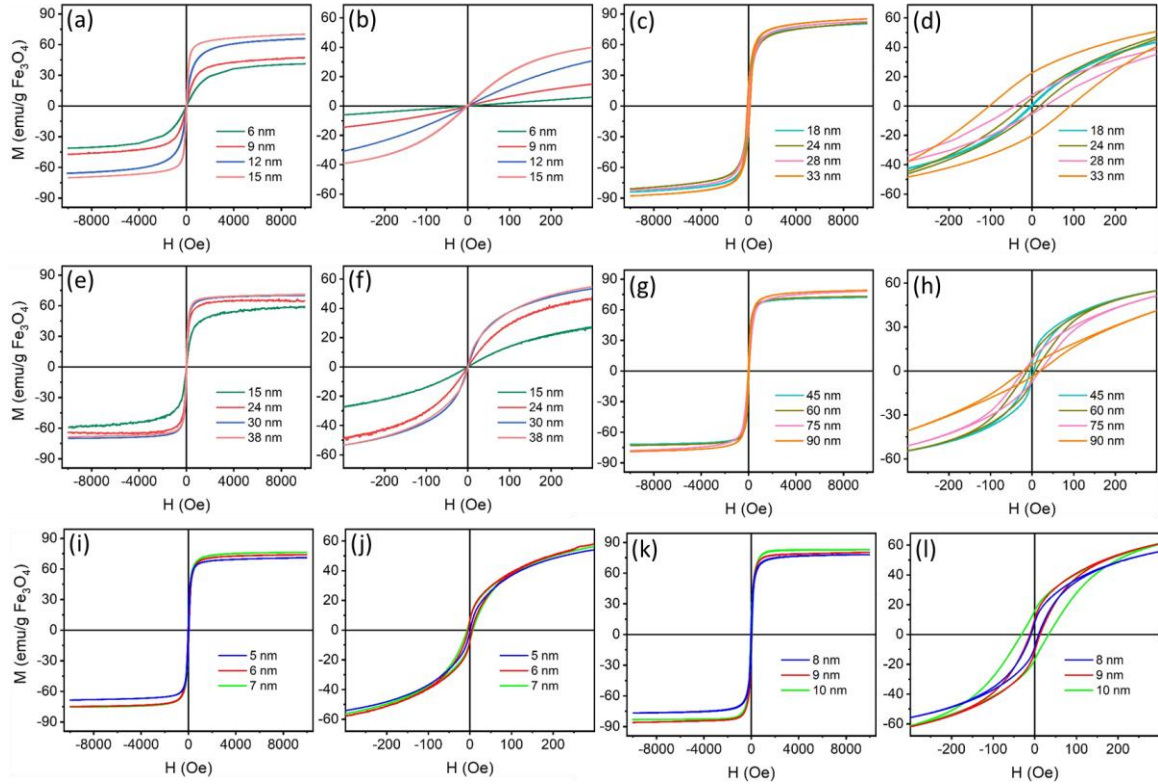


Figure S3. 6. The magnetic properties of the nanoparticles and clusters. (a-d) Magnetization curves of the isolated iron oxide nanoparticles. The nanoparticles are dispersed in wax. (e-h) Magnetization curves of the iron oxide clusters with different cluster diameter. The clusters were dispersed in gypsum. The primary nanocrystal size is around 5 nm. (e-h) Magnetization curves of clusters with different cluster diameter. The average cluster diameter is around 38 nm.

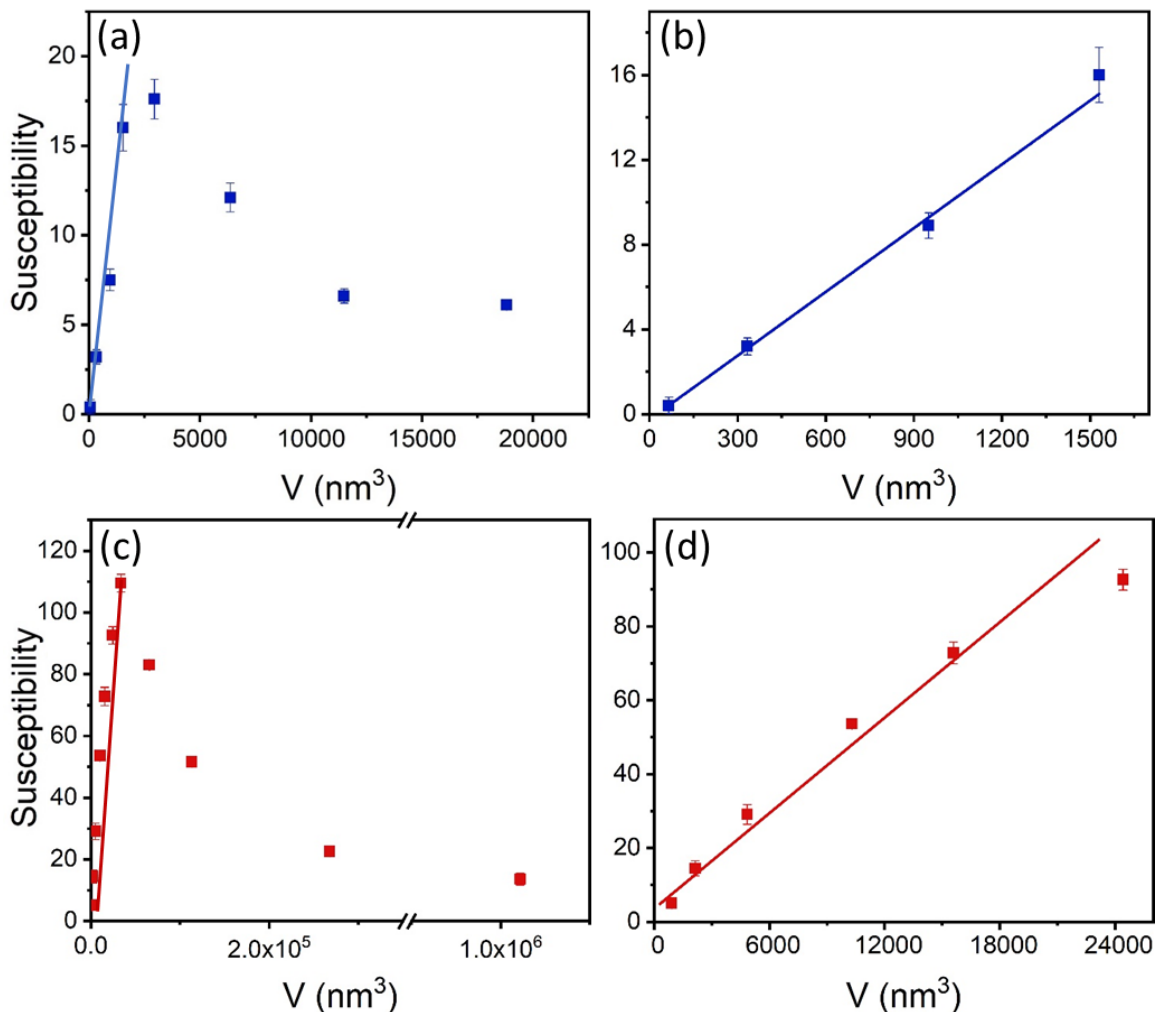


Figure S3. 7. Dependence of initial susceptibility of iron oxide nanomaterials on their volume. (a-b) Isolated nanoparticles with different volumes. (c-d) Clusters with different volumes. The primary nanocrystal size is 5 nm.

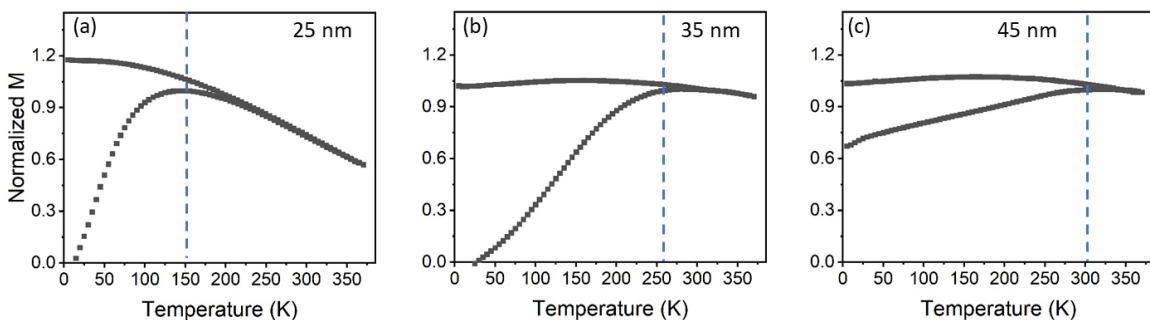


Figure S3. 8. The zero-field-cooled (ZFC) and field-cooled (FC) magnetization curves of the clusters. (a-c) The cluster diameter is 25 nm, 35 nm, and 45 nm. The primary nanocrystal size is 5 nm. The curves are scanned from 5 to 375 K with a magnetic field of 50 Oe. The blocking temperature is defined as the peak of the ZFC curve and is indicated

in these data by a vertical dashed line. Notably the blocking temperature of nanoclusters smaller than 40 nm is lower than 300 K, indicating they are superparamagnetic at room temperature. The blocking temperature of clusters larger than 40 nm is larger than 300 K, indicating that they are blocked single domain particles.

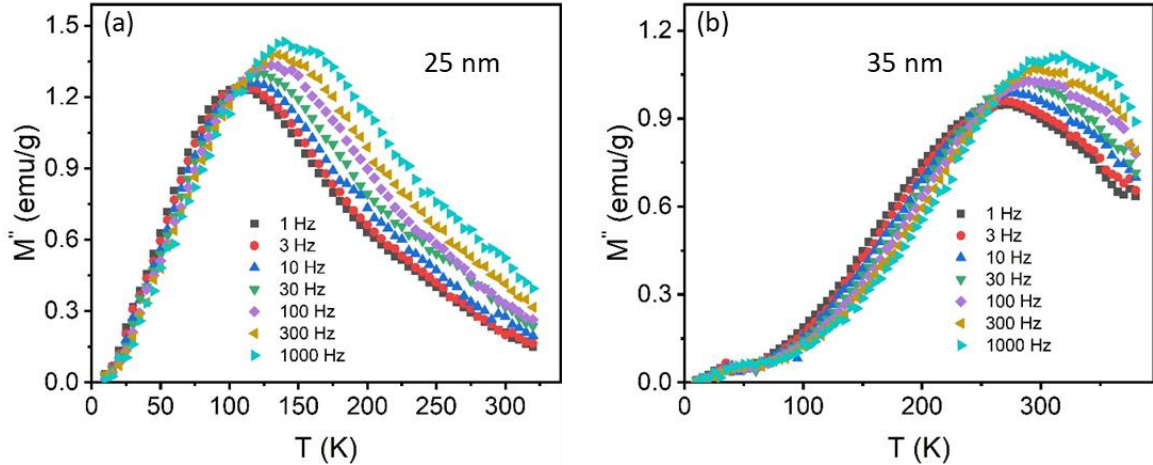


Figure S3. 9. The AC susceptibility of the clusters. (a-b) The cluster diameter is 25 nm and 35 nm. The primary nanocrystal size is 5 nm. Out-of-phase magnetic susceptibility of cluster is scanned from 5 to 380 K and with an AC field of 1 Hz to 1000 Hz at 4 Oe.

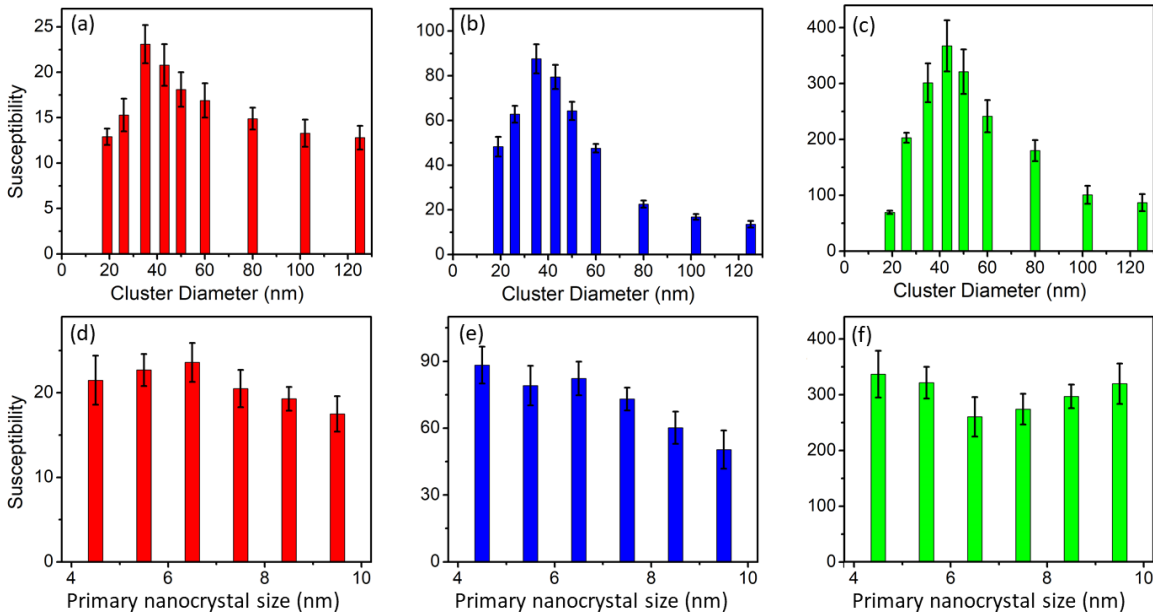


Figure S3. 10. The magnetic susceptibility of iron oxide clusters in different forms. (a-c) Clusters with different cluster diameter. The primary nanocrystal size is 5 nm. (d-f) Clusters with different primary nanocrystal size. The cluster diameter is 38 nm. a & d: clusters in the form of dried powders; b & e: Clusters dispersed in a solid matrix (gypsum); c & f: clusters in liquid solution.

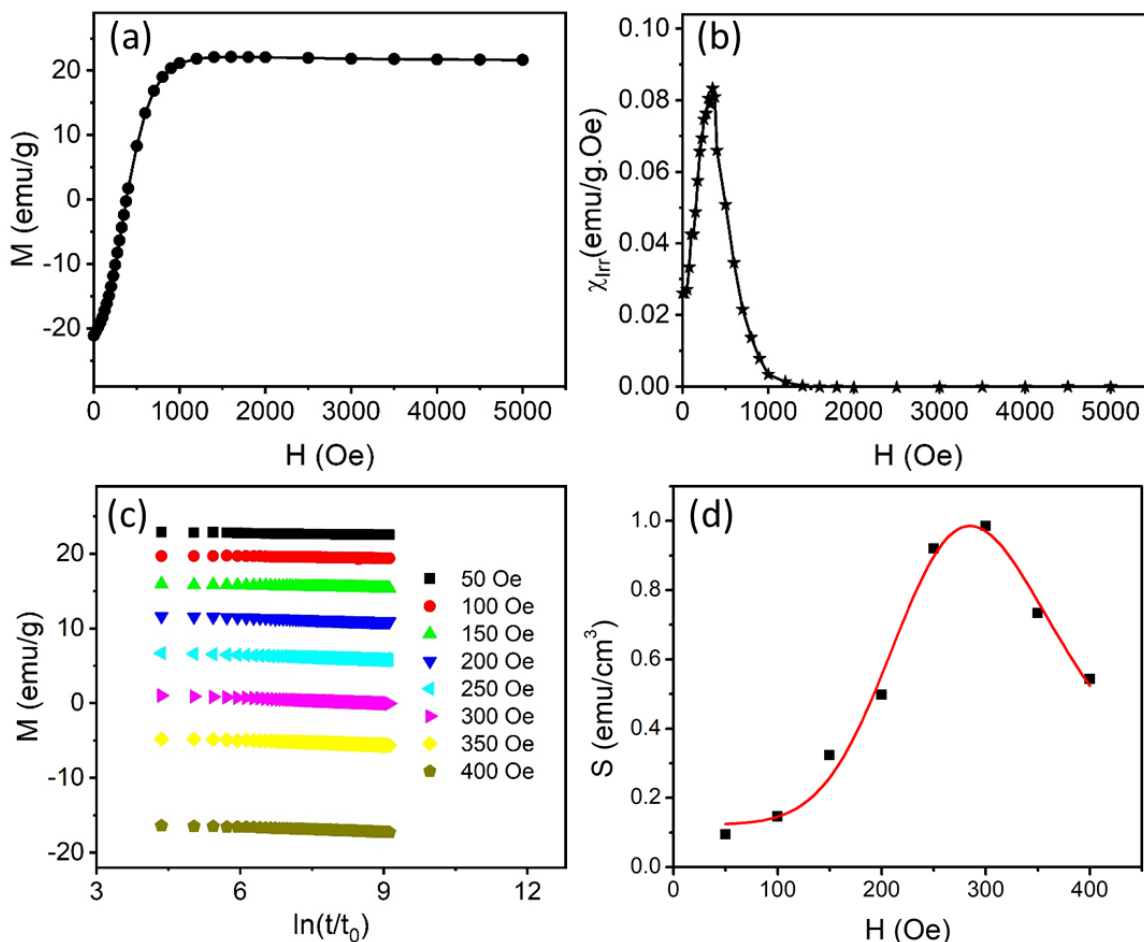


Figure S3. 11. The activation volume of the clusters. The cluster diameter is 35 nm and the primary nanocrystal size is 5 nm. (a) The direct current demagnetization (DCD) curve of the clusters. (b) The irreversible susceptibility of clusters at different magnetic field, which are calculated from the DCD curve shown in panel a. (c) The magnetic relaxation of the clusters at different magnetic field. (d) The magnetic viscosity of clusters at different magnetic field, which are calculated from the relaxation curve shown in panel a.

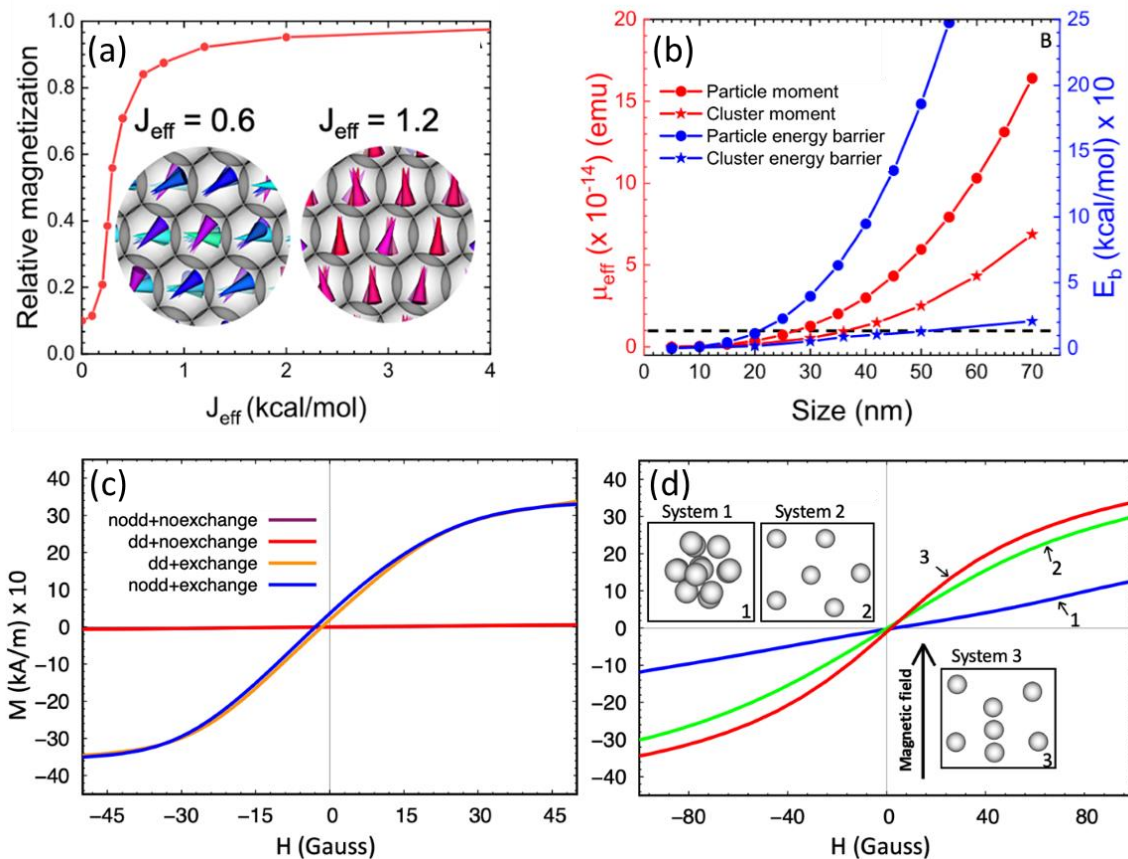


Figure S3. 12. The magnetic moment and anisotropy energy barrier of clusters and nanoparticles and the effect of magnetic interactions on the magnetic properties of clusters. (a) Relative magnetization of the 42 nm clusters at different J_{eff} . Inset shows the spin configuration within the clusters at $J_{\text{eff}} = 0.6$ and 1.2 kcal/mol. (b) Effective magnetic moment and energy barrier of Clusters and nanoparticles. (c) Contributions of dipole-dipole and exchange interactions to the magnetization and susceptibility of clusters. The diameters of primary nanocrystals and clusters are 5 nm and 42 nm, respectively. (d) The effect of d-d interactions on the susceptibility of isolated nanoparticles. System 1: All the NPs have a random orientation and the interparticle distance is less than 5 nm. System 2: All the NPs have a random orientation and the interparticle distance is larger than 100 nm. System 3: NPs have their easy axis parallel to external magnetic field and form a chain-like structure. In each system, there are 13 nanoparticles in total with a diameter of 13 nm.

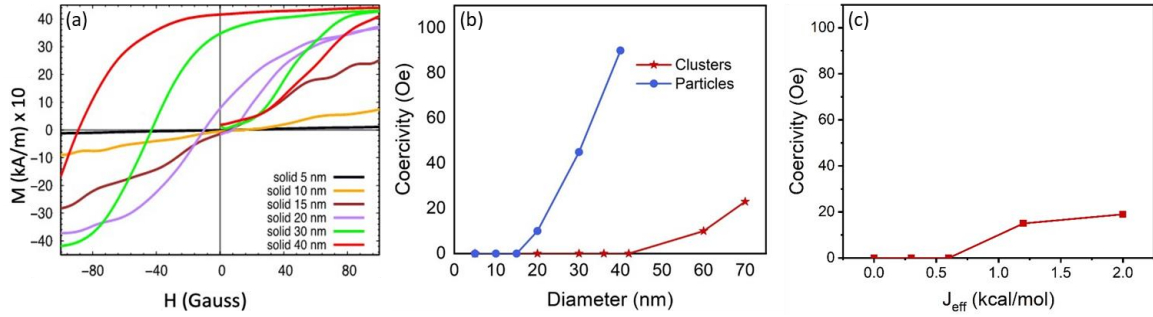


Figure S3. 13. The magnetic properties simulated using the Monte Carlo methods. (a) The simulated magnetization curves of isolated nanoparticles with different sizes. The J_{eff} of 15 kcal/mol was used to simulate the magnetization curve of the nanoparticles. (b) The simulated coercivity of clusters and nanoparticles with different diameters. (c) The simulated coercivity of clusters with different exchange constant. The cluster diameter is 42 nm and the primary nanocrystal size is 5 nm.

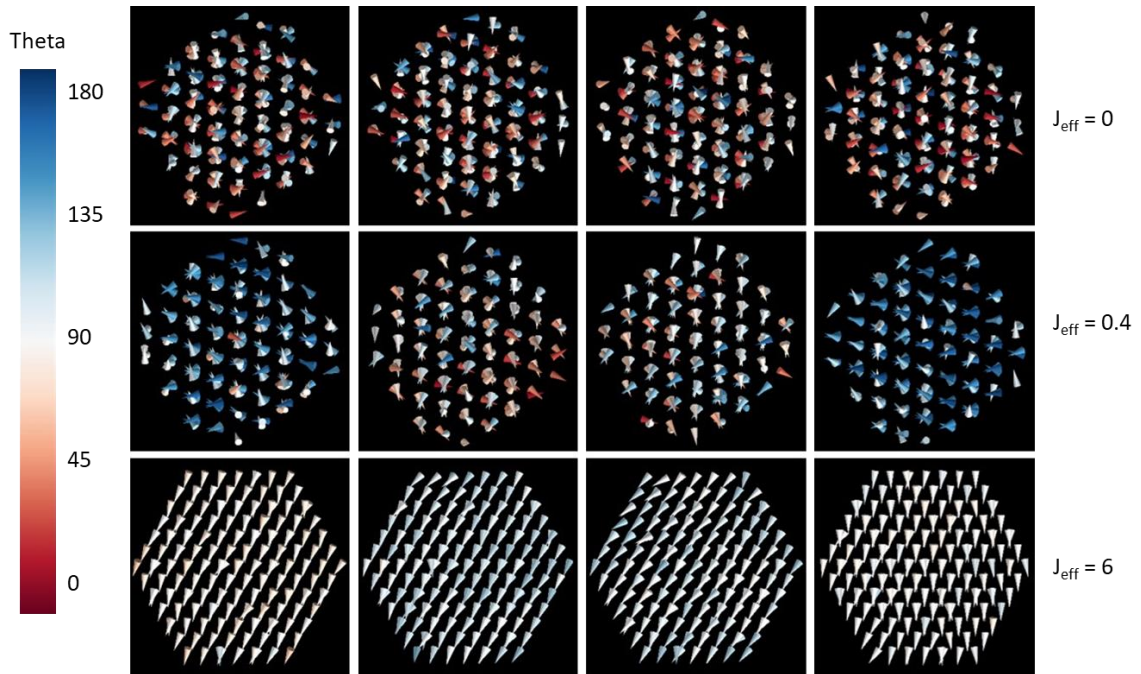


Figure S3. 14. Configuration of superspins within the clusters of different exchange constants. Each row represents the snapshots of the spin configuration within the clusters at different time. When $J_{\text{eff}} = 0$, the directions of the spins are all random. Each spin changes direction with time independently. When $J_{\text{eff}} = 0.4$, the spins within a cluster point to roughly the same direction. The spins within a cluster change direction with time. When $J_{\text{eff}} = 6$, the spins within a cluster point to the same direction and they do not change direction with time.

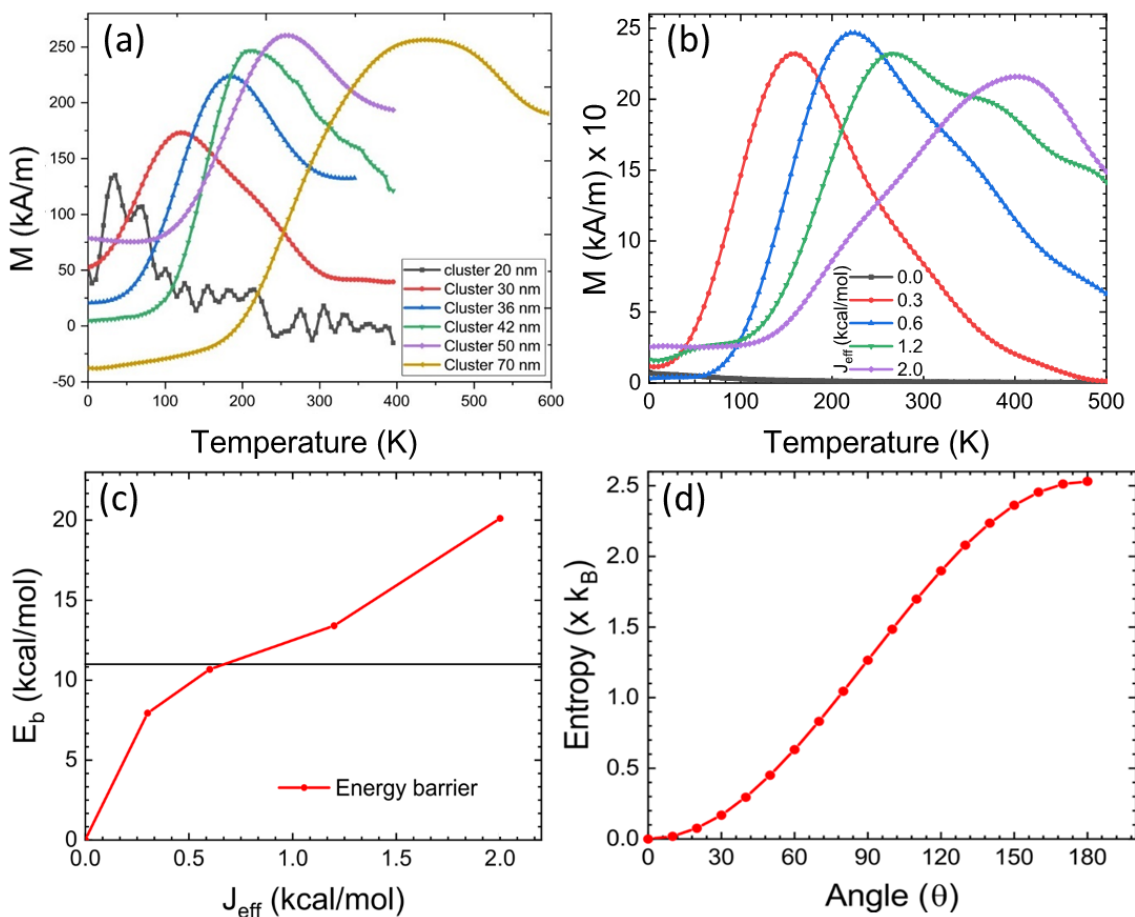


Figure S3. 15. Simulated zero-field-cooled magnetization curve of clusters and their energy barrier. (a) The simulated ZFC curves of clusters with different cluster diameters. (b) The simulated ZFC curves of the 42 nm clusters with different J_{eff} . (c) The energy barrier E_b for the 42 nm cluster at different J_{eff} . (d) The magnetic entropy as a function of an NP superspin angle restriction θ .

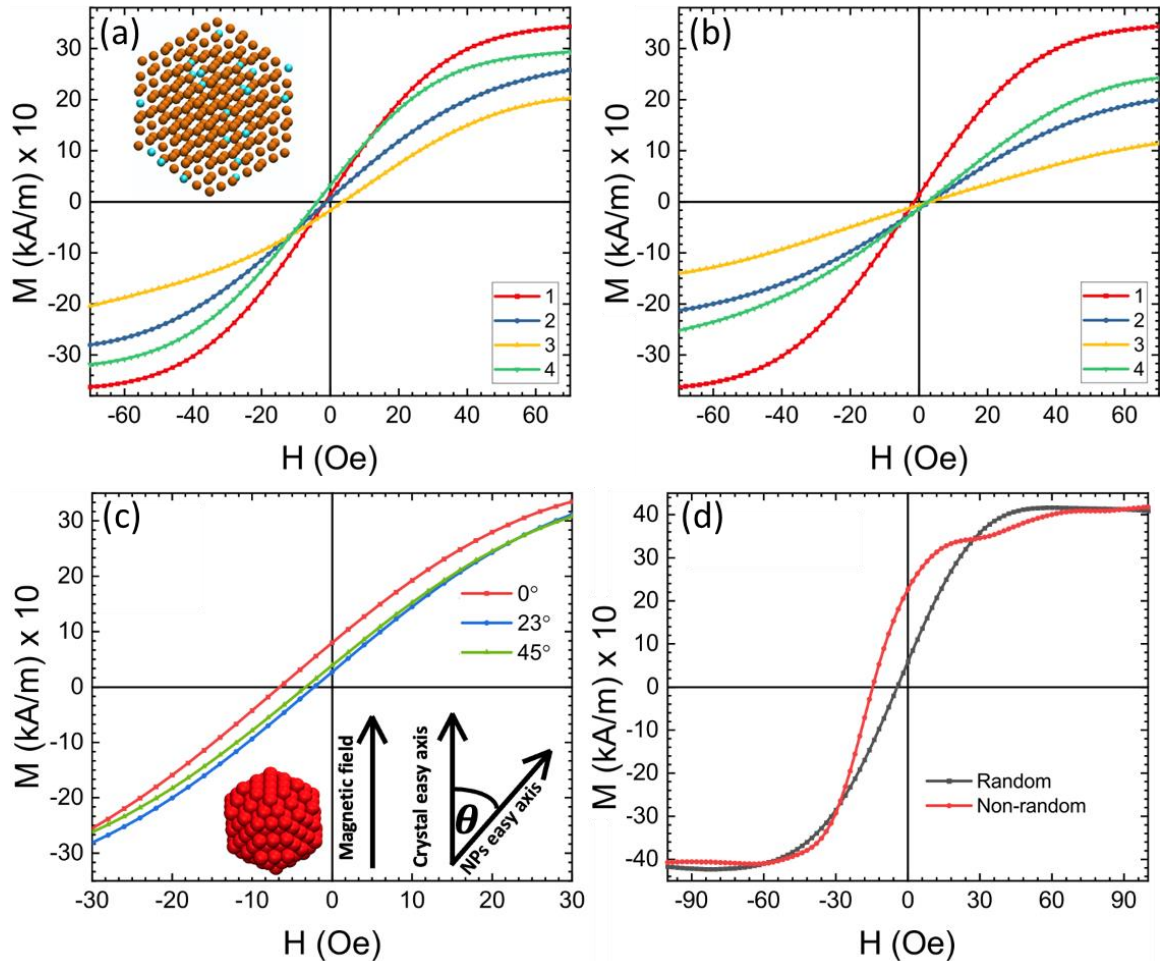


Figure S3.16. The effect of defects and the orientation of primary nanocrystals on the magnetization curves of the clusters. (a) The 36 nm cluster is composed of 177 primary nanocrystals (5 nm), where 30 primary nanocrystals (randomly chosen) have reduced exchange coupling or missing. 1-3: The effective exchange constants of the 30 primary particles are 0.6, 0.1, and 0 kcal/mol, respectively. 4: The randoms chosen 30 primary particles are removed (b) The 36 nm cluster with 50 primary nanocrystals (randomly chosen) having reduced exchange coupling or missing. (c) Magnetization of clusters where $[111]$ axes of individual NPs are rotated with respect to the $[111]$ supercrystal axis, which was parallel to the magnetic field ($J_{\text{eff}} = 0.6$ kcal/mol). (d) The magnetization of a 42 nm cluster ($J_{\text{eff}} = 1.2$ kcal/mol) formed from 5 nm NPs with the $[111]$ NPs easy axis aligned parallel to the $[111]$ supercrystal axis (red curve) or with the NPs randomly rotated (black curve).

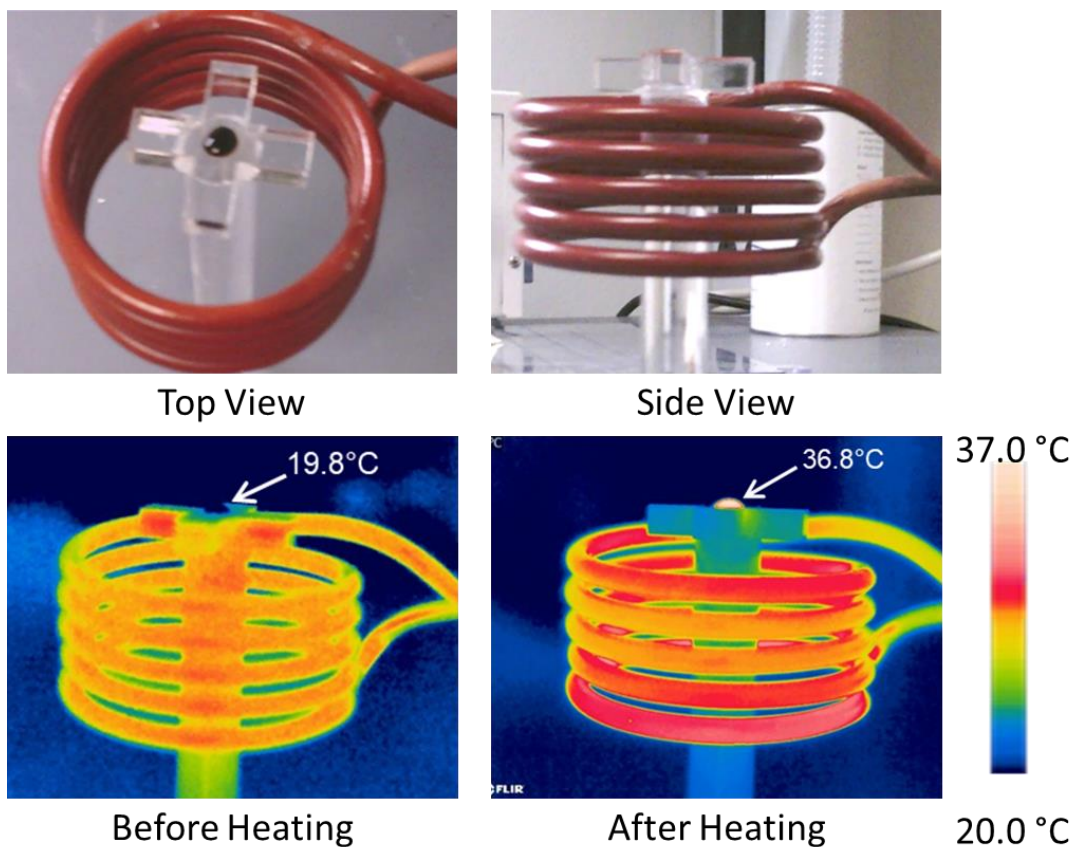


Figure S3. 17. Magnetic heating of iron oxide clusters solution above the coil. One drop of the clusters solutions (10 mg Fe/mL) is located 1 cm above the coil. The temperature of the clusters solution increased from 19.8°C to 36.8°C within 20 seconds as monitored by an IR camera. The quick increase of temperature indicates the clusters can be efficiently heated on top of the coils where the magnetic field is lower than that inside the coil.

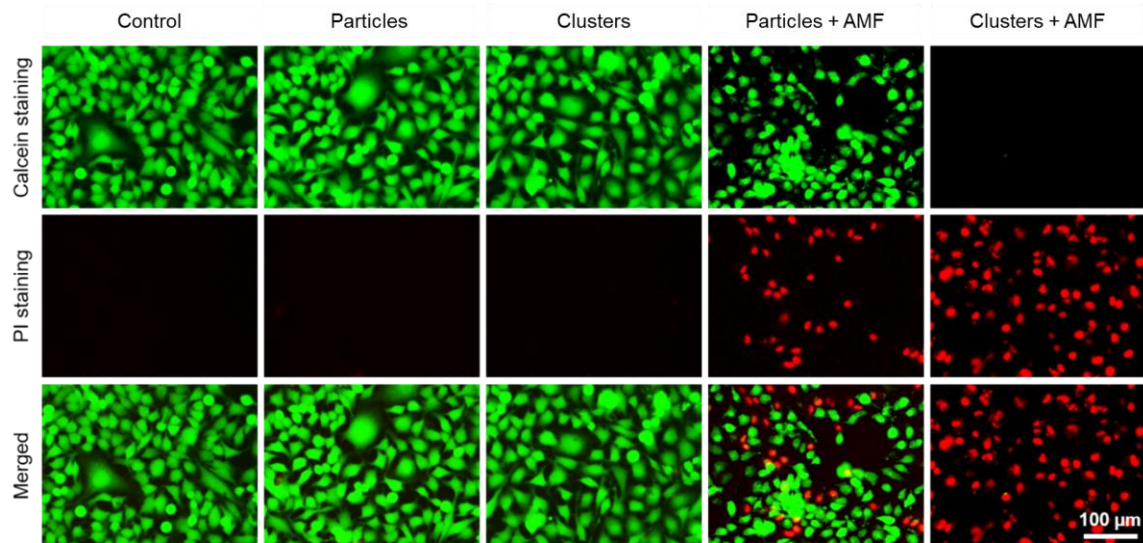


Figure S3. 18. Cell killing effect of clusters and nanoparticles in the battery-operated magnetic hyperthermia system. HeLa cells were used as an example. Red, dead cells labeled with propidium iodide (PI); green, live cells labeled with calcein. The HeLa cells were effectively killed by clusters under a low amplitude alternating magnetic field (40 Oe, 133 kHz).

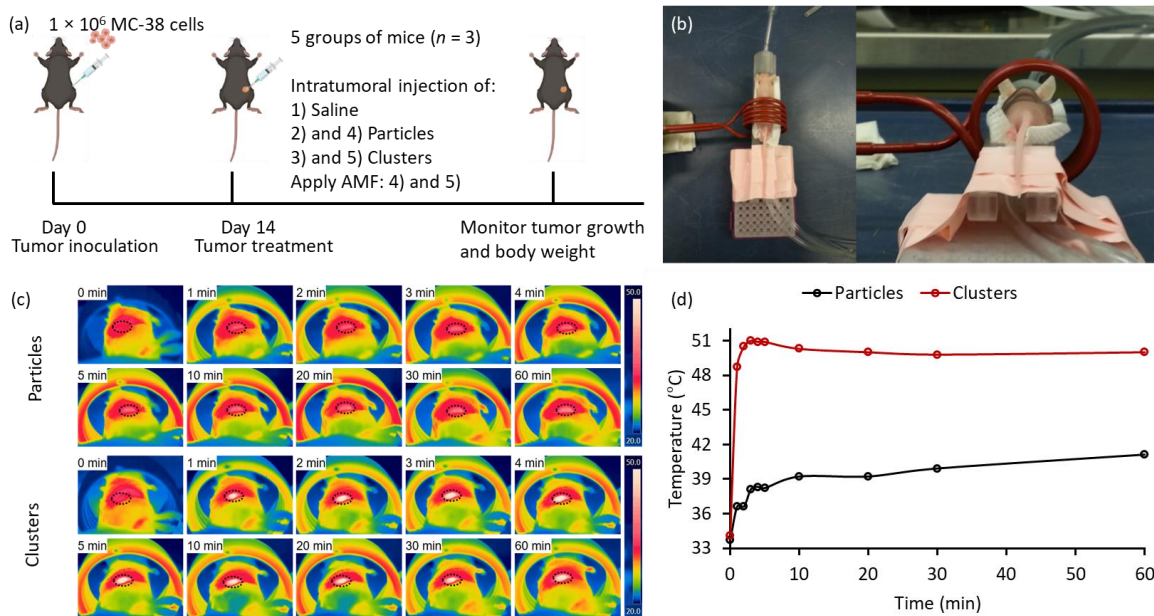


Figure S3. 19. Magnetic heating efficiency of iron oxide clusters in vivo. (a) The schematic illustration of the experimental design of in vivo magnetic hyperthermia cancer treatment. (b) The photograph of the mouse in the heating coil. (c) Representative IR images of tumor-bearing mice under magnetic heating with iron oxide particles or clusters. Tumors are indicated by black dashed circles. (d) The representative temperature profile of the tumor tissue.

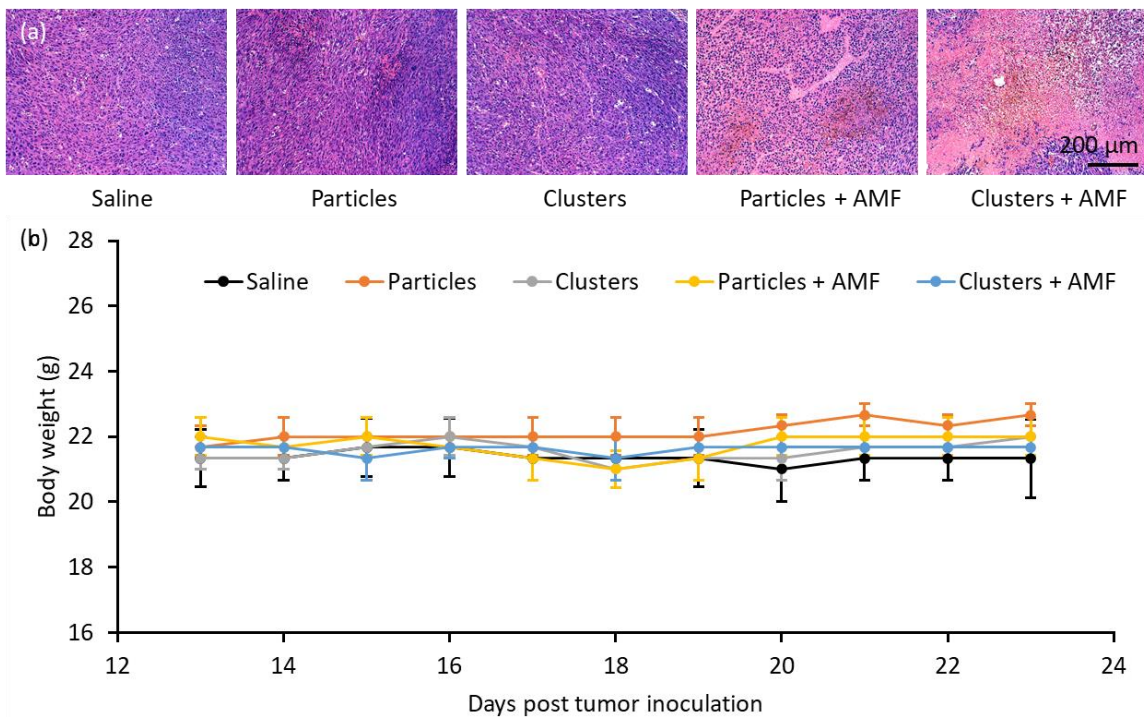


Figure S3. 20. The magnetic hyperthermia treatment of mice. (a) The histological examination of tumor tissues after different treatments. Hematoxylin and eosin (H&E) staining of tumor tissues was performed 24 hours after the treatments. The results show that iron oxide clusters led to more significant tumor-damaging activity than nanoparticles under alternating magnetic field. (b) The body weights of the mice after different treatments.

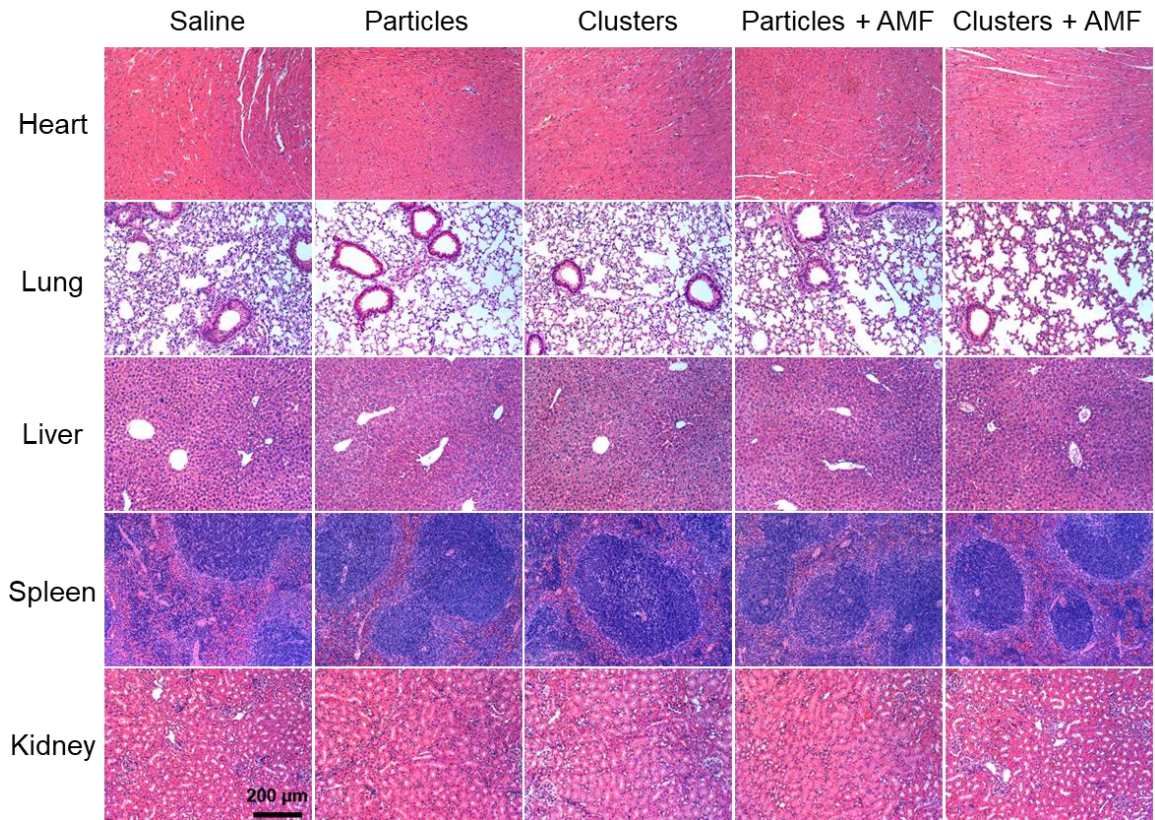


Figure S3. 21. *The histological examination of major organs after different treatments. Hematoxylin and eosin (H&E) staining of tumor tissues was performed 24 hours after the treatments. The results show that the treatments did not cause noticeable change to the major organs of the mice.*

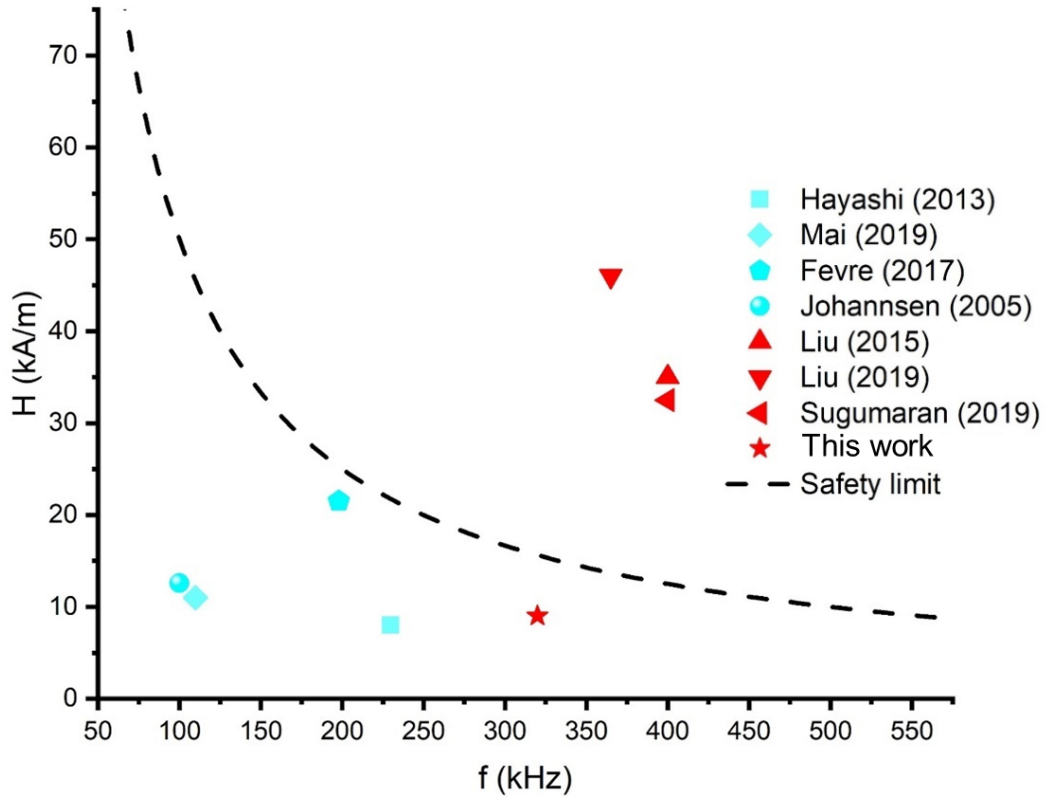


Figure S3. 22. Results of in vivo magnetic hyperthermia study using iron oxide nanomaterials in the literature and this work. Red color of the symbols represents complete elimination of the tumors; blue color of the symbols represents incomplete elimination of the tumors. The dash line is the safety limit of the magnetic field ($H \times f < 5 \times 10^9$ A/m Hz). The material in this work (clusters) is the only materials that is below the safety limit and eliminated the tumors.

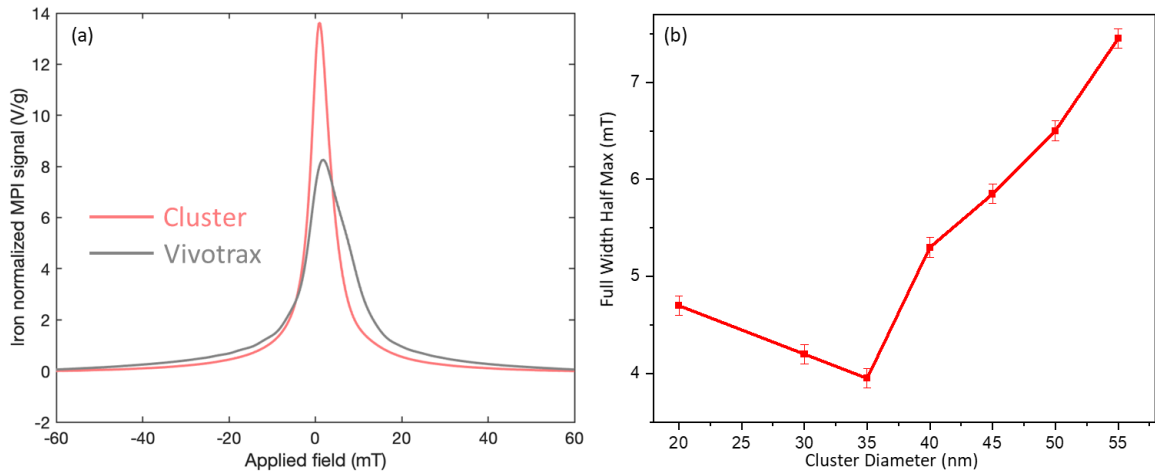


Figure S3. 23. The clusters as MPI contrast agents. (a) The magnetic particle imaging point spread function of clusters and nanoparticles (Vivotrax). The FWHM of Vivotrax and iron oxide Clusters are 11.4 mT (1.63 mm) and 6.4 mT (0.92 mm), respectively, indicating the higher performance of Clusters. (b) The full width at half maximum of iron oxide clusters with different diameters.

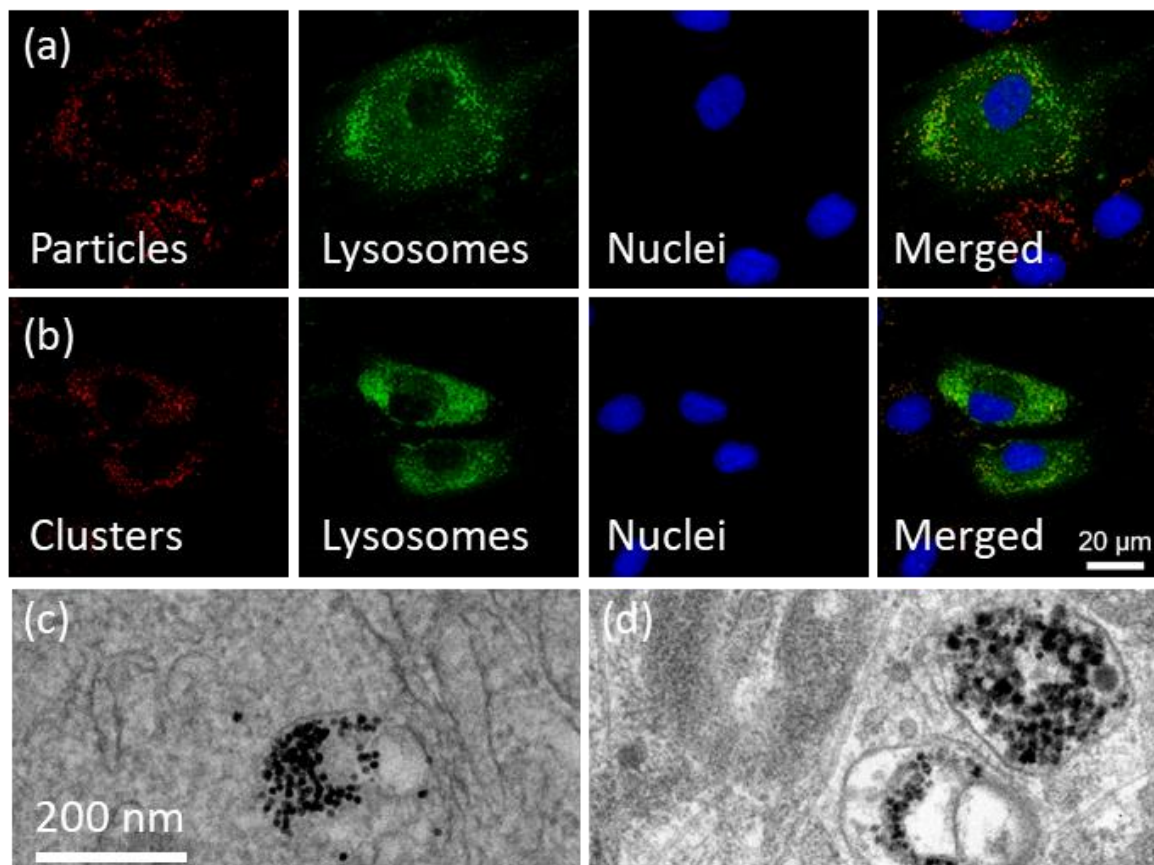


Figure S3. 24. Subcellular localization of the iron oxide clusters and nanoparticles in cells. (a) Fluorescence images of the isolated nanoparticles in human mesenchymal stem cells (hMSCs). (b) Fluorescence images of nanoparticles in hMSCs. (c) The TEM image of the isolated nanoparticles in hMSCs. (D) The TEM image of clusters in hMSCs.

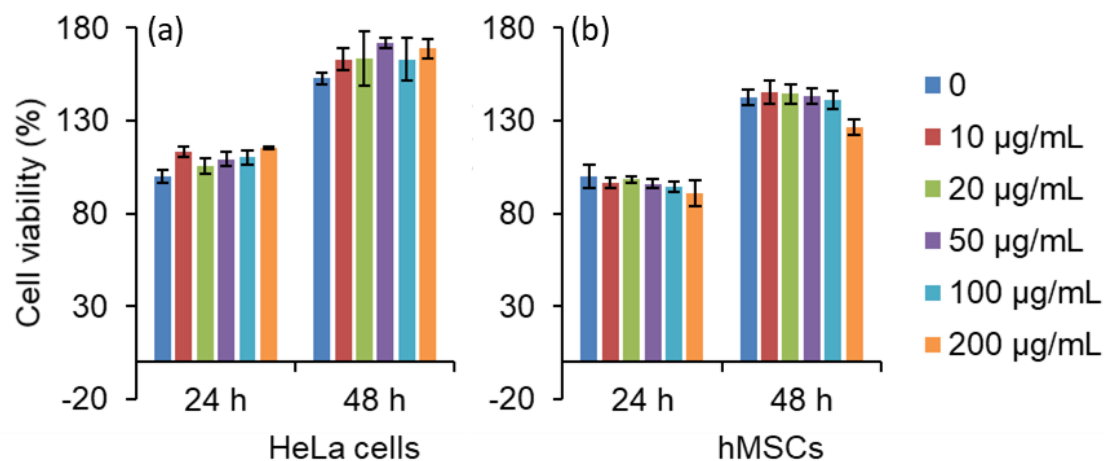


Figure S3. 25. The cytotoxicity of clusters. (a) *Hela cells* incubated with clusters at different concentrations. (b) *Human mesenchymal stem cells (MSCs)* incubated with clusters at different concentrations. The viability of cells was not changed 48 hours after the additions of the clusters, indicating the clusters are not toxic to *Hela cells* and *MSCs*.

Table S3. 1. Synthesis conditions of iron oxide Clusters with different dimensions.

Clusters		Synthesis conditions						
D _c (nm)	d _p (nm)	FeCl ₃ ·6H ₂ O (mg)	Ethylene glycol (mL)	PAA (mg)	Urea (mg)	Water (mL)	T (°C)	Time (h)
12	5	540	20	250	1200	5	200	6
16	5	540	20	250	1200	4	200	6
21	5	540	20	250	1200	3	200	6
25	5	540	20	250	1200	2.5	200	6
31	5	540	20	250	1200	2	200	6
36	5	540	20	250	1200	1.75	200	6
40	5	540	20	250	1200	1.5	200	6
44	5	540	20	250	1200	1	200	6
50	5	540	20	250	1200	0.75	200	6
60	5	540	20	250	1200	0.5	200	6
80	5	540	20	250	1200	0.3	200	6
102	5	540	20	250	1200	0.2	200	6
125	5	540	20	250	1200	0.1	200	6

38	5	540	20	250	1200	1.4	200	6
38	6	540	20	250	1200	1.4	215	6
38	7	540	20	250	1200	1.4	230	6
38	8	540	20	250	1200	1.4	245	6
38	9	540	20	250	1200	1.4	260	8
38	10	540	20	250	1200	1.4	275	10

Table S3. 2. Hydrodynamic diameters (HD) of the iron oxide clusters with different dimensions. For both TEM and DLS measurements, the polydispersity of the size distributions is less than 10%. # Indicates the as-synthesized clusters coated with PAA, while * indicates they have been modified with Poly (AA-co-AMPS-co-PEG).

TEM		DLS	
d _p (nm)	D _c (nm)	HD# (original)	HD* (modified)
4	28 ± 2	53	71
4	38 ± 3	72	87
4	50 ± 4	79	99
4	60 ± 5	83	106
4	80 ± 7	97	135
4	100 ± 9	121	150
4	125 ± 13	145	182

Table S3. 3. Magnetic properties of the iron oxide nanoparticles.

Nanoparticle Diameter (nm)	M _{Sat} (emu/g Fe ₃ O ₄)	χ (SI)	H _c (Oe)
6	42	0.3±0.04	0
8.6	47	2.6±0.3	0
12.2	66	9.6±0.6	0
14.3	70	16±0.9	0
17.8	78	18±1.1	1
23	80	12±0.8	8±0.5
28	83	6.5±0.4	61±2.8
33	86	6.3±0.2	111±3.6

Table S3. 4. Magnetic properties of the iron oxide clusters.

D _c (nm)	d _p (nm)	M _{Sat} (emu/g Fe ₃ O ₄)	χ (SI)	H _c (Oe)
12±1	5	58	5.1±0.8	0
16±2	5	61	14.5±2	0
21±2	5	65	29.1±2	0
27±3	5	70	53.6±1	0
31±3	5	71	72.8±3	0
36±3	5	72	92.6±3	1.0±0.1
40±4	5	73	109.5±5	1.2±0.1
42±4	5	73	121±5	1.5±0.2
46±5	5	73	101.5±4	3.2±0.2
50±5	5	74	83.3±4	6.7±0.7
60±6	5	74	51.6±4	9.4±0.9
80±8	5	76	22.6±1	14.9±1.6
102±10	5	77	16.9±0.2	17±1.2
125±13	5	78	13.6±2	19.1±1.5
38±4	5	73	98.6±6	0
38±4	6	74	95.2±6	4.8±0.2
38±4	7	76	88.3±5	6.7±0.7
38±4	8	79	75.1±5	8.9±0.9
38±4	9	81	60.2±4	12.5±1.4
38±4	10	83	50.4±4	29±2.6

References in Chapter 3

- [1] Guimarães, A. P.; Guimaraes, A. P., *Principles of nanomagnetism*. Springer: 2009; Vol. 7.
- [2] Muhlberger, M.; Unterweger, H.; Band, J.; Lehmann, C.; Heger, L.; Dudziak, D.; Alexiou, C.; Lee, G.; Janko, C., Loading of Primary Human T Lymphocytes with Citrate-Coated Superparamagnetic Iron Oxide Nanoparticles Does Not Impair Their Activation after Polyclonal Stimulation. *Cells* **2020**, *9* (2).
- [3] Gleich, B.; Weizenecker, R., Tomographic imaging using the nonlinear response of magnetic particles. *Nature* **2005**, *435* (7046), 1214-1217.
- [4] Chen, R.; Romero, G.; Christiansen, M. G.; Mohr, A.; Anikeeva, P., Wireless magnetothermal deep brain stimulation. *Science* **2015**, *347* (6229), 1477-1480.
- [5] Yavuz, C. T.; Mayo, J. T.; Yu, W. W.; Prakash, A.; Falkner, J. C.; Yean, S.; Cong, L. L.; Shipley, H. J.; Kan, A.; Tomson, M.; Natelson, D.; Colvin, V. L., Low-field magnetic separation of monodisperse Fe₃O₄ nanocrystals. *Science* **2006**, *314* (5801), 964-967.
- [6] Stanley, S. A.; Gagner, J. E.; Damanpour, S.; Yoshida, M.; Dordick, J. S.; Friedman, J. M., Radio-wave heating of iron oxide nanoparticles can regulate plasma glucose in mice. *Science* **2012**, *336* (6081), 604-608.
- [7] Cotin, G.; Piant, S.; Mertz, D.; Felder-Flesch, D.; Begin-Colin, S., Iron oxide nanoparticles for biomedical applications: Synthesis, functionalization, and application. In *Iron Oxide Nanoparticles for Biomedical Applications*, Elsevier: 2018; pp 43-88.
- [8] Mørup, S.; Frandsen, C.; Hansen, M. F., Magnetic properties of nanoparticles. In *Oxford Handbook of Nanoscience and Technology*, 2010.
- [9] Chen, R.; Christiansen, M. G.; Anikeeva, P., Maximizing hysteretic losses in magnetic ferrite nanoparticles via model-driven synthesis and materials optimization. *ACS nano* **2013**, *7* (10), 8990-9000.
- [10] Lee, J.-H.; Huh, Y.-M.; Jun, Y.-w.; Seo, J.-w.; Jang, J.-t.; Song, H.-T.; Kim, S.; Cho, E.-J.; Yoon, H.-G.; Suh, J.-S., Artificially engineered magnetic nanoparticles for ultra-sensitive molecular imaging. *Nature medicine* **2007**, *13* (1), 95-99.
- [11] Ghosh, I.; Sadhu, A.; Moriyasu, Y.; Bandyopadhyay, M.; Mukherjee, A., Manganese oxide nanoparticles induce genotoxicity and DNA hypomethylation in the moss *Physcomitrella patens*. *Mutation Research/Genetic Toxicology and Environmental Mutagenesis* **2019**, *842*, 146-157.
- [12] Sruthi, S.; Ashtami, J.; Mohanan, P., Biomedical application and hidden toxicity of Zinc oxide nanoparticles. *Materials today chemistry* **2018**, *10*, 175-186.
- [13] Xiao, Z.; Zhang, Q.; Guo, X.; Villanova, J.; Hu, Y.; Kulaots, I.; Garcia-Rojas, D.; Guo, W.; Colvin, V. L., Libraries of Uniform Magnetic Multicore Nanoparticles with Tunable Dimensions for Biomedical and Photonic Applications. *ACS Applied Materials & Interfaces* **2020**, *12* (37), 41932-41941.
- [14] Zeng, H.; Li, J.; Liu, J. P.; Wang, Z. L.; Sun, S. H., Exchange-coupled nanocomposite magnets by nanoparticle self-assembly. *Nature* **2002**, *420* (6914), 395-398.
- [15] Chen, B. B.; Xu, H. R.; Ma, C.; Mattauch, S.; Lan, D.; Jin, F.; Guo, Z.; Wan, S. Y.; Chen, P. F.; Gao, G. Y.; Chen, F.; Su, Y. X.; Wu, W. B., All-oxide-based

- synthetic antiferromagnets exhibiting layer-resolved magnetization reversal. *Science* **2017**, *357* (6347), 191-194.
- [16] Chen, W. O.; Sun, Z. Y.; Wang, Z. J.; Gu, L. H.; Xu, X. D.; Wu, S. W.; Gao, C. L., Direct observation of van der Waals stacking-dependent interlayer magnetism. *Science* **2019**, *366* (6468), 983-+.
- [17] Gao, S.; Rosales, H. D.; Gomez Albarracin, F. A.; Tsurkan, V.; Kaur, G.; Fennell, T.; Steffens, P.; Boehm, M.; Cermak, P.; Schneidewind, A.; Ressouche, E.; Cabra, D. C.; Rugg, C.; Zaharko, O., Fractional antiferromagnetic skyrmion lattice induced by anisotropic couplings. *Nature* **2020**, *586* (7827), 37-41.
- [18] Luo, Z. C.; Dao, T. P.; Hrabec, A.; Vijayakumar, J.; Kleibert, A.; Baumgartner, M.; Kirk, E.; Cui, J. Z.; Savchenko, T.; Krishnaswamy, G.; Heyderman, L. J.; Gambardella, P., Chirally coupled nanomagnets. *Science* **2019**, *363* (6434), 1435-+.
- [19] Skumryev, V.; Stoyanov, S.; Zhang, Y.; Hadjipanayis, G.; Givord, D.; Nogues, J., Beating the superparamagnetic limit with exchange bias. *Nature* **2003**, *423* (6942), 850-853.
- [20] Lee, J. H.; Jang, J. T.; Choi, J. S.; Moon, S. H.; Noh, S. H.; Kim, J. W.; Kim, J. G.; Kim, I. S.; Park, K. I.; Cheon, J., Exchange-coupled magnetic nanoparticles for efficient heat induction. *Nat Nanotechnol* **2011**, *6* (7), 418-22.
- [21] Tong, S.; Zhu, H.; Bao, G., Magnetic iron oxide nanoparticles for disease detection and therapy. *Materials Today* **2019**, *31*, 86-99.
- [22] Liu, J.; Sun, Z.; Deng, Y.; Zou, Y.; Li, C.; Guo, X.; Xiong, L.; Gao, Y.; Li, F.; Zhao, D., Highly water-dispersible biocompatible magnetite particles with low cytotoxicity stabilized by citrate groups. *Angewandte Chemie International Edition* **2009**, *48* (32), 5875-5879.
- [23] Lartigue, L.; Hugounenq, P.; Alloyeau, D.; Clarke, S. P.; Levy, M.; Bacri, J.-C.; Bazzi, R.; Brougham, D. F.; Wilhelm, C.; Gazeau, F., Cooperative organization in iron oxide multi-core nanoparticles potentiates their efficiency as heating mediators and MRI contrast agents. *ACS nano* **2012**, *6* (12), 10935-10949.
- [24] Park, J.; An, K.; Hwang, Y.; Park, J.-G.; Noh, H.-J.; Kim, J.-Y.; Park, J.-H.; Hwang, N.-M.; Hyeon, T., Ultra-large-scale syntheses of monodisperse nanocrystals. *Nature materials* **2004**, *3* (12), 891-895.
- [25] Ge, J.; Hu, Y.; Biasini, M.; Beyermann, W. P.; Yin, Y., Superparamagnetic magnetite colloidal nanocrystal clusters. *Angewandte Chemie International Edition* **2007**, *46* (23), 4342-4345.
- [26] Bogren, S.; Fornara, A.; Ludwig, F.; del Puerto Morales, M.; Steinhoff, U.; Hansen, M. F.; Kazakova, O.; Johansson, C., Classification of magnetic nanoparticle systems—synthesis, standardization and analysis methods in the nanomag project. *International journal of molecular sciences* **2015**, *16* (9), 20308-20325.
- [27] Dutta, P.; Pal, S.; Seehra, M.; Shah, N.; Huffman, G., Size dependence of magnetic parameters and surface disorder in magnetite nanoparticles. *Journal of Applied Physics* **2009**, *105* (7), 07B501.
- [28] Bean, C. P.; Livingston, J. D., Superparamagnetism. *Journal of Applied Physics* **1959**, *30* (4), S120-S129.

- [29] Mørup, S.; Hansen, M. F.; Frandsen, C., Magnetic interactions between nanoparticles. *Beilstein journal of nanotechnology* **2010**, *1* (1), 182-190.
- [30] Laureti, S.; Varvaro, G.; Testa, A.; Fiorani, D.; Agostinelli, E.; Piccaluga, G.; Musinu, A.; Ardu, A.; Peddis, D., Magnetic interactions in silica coated nanoporous assemblies of CoFe₂O₄ nanoparticles with cubic magnetic anisotropy. *Nanotechnology* **2010**, *21* (31), 315701.
- [31] Peddis, D.; Jönsson, P. E.; Laureti, S.; Varvaro, G., Magnetic interactions: a tool to modify the magnetic properties of materials based on nanoparticles. In *Frontiers of nanoscience*, Elsevier: 2014; Vol. 6, pp 129-188.
- [32] Singh, G.; Chan, H.; Baskin, A.; Gelman, E.; Repnin, N.; Král, P.; Klajn, R., Self-assembly of magnetite nanocubes into helical superstructures. *Science* **2014**, *345* (6201), 1149-1153.
- [33] Liu, F.; Hou, Y.; Gao, S., Exchange-coupled nanocomposites: chemical synthesis, characterization and applications. *Chem Soc Rev* **2014**, *43* (23), 8098-113.
- [34] Rosensweig, R. E., Heating magnetic fluid with alternating magnetic field. *Journal of magnetism and magnetic materials* **2002**, *252*, 370-374.
- [35] Manuchehrabadi, N.; Gao, Z.; Zhang, J.; Ring, H. L.; Shao, Q.; Liu, F.; McDermott, M.; Fok, A.; Rabin, Y.; Brockbank, K. G., Improved tissue cryopreservation using inductive heating of magnetic nanoparticles. *Science translational medicine* **2017**, *9* (379), eaah4586.
- [36] Carrey, J.; Mehdaoui, B.; Respaud, M., Simple models for dynamic hysteresis loop calculations of magnetic single-domain nanoparticles: Application to magnetic hyperthermia optimization. *Journal of applied physics* **2011**, *109* (8), 083921.
- [37] Christiansen, M. G.; Howe, C. M.; Bono, D. C.; Perreault, D. J.; Anikeeva, P., Practical methods for generating alternating magnetic fields for biomedical research. *Review of Scientific Instruments* **2017**, *88* (8), 084301.
- [38] Liu, X. L.; Yang, Y.; Ng, C. T.; Zhao, L. Y.; Zhang, Y.; Bay, B. H.; Fan, H. M.; Ding, J., Magnetic vortex nanorings: a new class of hyperthermia agent for highly efficient in vivo regression of tumors. *Adv Mater* **2015**, *27* (11), 1939-44.
- [39] Pan, J.; Hu, P.; Guo, Y.; Hao, J.; Ni, D.; Xu, Y.; Bao, Q.; Yao, H.; Wei, C.; Wu, Q.; Shi, J., Combined Magnetic Hyperthermia and Immune Therapy for Primary and Metastatic Tumor Treatments. *ACS Nano* **2020**, *14* (1), 1033-1044.
- [40] Chandrasekharan, P.; Tay, Z. W.; Zhou, X. Y.; Yu, E.; Orendorff, R.; Hensley, D.; Huynh, Q.; Fung, K. B.; VanHook, C. C.; Goodwill, P., A perspective on a rapid and radiation-free tracer imaging modality, magnetic particle imaging, with promise for clinical translation. *The British journal of radiology* **2018**, *91* (1091), 20180326.
- [41] Tay, Z. W.; Hensley, D. W.; Vreeland, E. C.; Zheng, B.; Conolly, S. M., The relaxation wall: experimental limits to improving MPI spatial resolution by increasing nanoparticle core size. *Biomedical physics & engineering express* **2017**, *3* (3), 035003.
- [42] Galanzha, E. I.; Shashkov, E. V.; Kelly, T.; Kim, J. W.; Yang, L.; Zharov, V. P., In vivo magnetic enrichment and multiplex photoacoustic detection of circulating tumour cells. *Nat Nanotechnol* **2009**, *4* (12), 855-60.

- [43] Silva, L. H.; Cruz, F. F.; Morales, M. M.; Weiss, D. J.; Rocco, P. R., Magnetic targeting as a strategy to enhance therapeutic effects of mesenchymal stromal cells. *Stem Cell Res Ther* **2017**, 8 (1), 58.
- [44] Kamei, N.; Ochi, M.; Adachi, N.; Ishikawa, M.; Yanada, S.; Levin, L. S.; Kamei, G.; Kobayashi, T., The safety and efficacy of magnetic targeting using autologous mesenchymal stem cells for cartilage repair. *Knee Surg Sports Traumatol Arthrosc* **2018**, 26 (12), 3626-3635.

Chapter 4

Enhanced Susceptibility of Manganese Doped Ferrite Clusters[†]

[†] Reprinted (adapted) with permission from Xiao, Z., Guo, X., Villanova, J., Bi, Y., Avidan, S., Effman, S., Zhang, Q. and Colvin, V.L. Portable Heating and Environmental Remediation Using the Giant Susceptibilities of Manganese-Doped Ferrite Clusters. In preparation.

4. Enhanced Susceptibility of Manganese Doped Ferrite Clusters

4.1 Abstract

Magnetic nanomaterials generating heat under the alternative magnetic field (AMF) have been well recognized in various fields due to their high efficiency and fast heat transfer between the heat source and medium. Low amplitude AMF is incredibly desired for environmental applications as it reduces energy costs and simplifies the heating equipment. However, effective heat generation under the low amplitude AMF has been elusive. We present the manganese ferrite clusters (MFCs) that could address this issue. The MFCs benefit from both exchange interactions of the primary nanocrystals and an increase in the saturation magnetization due to manganese doping. By optimizing the materials' nanoscale dimensions and manganese content, we achieve the maximum magnetic susceptibility and the highest heating performance at low amplitude AMF. We further apply the excellent heating capability to contaminant remediation using battery-operated portable devices and achieve highly efficient degradation of methylene blue and streptomycin. The exemplary performance makes the manganese ferrite clusters a strong candidate for cost-effective environmental remediations and potential biomedical applications.

4.2 Introduction

Magnetic fluid heating (MFH), also referred to as magnetic hyperthermia treatment in the biomedical field, is an emerging heating technology well recognized in biomedical studies such as cancer treatment and neuron stimulation.^[1-6] It also draws attention to environmental studies for contaminants remediation.^[7-9] When exposed to an alternating magnetic field (AMF), magnetic nanomaterials can generate heat localized around the

surface of the nanoparticles (nanoheaters) and gradually dissipate to the surrounding media.^[10-14] In biomedical studies, nanoheaters delivered to the target region can raise the surrounding temperature in a short period.^[15-17] Moreover, the magnetic field could reach the tissue in-depth, offering flexible treatment for internal organs.^[3] Superparamagnetic iron oxide nanoparticles are biocompatible and are therefore the ideal candidate for clinical hyperthermia treatment.^[18, 19] In environmental studies, except for the rapid response in a localized area, energy consumption is also an issue to be addressed. MFH has a high energy conversion efficiency, while the high surface areas of magnetic nanomaterials can effectively facilitate the degradation of the contaminants.^[20, 21] Therefore, MFH has many advantages over conventional therapies and remediation techniques.

An important parameter to evaluate the magnetic heating of nanoheaters is the specific absorption rate (SAR), the rate of energy absorbed by the unit mass. The high SAR value of the nanoheater demonstrates the effective heating performance of the nanoheaters, allowing for a more thorough heat transfer to effectively facilitate chemical or biological reactions. Many studies have worked on developing high SAR magnetic nanomaterials. One strategy is achieved through dimensional and structural control by making cubic nanoparticles, core-shell nanoparticles, or clustering tens to hundreds of nanoparticles to form either the self-assembly (superparticles) or hard aggregates (clusters).^[22-25] Another effective way is to increase the saturation magnetizations of the materials by doping other divalent metals such as Zn, Mn, Co, and Ni and forming ferrites ($M_xFe_{3-x}O_4$, $M = Zn, Mn, Co, Ni$).^[26-29] For example, Noh et al. reported the Zn and Co-doped core-shell materials with a SAR as high as 4,000 W/g.^[30] In contrast, the undoped iron oxide is only about 106

W/g in the same AMF. Nevertheless, metals like Ni and Co should be avoided as they are highly toxic.^[31, 32]

However, the above high SAR values are usually achieved in the AMF with high amplitude (200 to 800 Oe, 16 to 64 kAm⁻¹) and frequency (300 to 500 kHz).^[5, 22, 24, 30] The high amplitude AMF demands costly and complicated equipment. More importantly, nonspecific heating via eddy current poses a potential danger to normal tissues or organs in biomedical applications.^[33, 34] The general guideline for safe biomedical operation is that the product of the frequency and amplitude should not exceed $5 \times 10^9 \text{ Am}^{-1}\text{s}^{-1}$, where a more restrictive limit is $4.85 \times 10^8 \text{ Am}^{-1}\text{s}^{-1}$, based on the AMF duration.^[34, 35] To make nanoheaters perform well in the AMF that is both safe and energy-efficient, improving the magnetic susceptibility is essential as susceptibility represents the responsiveness of the material to the external field at low amplitude.^[26, 36-38] However, magnetic nanomaterials usually have a low susceptibility value.^[38-40] There is a need for highly susceptible materials to heat under AMF with low amplitude and frequency.

Here, we report the manganese ferrite clusters (MFCs) with tunable dimensions and compositions for efficient heating under low amplitude AMF. Benefit from exchange interactions of the primary nanocrystals, clusters are prone to align under low field while doping Mn can increase the saturation magnetization.^[41-44] We explore how different parameters of the MFCs affect magnetic susceptibility and their SAR values under low amplitude AMF. The SAR is highly associated with susceptibility, where the cluster dimensions and manganese content play an important role. The highest susceptibility ($\chi \sim 178$) is almost twice that of the best iron oxide samples. The SAR reaches 6 W/g with

a power input of only 10 W. We further apply their excellent heating capability at low amplitude AMF contaminants remediation. The high degradation efficacy is examined through a model using methylene blue and streptomycin as the target pollutant. The exemplary performance makes the manganese ferrite clusters a strong candidate for cost-effective environmental remediations and potential biomedical applications.

4.3 Characterizations of the manganese ferrite clusters

We have prepared the manganese ferrite clusters (MFC) with uniform size distributions under hydrothermal conditions using the well-established polyol synthesis. After magnetic separation and purification, the MFC aqueous solution forms a black ferrofluid that manifests strong attraction to a permanent handheld magnet (supplemental Figure S4.1). To reveal these materials' morphology, composition, and properties, we have performed a series of characterizations on them, and the result is shown in Figure 4.1. As seen in Figure 4.1 a and b, the transmission electron microscopy (TEM) images demonstrate a uniform size distribution of these clusters with an average overall diameter of 84 ± 7 nm. Each cluster comprises hundreds of primary nanocrystals, with an average nanocrystal diameter of 5.5 nm. As shown in Figure 4.1 c, further magnification indicates the lattice fringes are parallel within the neighboring primary nanocrystals. Figure 4.1 d is the selected area electron diffraction (SAED) pattern of a single cluster. Instead of the continuous ring pattern of the typical polycrystals, the scattered dots indicate a near-single crystal nature of the cluster.^[45] The parallel lattices and the particular SAED pattern can be ascribed to the oriented attachment of the primary nanocrystals. When the primary nanocrystals aggregate to form the clusters, they align their crystal lattices and gradually merge into single crystals with shared boundaries.^[46, 47] The alignment of these primary nanocrystals plays a vital role

in the magnetic properties of the clusters and could help the magnetization of the clusters under a low external magnetic field.^[22]

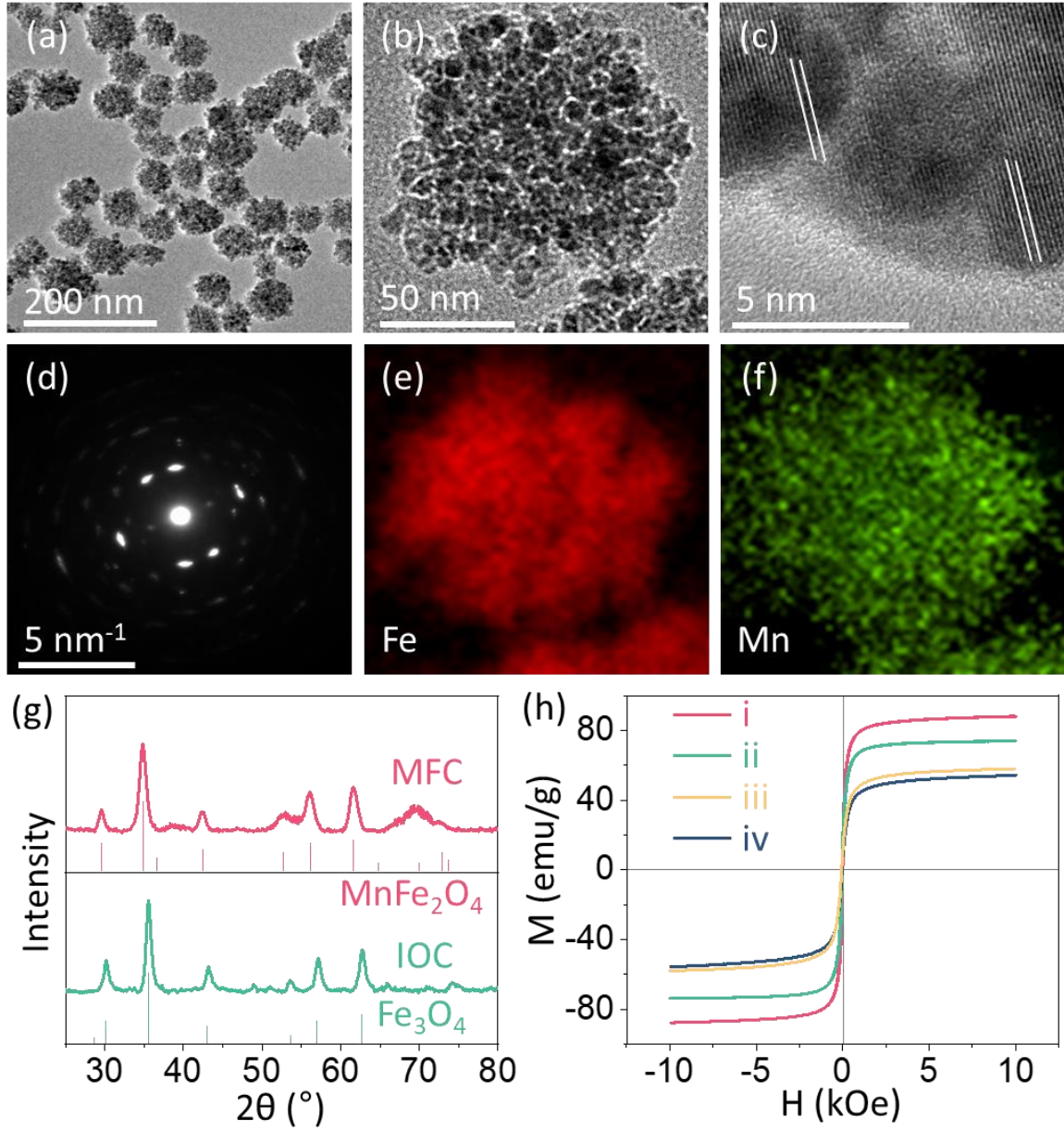


Figure 4. 1. The morphologies, composition, and magnetic properties of the manganese ferrite clusters (MFC). (a, b) Transmission electron microscopy (TEM) images of these clusters. (c) High-resolution TEM (HRTEM) image. (d) Selected area electron diffraction (SAED) pattern of a single cluster. (e, f) Element mapping of Fe and Mn for the cluster shown in b. (g) The XRD of the manganese ferrite clusters and iron oxide cluster (IOC). (h) The magnetization curves of MFC (i), IOC (ii), manganese ferrite nanoparticles (iii), and iron oxide nanoparticles (iv).

Figure 4.1 e and f represent the element (Fe and Mn) mapping of the manganese ferrite cluster shown in Figure 4.1 b. The homogenous distribution of the two elements suggests Mn is evenly doped into the ferrite crystal structures. Using inductively coupled plasma (ICP), the composition of the MFC sample is quantitatively determined to be $\text{Mn}_{0.15}\text{Fe}_{2.85}\text{O}_4$. The low manganese content can ensure the Mn^{2+} dopant only replaces the Fe^{2+} on the octahedral site, which is essential for improving magnetic properties.^[28, 48, 49] The XRD of the MFC and the iron oxide cluster (IOC) is shown in Figure 4.1 g. Compared with the standard XRD pattern of MnFe_2O_4 and Fe_3O_4 , the MFC has a mixed pattern, while the IOC is only consistent with the Fe_3O_4 standard. Finally, the magnetization curves of the MFC, IOC, manganese ferrite nanoparticle (MFNP), and iron oxide nanoparticles (IONP) are shown in Figure 4.1 e. The IOC has a comparable cluster diameter (53 nm) to the MFC. The MFNP and IONP have an equivalent particle size (6 nm) to the primary nanocrystal of the MFC and IOC. A near superparamagnetic pattern with negligible coercivity and remanence is observed for all samples. The clustered materials have higher saturation magnetizations than their nanoparticle counterparts. Meanwhile, the manganese ferrite material is better than iron oxide, indicating the improvement by doping Mn into the Fe_3O_4 lattices. MFC has the highest saturation magnetization, up to 89 emu/g, and the fastest response to the low field.

Figure 4.2 a shows the schematics for the manganese ferrite clusters: the cluster diameter (D_c) that represents the overall physical dimension of the entire cluster, the primary nanocrystal diameter (d_p) that represents the dimension of the primary nanocrystal, and along with the material composition, are the three essential parameters that govern the

magnetic properties of the manganese ferrite clusters. The key to discovering and optimizing the dimensional- and compositional-dependent magnetic properties of these materials relies on the flexibility of the synthesis. Similar to the iron oxide nanocluster synthesis, the cluster diameter, and primary nanocrystal size are independently tuned by water and reaction temperature, respectively.^[50] Additionally, we use Mn/Fe ratio in the synthesis to control the material composition.

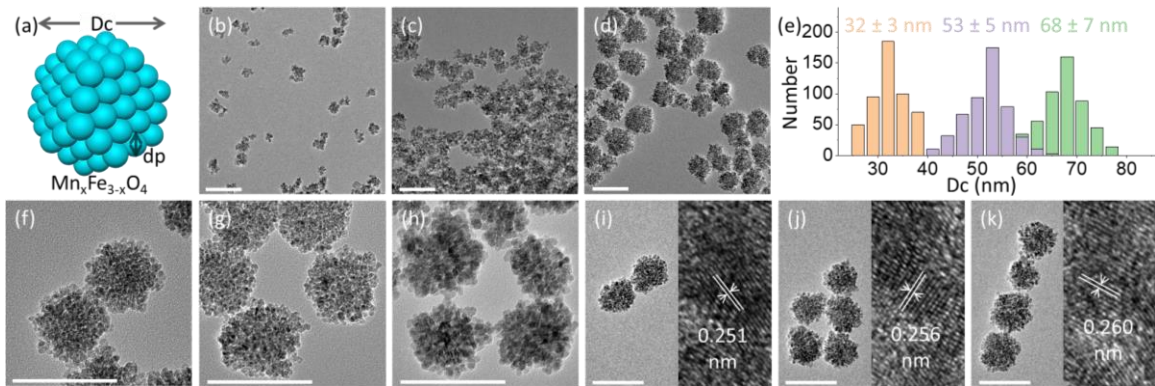


Figure 4. 2. Manganese ferrite clusters with varying dimensions and compositions. (a) The clusters' schematics show they are the hard aggregates of hundreds of primary nanocrystals. (b-d) MFC with increasing cluster diameter of 32 ± 3 nm, 53 ± 5 nm, 68 ± 7 nm, respectively, with the cluster size distribution shown in e. (f-h) MFC with increasing d_p of 3.5 nm, 5.5 nm, 10.5 nm. (h-j) MFC with increasing manganese content of $Mn_{0.05}Fe_{2.95}O_4$, $Mn_{0.15}Fe_{2.85}O_4$, $Mn_{0.6}Fe_{2.4}O_4$. Scale bar: 100 nm.

Shown in Figure 4.2 b-d are the MFC samples with increasing cluster diameters of 32 ± 3 nm, 53 ± 5 nm, 68 ± 7 nm by reducing the amount of water in the synthesis: the deviation is less than 10% (Figure 4.2 e) and therefore, the clusters are pretty monodisperse. Meanwhile, the primary nanocrystal size is constant at 5.5 nm. Water contributes to the metal precursor hydrolysis and primary nanocrystal aggregation processes, and more water leads to a smaller cluster diameter.^[50] Our synthetic method can make manganese ferrite nanoclusters with uniform size distributions from 24 to 100 nm (Table S4.1). Shown in

Figure 4.2 f-h are the MFC samples synthesized at different temperatures, where the increasing primary nanocrystal size of 3.5 nm, 5.5 nm, 10.5 nm, and an equivalent cluster diameter of 68 nm can be observed. The reaction temperature is essential in the primary nanocrystal formation process, and a higher temperature can lead to a larger nanocrystal, which is consistent with the LaMer growth mechanism. The nanocrystal size can be independently tuned from 2 to 11 nm (Table S4.2).

As determined by ICP, the composition is equivalent to $\text{Mn}_{0.15}\text{Fe}_{2.85}\text{O}_4$ for all the MFC samples in Figure 4.2 b-d and f-h. We have noted that the composition of the as-synthesized clusters is only associated with the molar ratio of Mn to Fe in the precursors of the synthesis. However, there is a consistent difference between the final composition of the MFC sample and the Mn/Fe ratio in the precursors. The conversion for Fe into MFC is nearly 100%, while that of Mn is about 8 to 12%. The non-stoichiometry doping of Mn into Fe_3O_4 has been found in many other polyol synthesis systems, which can be attributed to the fact that Fe^{2+} and Fe^{3+} is easier to undergo forced hydrolysis to form oxide than Mn^{2+} .^[15, 49, 51-53] Shown in Figure 4.2 i-k are the MFC samples with increasing Mn content ($\text{Mn}_{0.05}\text{Fe}_{2.95}\text{O}_4$, $\text{Mn}_{0.15}\text{Fe}_{2.88}\text{O}_4$, $\text{Mn}_{0.6}\text{Fe}_{2.4}\text{O}_4$) but equivalent cluster diameter (68 nm) and primary nanocrystal size (5.5 nm). Note that larger clusters tend to be formed when increasing Mn precursors in the synthesis (Table S4.3). More water is needed to reduce the cluster diameter to keep the cluster diameter constant. Moreover, the high-resolution TEM (HRTEM) images indicate a larger spacing along the $\langle 111 \rangle$ direction at higher manganese content, corresponding to the larger Ionic radius of Mn^{2+} than Fe^{2+} . Our synthetic method allows the independent control of the MFC dimensions and compositions, forming a library of the MFC samples.

4.4 The magnetic and magnetothermal properties of manganese ferrite clusters

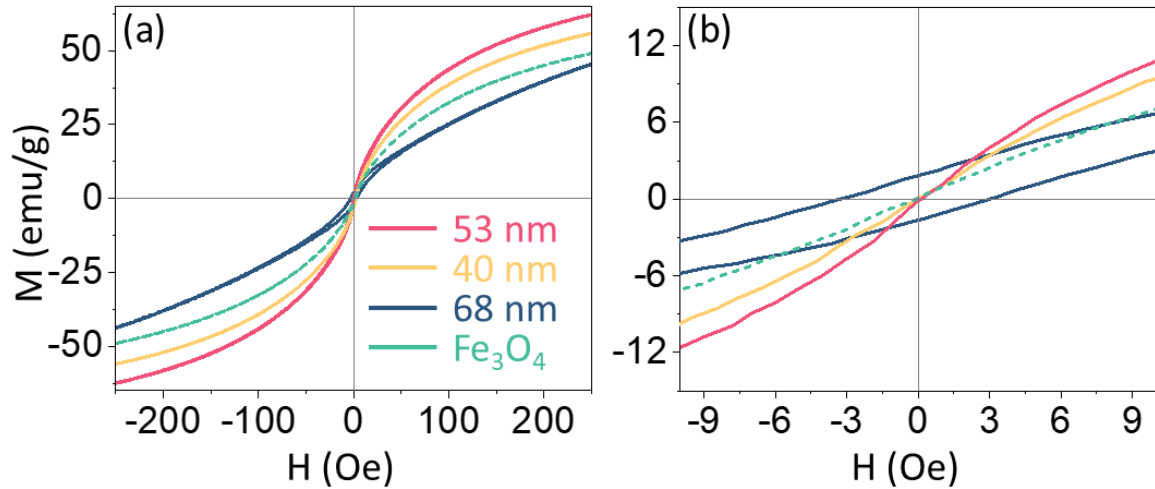


Figure 4. 3. The size-dependent magnetic properties of the manganese ferrite nanoclusters. (a) The magnetization loop curves from -250 Oe to 250 Oe and (b) the loop curves from -10 Oe to 10 Oe. The cluster size (D_c) of the MFCs are 40 nm, 53 nm, and 68 nm, respectively, with the same primary nanocrystal size (d_p) of 5.5 nm and the same composition $Mn_{0.15}Fe_{2.88}O_4$. As a reference, the Fe_3O_4 sample has a D_c of 40 nm and d_p of 5.5 nm.

To understand the magnetic behaviors of the clustered materials at the low field, we compare the magnetization loop curves from -250 Oe to 250 Oe of the MFC samples (d_p 5.5 nm, $Mn_{0.15}Fe_{2.88}O_4$) with different cluster diameters, as shown in Figure 4.3. Here, an iron oxide cluster sample (D_c 40 nm, d_p 5.5 nm) is used as a reference, whose magnetic susceptibility has been proven the highest among IOCs. The MFC and IOC samples generally reach their saturation at around 1,000 Oe (Figure 4.1 h), while at a low field of 100 Oe, equivalent to the surface of a fridge magnet, more than 50% of the saturation magnetization can be achieved for the 53 nm MFC (Figure 4.3 a), indicating a fast response to the external field. The magnetizations of the MFC samples at 100 Oe are about 20% to 40% higher than that of the IOC, suggesting that manganese doping can improve the magnetic properties of the iron oxide materials. Moreover, it is clear that the

magnetizations are dimensional dependent but are not simply proportional to the cluster diameter. To further reveal such dimensional-dependent magnetic properties of the manganese ferrite clusters and optimize their properties, more samples need to be examined, which is shown in the following content.

At an even low field from -10 to 10 Oe, as shown in Figure 4.3 b, a clear difference among the samples is seen: smaller clusters, including the 53 nm and 40 nm MFCs and the 40 nm IOC, are superparamagnetic with zero coercivities, while the larger clusters, 68 nm MFC is ferromagnetic with a coercivity of 2.3 Oe. The presence of coercivity indicates the magnetic spins become “blocked”, which can impede the alignment of the clusters with the external field, corresponding to the lower magnetization value of the 68 nm MFC compared to other samples. As the magnetization curves become more linear at around zero field, we rely on the slope of the initial curve to calculate magnetic susceptibility and find such values of the 40 nm, 53 nm, and 68 nm MFC are 135, 182, and 119, respectively, where the reference 40 nm IOC has a susceptibility of 93. Therefore, the higher susceptibility indicates a better performance of the manganese ferrite materials under the low field than the iron oxide materials.

Conventional magnetic nanomaterials rely on AMF with high magnitude and frequency to achieve desired heating performances. For example, the VEVOR High Frequency Induction Heater can generate a field amplitude of 40 to 800 Oe and frequency up to 1,000 kHz, as illustrated in Figure 4.4 a and Table 4.1. The energy input starts from 15 kW, and the machine needs an extra water-cooling system to maintain a sustainable operation. Such heaters have been widely used for various biomedical and environmental applications. The low voltage heating module (Figure 4.4 b and Figure S4.2), on the contrary, generates an

AMF with a frequency of 133 kHz and a field amplitude from 10 to 50 Oe, and more importantly, it has a power input as low as 10 W and can be powered by the 9 V batteries. Such portable heating devices do not need a complicated cooling system as air cooling is sufficient. According to the linear response theory, the heat generated by the superparamagnetic nanomaterial is proportional to the magnetic susceptibility, the square of the field amplitude, and the frequency of the AMF.⁶ Therefore, applying such a low voltage heating module poses a considerable challenge for magnetic nanomaterials that are greatly limited by their low susceptibilities.

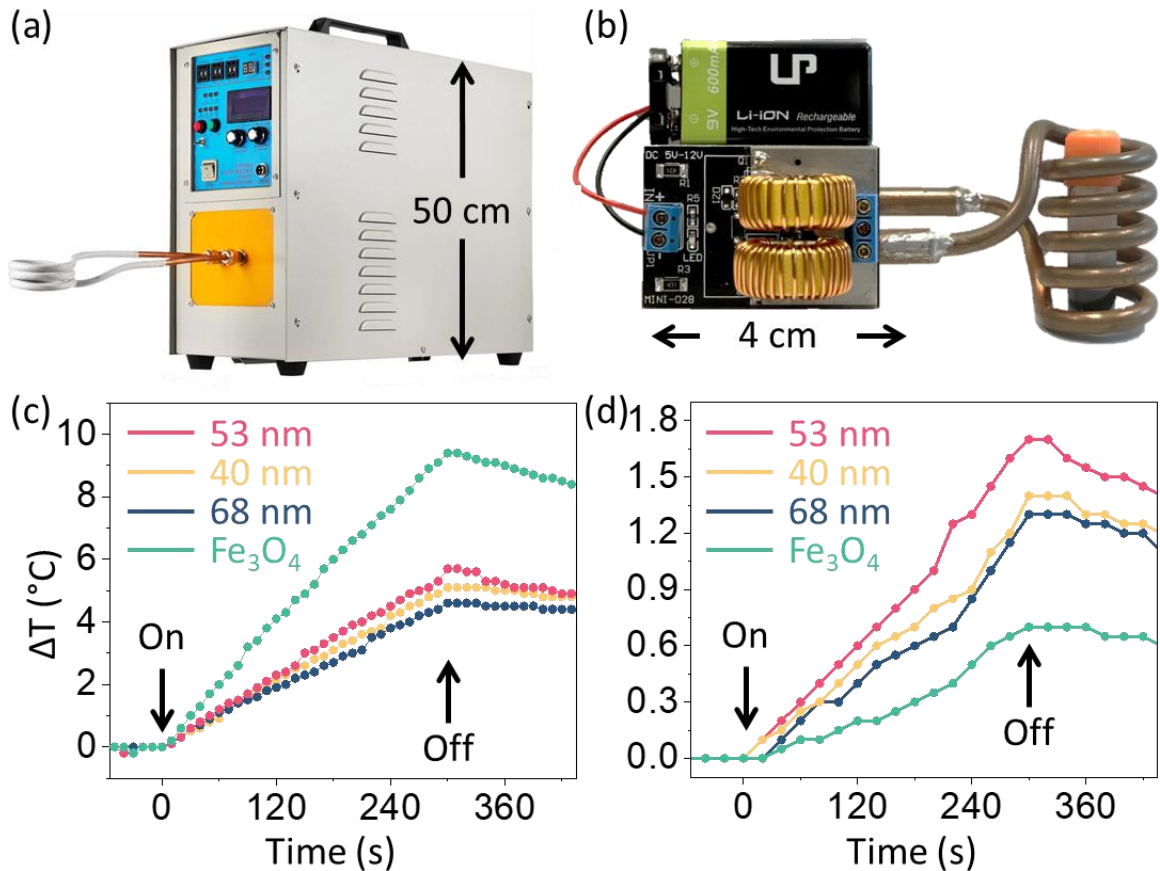


Figure 4. 4. The magnetothermal properties of the manganese ferrite nanoclusters. (a) The commercial induction heater and (c) the temperature-time profile of the samples heated by the commercial induction heater. The sample concentrations are kept at 1 mg/mL and with a frequency of 373 kHz and field strength of 40 Oe. (b) The portable induction heater used in this study and (c) the temperature-time profile of samples heated by the

portable heater. The concentrations of the samples are kept at 4 mg/mL. A 9 V battery powers the device that generates a frequency of 133 kHz and field strength of 25 Oe.

We first examine the heating performance of the MFCs in the conventional heater that provides a field amplitude of 40 Oe and a frequency of 373 kHz, and the result is shown in Figure 4.4 c. As seen from the curves, the temperature of the solution starts to increase as soon as the field is turned on and decreases a little when the field is off, indicating the magnetic heating of these materials. For the 40 nm, 53 nm, and 68 nm MFC, the temperature change in 5 min is 4.9 °C, 5.8 °C, and 4.1 °C, respectively, consistent with their magnetic susceptibilities. However, the iron oxide clusters have a much higher heating performance as the temperature change is 9.7 °C. We attribute this discrepancy to our prior magnetic analysis centers on the DC susceptibility, where the heating of magnetic nanomaterials involves the alternative magnetic field and the AC susceptibility. Although an improved DC susceptibility can lead to a gain in the AC susceptibility, the relationship between the two terms is especially complicated under high frequency.^[24]

Table 4. 1. Comparison of the commercial induction heater and the portable heating device used in this study.

	Commercial	Portable
Cost	\$4,000~10,000	\$10
Power input	15 kW	6~15 W
Cooling	Water cooling	Air cooling
Field Strength	40 ~ 800 Oe	10 ~50 Oe
Frequency	300 ~ 1,000 kHz	133 kHz

Further, we examine the MFCs' ability to operate under low amplitude AMF, which is generated in the coil of the portable induction heater powered by one 9V battery. The field strength and frequency are 25 Oe and 133 kHz, respectively, as measured by an oscilloscope with a sniffer coil probe (Figure S4.3). The power consumption of the portable heater applied in this study is 10 watts as monitored by the ampere meter. The magnetic heating profiles of these samples are shown in Figure 4.4 d. The heating pattern is largely similar to what is seen in Figure 4.4 c, but the scope of the temperature is much lower, which is anticipated due to the low field amplitude and frequency. For the iron oxide sample, the temperature change over 5 min is only 0.7 °C, whereas the temperature increases 1.3 °C, 1.7 °C, and 1.2 °C for the 40 nm, 53 nm, and 68 nm MFC, respectively. The better heating performances of the MFC are consistent with their higher magnetic susceptibilities under the low-frequency field. We also note that the isolated nanoparticles have a negligible response to the portable induction heater. We prepare the 6 nm iron oxide nanoparticles and the 6 nm manganese ferrite nanoparticles, whose magnetic susceptibilities are 9.7 and 12.6, respectively. At the same colloidal concentration, the temperature change is only 0.1 °C in 5 min (Figure S4.4). Our finding confirms that a high susceptibility of the magnetic nanomaterial is the key to magnetic heating under low amplitude AMF. Based on the colloidal concentration and the temperature change, we calculate the specific absorption rate (SAR) for the 53 nm MFC is 6 W/g. Although typical SAR values for biomedical applications are on the order of hundreds to thousands W/g, our materials are more energy-efficient considering the low power input of the heating device.^[22, 23, 30, 47]

To fully explore the manganese ferrite materials' size- and composition-dependent magnetic properties, we rely on our flexible synthesis and compare the susceptibilities and SAR values with different cluster diameters, primary nanocrystal sizes, and compositions. The result is shown in Figure 4.5. In our previous work, where we focused on the iron oxide clusters, we discovered 40 nm is the superparamagnetism to blocked single domain (BSD) transition, where IOC smaller than 40 nm are superparamagnetic and those larger become ferrimagnetic. According to the Langevin model and Neel model, the susceptibility of superparamagnetic material is governed by:^[40, 54]

$$\chi \cong \frac{\mu_0 M_s^2 V}{3kT}$$

Where susceptibility is proportional to the magnetic volume and square of the saturation magnetization, therefore, it is the largest superparamagnetic material that has the highest susceptibility. In this study, we find susceptibility of the MFCs increases with the increasing cluster diameter first and then decreases, reaching the maximum at around 53 nm, as shown in Figure 4.5 a. Moreover, the susceptibility of the MFCs is generally a lot higher than the best of the iron oxide materials (indicated by the dashed line). The susceptibility enhancement by doping Mn into Fe₃O₄ is realized through two factors. On the one hand, the MFCs have higher saturation magnetizations than those of the Fe₃O₄ materials.^[29, 41, 42] On the other hand, MFCs have a larger transition volume: the MFCs with cluster diameter smaller than 55 nm are superparamagnetic, while those larger than 60 nm become ferromagnetic – a pattern similar to the iron oxide materials but the transition occurs at a larger cluster diameter for the MFCs. As susceptibility is proportional to the cubic of the cluster diameter, a much higher susceptibility for the MFCs can be expected.^{[39,}

40]

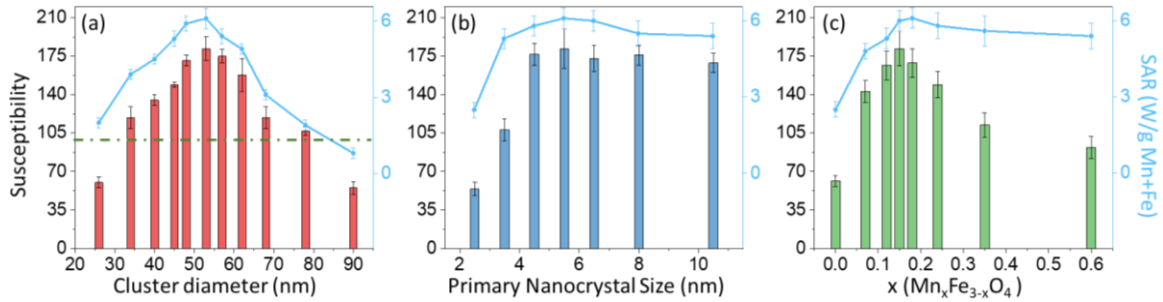


Figure 4. 5. The magnetic susceptibility and SAR values of the MFC samples with varying parameters. (a) The MFC samples have the same d_p of 5.5 nm and composition of $Mn_{0.15}Fe_{2.85}O_4$, where the D_c varies from 25 to 90 nm. The dashed line indicates the susceptibility of the IOC with D_c of 40 nm. (b) The MFC samples have the same D_c of 53 nm and composition of $Mn_{0.15}Fe_{2.85}O_4$, where the d_p varies from 2.5 to 10.5 nm. (c) The MFC samples have the same D_c of 53 nm and d_p of 5.5 nm, where the manganese content in the ferrite composition (x) varies from 0 to 0.6.

The effect of the primary nanocrystal size on the magnetic susceptibility is shown in Figure 4.5 b. Although susceptibility is low when the primary nanocrystal size is smaller than 4 nm, it becomes nearly constant when d_p is larger than 5.5 nm. When the primary nanocrystal is small, they tend to have large surface areas, and the spin-canting effect is prominent, leading to a decreased saturation magnetization (Table S4.2). Another factor is that the exchange interaction, which only occurs in a very short range, is not enough to reconcile among the entire cluster as there are too many primary nanocrystals within.^[40] As a result, a low susceptibility can be anticipated. When the primary nanocrystal is big enough, its dimension has little influence on the magnetic properties, consistent with our previous study on iron oxide materials.

Finally, we show that the content of doped manganese also plays a vital role in their magnetic properties. As seen in Figure 4.5 c, a volcano shape similar to the cluster diameter is found for the manganese doping: susceptibility increases with the increasing manganese content (x) first. It then decreases, and a maximum is located at the composition of

$\text{Mn}_{0.15}\text{Fe}_{2.85}\text{O}_4$. When the manganese content is low, doping more manganese can increase the materials' saturation magnetization as well as susceptibility (Table S4.3). However, when the manganese content is high, the position of the dopant in the Fe_3O_4 lattice has to be considered. Doping Mn^{2+} intends to substitute Fe^{2+} at the octahedral site of the Fe_3O_4 lattice. Studies on the ferrite materials have found that the divalent cation dopant can occupy both the octahedral and tetrahedral sites, which is more common when the dopant to iron ratio is high.^[28, 53, 55, 56] As the magnetic dipoles in the octahedral and tetrahedral sites are antiferromagnetically aligned, the misposition of the dopant cation is unfavorable to the overall magnetization.^[55, 56] Therefore, in the case of our manganese ferrite clusters, a relatively low manganese content contributes to the optimized susceptibility.

4.5 Applying manganese ferrite clusters for contaminants remediation

As we expect, among these parameters, the SAR of the MFCs follows the trend of magnetic susceptibility. This is in agreement with the linear response theory for magnetic fluid heating that a higher magnetic susceptibility ensures a higher heating efficiency.^[26] Based on the observations above, we conclude the MFC with a cluster diameter of 53 nm, primary nanocrystal size of 5.5 nm, and composition of $\text{Mn}_{0.15}\text{Fe}_{2.85}\text{O}_4$ to have the highest magnetic susceptibility heating efficiency among the library of the MFC samples and the highest SAR under the low amplitude AMF generated by a portable heating device. We further apply such excellent heating performance for contaminants remediation.

We first use methylene blue as the target contaminant, which is a type of organic azo-dyes whose concentration in wastewater has raised concerns for both public health and biological ecosystems.^[9, 46] Here, for the first time, we show the feasibility of applying the battery-powered portable heater and the manganese ferrite clusters for methylene blue

degradation. MFC, hydrogen peroxide and methylene blue are mixed and placed right through the central vacancy of the portable heater's coil. The mixture is heated for 60 min while the solution's temperature and the methylene blue concentration are monitored, as shown in Figure 4.5 a and b. Methylene blue degrades as the color fades over time. The temperature of the solution, starting from room temperature at 18 °C, increases linearly in the first 30 min and gradually stabilizes at 31 °C after 40 min, which is due to the heat dissipation from the solution. Using UV-Vis absorption, we determine that 95% of methylene is neutralized over 60 min, indicating a high degradation efficiency for organic dyes.

We further test the remediation capability of the MFCs with streptomycin. Streptomycin is one of the most common antibiotics for bacterial infections, whose overuse can contribute to the antibiotic resistance of the bacteria and make the antibiotics treatment less effective.^[57] In a similar setup, streptomycin is mixed with the MFC and hydrogen peroxide and magnetically heated using the portable heating device for an hour. After decomposing the unreacted hydrogen peroxide with additional MnO₂ and eliminating the colloidal particles by filtration, the reaction mixture is analyzed using HPLC (Figure S4.5), where 76% of the streptomycin is degraded. In the control experiment, the MFCs or hydrogen peroxide alone is insufficient to degrade streptomycin and methylene blue, as shown in Figure 4.5 c. We speculate hydrogen peroxide is activated near the surface of the MFCs to generate hydroxyl radical species that further neutralize the organic molecules.^[58] Studies on magnetic fluid heating show the surface temperature on the magnetic nanoparticles is usually 10 to 20 °C higher than the bulk solution due to localized heating of the nanoparticles.^[10-14] In another control experiment, the degradation is less significant even

when hydrogen peroxide is put in an elevated temperature (35 °C water bath) slightly higher than the magnetically heated MFCs solution. The above experiments confirm that our manganese ferrite clusters are highly efficient nanoheaters under low amplitude AMF, which opens the potential to reduce the cost of commercial heating devices.

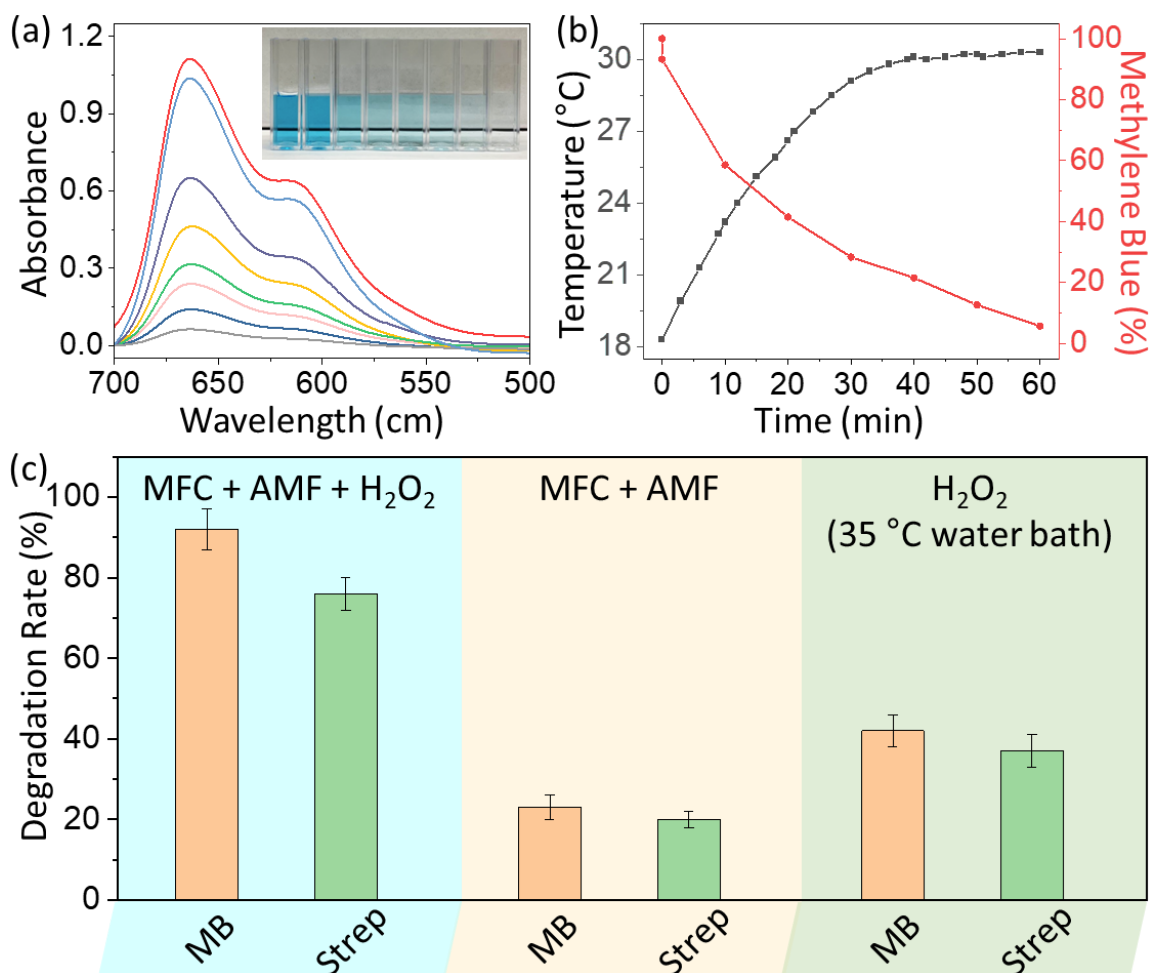


Figure 4. 6. Applying the MFC for the remediation of emerging contaminants. (a) The UV-Vis absorbance before, during, and after the magnetothermal treatment of methylene blue. Inset shows the picture of these cuvettes after being diluted 100 times using water. (b) The temperature and the methylene blue concentration of the mixture over time. (c) Comparison of the contaminants degradation efficiency under different conditions. The concentration is 4 mg/mL for MFC, 0.2 mg/mL for methylene blue, 0.4 mg/mL for streptomycin, and 3 mg/mL H₂O₂.

4.6 Conclusion

In summary, we have explored the dimension- and composition-dependent magnetic properties of the manganese ferrite clusters. Using our flexible synthesis, we have developed a library of MFCs where the cluster diameter, primary nanocrystal size, and manganese content can be independently controlled. The highest susceptibility and magnetic heating performance are found at an intermediate cluster diameter of 53 nm and manganese content of $\text{Mn}_{0.15}\text{Fe}_{2.85}\text{O}_4$. The optimized MFC demonstrates excellent heating performance at low amplitude AMF generated by the battery-operated inductive heating device. We have achieved highly efficient degradation of emerging contaminants using the MFCs. Because our portable devices are self-contained, they can be easily incorporated into many industrial and biological applications, such as wastewater treatment plants and biological incubators. These results demonstrate that our MFCs products are well-positioned for environmental applications and biotechnologies.

4.7 Experimental section

4.7.1 MFC Preparation

The detailed procedures for the synthesis and surface coating of the MFCs can be found in our previous video publication on JoVE. To prepare the MFCs with specific dimensions and composition, FeCl_3 and MnCl_2 with a total amount of 2 mmol is dissolved in 20 mL ethylene glycol, followed by 250 mg polyacrylic acid (PAA, $M_w \sim 6000$), 1,200 mg urea, and 0.2 to 2.0 mL water. This reaction mixture is mixed well and transferred to a 50 mL polyphenylene-lined (PPL) reactor sealed in a stainless-steel autoclave. The reactor is heated at 170 to 260 °C for 20 hours in an oven. The as-synthesized MFCs with PAA coating are washed using magnetic separation and dissolved in water. The detailed molar

ratio of Mn to Fe, the amount of water, and the reaction temperature for synthesis are listed in Table S1-S3.

To graft polysulfonate to the MFCs, the original PAA coating is first replaced by nitrodopamine. The amine groups are then chemically conjugated with carboxylic groups of the polysulfonate, P(AA-co-AMPS-co-PEG), using EDC reaction. Add 10 mg nitrodopamine in 10 mL MFCs solution with a concentration of roughly 10 mg/mL. The nitrodopamine-coated MFCs will rapidly aggregate and can be easily magnetically collected. Add 20 mg EDC, 100 mg MES, 60 mg P(AA-co-AMPS-co-PEG), and 5 mL water into this magnetic collection and place the mixture in a probe sonicator. The strong sonication effect can facilitate the conjugation between the nanoclusters and the polysulfonate and allow the nanoclusters to disperse in water homogeneously. The polysulfonate coated MFCs are washed several times using magnetic separation.

Preparation of the 6 nm iron oxide nanoparticles (IONP-6) and the 6 nm manganese ferrite nanoparticles (MFNP-6) follows the well-established protocol by Sun et al. To synthesize IONP-6, add 2 mmol Fe(acac)₃, 10 mmol 1,2-hexadecadiol, 6 mmol oleic acid, and 6 mmol oleylamine in 20 mL benzyl ether. Heat the mixture to 200 °C for 2 h and then reflux at 300 °C for another 1 h. To synthesize MFNP-6, add 1.5 mmol Fe(acac)₃ and 0.5 mmol Mn(acac)₂ as the metal precursors while keeping other conditions the same. After cooling down, the as-synthesized nanoparticles are washed by ultracentrifuge using hexane for several times. The as-synthesized nanoparticles are transferred to water by ligand exchange reaction using polyethylene glycol. Mix 1 mL hexane dispersion of the nanoparticles (10 mg/mL) with 3 mL diethyl ether and add 10 mg nitro-dopamine functionalized polyethylene glycol (nitro-Dopa-PEG, 5 k). Vigorously stir the mixture for 30 min and add

5 mL to stir for another 30 min. The nanoparticles are washed again by ultracentrifuge using water and finally are dispersed in water. The concentration of the nanoparticles is determined by ICP using the same procedures as the MFCs.

4.7.2 Materials characterization

The morphologies of the MFCs are characterized by transmission electron microscope (TEM, JOEL 2100F). To prepare the TEM sample, add 5 μ L diluted MFC aqueous solution (\sim 0.1 mg/mL) on a TEM grid and dry at room temperature. The overall cluster diameter (D_c) and the primary nanocrystal size (d_p) are surveyed. The selected area electron diffraction (SAED) pattern is obtained on a single cluster. The element mapping of manganese and iron is acquired through electron energy loss spectroscopy (EELS).

The crystalline structure of the MFCs is determined by X-ray diffraction (XRD). To prepare the XRD samples, drop 0.1 mL MFC aqueous solution (\sim 4 mg/mL) in the center of a glass slide. This process can be assisted by putting a magnet beneath the glass slide, and the MFCs would accumulate in the center. The XRD patterns are acquired on the Bruker D8 Discovery 2D X-ray Diffractometer with two-theta (2θ) from 20 to 80°.

The composition of the materials ($Mn_xFe_{3-x}O_4$) and the concentration of the MFCs aqueous solution are quantitatively determined by inductively coupled plasma (ICP). To prepare the ICP samples, mix 0.1 mL MFCs solution with 0.4 mL hydrochloric acid (37%) to fully dissolve the nanomaterials until a clear yellow solution is seen. Add 9.5 mL nitric acid (1%). Prepare the Mn and Fe standard solutions with a concentration of 1 ppm, 5 ppm, 10 ppm, 20 ppm, 50 ppm, and 100 ppm, respectively, where 1,000 ppm is equivalent to 1

mg/mL. The samples and the standard solutions are then run through the ICP to measure the concentrations of Mn (C_{Mn}) and Iron (C_{Fe}) of the initial MFCs solutions.

The materials composition is calculated as:

$$x = \frac{3C_{Mn}}{C_{Fe} + C_{Mn}}$$

The dimensions and compositions of the MFCs discussed in this work are listed in Table S1-S3.

The concentration of MFCs aqueous solution is calculated as:

$$C_{Mn_xFe_{3-x}O_4} = C_{Mn} + C_{Fe} + \frac{64x}{54.94}$$

Then these MFCs solutions are diluted or concentrated to 4 mg/mL and 8 mg/mL for further magnetic heating evaluation.

The magnetic properties of the MFCs are characterized by the vibrating-sample magnetometer (VSM). To prepare the VSM samples, first put 10 mg gypsum on a glass slide and 0.1 mL concentrated MFCs aqueous solution (~4 mg/mL) and mix well to form a dark brown paste. This paste is dried at room temperature overnight, ground into fine powders, and then transferred into the sample holder for VSM. The magnetization loop curves are obtained in the following range: -10,000 Oe to 10000 Oe with a step of 100 Oe, -100 Oe to 100 Oe with a step of 1 Oe, and -5 Oe to 5 Oe with a step 0.05 Oe. Each data point takes 1 second to collect.

The exact mass of the materials (m) in each VSM measurement is determined by ICP. Add 0.4 mL hydrochloric acid (37%) in the above VSM samples, followed by 9.6 mL nitric acid

(1%). This solution is then filtered to get rid of the gypsum and subject to the same ICP measurement as mentioned above. The saturation magnetization (M_{sat}) is calculated based on the maximum magnetization of the curve from -10,000 to 10,000 Oe:

$$M_{sat} = \frac{M_{max}}{m}$$

The volume susceptibility (χ) of the MFCs is calculated based on the slope (dM/dH) of the magnetization curve from 0 to 5 Oe:

$$\chi = \frac{4\pi \rho}{m} \frac{dM}{dH}$$

Where ρ is the density of the materials and is close to bulk magnetite (5.17 g/cm³).

4.7.3 Magnetic heating and contaminants remediation

The low amplitude AMF is generated by the ZVS Driver Module (5V-12V ZVS Low Voltage Induction Heating Board). The heating coil has 5 turns with a diameter of 2 cm. The device is powered using one 9 V battery (rechargeable, 600 mAh) and monitored by a digital DC ampere meter. The field amplitude and frequency of the AMF generated by the battery-operated heating device is determined by an oscilloscope. The probe of the oscilloscope is a sniffer coil with 3 turns and a diameter of 9.78 mm. The field frequency is directly given by the oscilloscope when placing the probe in the center of the heating coil. The amplitude is calculated as:

$$B = \frac{V_{PP}}{4\pi^2 R^2 N f}$$

Where VPP is the peak-to-peak voltage given by the oscilloscope, R is the radius of the sniffer coil (4.89×10^{-3} m), N is the number of turns (3), and f is the frequency. The unit of the calculated field amplitude is Tesla and is then converted into Oersted with a conversion of $1 \text{ T} = 10,000 \text{ Oe}$.

Put a 3.5 mL glass vial in the center of the heating coil and add 1 mL 4 mg/mL MFCs solution. The heating module is turned on for 5 min while an optical fiber temperature probe monitors the temperature of the solution. The specific absorption rate of the materials is calculated based on the temperature change (ΔT):

$$SAR = \frac{\Delta T c_{H_2O}}{t C_{MFC}}$$

Where c_{H_2O} is the specific heat capacity of water ($4.184 \text{ J/g } ^\circ\text{C}$), C_{MFC} is the concentration of the MFCs (4 mg/mL), t is the measurement time (300 s).

To evaluate the application of the MFCs toward the contaminant remediation, methylene blue and streptomycin are used as the target contaminants, with hydrogen peroxide as the radical generator. For methylene degradation experiment, add 0.5 mL MFCs solution (8 mg/mL , Dc 53 nm, dp 5.5 nm, $\text{Mn}_{0.15}\text{Fe}_{2.85}\text{O}_4$), 0.1 mL methylene blue (2 mg/mL), 0.1 mL hydrogen peroxide (30 mg/mL), and 0.3 mL water into a 3.5 mL glass vial. The solution is mixed well and placed in the coil. The heating module is turned on for 60 min with the temperature of the solution monitored. Note that this process usually takes two to three batteries consecutively. Every 5 min, 0.01 mL solution is taken out of the vial and diluted to 1 mL for UV-Vis test from 500 to 700 nm to analyze the concentration of methylene blue.

The degradation of streptomycin is carried out in a similar setting. Add 0.5 mL MFCs solution (8 mg/mL, Dc 53 nm, dp 5.5 nm, $\text{Mn}_{0.15}\text{Fe}_{2.85}\text{O}_4$), 0.1 mL streptomycin (4 mg/mL), 0.1 mL hydrogen peroxide (30 mg/mL), and 0.3 mL water into a 3.5 mL glass vial. The solution is mixed well, and the heating module is turned on for 60 min. After magnetic heating treatment, add 1 mg solid manganese dioxide to the solution to remove unreacted hydrogen peroxide. The solution is then filtered using a 100 kDa membrane to remove the MFCs and solid MnO_2 . Add 0.1 mL of the filtered solution, 0.4 mL H_3PO_4 (0.25 M, pH = 6), and 0.5 mL acetone nitrile. The mixture is analyzed by reversed-phase high-performance liquid chromatography (RP-HPLC) to determine the remaining streptomycin content.

The first control experiment is performed by mixing the MFCs with methylene or streptomycin with the same concentration and placed in the AMF for 60 minutes. The second control experiment is performed by mixing hydrogen peroxide with methylene or streptomycin in a 35 °C water bath for 60 minutes.

4.8 Supplemental figures and tables

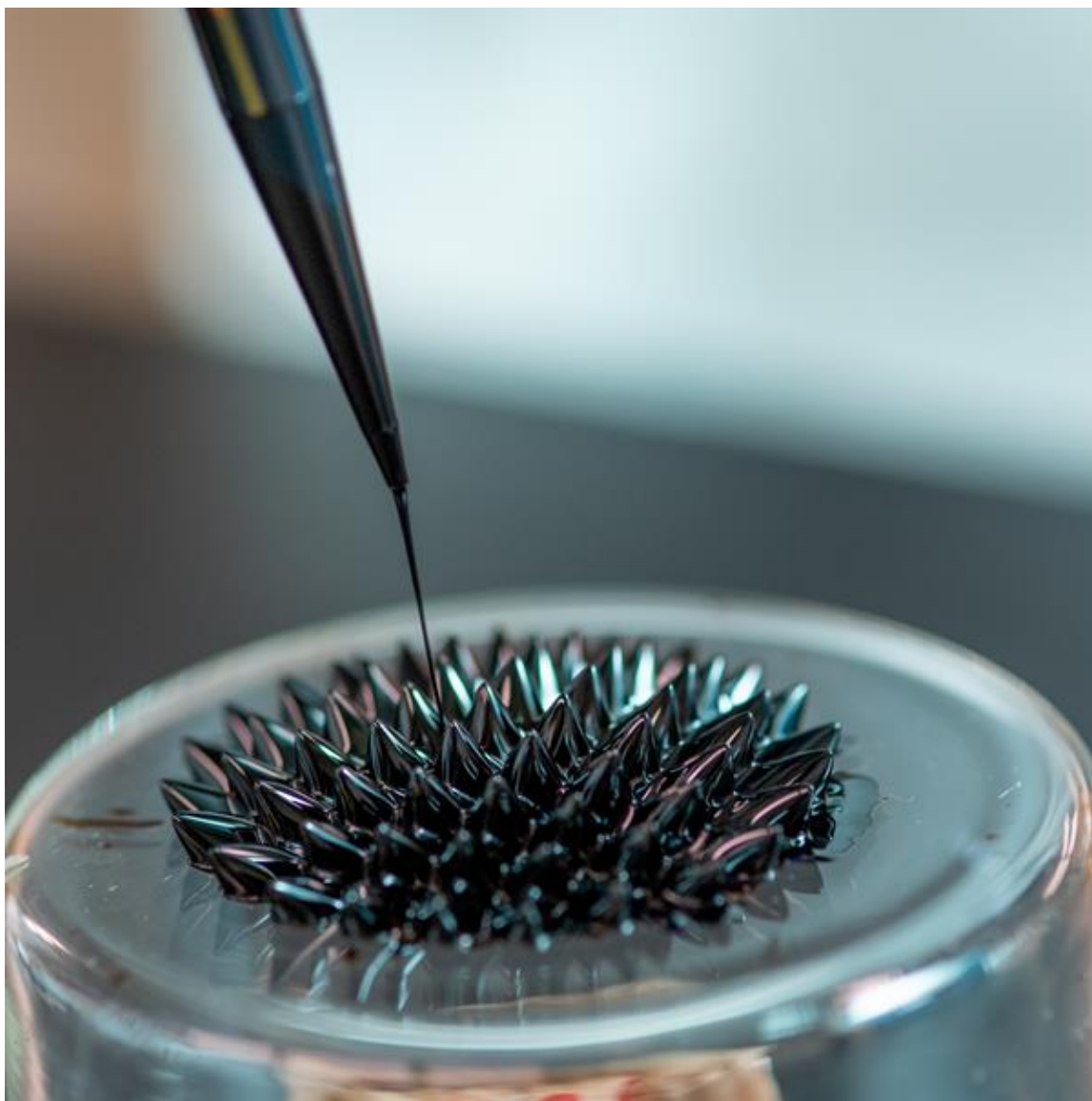


Figure S4. 1. Manganese ferrite nanoclusters as ferrofluid. The aqueous solution of the manganese ferrite nanoclusters (D_c 53 nm, d_p 5.5 nm, $Mn_{0.15}Fe_{2.85}O_4$) is placed on top of a handheld magnet. The concentration of the solution is 20 mg/mL.

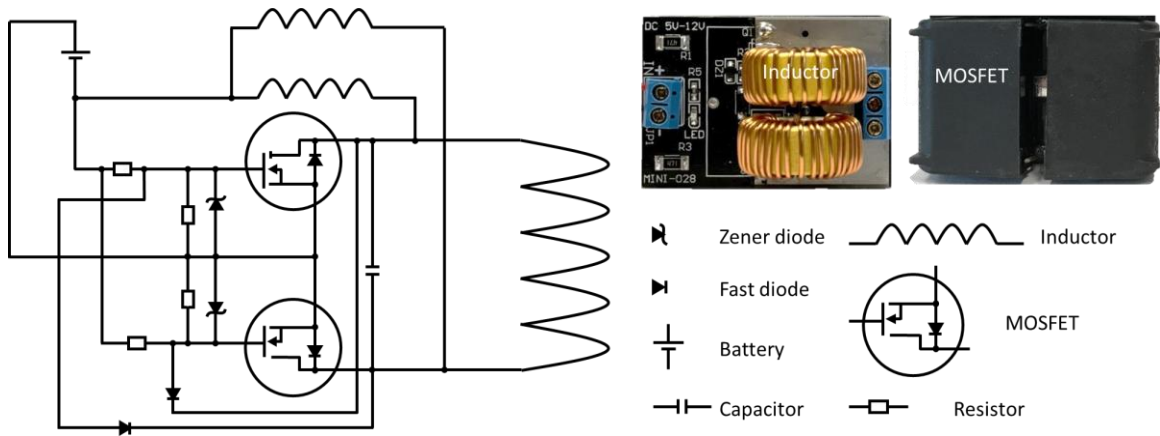


Figure S4. 2. The electronic circuit diagram of the portable heating device used in this study.

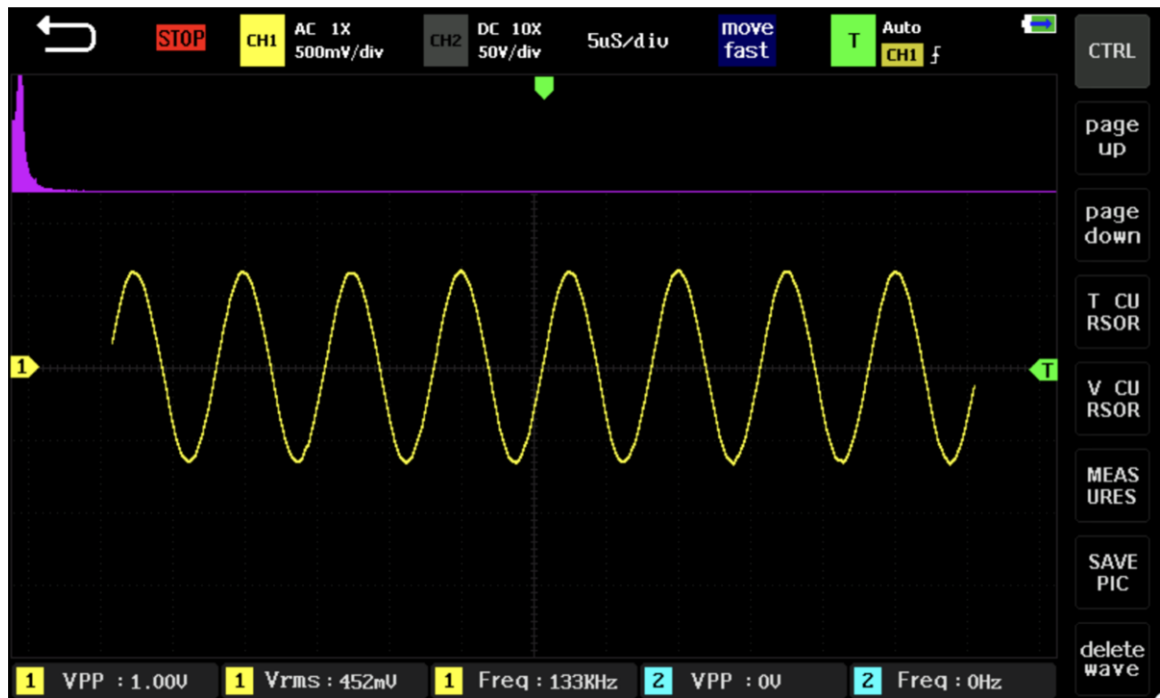


Figure S4. 3. Reading from the oscilloscope. Based on the frequency of 133 kHz and the peak-to-peak voltage of 1.00 V, the field amplitude is calculated to be 25 Oe.

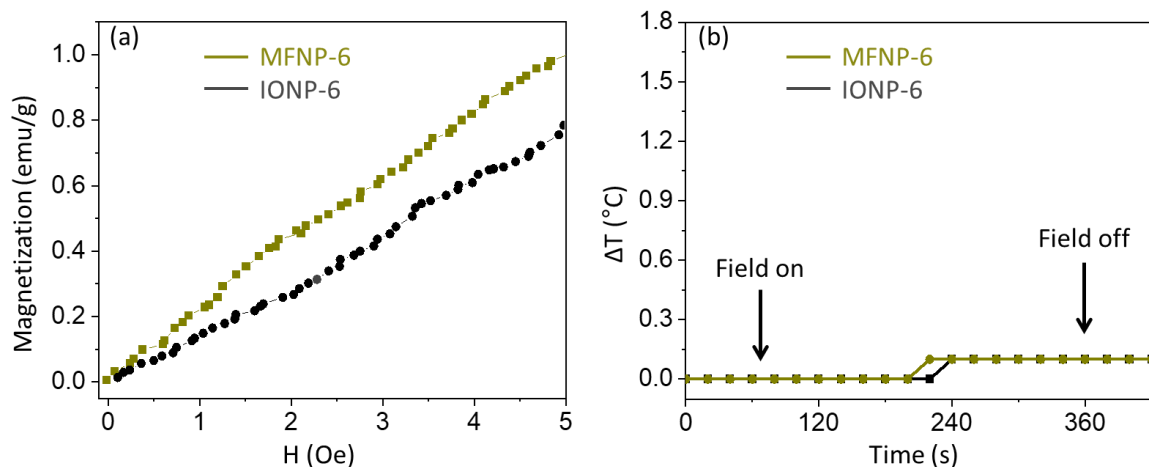


Figure S4. 4. The magnetic and magnetothermal properties of the isolated nanoparticles. (a) The magnetization curve of the MFNP-6 and IONP-6 from 0 to 5 Oe. The initial magnetic susceptibility for MFNP-6 and IONP-6 is 12.6 and 9.7, respectively. (b) The temperature-time profile of MFNP-6 and IONP-6 heated by the portable heater. The concentrations are 4 mg/mL. The frequency is 133 kHz, and the field strength inside the coil is 25 Oe. The temperature increase is negligible.

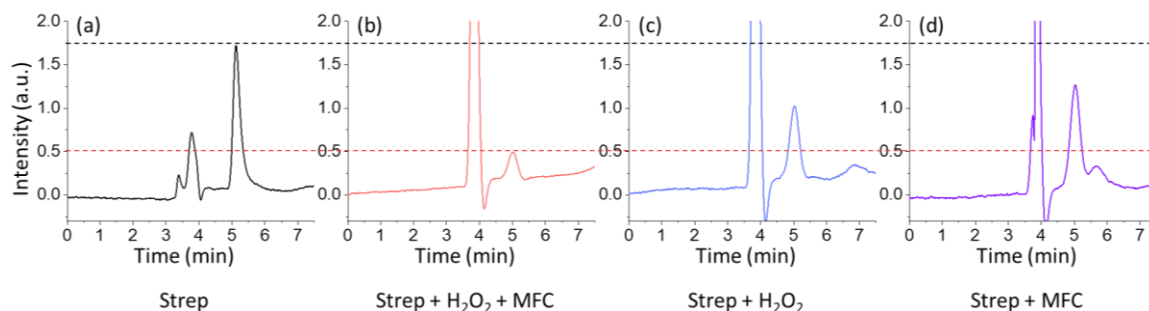


Figure S4. 5. HPLC analysis of streptomycin and its degradation by the MFCs and hydrogen peroxide. (a) Pure streptomycin. (b) Streptomycin with hydrogen peroxide and the MFCs heated using the portable heating device. (c) Streptomycin with hydrogen peroxide in a 35 °C water bath. (d) Streptomycin with the MFCs heated using the portable heating device. Streptomycin is eluted at 4.5~5.5 min. Compared to the pure streptomycin, the content of streptomycin left in b-d is 24%, 63%, 80%, respectively.

Table S4. 1. Information of the MFCs shown in Figure 4.4 a. The cluster size of the MFCs is increased by reducing the amount of water added in the synthesis.

Composition	H ₂ O (mL)	Temp (°C)	Mn/Fe	Dc (nm)	dp (nm)	Msat (emu/g)	Coercivity (Oe)	Susceptibility
Mn _{0.15} Fe _{2.85} O ₄	1.95	215	0.525	26	5.5	72	0	60
Mn _{0.15} Fe _{2.85} O ₄	1.5	215	0.525	34	5.5	80	0	119
Mn _{0.15} Fe _{2.85} O ₄	1.25	215	0.525	40	5.5	84	0	135
Mn _{0.15} Fe _{2.85} O ₄	1	215	0.525	45	5.5	86	0	149
Mn _{0.15} Fe _{2.85} O ₄	0.85	215	0.525	48	5.5	88	0	171
Mn _{0.15} Fe _{2.85} O ₄	0.75	215	0.525	53	5.5	89	0	182
Mn _{0.15} Fe _{2.85} O ₄	0.7	215	0.525	57	5.5	90	0.7	175
Mn _{0.15} Fe _{2.85} O ₄	0.6	215	0.525	62	5.5	91	1.5	158
Mn _{0.15} Fe _{2.85} O ₄	0.55	215	0.525	68	5.5	91	2.3	119
Mn _{0.15} Fe _{2.85} O ₄	0.45	215	0.525	78	5.5	92	4.6	107
Mn _{0.15} Fe _{2.85} O ₄	0.2	215	0.525	90	5.5	93	15.8	55

Table S4. 2. Information of the MFCs shown in Figure 4.4 b. The primary nanocrystal size the MFCs is increased by increasing the reaction temperature.

Composition	H ₂ O (mL)	Temp (°C)	Mn/Fe	Dc (nm)	dp (nm)	Msat (emu/g)	Coercivity (Oe)	Susceptibility
Mn _{0.15} Fe _{2.85} O ₄	0.75	170	0.525	53	2.5	74	3.5	54
Mn _{0.15} Fe _{2.85} O ₄	0.75	185	0.525	53	3.5	80	2.8	108
Mn _{0.15} Fe _{2.85} O ₄	0.75	200	0.525	53	4.5	88	0.2	177
Mn _{0.15} Fe _{2.85} O ₄	0.75	215	0.525	53	5.5	89	0	182
Mn _{0.15} Fe _{2.85} O ₄	0.75	230	0.525	53	6.5	89	0	173
Mn _{0.15} Fe _{2.85} O ₄	0.75	245	0.525	53	8	90	0.2	176
Mn _{0.15} Fe _{2.85} O ₄	0.75	260	0.525	53	10.5	91	0.2	169

Table S4. 3. Information of the MFCs shown in Figure 4.4 c. The manganese content of the MFCs is increased by increasing the Mn/Fe ratio of the precursors.

Composition	H ₂ O (mL)	Temp (°C)	Mn/Fe	Dc (nm)	dp (nm)	Msat (emu/g)	Coercivity (Oe)	Susceptibility
Fe ₃ O ₄	1.35	215	0	53	5.5	83	5.8	61
Mn _{0.06} Fe _{2.94} O ₄	0.6	215	0.333	53	5.5	84	1.4	143
Mn _{0.12} Fe _{2.88} O ₄	0.65	215	0.429	53	5.5	87	0.3	167
Mn _{0.15} Fe _{2.85} O ₄	0.75	215	0.525	53	5.5	88	0	182
Mn _{0.18} Fe _{2.82} O ₄	1.05	215	0.6	53	5.5	90	0.2	169
Mn _{0.24} Fe _{2.76} O ₄	1.3	215	0.667	53	5.5	92	0.6	149
Mn _{0.35} Fe _{2.65} O ₄	1.65	215	0.818	53	5.5	95	1.1	112
Mn _{0.6} Fe _{2.4} O ₄	2	215	1	53	5.5	102	6.8	92

References in Chapter 4

- [1] Akbarzadeh, A.; Samiei, M.; Davaran, S., Magnetic nanoparticles: preparation, physical properties, and applications in biomedicine. *Nanoscale research letters* **2012**, *7* (1), 1-13.
- [2] Albarqi, H. A.; Wong, L. H.; Schumann, C.; Sabei, F. Y.; Korzun, T.; Li, X. N.; Hansen, M. N.; Dhagat, P.; Moses, A. S.; Taratula, O.; Taratula, O., Biocompatible Nanoclusters with High Heating Efficiency for Systemically Delivered Magnetic Hyperthermia. *Acs Nano* **2019**, *13* (6), 6383-6395.
- [3] Chen, R.; Romero, G.; Christiansen, M. G.; Mohr, A.; Anikeeva, P., Wireless magnetothermal deep brain stimulation. *Science* **2015**, *347* (6229), 1477-1480.
- [4] Di Corato, R.; Espinosa, A.; Lartigue, L.; Tharaud, M.; Chat, S.; Pellegrino, T.; Ménager, C.; Gazeau, F.; Wilhelm, C., Magnetic hyperthermia efficiency in the cellular environment for different nanoparticle designs. *Biomaterials* **2014**, *35* (24), 6400-6411.
- [5] Guardia, P.; Di Corato, R.; Lartigue, L.; Wilhelm, C.; Espinosa, A.; Garcia-Hernandez, M.; Gazeau, F.; Manna, L.; Pellegrino, T., Water-soluble iron oxide nanocubes with high values of specific absorption rate for cancer cell hyperthermia treatment. *ACS nano* **2012**, *6* (4), 3080-3091.
- [6] Noh, S. H.; Moon, S. H.; Shin, T. H.; Lim, Y.; Cheon, J., Recent advances of magneto-thermal capabilities of nanoparticles: From design principles to biomedical applications. *Nano Today* **2017**, *13*, 61-76.
- [7] Gallo-Cordova, A.; Castro, J. J.; Winkler, E. L.; Lima Jr, E.; Zysler, R. D.; del Puerto Morales, M.; Ovejero, J. G.; Streitwieser, D. A., Improving degradation of real wastewaters with self-heating magnetic nanocatalysts. *Journal of Cleaner Production* **2021**, *308*, 127385.
- [8] Ribeiro, R. S.; Gallo, J.; Bañobre-López, M.; Silva, A. M.; Faria, J. L.; Gomes, H. T., Enhanced performance of cobalt ferrite encapsulated in graphitic shell by means of AC magnetically activated catalytic wet peroxide oxidation of 4-nitrophenol. *Chemical Engineering Journal* **2019**, *376*, 120012.
- [9] Rivera, F.; Recio, F.; Palomares, F.; Sánchez-Marcos, J.; Menéndez, N.; Mazarío, E.; Herrasti, P., Fenton-like degradation enhancement of methylene blue dye with magnetic heating induction. *Journal of Electroanalytical Chemistry* **2020**, *879*, 114773.
- [10] Capistrano, G.; Rodrigues, H. F.; Zufelato, N.; Goncalves, C.; Cardoso, C. G.; Silveira-Lacerda, E. P.; Bakuzis, A. F., Noninvasive intratumoral thermal dose determination during in vivo magnetic nanoparticle hyperthermia: combining surface temperature measurements and computer simulations. *International Journal of Hyperthermia* **2020**, *37* (3), 120-140.
- [11] Dong, J.; Zink, J. I., Taking the temperature of the interiors of magnetically heated nanoparticles. *ACS nano* **2014**, *8* (5), 5199-5207.
- [12] Huang, H.; Delikanli, S.; Zeng, H.; Ferkey, D. M.; Pralle, A., Remote control of ion channels and neurons through magnetic-field heating of nanoparticles. *Nature nanotechnology* **2010**, *5* (8), 602-606.
- [13] Riedinger, A.; Guardia, P.; Curcio, A.; Garcia, M. A.; Cingolani, R.; Manna, L.; Pellegrino, T., Subnanometer local temperature probing and remotely controlled

- drug release based on azo-functionalized iron oxide nanoparticles. *Nano letters* **2013**, *13* (6), 2399-2406.
- [14] Rodrigues, H. F.; Capistrano, G.; Mello, F. M.; Zufelato, N.; Silveira-Lacerda, E.; Bakuzis, A. F., Precise determination of the heat delivery during in vivo magnetic nanoparticle hyperthermia with infrared thermography. *Physics in Medicine & Biology* **2017**, *62* (10), 4062.
- [15] Gupta, R.; Sharma, D., Manganese-Doped Magnetic Nanoclusters for Hyperthermia and Photothermal Glioblastoma Therapy. *Acs Applied Nano Materials* **2020**, *3* (2), 2026-2037.
- [16] Manuchehrabadi, N.; Gao, Z.; Zhang, J.; Ring, H. L.; Shao, Q.; Liu, F.; McDermott, M.; Fok, A.; Rabin, Y.; Brockbank, K. G., Improved tissue cryopreservation using inductive heating of magnetic nanoparticles. *Science translational medicine* **2017**, *9* (379), eaah4586.
- [17] Song, Q.; Zhang, Z. J., Controlled Synthesis and Magnetic Properties of Bimagnetic Spinel Ferrite CoFe₂O₄ and MnFe₂O₄ Nanocrystals with Core-Shell Architecture. *Journal of the American Chemical Society* **2012**, *134* (24), 10182-10190.
- [18] Lak, A.; Dieckhoff, J.; Ludwig, F.; Scholtyssek, J. M.; Goldmann, O.; Lünsdorf, H.; Eberbeck, D.; Kornowski, A.; Kraken, M.; Litterst, F., Highly stable monodisperse PEGylated iron oxide nanoparticle aqueous suspensions: a nontoxic tracer for homogeneous magnetic bioassays. *Nanoscale* **2013**, *5* (23), 11447-11455.
- [19] Tromsdorf, U. I.; Bruns, O. T.; Salmen, S. C.; Beisiegel, U.; Weller, H., A highly effective, nontoxic T₁ MR contrast agent based on ultrasmall PEGylated iron oxide nanoparticles. *Nano letters* **2009**, *9* (12), 4434-4440.
- [20] Kirschning, A.; Kupracz, L.; Hartwig, J., New Synthetic Opportunities in Miniaturized Flow Reactors with Inductive Heating. *Chemistry Letters* **2012**, *41* (6), 562-570.
- [21] Wang, W.; Tuci, G.; Cuong, D. V.; Liu, Y. F.; Rossin, A.; Luconi, L.; Nhut, J. M.; Lam, N. D.; Cuong, P. H.; Giambastiani, G., Induction Heating: An Enabling Technology for the Heat Management in Catalytic Processes. *Acs Catalysis* **2019**, *9* (9), 7921-7935.
- [22] Lartigue, L.; Hugounenq, P.; Alloyeau, D.; Clarke, S. P.; Levy, M.; Bacri, J.-C.; Bazzi, R.; Brougham, D. F.; Wilhelm, C.; Gazeau, F., Cooperative organization in iron oxide multi-core nanoparticles potentiates their efficiency as heating mediators and MRI contrast agents. *ACS nano* **2012**, *6* (12), 10935-10949.
- [23] Niculaes, D.; Lak, A.; Anyfantis, G. C.; Marras, S.; Laslett, O.; Avugadda, S. K.; Cassani, M.; Serantes, D.; Hovorka, O.; Chantrell, R., Asymmetric assembling of iron oxide nanocubes for improving magnetic hyperthermia performance. *ACS nano* **2017**, *11* (12), 12121-12133.
- [24] Tong, S.; Quinto, C. A.; Zhang, L.; Mohindra, P.; Bao, G., Size-dependent heating of magnetic iron oxide nanoparticles. *ACS nano* **2017**, *11* (7), 6808-6816.
- [25] Vasilakaki, M.; Binns, C.; Trohidou, K., Susceptibility losses in heating of magnetic core/shell nanoparticles for hyperthermia: a Monte Carlo study of shape and size effects. *Nanoscale* **2015**, *7* (17), 7753-7762.
- [26] Anandhi, J. S.; Jacob, G. A.; Joseyphus, R. J., Factors affecting the heating efficiency of Mn-doped Fe₃O₄ nanoparticles. *Journal of Magnetism and*

Magnetic Materials **2020**, 512.

- [27] Del Sol-Fernandez, S.; Portilla-Tundidor, Y.; Gutierrez, L.; Odio, O. F.; Reguera, E.; Barber, D. F.; Morales, M. P., Flower-like Mn-Doped Magnetic Nanoparticles Functionalized with $\alpha(v)\beta(3)$ -Integrin-Ligand to Efficiently Induce Intracellular Heat after Alternating Magnetic Field Exposition, Triggering Glioma Cell Death. *Acs Applied Materials & Interfaces* **2019**, 11 (30), 26648-26663.
- [28] Jang, J. T.; Nah, H.; Lee, J. H.; Moon, S. H.; Kim, M. G.; Cheon, J., Critical Enhancements of MRI Contrast and Hyperthermic Effects by Dopant-Controlled Magnetic Nanoparticles. *Angewandte Chemie-International Edition* **2009**, 48 (7), 1234-1238.
- [29] Qu, Y.; Li, J. B.; Ren, J.; Leng, J. Z.; Lin, C.; Shi, D. L., Enhanced Magnetic Fluid Hyperthermia by Micellar Magnetic Nanoclusters Composed of $MnxZn1-xFe_2O_4$ Nanoparticles for Induced Tumor Cell Apoptosis. *Acs Applied Materials & Interfaces* **2014**, 6 (19), 16867-16879.
- [30] Noh, S.-h.; Na, W.; Jang, J.-t.; Lee, J.-H.; Lee, E. J.; Moon, S. H.; Lim, Y.; Shin, J.-S.; Cheon, J., Nanoscale magnetism control via surface and exchange anisotropy for optimized ferrimagnetic hysteresis. *Nano letters* **2012**, 12 (7), 3716-3721.
- [31] Das, K. K.; Reddy, R. C.; Bagoji, I. B.; Das, S.; Bagali, S.; Mullur, L.; Khodnapur, J. P.; Biradar, M., Primary concept of nickel toxicity—an overview. *Journal of basic and clinical physiology and pharmacology* **2019**, 30 (2), 141-152.
- [32] Leyssens, L.; Vinck, B.; Van Der Straeten, C.; Wuyts, F.; Maes, L., Cobalt toxicity in humans—A review of the potential sources and systemic health effects. *Toxicology* **2017**, 387, 43-56.
- [33] Christiansen, M. G.; Howe, C. M.; Bono, D. C.; Perreault, D. J.; Anikeeva, P., Practical methods for generating alternating magnetic fields for biomedical research. *Review of Scientific Instruments* **2017**, 88 (8), 084301.
- [34] Obaidat, I. M.; Narayanaswamy, V.; Alaabed, S.; Sambasivam, S.; Muralee Gopi, C. V., Principles of magnetic hyperthermia: a focus on using multifunctional hybrid magnetic nanoparticles. *Magnetochemistry* **2019**, 5 (4), 67.
- [35] Hergt, R.; Dutz, S., Magnetic particle hyperthermia—biophysical limitations of a visionary tumour therapy. *Journal of Magnetism and Magnetic Materials* **2007**, 311 (1), 187-192.
- [36] Araújo-Neto, R.; Silva-Freitas, E.; Carvalho, J.; Pontes, T.; Silva, K.; Damasceno, I.; Egito, E.; Dantas, A. L.; Morales, M. A.; Carrico, A. S., Monodisperse sodium oleate coated magnetite high susceptibility nanoparticles for hyperthermia applications. *Journal of Magnetism and Magnetic Materials* **2014**, 364, 72-79.
- [37] Linh, P. H.; Phuc, N. X.; Hong, L. V.; Uyen, L. L.; Chien, N. V.; Nam, P. H.; Quy, N. T.; Nhung, H. T. M.; Phong, P. T.; Lee, I. J., Dextran coated magnetite high susceptibility nanoparticles for hyperthermia applications. *Journal of Magnetism and Magnetic Materials* **2018**, 460, 128-136.
- [38] Yoon, K. Y.; Xue, Z.; Fei, Y. P.; Lee, J. H.; Cheng, V.; Bagaria, H. G.; Huh, C.; Bryant, S. L.; Kong, S. D.; Ngo, V. W.; Rahmani, A. R.; Ahmadian, M.; Ellison, C. J.; Johnston, K. P., Control of magnetite primary particle size in aqueous dispersions of nanoclusters for high magnetic susceptibilities. *Journal of Colloid and Interface Science* **2016**, 462, 359-367.

- [39] van Ommering, K.; Nieuwenhuis, J. H.; van IJzendoorn, L. J.; Koopmans, B.; Prins, M. W., Confined Brownian motion of individual magnetic nanoparticles on a chip: Characterization of magnetic susceptibility. *Applied physics letters* **2006**, *89* (14), 142511.
- [40] Chantrell, R. W.; Walmsley, N.; Gore, J.; Maylin, M., Calculations of the susceptibility of interacting superparamagnetic particles. *Physical Review B* **2000**, *63* (2).
- [41] Kim, Y. J.; Park, B. C.; Choi, Y. S.; Ko, M. J.; Kim, Y. K., Quantitative Analysis on Cellular Uptake of Clustered Ferrite Magnetic Nanoparticles. *Electronic Materials Letters* **2019**, *15* (4), 471-480.
- [42] Mohapatra, J.; Nigam, S.; Gupta, J.; Mitra, A.; Aslam, M.; Bahadur, D., Enhancement of magnetic heating efficiency in size controlled MFe₂O₄ (M = Mn, Fe, Co and Ni) nanoassemblies. *Rsc Advances* **2015**, *5* (19), 14311-14321.
- [43] Yang, L. J.; Ma, L. C.; Xin, J. Y.; Li, A.; Sun, C. J.; Wei, R. X.; Ren, B. W.; Chen, Z.; Lin, H. Y.; Gao, J. H., Composition Tunable Manganese Ferrite Nanoparticles for Optimized T-2 Contrast Ability. *Chemistry of Materials* **2017**, *29* (7), 3038-3047.
- [44] Liu, F.; Hou, Y.; Gao, S., Exchange-coupled nanocomposites: chemical synthesis, characterization and applications. *Chem Soc Rev* **2014**, *43* (23), 8098-113.
- [45] Ge, J.; Hu, Y.; Biasini, M.; Beyermann, W. P.; Yin, Y., Superparamagnetic magnetite colloidal nanocrystal clusters. *Angewandte Chemie International Edition* **2007**, *46* (23), 4342-4345.
- [46] Guo, P. Z.; Zhang, G. L.; Yu, J. Q.; Li, H. L.; Zhao, X. S., Controlled synthesis, magnetic and photocatalytic properties of hollow spheres and colloidal nanocrystal clusters of manganese ferrite. *Colloids and Surfaces a-Physicochemical and Engineering Aspects* **2012**, *395*, 168-174.
- [47] Xie, J.; Yan, C. Z.; Zhang, Y.; Gu, N., Shape Evolution of "Multibranching" Mn-Zn Ferrite Nanostructures with High Performance: A Transformation of Nanocrystals into Nanoclusters. *Chemistry of Materials* **2013**, *25* (18), 3702-3709.
- [48] Aslibeiki, B.; Kameli, P., Effect of ZnO on Structural and Magnetic Properties of MnFe₂O₄/ZnO Nanocomposite. *Journal of Superconductivity and Novel Magnetism* **2015**, *28* (11), 3343-3350.
- [49] Casula, M. F.; Conca, E.; Bakaimi, I.; Sathya, A.; Materia, M. E.; Casu, A.; Falqui, A.; Sogne, E.; Pellegrino, T.; Kanaras, A. G., Manganese doped-iron oxide nanoparticle clusters and their potential as agents for magnetic resonance imaging and hyperthermia. *Physical Chemistry Chemical Physics* **2016**, *18* (25), 16848-16855.
- [50] Xiao, Z.; Zhang, Q.; Guo, X.; Villanova, J.; Hu, Y.; Kulaots, I.; Garcia-Rojas, D.; Guo, W.; Colvin, V. L., Libraries of Uniform Magnetic Multicore Nanoparticles with Tunable Dimensions for Biomedical and Photonic Applications. *ACS Applied Materials & Interfaces* **2020**, *12* (37), 41932-41941.
- [51] Liu, X.; Liu, J.; Zhang, S. H.; Nan, Z. D.; Shi, Q., Structural, Magnetic, and Thermodynamic Evolutions of Zn-Doped Fe₃O₄ Nanoparticles Synthesized Using a One-Step Solvothermal Method. *Journal of Physical Chemistry C* **2016**, *120* (2), 1328-1341.
- [52] Choi, Y. S.; Yoon, H. Y.; Lee, J. S.; Wu, J. H.; Kim, Y. K., Synthesis and magnetic

- properties of size-tunable $\text{Mn}_x\text{Fe}_{3-x}\text{O}_4$ ferrite nanoclusters. *Journal of Applied Physics* **2014**, *115* (17).
- [53] Qi, Y. Z.; Shao, C.; Gu, W.; Li, F. Y.; Deng, Y. L.; Li, H. S.; Ye, L., Carboxylic silane-exchanged manganese ferrite nanoclusters with high relaxivity for magnetic resonance imaging. *Journal of Materials Chemistry B* **2013**, *1* (13), 1846-1851.
- [54] Xiang, Z.; Ducharne, B.; Della Schiava, N.; Capsal, J.-F.; Cottinet, P.-J.; Coativy, G.; Lermusiaux, P.; Le, M. Q., Induction heating-based low-frequency alternating magnetic field: High potential of ferromagnetic composites for medical applications. *Materials & Design* **2019**, *174*, 107804.
- [55] Otero-Lorenzo, R.; Fantechi, E.; Sangregorio, C.; Salgueirino, V., Solvothermally Driven Mn Doping and Clustering of Iron Oxide Nanoparticles for Heat Delivery Applications. *Chemistry-a European Journal* **2016**, *22* (19), 6666-6675.
- [56] Al-Rashdi, K.; Widatallah, H.; Ma'Mari, A.; Cespedes, O.; Elzain, M.; Al-Rawas, A.; Gismelseed, A.; Yousif, A., Structural and Mössbauer studies of nanocrystalline Mn^{2+} -doped Fe_3O_4 particles. *Hyperfine Interactions* **2018**, *239* (1), 1-11.
- [57] Granados, O.; Meza, G., A direct HPLC method to estimate streptomycin and its putative ototoxic derivative, streptidine, in blood serum: application to streptomycin-treated humans. *Journal of pharmaceutical and biomedical analysis* **2007**, *43* (2), 625-630.
- [58] Kim, J.; Cho, H. R.; Jeon, H.; Kim, D.; Song, C.; Lee, N.; Choi, S. H.; Hyeon, T., Continuous O-2-Evolving MnFe_2O_4 Nanoparticle-Anchored Mesoporous Silica Nanoparticles for Efficient Photodynamic Therapy in Hypoxic Cancer. *Journal of the American Chemical Society* **2017**, *139* (32), 10992-10995.

Chapter 5

Tunable Magnetic Cluster Chains and Their Enhanced Magnetic Properties[†]

[†] Reprinted (adapted) with permission from Xiao, Z., Villanova, J., Lee, M.J., Stueber, D.D., Zhang, Q. and Colvin, V.L. Tunable Magnetic Cluster Chains and Their Enhanced Magnetic Properties. In preparation.

5. Tunable Magnetic Cluster Chains and Their Enhanced Magnetic Properties

5.1 Abstract

The assembly of magnetic nanocrystals into one dimensional chains is a strategy adopted in natural magnetotactic bacteria to enable their sensitivity to minute variations in the earth's small magnetic field. Inspired by these magnetosomes, we applied an external field to induce controllable particle-particle assembly between superparamagnetic nanoclusters that can yield materials with aspect ratios of up to 125 and tunable lengths from 0.8 to 5.0 μm . Silica deposition can permanently capture these structures, termed here nanoworms, allowing for their magnetic characterization in the liquid and solid state. These materials can form stable aqueous suspensions, and in solution they are superparamagnetic at room temperature with exceptional initial DC magnetic susceptibilities that increase with chain length; the longest assemblies are ten times more susceptible than that of individual nanoclusters. Higher susceptibilities translate into improved MRI T2 contrast, for example, and these assembled iron oxides have maximum relaxivities (r_2) of $549 \text{ s}^{-1} \text{ mM}^{-1}$ as compared to $350 \text{ s}^{-1} \text{ mM}^{-1}$ for isolated nanoclusters. In solid form the chains can pack into parallel bundles that are ferrimagnetic; the coercivity of these bulk samples is large if external fields are applied parallel to the long axis of the chains but is near-zero for field application perpendicular to the texture of the chains. Anisotropic magnetic coercivity in magnetic thin films has long been of interest in data storage schemes, and this a typical demonstration of such a property in materials formed from chemical assembly strategies.

5.2 Introduction

The design and assembly of magnetic nanocrystals into higher-order structures opens up new avenues for photonic crystals, responsive biomaterials, and magnetic imaging.^[1-6] The collective properties of closely interacting magnetic nanocrystals can yield a rich array of improved and novel magnetic behaviors.^[2] In three dimensions, magnetic nanocrystals have been explored as artificial atoms which when assembled into superlattices can possess larger magnetic moments relevant for magneto-mechanical cancer therapeutics.^[4] Alternatively, particle assembly may offer a route to optimizing the low field sensitivity of magnetic particles. One dimensional chains are a promising motif in this regard as it is this architecture that permits magnetotactic bacteria to sense small variations in the earth's magnetic field (0.3 – 0.6 Gauss).^[7-11] Recovery of these natural magnetosome chains, or application of the complete organism, has led to some spectacular demonstrations of hyperthermic cancer treatments as well as externally activated drug delivery.^[7, 8, 11-14]

Chemical assembly of magnetic nanocrystal chains has revealed the importance of close particle-particle contact and crystallographic alignment within chains to developing behaviors that recapitulate natural magnetosomes. The simplest approach to forming one-dimensional assemblies has relied on chemical cross-linking of smaller nanoparticles (5 to 10 nm) to yield chains of up to 200 nm.^[15-17] These materials can possess high T_2 contrast ($r_2 = 100\sim 400 \text{ s}^{-1} \text{ mM}^{-1}$) for magnetic resonance imaging (MRI) by virtue of their large magnetic volume as well as more extended blood circulation due to their elongated shape.^[15, 17] However, the individual magnetic nanocrystals are not magnetically aligned, and particle-particle interactions are dominated by dipolar interactions known to reduce the initial magnetic susceptibility of these assemblies.^[13, 18-20] A more promising approach

utilizes the particle-particle attraction between superparamagnetic nanoparticles induced by the application of external magnetic fields.^[19-22] Such magnetically generated structures line up the crystallographic and magnetic axes of the individual particles via magnetic dipole forces.^[23-25] For example, colloidal dispersions of sub-micron magnetic particles can form dynamic photonic crystals when placed near a handheld magnet. Interparticle distances on the order of hundreds of nanometers result in the Bragg diffraction of visible light, and these particle distances are inversely proportional to the external field strength.^[26] Such magnetically assembled chains can be harvested with introduction of silica or polydopamine coatings and are prone to bundling as a result of their dimensions.^[25, 27-32] While aggregation is not an issue for some applications in mixing and in-vitro diagnostics, other applications particularly in-vivo require magnetic nanostructures with a great degree of colloidal stability.^[27, 29, 31] The relatively large dimension, microns in length and individual particles over a hundred nanometers in diameter, of these chains has limited their use in applications which require non-sedimenting and colloidally stable suspensions.^[2, 33]

There are significant challenges in downsizing this magnetic assembly approach to forming shorter chains with the smaller nanocrystals more representative of natural magnetosomes. Most notably is that the particle-particle attraction that drives chain assembly in external fields falls with diameter while the repulsive interactions that keep chains separated do not show such a dependence.^[21, 34] As a result three-dimensional aggregation is the rule for small nanocrystals with modest colloidal stability subjected to larger external fields.^[3, 19-23] Moreover, the additional coating layers necessary to physically link the constituent nanocrystals can shield steric repulsions from original coatings and increase the Van de

Waals attractions, compromising colloidal stability.^[24, 35, 36] Therefore, a robust electrostatic coating on constituent particles is ideal for biomedical applications.^[36] We reasoned that our recent work on optimizing the magnetic susceptibility of smaller magnetic nanoclusters would make it possible to form one-dimensional chains in these systems.

Here we present the synthesis of uniform ($\sigma < 20\%$), colloidally stable chains of nanoclusters that we refer to as nanoworms. These materials are comprised of 40 nm diameter, polysulfonate-coated iron oxide nanoclusters that possess a high saturation magnetization and substantial DC magnetic susceptibility.^[36] The curvature of the resulting chains can be manipulated by varying the uniformity of the external field, while the average chain length increases from 0.8 to 5 μm as the strength of the magnetic field increases. For the first time we report how the magnetic properties of one-dimensional assembled chains vary with chain length and morphology; in solution the magnetic susceptibility of the superparamagnetic materials increases monotonically with chain length. Moreover, any curvature in the chain greatly reduces the measured DC magnetic susceptibility. In aqueous solutions, nanoworms have excellent colloidal stability at high applied fields and are superparamagnetic with magnetic susceptibilities and T_2 relaxivities significantly greater than the constituent nanoclusters alone. Solid-state nanoworms are ferrimagnetic with coercivities that depend on the orientation of the applied field. Nanoworms will align with their long-axis parallel to an external field allowing for the generation of structurally anisotropic solids for magnetic measurement. Coercivity reaches a maximum (up to 100 Oe) if measured parallel to the long axis of the chains while the samples have negligible coercivity in the perpendicular direction. These unique and sensitive magnetic properties,

and their nanoscale dimensions, can enable the movement, heating, and imaging of these materials at lower magnetic fields and are therefore potentially suitable for many biomedical and industrial applications.^[37-41]

5.3 Nanoworm synthesis and characterizations

Magnetic nanoparticles colloidally stabilized with polymer coatings can experience three major interparticle forces in an external magnetic field: attractive Van der Waals forces, attractive magnetic dipolar forces induced when particles are magnetized, and charge-mediated repulsive and steric interactions (Figure 5.1). The second of these, charge repulsion, is central to the forming non-aggregating particle dispersions and often magnetic particles are coated with thick and/or charged polymers such as polyacrylic acid or high molecular weight polyethylene glycol.^[36] When these suspensions are subjected to external fields, magnetic dipolar forces are generated between the magnetic moments of nearby particles.^[21] Simultaneously the external field also can also generate a motive force if the particles are large enough. This unidirectional movement parallel to the external field lines, much like the alignment of particles via flow-driven processes, drives one-dimensional chain formation as opposed to three-dimensional assembly of clusters. If concentrated enough, the one-dimensional chains can experience Van der Waals attraction forming well-defined bundles with more three-dimensional character.^[24, 36] The strength of the repulsive interactions limits both of these processes making both the one-dimensional particle chaining and chain-bundling more difficult.

Assemblies can be permanently captured via silica deposition resulting in a shell on the surface of the particles leading to nanochain geometries that persist after the removal of the applied field (Figure 5.1 b). We expect that the length of each chain – proportional to

the number of particles in the chain – is determined by the balance between the relevant attractive and repulsive forces. Stronger external fields can induce greater attractive magnetic dipole forces to offset repulsive forces, thus bringing particles closer together and allowing more chaining and vice versa. However, if repulsive forces are weaker and attractive Van der Waals forces prevail, the interchain distance becomes smaller causing bundles of chains to form and become encapsulated (Figure 5.1 c). Magnetic dipole coupling between chains in a bundle could cause anti-alignment of spins, thereby diminishing their magnetic properties similar to what is seen in the multidomain materials with even smaller coercivities and susceptibilities.^[42]

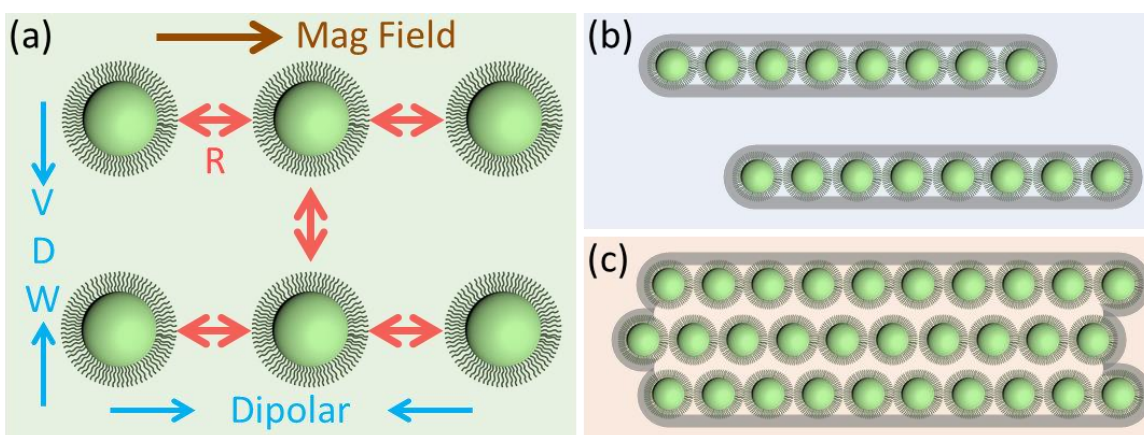


Figure 5. 1. Forming the magnetic nanochains via magnetic interactions. (a) Many forces act on colloidal magnetic nanoparticles in an external magnetic field: repulsive force (R) from like charges on neighboring particles, magnetic dipolar attraction induced by the external field, and Van der Waals (VDW) forces. A careful balance between the dipolar attraction, surface repulsion, and the Van der Waals attraction determines the morphologies of the final assemblies, which are then “frozen” by depositing a layer of silica. (b) Individual chains of magnetic nanoparticles form only when the interparticle repulsion is strong enough to overcome the interchain bundling. The silica coating encapsulates particles parallel to the field. (c) Bundles form when the interparticle repulsion is weak, and for these circumstances the silica coating encapsulates several chains in a bundle.

Isolated chains of magnetic nanoclusters could be formed under the application of modest applied fields, and the structures captured permanently using a silica coating (Figure 5.2).

To optimize the formation of relatively short magnetic chains with large magnetic susceptibilities, this work uses iron oxide nanoclusters (FNC) coated with a highly charged sulfonated copolymer as building blocks. We selected nanoclusters forty nanometers in dimension ($D_c = 40\text{nm}$), containing roughly 400 individual nanocrystals with a diameter of 6 nm, because these systems offer the largest initial magnetic susceptibility in a relatively small, nanoscale particle; this general class of magnetic particle has been widely applied in diverse biomedical applications.^[36] To "freeze" the chains of nanoclusters and isolate the nanoworms, tetraethoxysilane (TEOS) is applied to coat assembled nanoclusters with a layer of silica. The best results were obtained when TEOS was added to the colloidal solutions before field application, as the coating deposition occurs concurrently with chain formation. Because of this the magnetic particles in these chains are not in close contact and instead separated by a layer of silica.

Figure 2 illustrates the central role that the field application geometry plays in defining the chain morphology. Under field-free conditions (Figure 5.2 a, d, and g) a suspension of iron oxide nanoclusters and TEOS show no chaining behavior. Silica is deposited uniformly around the particle yielding core-shell particles with an iron oxide core and silica shell (Figure 5.2 d, g). When a single permanent magnet is placed within a few centimeters of the reaction vessel (Figure 5.2 b), we observe the chaining of nanoclusters into one-dimensional bent and curved morphologies. The non-linear structures capture the flow-fields generated by the magnetophoretic transport of particles towards the areas of greatest field gradient (Figure 5.2 b) which is not uniform for a single magnet placement.^[43] A variety of structures, including twisted nanoworms (TNW) or curved nanoworms (CNW), result from varying the strength of the applied magnetic field (Figure S5.1).

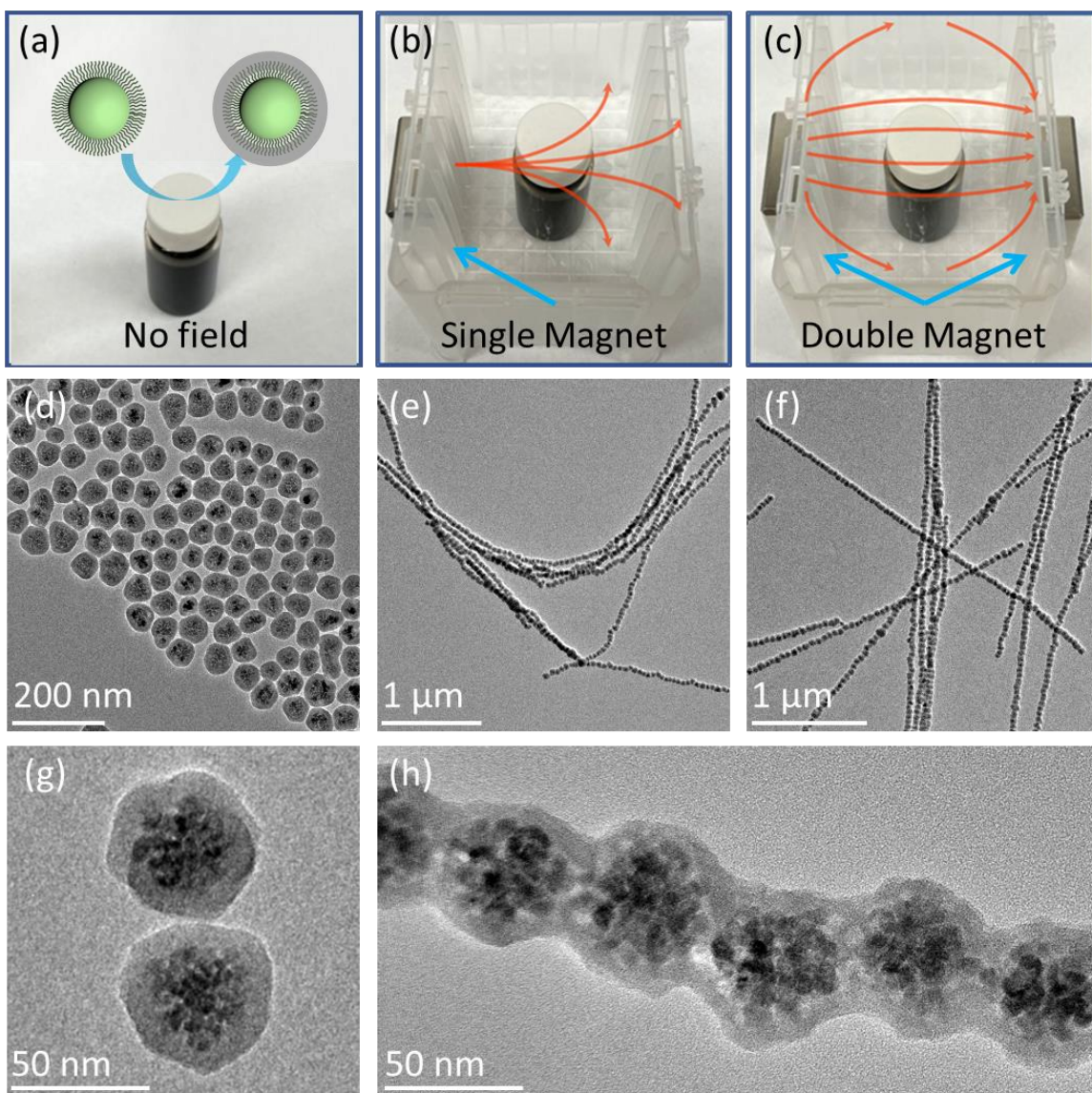


Figure 5. 2. Role of magnetic field application in the formation of magnetic nanocluster chains. (a) The silica deposition forms the core-shell structure on the nanoclusters with no applied field, as shown in d and g. (b) Curved chains are formed under the nonuniform magnetic field alongside the pole of a single magnet, as shown in e. (c) Linear chains of the nanoclusters are formed when a uniform magnetic field is applied by two oppositely facing magnets, as shown in g and h. The nanoclusters within the chains are captured in a permanent structure by a silica shell and with their magnetocrystalline easy axes aligned.

When two magnets with their north and south poles oppositely facing each other (Figure 5.2 c) are used to generate the external field, linear one-dimensional chains are formed (Figure 5.2 f). This geometry has been previously used for efficient magnetophoresis and

is known to generate a uniform magnetic field gradient whose field lines are nearly parallel.^[43] With two cubic neodymium magnets (N52) separated by 11.5 cm, roughly forty nanoclusters assemble into a 1.8 μm chain with a 10 nm spacing between nanoclusters (Figure 5.2 h).

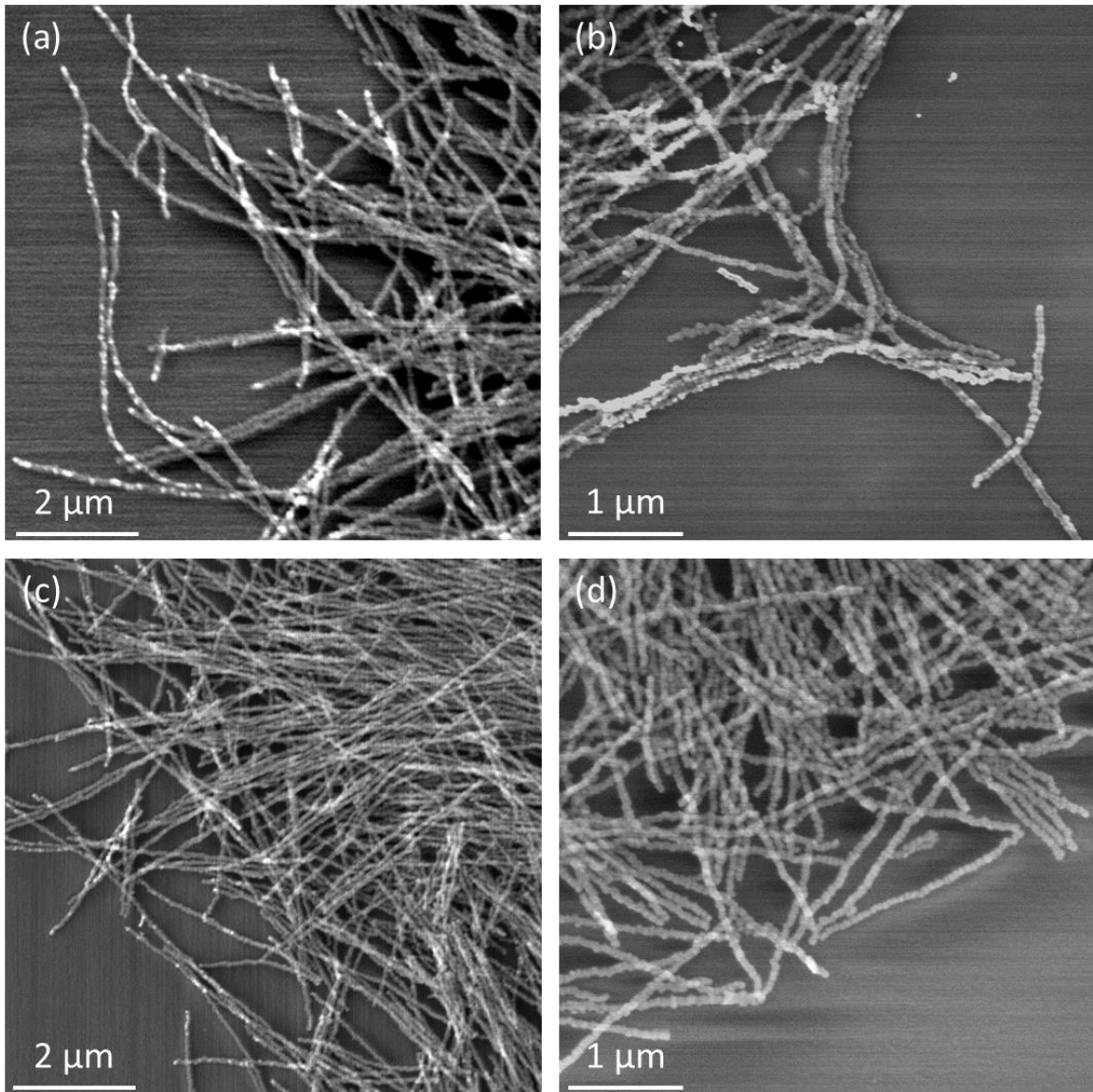


Figure 5. 3. Scanning electron micrographs of magnetic nanochains with different curvatures generated by single magnetic assembly processed. (a-b) Curved chains and (c-d) linear chains.

The uniformity of the morphology and length of these one-dimensional assemblies is apparent in lower magnification scanning electron microscopy (SEM) images (Figure 3). Most striking in these images is the different morphologies formed by the different field application geometries (Figure 5.3). After purification via washing and magnetic separation, the magnetic chains are redispersed in water where they form stable colloidal solutions for up to five days (Figure S5.2). The assembled materials are somewhat less stable than the starting nanoclusters given their larger dimensions which both leads to sedimentation as well as loose aggregation particularly if placed in magnetic fields for long periods of time.

The surface coating of the starting nanoclusters plays a significant role in defining the morphology of the resulting one-dimensional assembly process; most notably, less charge repulsion at the surface results in chains that have a greater tendency to bundle. Both the as-synthesized coating, polyacrylic acid (PAA), as well as nitro-dopamine functionalized polyethylene glycol (PEG) can yield nanoclusters that are well dispersed in water prior to magnetic assembly. Figure S5.3 a and b show nanoworms composed of nanoclusters with PAA and PEG coatings, respectively. They possess a similar morphology that has been previously termed nanobundles as there are usually several chains bundled together. We can understand the bundling seen here through a consideration of their surface charges which are known to be smaller than that of the sulfonate. Their smaller hydrodynamic sizes (61 nm for PAA, 75 nm for PEG, and 90 nm for the sulfonated copolymer) as well as less negative zeta potential (-25.3 mV, -17.7 mV, and -45.5 mV, respectively) suggest PAA or PEG provides less electrostatic repulsions (Table S5.1). Therefore, the same dipolar force can compress more particles in a single chain with these coatings.^[36] Meanwhile, the

distance among the chains becomes shorter so that they are subject to crosslinking by silica deposition.

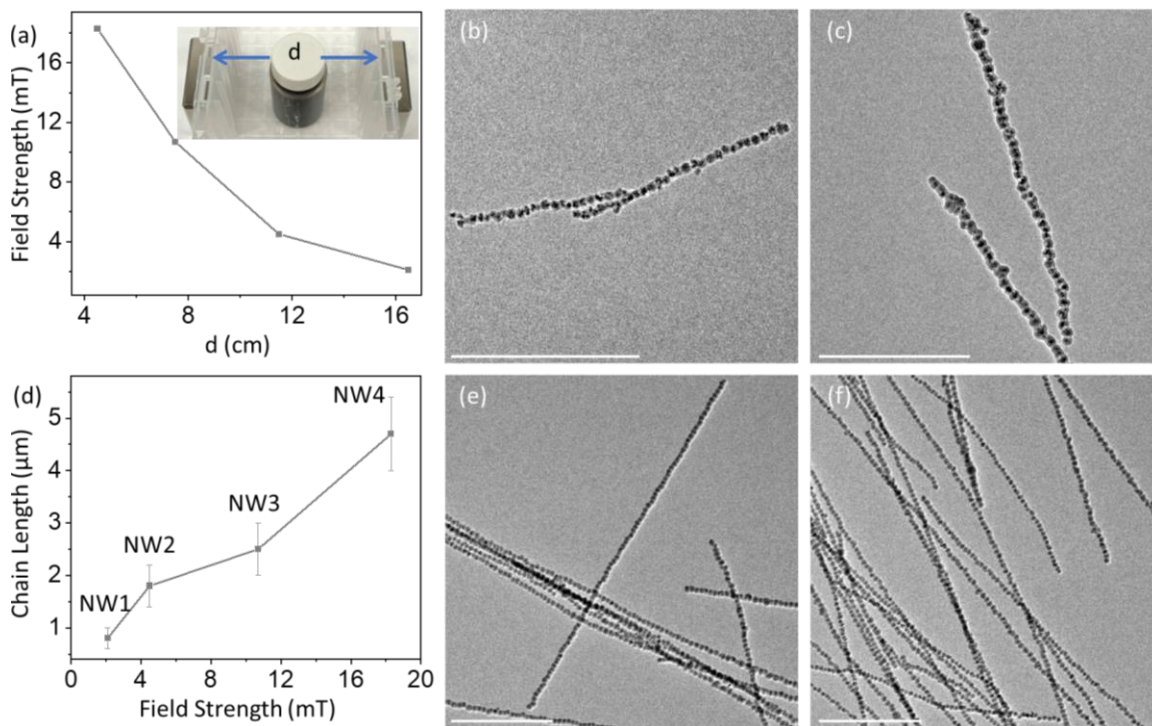


Figure 5. 4. Effect of magnetic field strength on the average length of the chains. (a) The magnetic field strength of the two oppositely faced magnets at a separation distance of d . (b, c, e, f) TEM of the nanoworm samples. Scale Bar: 1 μm . The average chain length for NW1, NW2, NW3, and NW4 is $0.8 \pm 0.2 \mu\text{m}$, $1.8 \pm 0.4 \mu\text{m}$, $2.5 \pm 0.5 \mu\text{m}$, and $4.7 \pm 0.7 \mu\text{m}$, respectively. (f) The chain length of the nanoworms synthesized at different field strengths.

The diameter of the nanocluster is also important in this assembly process; particles that are too small will not undergo substantial unidirectional movement while those that are too large are more likely to form chain bundles. Figure S5.3 c and d show samples prepared with 25 and 65 nm diameter polysulfonated nanoclusters as compared to the 40 nm nanoclusters. Under the same external field, nanoworms prepared using larger nanoclusters (65 nm) exhibit a bundled morphology reminiscent of the structures seen for smaller nanoclusters with PAA- and PEG-coatings.^[28, 44, 45] These bundles have poor colloidal

stability and rapidly undergo gravitational sedimentation. In contrast, nanoworms prepared using smaller nanoclusters are much shorter with only two or three nanoclusters. Additionally, the assembly yield is low for smaller nanoclusters (< 20%) as compared to the 40 nm nanoclusters (83%). To synthesize nanoworms of similar length to those formed with 40 nm clusters, 25 nm clusters would require a much greater external field because of their lower magnetic moment. Therefore, nanocluster size and surface coating are essential to optimize the synthesis of well-defined nanoworms with desired colloidal stability and magnetic properties.

The diameter dependence found above suggests that the chain lengths could be altered via changes in the magnetic field strength. Using the 40 nm nanoclusters with polysulfonate coating, we have prepared a series of nanoworms with different lengths. The chain length depends sensitively on the external field strength, a parameter easily adjusted by the distance between the two oppositely facing magnets. Field strength decreases as the distance between magnets increases (Figure 5.4 a). When the distance between magnets is decreased from 16.5 cm to 4.5 cm, the field strength in the center increases from 2.1 mT to 18.3 mT as measured using a gauss meter. Over this same range, nanoworms' average chain length increases from 0.8 to 4.7 μm , consistent with an increase in the number of assembled particles, from 16 to 120. Chains synthesized under these conditions have relatively high length uniformity (< 20 %) a feature found by quantifying the length of more than 100 chains Figure S5.4.

We have also noticed that magnetic field strengths outside 2.1 mT to 18.3 mT are not ideal for nanoworm synthesis. When magnets are separated too far from one another (> 18 cm), nanoworm yield is very low, with most products being silica-coated free clusters, similar

to what is seen in Figure 5.2 d. This is because the magnetic field is too weak to assemble nanoclusters close enough to be crosslinked by silica deposition. On the contrary, when the two magnets are too close (< 3.5 cm), nanoclusters dispersed in ethanol rapidly accumulate at the magnet-adjacent sides of the reaction vessel before effective TEOS hydrolysis can occur – preventing silica encapsulation. The final product is in a bulk form that is highly colloiddally unstable.

5.4 Aqueous-phase Magnetic Characterization

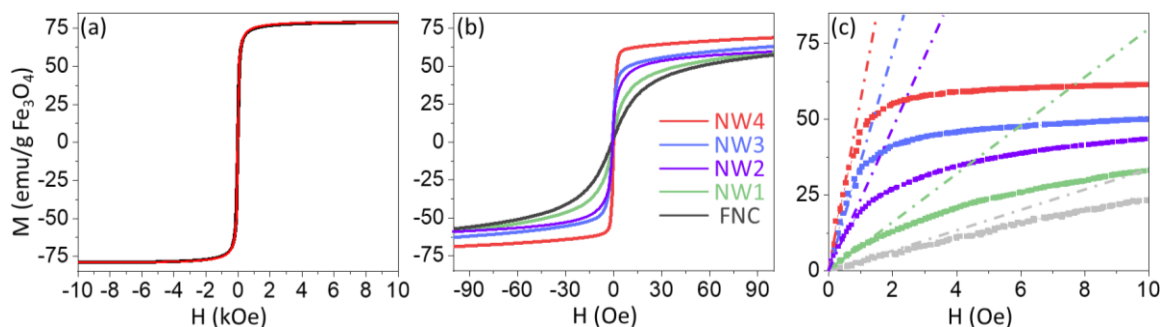


Figure 5.5. The magnetic properties of the nanoworms in aqueous solution. (a-c) Magnetization curves of the free nanoclusters and the linear chain samples with equivalent concentrations of 1 mg/mL. In panel a, at a high applied field, the magnetization curves for all samples are difficult to distinguish. The samples are superparamagnetic with zero coercivity and remanence magnetization. Compared to free nanoclusters, the chained samples saturate much more extensively at lower applied fields. Nanoworms with longer chains have a greater initial magnetic susceptibility than individual magnetic nanoclusters.

When dispersed in water colloidal solutions of these captured magnetic chains exhibit zero coercivity and remanence magnetization and are well characterized as superparamagnetic (Figure 5.5). We apply vibrating-sample magnetometry (VSM) at room temperature to characterize the magnetic properties of these assemblies. The technique provides a measure of the magnetization of a sample, typically a few millimeters in dimension, as a function of applied field. The high-field behavior of these samples is remarkably similar (Figure 5.5

a). Above roughly one Tesla the magnetization of the linear assemblies, independent of length, saturate at 79 emu/g Fe_3O_4 similar to unchained silica-coated nanoclusters (FNC). This saturation magnetization compares well to the bulk saturation magnetization of magnetite (92 emu/g Fe_3O_4); the modest reduction in these materials is likely due to their small dimensions and high surface to volume ratio.^[36] Well below 10 kOe (100 Oe) there are marked differences in the magnetization behavior that depend on the length of straight linear assemblies, as well as on their geometry (e.g., linear vs. non-linear) (Figure S5.5). Much of the differences in the response at low field is in the initial magnetic susceptibility of the samples (Figure 5.5 c); this central parameter is at the low field limit defined by the slope of the largely proportional magnetization versus applied field response. The one-dimensional linear assemblies (nanoworms) have greater magnetic susceptibilities than free nanoclusters (FNC) which we ascribe to the rotation of the nanochains in solution in alignment with the external field. Moreover, the measured initial magnetic susceptibilities increase with increasing chain length. At an applied field strength of 0.5 Oe, equivalent to the earth's magnetic field strength, a moderately long chain of 2.5 μm (NW3) magnetizes to 47% of its saturation magnetization. For comparison the free nanocluster is only 4% magnetized.

The volume susceptibility ($\chi = M/H$) of a superparamagnetic material describes how responsive the systems are to applied magnetic fields, and is a central metric in defining the performance of these materials in technologies that seek to image, move, or heat the systems at a distance.^[46-48] A large magnetic susceptibility not only results in better performance in these areas but also permits the use of simple and inexpensive approaches to external field generation.^[48] We extracted magnetic susceptibility from the slopes of data

such as that shown in Figure 5.5 c and compared these across different sample types and morphologies (Figure 5.6). Free nanoclusters have in solution a magnetic susceptibility of 295, while the magnetic susceptibilities of the linear chains are 581, 1190, 1712, and 2665 for 0.8, 1.8, 2.5, and 4.7 μm chains, respectively. A linear chain morphology for nanoworms is essential to their excellent magnetic properties. The striking increases in magnetic susceptibility with chain length are only seen for linear materials; twisted nanoworms (TNW) or curved nanoworms chains (CNW) as seen in Figure S5.1, their typical magnetic susceptibility is only comparable to FNC, showing minor enhancement due to their irregular morphologies. For chains twisted into a circle arrangement (TNW), particularly TNW3 (Figure S5.1 d), the magnetic susceptibility is actually less than that of the free non-chained magnetic clusters.

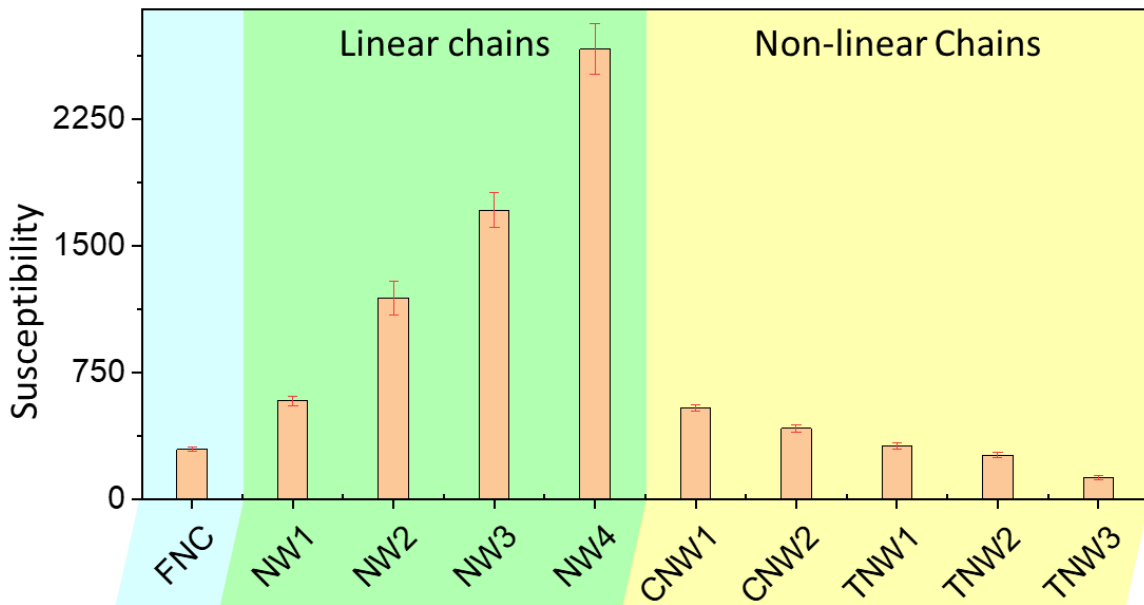


Figure 5. 6. Comparison of the initial magnetic susceptibilities of all nanoworm samples and the free nanoclusters. The susceptibility is derived from the slope of the magnetization curve near the zero fields (Figure 5.5 and S5.5) and converted to SI unit system, resulting in a dimensionless number. Higher susceptibility (greater slope) indicates faster saturation of the magnetization curve. FNC = free nanocluster; NW1 = $0.8 \pm 0.2 \mu\text{m}$, NW2 = $1.8 \pm 0.4 \mu\text{m}$, NW3 = $2.5 \pm 0.5 \mu\text{m}$, and $4.7 \pm 0.7 \mu\text{m}$.

We confirmed that the materials experience some physical movement in response to small applied fields by applying them to solution mixing; such an application has been envisioned for sub-micron stir bars used in droplet mixing.^[27,39] Diluted aqueous solutions (0.1 mg/mL or 100 ppm) of the captured chains were placed on a conventional magnetic stir plate with a field strength of 0.2 mT and a rotation speed of 990 rpm; a clear disturbance of the solution is apparent when the stir plate is turned on. After adding a drop of concentrated methylene blue into the solution, the dye is rapidly and homogeneously distributed in the solution containing nanoworms as compared to a similar solution of nanoclusters subjected to the same stir plate. These highly susceptible nanoworms should provide a strong candidate for efficient magnetic separation and drug delivery applications that involve the movement of the magnetic materials in liquid.^[6,49]

With relatively high saturation magnetizations (Table 5.1), nanoworms may prove useful as T_2 MRI contrast agents for cell tracking applications. This property allows for the spontaneous generation of particle-localized magnetic fields that facilitate the relaxation of water protons – the principal process by which contrast is enhanced in MRI. The ability of a contrast agent to accelerate the relaxation rate of water protons and therefore enhance image contrast is called relaxivity ($\text{mM}^{-1}\text{s}^{-1}$). However, any consideration of applying magnetic nanomaterials as MRI contrast agent requires them to retain colloidal stability in an external field. Though our nanoworms are microscale in length, they do not aggregate at a clinically relevant field strength for an MRI scanner (3 T) over the course of 15 minutes. The surface coatings present on these materials are clearly central in maintaining a high degree of colloidal stability and is consistent with our previous report.^[36]

We plot the longitudinal ($1/T_1$) and transverse ($1/T_2$) relaxation rates (s^{-1}) of our nanoworm and cluster solutions as a function of concentration (mM Fe) to measure their T_1 and T_2 relaxivities – r_1 and r_2 , respectively (Figure S5.7). The r_1 and r_2 values for FNC and NW1 – NW4 are reported in Table 1. Notably, the r_2 of our nanoworms, as opposed to their r_1 , exhibit a significant size dependence. This has to do with their robust surface coating and the mechanistic differences between T_1 and T_2 relaxation processes.^[50] In terms of contrast performance, a large r_2 makes for an ideal T_2 contrast agent, and a large r_1 makes for an ideal T_1 contrast agent. Our nanoworms make for promising T_2 contrast agents because they have exceptionally high r_2 (450 – 550 $\text{mM}^{-1}\text{s}^{-1}$) when compared to commercially available T_2 contrast agents ($< 200 \text{ mM}^{-1}\text{s}^{-1}$), micron-scale materials reported elsewhere ($< \sim 350 \text{ mM}^{-1}\text{s}^{-1}$), and single-core magnetic nanocrystals ($< 390 \text{ mM}^{-1}\text{s}^{-1}$).^[15, 17, 46, 51-53] Conversely, they have relatively low r_1 ($\sim 2 \text{ mM}^{-1}\text{s}^{-1}$) when compared to the clinical standard for T_1 contrast agents, Gadolinium-containing chelates (3 - 4 $\text{mM}^{-1}\text{s}^{-1}$).^[54] The exceptionally large r_2 of these nanoworms are ideal for cell tracking applications, which generally prefer T_2 contrast agents for their greater sensitivity.^[46] Also, their relatively large sizes can obstruct rapid exocytosis, allowing for greater tracking duration.^[53]

5.5 Solid-state Magnetic Characterization

Contrary to the superparamagnetic behavior observed in aqueous solution, solid-state nanoworms exhibit ferrimagnetism, with coercivity and remanence magnetization proportional to chain length (Table 5.1 and Figure S5.5). This is not surprising given the dimensions of the materials and the expectation that the superparamagnetism observed in solution was due to rotation of the materials.^[34] We analyze the magnetic behavior of nanoworms in the solid-state with VSM by drying aqueous samples in gypsum. Coercivity

and remanence increase with chain length because of increased dipolar interaction between constituent nanoclusters resulting in greater spontaneous magnetization.^[13, 14, 42] Solid-state nanoworm movement is primarily restricted, which significantly reduces the Brownian relaxation of nanoworms.^[34] As a result, there is a large remanence magnetization at zero fields and a strong resistance to the reverse field. Ferrimagnetic and superparamagnetic materials when formed in thin film and solid formats can be relevant for data storage and spintronic applications.^[55] The large and anisotropic coercivities measured here suggest that these materials are excellent candidates for data writing and reading as they can both maintain spin alignment while having low susceptibility for easy of reversing any recorded information.^[56]

Table 5. 1. Summary of the properties of the nanoworm samples. M_{sat} is the saturation magnetization of the sample. χ is the initial magnetic susceptibility derived from the slope of the magnetization curve near the zero fields (Figure 5 and S5) and converted to SI unit system, resulting in a dimensionless number. Solid samples are prepared by dropping the nanoworms solution into gypsum and drying. The drying process is without the external magnetic field. To measure the initial magnetic susceptibility in solid state, the nanoworms are first demagnetized by applying a small reverse field to offset the remanence magnetization. H_c is the coercivity in solid state. r_2 and r_1 are derived the slope of the T_2 and T_1 relaxation curve (Figure S7), respectively.

Sample	Length (μm)	M_{sat} (emu/g Fe_3O_4)	χ (Liquid)	χ (Solid*)	H_c (Solid*) (Oe)	r_2 ($\text{s}^{-1} \text{mM}^{-1}$)	r_1 ($\text{s}^{-1} \text{mM}^{-1}$)
FNC	0.04 ± 0.003	79.1	295	93	0	350.0	2.2
NW1	0.8 ± 0.2	78.9	581	79.9	9	524.5	1.5
NW2	1.8 ± 0.4	78.7	1190	77.8	21	549.5	1.8
NW3	2.5 ± 0.5	78.9	1712	69.5	42	453.8	2.4
NW4	4.7 ± 0.7	78.9	2665	61.4	72	459.5	2.1

The one-dimensional nature of these magnetic materials, and their propensity to align along external field lines, creates an opportunity for bottoms-up assembly of solid magnetic

materials with spatially distinct magnetic behavior. Figure 5.7 a shows the magnetization of solid nanochains formed during magnetic field alignment of evaporating solutions of the linear assemblies as compared to Figure S5.6 which reports data on solid phase materials randomly aligned after conventional evaporation of water.^[27, 29] These samples are prepared in a setup similar to that is used to form the original chains (Figure 7 a) and we include gypsum as a non-magnetic solid matrix thereby forming materials with equivalent iron content to those reported in Figure 5.5. Dipolar interactions can only facilitate the alignment of magnetic dipoles along the long axis of a chain, and these interactions are ineffective for structures oriented perpendicular to the applied field, leading to little spontaneous magnetization.^[12-14] Shown in Figure 5.7 a is a similar setup to the nanoworms synthesis. The nanoworms can now be aligned to the external field during the drying process. Transmission electron micrographs reveal that when samples are evaporated under the influence of an applied field the resulting one-dimensional structures are aligned uniaxially as opposed to samples prepared in the absence of external fields (Figure 5.7 a). Magnetization measurements of the field-alignment 1D assembly solids demonstrates samples exhibit completely different behavior depending on their orientation with respect to the experimental magnetization of the instrument. When the assemblies are oriented parallel to the applied measurement field, they have notable remanent magnetization with a much higher coercivity (93 Oe) than those formed without field alignment (42 Oe) (Figure 5.7 b); along this direction the material is a hard magnet with coercivities comparable to bulk metals and metal alloy materials.^[56] In contrast, when the field-aligned samples are oriented approximately perpendicular to the measurement field the coercivity drops substantially (3.3 Oe). Such highly anisotropic coercivity and the existence of both

superparamagnetism to ferromagnetism depending on the measurement axis is consistent with previous studies on magnetic nanochains.^[44, 57-60] It is also notable that the susceptibility of nanoworms perpendicular to the VSM field is much lower than that of the free nanoclusters; the elongated morphology may impede spin alignment in a direction perpendicular to the chains.^[13, 14] The highly anisotropic coercivity properties of these solid samples offer an interesting opportunity for applications in data storage.^[55, 56]

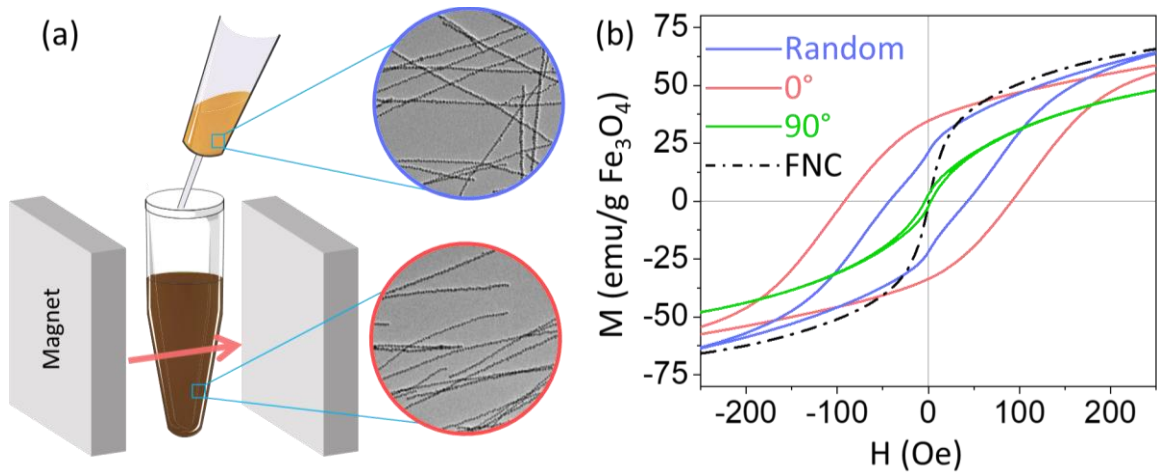


Figure 5. 7. The anisotropic magnetic properties of the nanoworm (2.5 μm long, 40 nm nanocluster diameter) in the solid state. (a) A schematic illustrating the sample preparation for field-aligned one-dimensional chains. The transmission electron micrographs show (top/blue) randomly distributed nanochains and (bottom red) parallel aligned ones. (b) The magnetization curves of the nanoworms in gypsum at 1% mass ratio. The red curve corresponds to parallel alignment between the field-alignment axis and the measurement field axis while the green corresponds to perpendicular alignment. The coercivities are 42 Oe (random), 93 Oe (0° detection, parallel), 3.3 Oe (90° detection, perpendicular), and 0 Oe (free nanoclusters), respectively. We attribute this negligible coercivity to our experimental error where the rotation might not be precise as 90° .

5.6 Conclusion

Uniform linear chains of magnetic nanoclusters, referred to here nanoworms, with short axes of 40 nm can be formed as stable colloidal suspensions of nanoscale materials. Chain lengths can vary from 0.8 to 4.7 μm with corresponding aspect ratios of a to b with very

little bundling. The chaining process is driven by dipole-dipole interactions between the highly susceptible magnetic particles and mediated by the concurrent deposition of silica as well as repulsive interactions between the negatively charged nanoclusters; different magnetic field application geometries can result in both twisted and bent configurations illustrating that particle assembly occurs along the applied magnetic field lines. In aqueous solutions nanoworms exhibit superparamagnetism with large magnetic susceptibilities, up to nearly ten times that observed for isolated nanoclusters; even modest fields from a conventional stir plate can cause substantial torque on the nanoworms sufficient to mix bulk solutions. When the nanoworms are not able to move, as is the case when they are formed as solids evaporated from the solution phase, they are ferromagnetic with remanent magnetization. When these solids are formed in the presence of magnetic fields nanoworms align along the axis of the applied fields. When measurement fields are aligned along the same direction, the samples have coercivities up to 100 Oe, but when measurement fields are rotated perpendicular the samples have near-zero coercivity.

5.7 Experimental Section

Chemicals: ethanol (ACS reagent, $\geq 99.5\%$), 4-Morpholineethanesulfonic acid, 2-(N-Morpholino)ethanesulfonic acid (MES, 99%), ammonium hydroxide solution ($\sim 30\%$), tetraethyl orthosilicate (TEOS, 99%, GC), ethylene glycol (anhydrous, 99.8%), iron(III) chloride hexahydrate ($\text{FeCl}_3 \cdot 6\text{H}_2\text{O}$, ACS reagent, 97%), urea (ACS reagent, 99.0%), O-Methyl-O'-succinylpolyethylene glycol (PEG-COOH, Mw $\sim 5,000$), azobisisobutyronitrile (AIBN, 98%), acrylic acid (anhydrous, contains 200 ppm MEHQ as inhibitor, 99%), poly(ethylene glycol) methyl ether acrylate (Acryl-PEG, Mw ~ 480 , contains 100 ppm BHT and 100 ppm MEHQ as inhibitor), 2-acrylamido-2-methylpropane sulfonic acid (AMPS,

99%), dimethylformamide (DMF, anhydrous, 99.8%), 3,4-dihydroxyphenethylamine hydrochloride (dopamine), and sodium nitrite (ACS reagent, $\geq 97.0\%$) were purchased from Sigma-Aldrich. Polyacrylic acid sodium salt (PAA, $M_w \sim 6,000$) was from Polyscience Inc. 1-ethyl-3-(3-dimethylaminopropyl)carbodiimide hydrochloride (EDC), sulfuric acid (ACS grade, 98%), hydrochloric acid (ACS grade, 37%) and hydrogen peroxide (30%) were purchased from Fisher Scientific. Water is purified using a Milli-Q water machine.

5.7.1 Preparation of nanoclusters with different coatings

40 nm nanoclusters. The synthesis of the 40 nm nanoclusters follows our previous protocols. Add 540 mg $\text{FeCl}_3 \cdot 6\text{H}_2\text{O}$ in 20 mL ethylene glycol, followed by 250 mg sodium polyacrylate ($M_w \sim 6,000$), 1200 mg urea, and 2000 mg water. The mixture is transferred to an autoclave and then heated at 215 °C for 6 hours. Magnetically wash the nanoclusters to form a stable colloidal solution. The nanoclusters have an average diameter of 40.0 ± 3.0 nm as measured by transmission electron microscope (TEM, JOEL 2100F) of over 300 particles. The hydrodynamic size is 61 nm as measured by dynamic light scattering (DLS).

25 nm and 65 nm nanoclusters. To synthesize the 25 nm and 65 nm nanoclusters, add 2,800 mg and 700 mg water, respectively. The as-synthesized nanoclusters have an average diameter of 25.3 ± 1.0 nm and 65.8 ± 6.0 nm as measured by TEM. The hydrodynamic size after polysulfonate coating is 48 nm and 113 nm as measured by DLS.

Polysulfonate coated nanoclusters. To graft polysulfonate coating to the nanoclusters, the original polyacrylic acid coating is first replaced by nitro-dopamine. Add 10 mg nitro-dopamine in 100 mg nanocluster dispersed in 10 mL water. The nitro-dopamine-coated nanoclusters will aggregate fast and can be magnetically collected. Add 20 mg EDC, 100

mg MES, 60 mg polysulfonate [Poly(AA-co-AMPS-co-PEG)], and 5 mL water into this magnetic collection and place the mixture in a probe sonicator for 30 min. The strong sonication can facilitate the conjugation of the polysulfonate to nitro-dopamine and allow the nanoclusters to disperse in water homogeneously. The polysulfonate coated 40 nm nanoclusters have a hydrodynamic size of 90 nm.

Synthesis of nitro-dopamine. Add 1 g dopamine in 30 mL water and stir at 1000 rpm in an ice bath, followed by the addition of 1.3 g sodium nitrate. Slowly add 10 mL 20% sulfuric acid to the mixture and vent the nitrogen dioxide gas from the reaction. Remove the ice bath and leave the mixture stirring at room temperature overnight. To obtain the powdered nitrodopamine hydrogensulfate (nitro-dopamine), filter the mixture and wash the residue with cold water several times, after which it can be freeze dried into a yellow powder. The reaction yield is nearly 100% based on the mass of the dried nitro-dopamine.

Nitro-dopamine functionalized polyethylene glycol (nitro-dopa-PEG). Add 200 mg PEG-COOH ($M_w \sim 5,000$) in 10 mL 0.1 M MES buffer solution, followed by 12 mg EDC and 20 mg dried nitro-dopamine. Stir the mixture at room temperature for 2 h to allow the EDC conjugation of the carboxylic acid groups on PEG-COOH and the amine groups on nitro-dopamine. Purify the product (nitro-dopa-PEG) using a dialysis bag (Cellulose Membrane, MWCO: 3 kDa, Sigma-Aldrich) in water. After dialysis purification, the functionalized polymer is dissolved in water with a concentration around 10 mg/mL based on the final volume.

PEG coated nanoclusters. To make the 40 nm nanoclusters coated with PEG, mix 10 mL nanoclusters solution (1mg/mL) and 10 mL nitro-dopa-PEG solution obtained in the

previous step for 2 h. Magnetically wash the nanoclusters several times. The hydrodynamic size of the nitro-dopa-PEG coated nanoclusters is 75 nm as measured by DLS.

Synthesis of the polysulfonate. The polysulfonate [Poly(AA-co-AMPS-co-PEG)] copolymer is prepared using free radical polymerization. Add 200 mg AIBN, 750 mg AMPS, 250 mg acrylic acid, and 1,000 mg Acryl-PEG in 10 mL DMF. Heat the mixture in a 70 °C water bath for 1 hour. After cooling to room temperature, add 10 mL water in the reaction mixture and transfer it to a dialysis bag (3 kDa) in water. After dialysis purification, the polysulfonate copolymer is dissolved in water with a concentration around 40 mg/mL based on the final volume.

5.7.2 Nanoworm synthesis

In a 20 mL glass vial, add 1 mL nanoclusters solution (4 mg/mL) followed by 10 mL ethanol, 1 mL ammonium hydroxide solution (~30%), and 0.025 mL TEOS.

To make nanoworms (NW) with linear chains, immediately place the vial in the center between two oppositely facing magnets (40x40x20mm strong neodymium cube magnets, N52) for 1 hour. Sample NW1, NW2, NW3, and NW4 are prepared with the distance of 16.5 cm, 11.5 cm, 7.5 cm, 4.5 cm between the two magnets, respectively. Take out the vial and place it on a magnet to separate the nanoworms and pour out the supernatant pale-yellow solution. Add water and turn on probe sonication until the nanoworms are homogeneously dispersed in water. Repeat this process several times to eliminate the unchained nanoclusters. The yield of the nanoworms is about 50% to 70%.

To make curved chains (CNW) or twisted chains (TNW), immediately place the vial near the pole of a single magnet for 1 hour. Sample CNW1 and CNW2 are prepared with a

distance from the vial to the magnet of 8 cm and 6 cm, while TNW 1, TNW2, and TNW3 are prepared with 5 cm, 4 cm, and 3 cm, respectively. Perform magnetic separation and sonication to purify these samples.

To make free nanoclusters (FNC) with a layer of silica shell, place the vial in a mixer at a speed of 1000 rpm for 1 hour. Perform magnetic separation and sonication to obtain the silica-coated nanoclusters.

5.7.3 Materials characterizations

The morphology and average length of the nanoworm samples are characterized by transmission electron microscopy (TEM) and scanning electron microscopy (SEM). Prepare diluted nanoworms aqueous solution (~0.2 mg/mL, as seen in Figure S5.3) and sonicate well. Load the samples on a 200-mesh carbon-coated copper grid by pipette 30 μ L on the grid and let it dry at room temperature. The nanoworms will form a single layer on the grid with random orientation. Note magnets should be put away as far as possible to avoid the nanoworm stacking on the grid. TEM images of the nanoworms were acquired by JEOL 2100 Field Emission Gun Transmission Electron Microscope at an acceleration voltage of 200 kV. The average chain length is calculated based on the survey of 100 chains for each nanoworm sample. The SEM images were acquired by Quattro Environmental Scanning Electron Microscope at an acceleration voltage of 20 kV.

5.7.4 Determination of the material mass in the VSM sample

The exact mass of the iron oxide (Fe_3O_4) in the solid VSM measurement is determined by inductively coupled plasma (ICP). Take out the solid VSM sample and add 0.4 mL HCl (37%). After 10 min. added another 9.6 mL HNO_3 (1%). The solution is then filtered to get

rid of the gypsum and subject to ICP measurement, with the Fe standard solution of 1 ppm, 5 ppm, 10 ppm, 20 ppm, 50 ppm, and 100 ppm. The concentration of Fe in the VSM sample is then converted to the mass of Fe_3O_4 . The saturation magnetization (M_{sat}) is calculated based on the maximum magnetization divided by the mass of Fe_3O_4 in the samples.

5.7.5 Zeta potential and hydrodynamic size measurement

Zeta potential and hydrodynamic size of the nanoclusters with different coatings are measured on a Zetasizer Nano ZS (Malvern Instruments Ltd, Malvern, UK) at room temperature. All the colloidal solutions have a pH of 7. All samples are measured in triplicate.

5.7.6 Magnetic Characterization

The magnetic properties are evaluated by the vibrating-sample magnetometer (VSM) in both liquid and solid form. Prepare the nanoworms aqueous solution with a concentration of roughly 1 mg/mL and sonicate well. For liquid measurement, fill the nanoworms solution (780 μL) in the liquid sample holder. For solid measurement, put 10 mg gypsum in the solid sample holder. Slowly add 0.1 mL nanoworms solution dropwise into gypsum and let it dry in a magnetic field-free area overnight. The nanoworms will have random orientation. To measure the initial magnetic susceptibility in solid state, the nanoworms are first demagnetized by applying a small reverse field to offset the remanence magnetization. To pre-align the nanoworms parallel to the applied field, the nanoworm solution is dried in the center of two oppositely facing magnets. The magnetization loop curves are obtained in the following range: -10,000 Oe to 10000 Oe with a step of 100 Oe, -300 Oe to 300 Oe

with a step of 1 Oe, and -10 Oe to 10 Oe with a step 0.1 Oe. Each data point takes 1 second to collect.

5.7.7 Relaxivity Characterization

The relaxivities of the nanoworm samples are acquired on the Siemens 3 T PRISMA scanner equipped with 64 receive channels and high-performance XR 80/200 gradients. For T2 measurements, a spin echo sequence is used with the following parameters: 2280 ms TR with 16 echoes at 9.4 ms intervals. For T1 measurements, a fast spoiled gradient echo sequence is used with the following parameters: 15 ms TR, 13 – 67 degree flip angles, and 3 mm slice thickness (12 slices total). Iron concentrations for stock solutions of free nanoclusters and nanoworms are measured using ICP and are then diluted for T1 (0.5, 0.185, 0.07, 0.026, and 0.01 mM Fe) and T2 (0.185, 0.07, 0.026, and 0.01 mM Fe) measurements.

5.8 Supplemental Figures and Tables

Table S5. 1. The hydrodynamic size and the zeta potential of the 40 nm nanoclusters with different coatings. The measurement is performed at a pH of 7.

Sample	Hydrodynamic size (nm)	Zeta potential (mV)
Cluster@PAA	61	-25.3
Cluster@PEG	75	-17.7
Cluster@PAPMS	90	-45.5

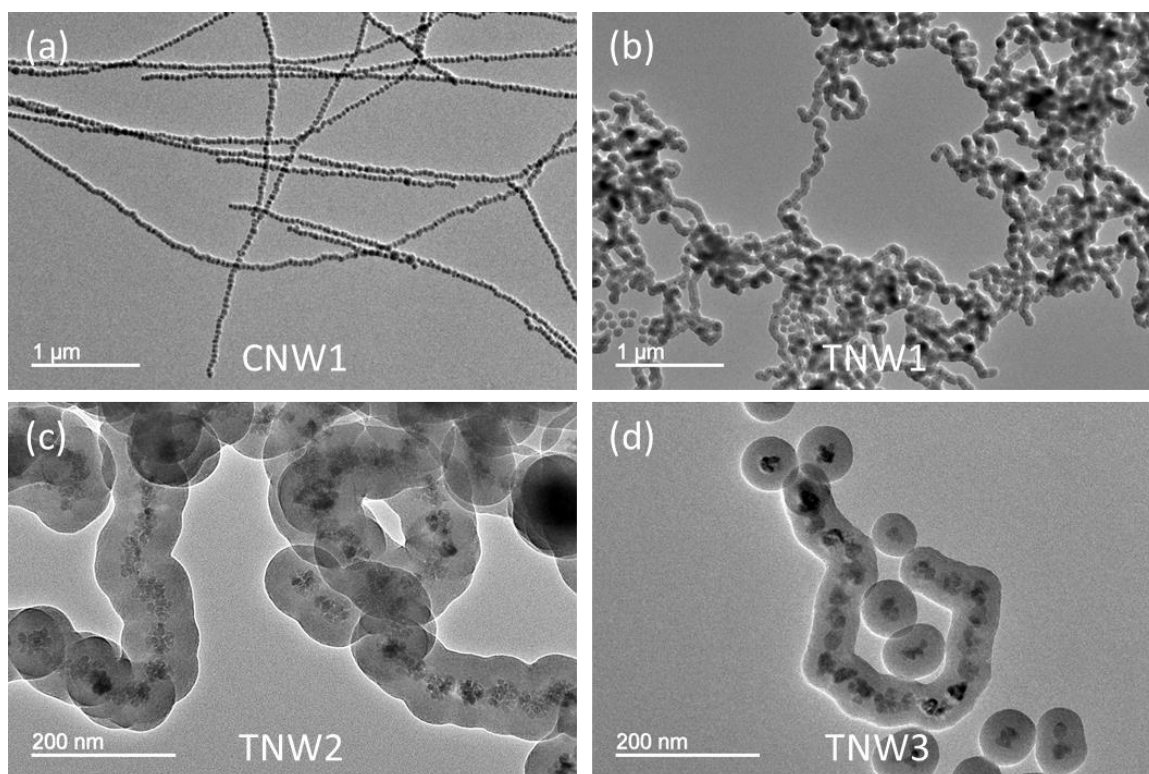


Figure S5. 1. The effect of magnetic field uniformity on the curvature of the chains. The magnetic field is created by a single magnet placed on one side of the vial. (a-d) TEM images of curved nanoworms (CNW1) and twisted nanoworms (TNW1~3), with the magnet distance of 3.5 cm, 7.5 cm, 9.0 cm, 12.0 cm, respectively.

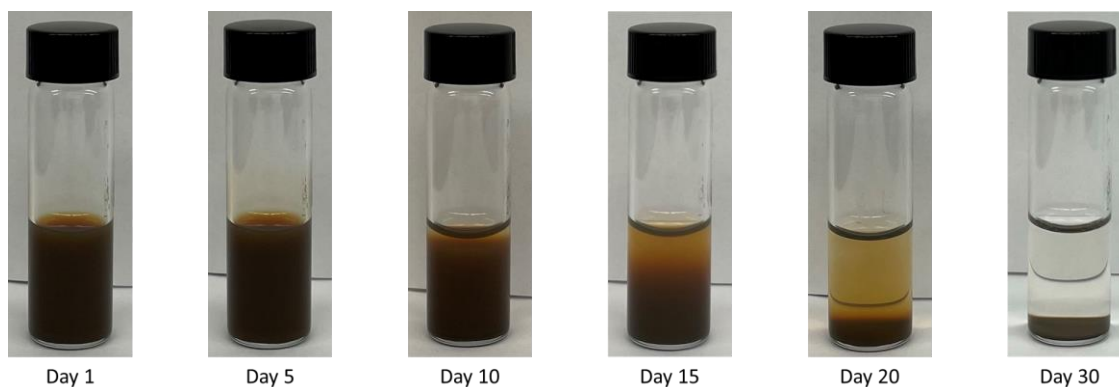


Figure S5. 2. The optical images of the aqueous nanoworms solution show the excellent colloidal stability. The concentration of NW3 is 1 mg/mL. The solution is first sonicated well and then left undisturbed for a month. The nanoworms have excellent colloidal stability and can remain homogeneous in solution for several days without visible aggregation.

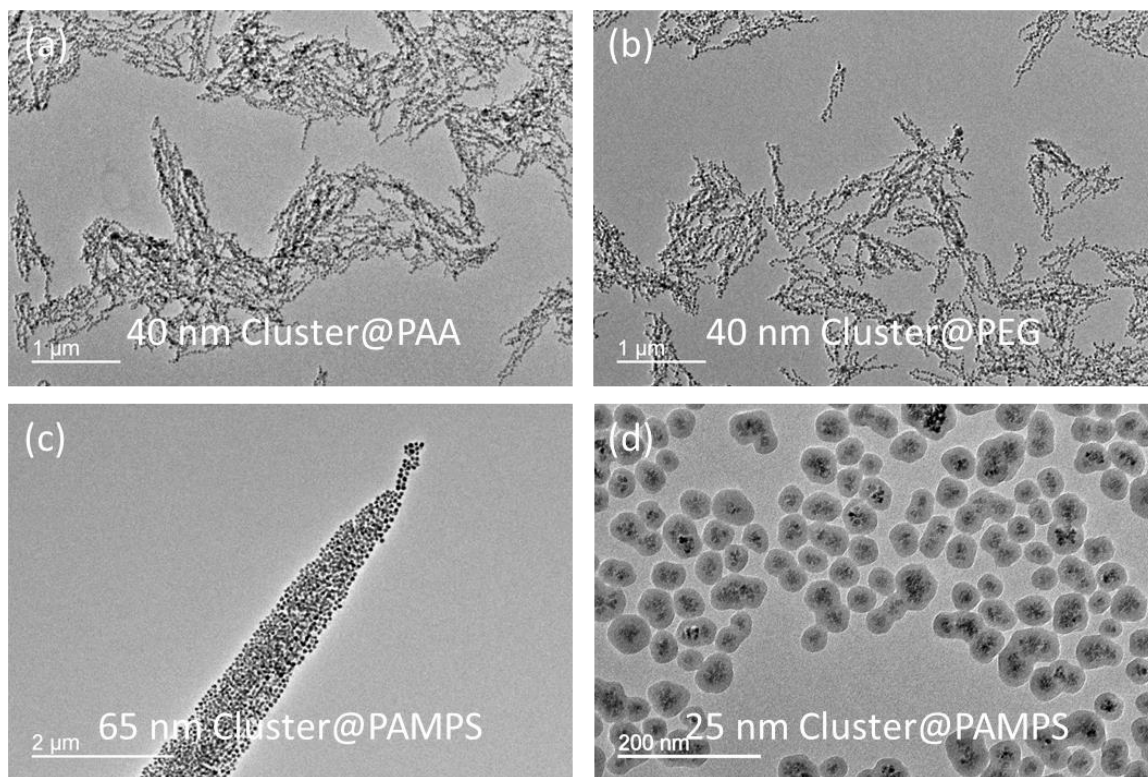


Figure S5. 3. The effect of the cluster size and surface coating on the formation of the nanoworms. The magnetic field used in each synthesis is the same as that for NW3. (a-d) TEM images of the nanoworms prepared using 40 nm clusters with PAA coating, 40 nm clusters with PEG, 65 nm clusters with PAMPS, and 25 clusters with PAMPS, respectively. The hydrodynamic size for each cluster sample is 61 nm, 75 nm, 113 nm, and 48 nm, respectively. Clusters with less robust coating or larger dimensions tend to form bundles, while smaller clusters cannot be chained effectively.

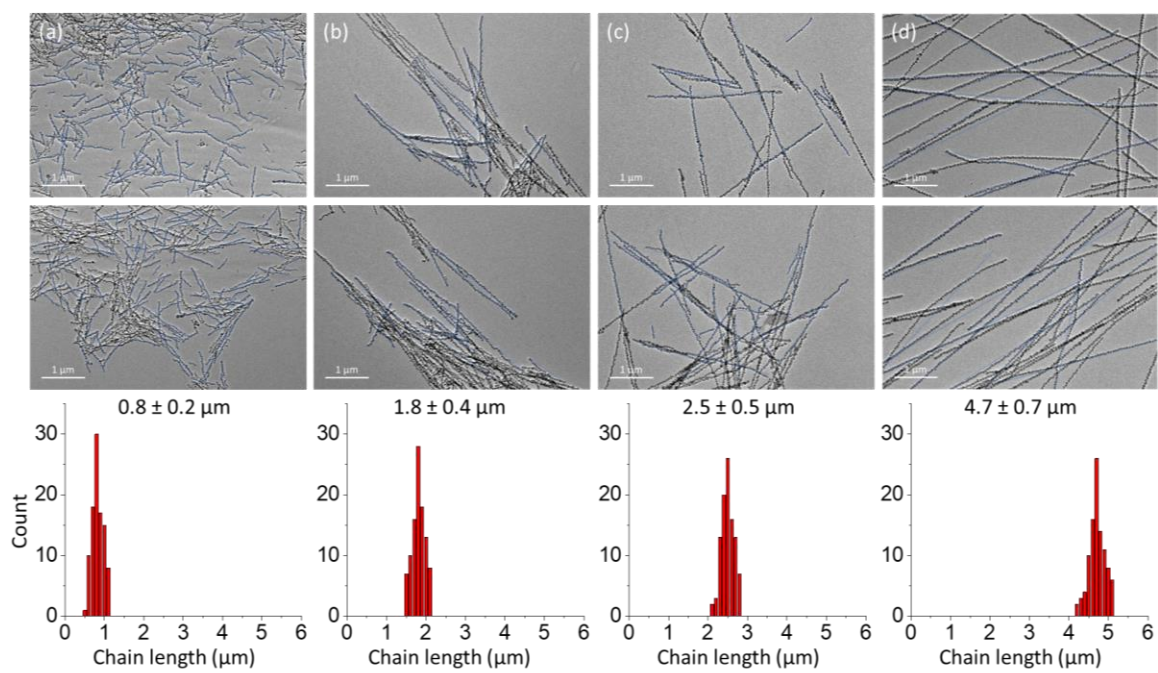


Figure S5. 4. *The chain length distribution of the nanoworm samples. The average length for a-d is $0.8 \pm 0.2 \mu\text{m}$, $1.8 \pm 0.4 \mu\text{m}$, $2.5 \pm 0.5 \mu\text{m}$, and $4.7 \pm 0.7 \mu\text{m}$.*

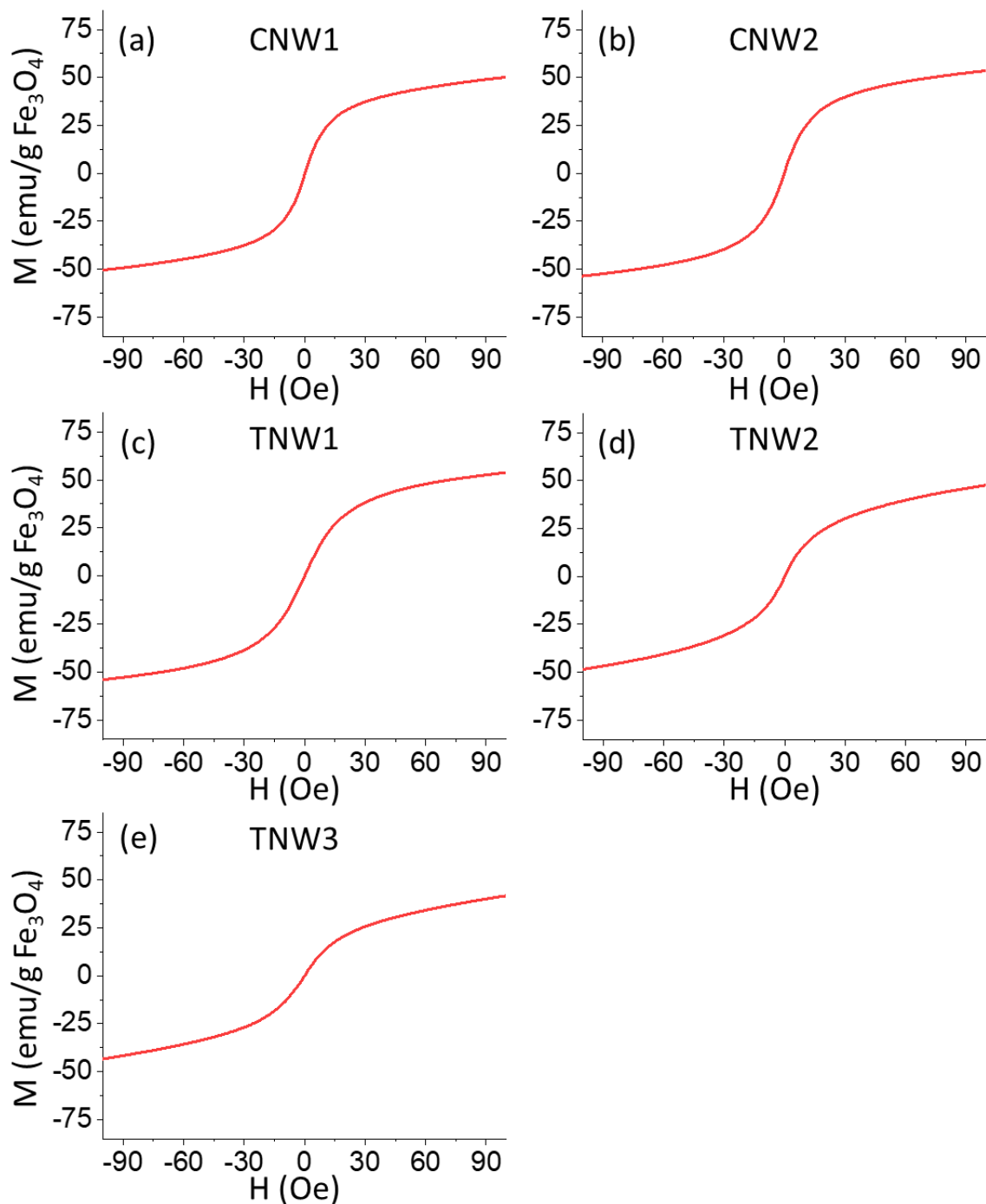


Figure S5. 5. The magnetization curves of the non-straight nanoworms in aqueous solution. (a-b) CNW 1 and CNW2; (c-d) TNW1, TNW2, TNW3. The concentration of nanoworms is 1 mg/mL.

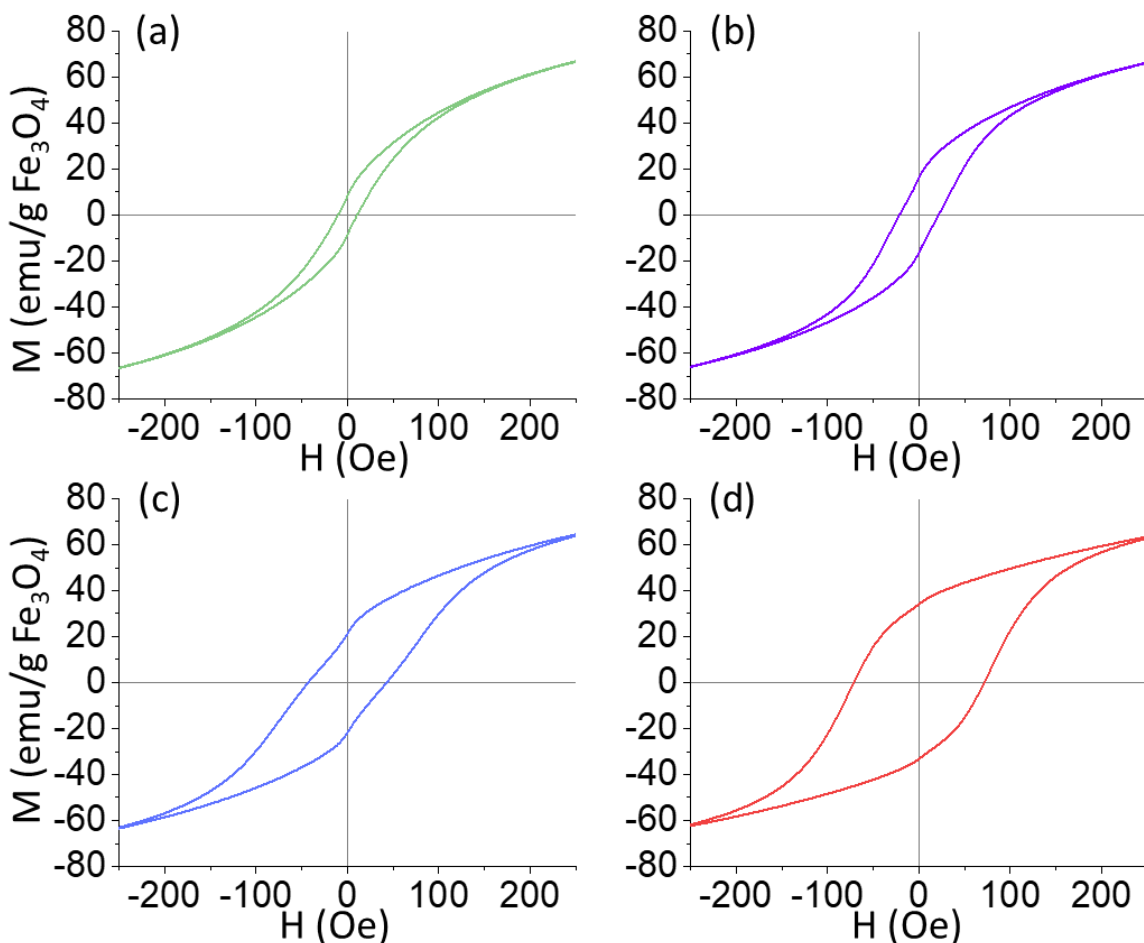


Figure S5. 6. Magnetic properties of the solid nanoworms. (a-d) The magnetization loop curves from -250 to 250 Oe of NW1, NW2, NW3, NW4, with an increasing coercivity of 9, 21, 42, 72 Oe, respectively.

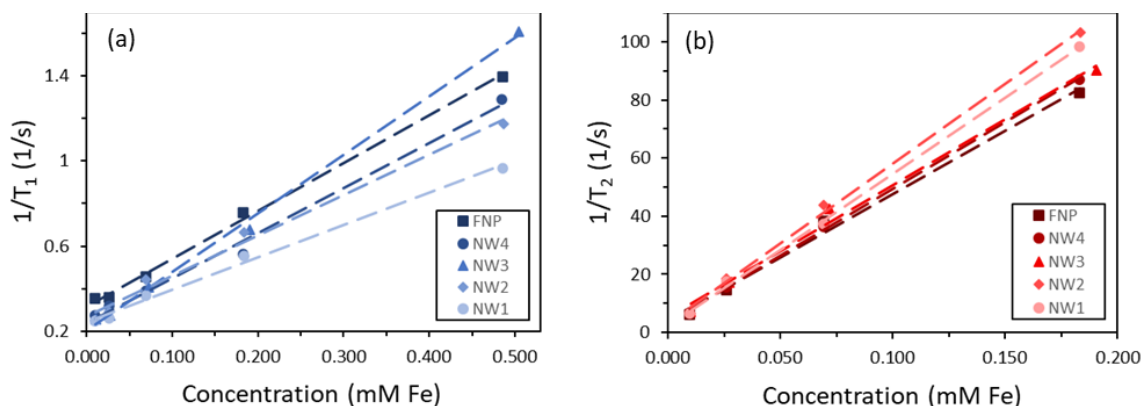


Figure S5. 7. Nanoworms as MRI contrast agent. Plots of (a) $1/T_1$ and (b) $1/T_2$ values versus iron concentration (mM) for iron oxide clusters (FNP) and nanoworms (NW1, NW2, NW3, and NW4) at 3 T.

References in Chapter 5

- [1] Chen, O.; Riedemann, L.; Etoc, F.; Herrmann, H.; Coppey, M.; Barch, M.; Farrar, C. T.; Zhao, J.; Bruns, O. T.; Wei, H., Magneto-fluorescent core-shell supernanoparticles. *Nature communications* **2014**, *5* (1), 1-8.
- [2] Li, Z.; Fan, Q.; Yin, Y., Colloidal Self-Assembly Approaches to Smart Nanostructured Materials. *Chemical Reviews* **2021**.
- [3] Zhuang, J. Q.; Wu, H. M.; Yang, Y. A.; Cao, Y. C., Supercrystalline colloidal particles from artificial atoms. *Journal of the American Chemical Society* **2007**, *129* (46), 14166-+.
- [4] Wang, T.; Wang, X. R.; LaMontagne, D.; Wang, Z. L.; Wang, Z. W.; Cao, Y. C., Shape-Controlled Synthesis of Colloidal Superparticles from Nanocubes. *Journal of the American Chemical Society* **2012**, *134* (44), 18225-18228.
- [5] Singh, G.; Chan, H.; Baskin, A.; Gelman, E.; Repnin, N.; Král, P.; Klajn, R., Self-assembly of magnetite nanocubes into helical superstructures. *Science* **2014**, *345* (6201), 1149-1153.
- [6] Varadan, V. K.; Chen, L.; Xie, J., *Nanomedicine: design and applications of magnetic nanomaterials, nanosensors and nanosystems*. John Wiley & Sons: 2008.
- [7] Alphandery, E.; Faure, S.; Seksek, O.; Guyot, F.; Chebbi, I., Chains of Magnetosomes Extracted from AMB-1 Magnetotactic Bacteria for Application in Alternative Magnetic Field Cancer Therapy. *Acs Nano* **2011**, *5* (8), 6279-6296.
- [8] Gandia, D.; Gandarias, L.; Rodrigo, I.; Robles-Garcia, J.; Das, R.; Garaio, E.; Garcia, J. A.; Phan, M. H.; Srikanth, H.; Orue, I.; Alonso, J.; Muela, A.; Fdez-Gubieda, M. L., Unlocking the Potential of Magnetotactic Bacteria as Magnetic Hyperthermia Agents. *Small* **2019**, *15* (41).
- [9] Ginet, N.; Pardoux, R.; Adryanczyk, G.; Garcia, D.; Brutesco, C.; Pignol, D., Single-step production of a recyclable nanobiocatalyst for organophosphate pesticides biodegradation using functionalized bacterial magnetosomes. *PLoS One* **2011**, *6* (6), e21442.
- [10] Alphandéry, E.; Guyot, F.; Chebbi, I., Preparation of chains of magnetosomes, isolated from *Magnetospirillum magneticum* strain AMB-1 magnetotactic bacteria, yielding efficient treatment of tumors using magnetic hyperthermia. *International journal of pharmaceutics* **2012**, *434* (1-2), 444-452.
- [11] Fdez-Gubieda, M.; Alonso, J.; García-Prieto, A.; García-Arribas, A.; Fernández Barquín, L.; Muela, A., Magnetotactic bacteria for cancer therapy. *Journal of Applied Physics* **2020**, *128* (7), 070902.
- [12] Martinez-Boubeta, C.; Simeonidis, K.; Makridis, A.; Angelakeris, M.; Iglesias, O.; Guardia, P.; Cabot, A.; Yedra, L.; Estradé, S.; Peiró, F., Learning from nature to improve the heat generation of iron-oxide nanoparticles for magnetic hyperthermia applications. *Scientific reports* **2013**, *3* (1), 1-8.
- [13] Mørup, S.; Hansen, M. F.; Frandsen, C., Magnetic interactions between nanoparticles. *Beilstein journal of nanotechnology* **2010**, *1* (1), 182-190.
- [14] Peddis, D.; Jönsson, P. E.; Laureti, S.; Varvaro, G., Magnetic interactions: a tool to modify the magnetic properties of materials based on nanoparticles. In *Frontiers of nanoscience*, Elsevier: 2014; Vol. 6, pp 129-188.
- [15] Park, J. H.; von Maltzahn, G.; Zhang, L. L.; Derfus, A. M.; Simberg, D.; Harris,

- T. J.; Ruoslahti, E.; Bhatia, S. N.; Sailor, M. J., Systematic Surface Engineering of Magnetic Nanoworms for in vivo Tumor Targeting. *Small* **2009**, *5* (6), 694-700.
- [16] Park, J. H.; von Maltzahn, G.; Zhang, L. L.; Schwartz, M. P.; Ruoslahti, E.; Bhatia, S. N.; Sailor, M. J., Magnetic iron oxide nanoworms for tumor targeting and imaging. *Advanced Materials* **2008**, *20* (9), 1630-+.
- [17] Wang, G. K.; Inturi, S.; Serkova, N. J.; Merkulov, S.; McCrae, K.; Russek, S. E.; Banda, N. K.; Simberg, D., High-Relaxivity Superparamagnetic Iron Oxide Nanoworms with Decreased Immune Recognition and Long-Circulating Properties. *Acs Nano* **2014**, *8* (12), 12437-12449.
- [18] Serantes, D.; Simeonidis, K.; Angelakeris, M.; Chubykalo-Fesenko, O.; Marciello, M.; Morales, M. D.; Baldomir, D.; Martinez-Boubeta, C., Multiplying Magnetic Hyperthermia Response by Nanoparticle Assembling. *Journal of Physical Chemistry C* **2014**, *118* (11), 5927-5934.
- [19] Nandakumaran, N.; Barnsley, L.; Feoktystov, A.; Ivanov, S. A.; Huber, D. L.; Fruhner, L. S.; Leffler, V.; Ehlert, S.; Kentzinger, E.; Qdemat, A.; Bhatnagar-Schoffmann, T.; Rucker, U.; Wharmby, M. T.; Cervellino, A.; Dunin-Borkowski, R. E.; Bruckel, T.; Feygenson, M., Unravelling Magnetic Nanochain Formation in Dispersion for In Vivo Applications. *Adv Mater* **2021**, *33* (24), e2008683.
- [20] Wang, H.; Chen, Q. W.; Sun, L. X.; Qi, H. P.; Yang, X.; Zhou, S.; Xiong, J., Magnetic-Field-Induced Formation of One-Dimensional Magnetite Nanochains. *Langmuir* **2009**, *25* (12), 7135-7139.
- [21] Xu, X.; Friedman, G.; Humfeld, K. D.; Majetich, S. A.; Asher, S. A., Synthesis and utilization of monodisperse superparamagnetic colloidal particles for magnetically controllable photonic crystals. *Chemistry of Materials* **2002**, *14* (3), 1249-1256.
- [22] Tracy, J. B.; Crawford, T. M., Magnetic field-directed self-assembly of magnetic nanoparticles. *Mrs Bulletin* **2013**, *38* (11), 915-920.
- [23] Ge, J. P.; Yin, Y. D., Responsive Photonic Crystals. *Angewandte Chemie-International Edition* **2011**, *50* (7), 1492-1522.
- [24] He, L.; Wang, M. S.; Ge, J. P.; Yin, Y. D., Magnetic Assembly Route to Colloidal Responsive Photonic Nanostructures. *Accounts Chem. Res.* **2012**, *45* (9), 1431-1440.
- [25] Hu, Y. X.; He, L.; Yin, Y. D., Magnetically Responsive Photonic Nanochains. *Angewandte Chemie-International Edition* **2011**, *50* (16), 3747-3750.
- [26] Xia, H.; Zhang, L.; Chen, Q. D.; Guo, L.; Fang, H. H.; Li, X. B.; Song, J. F.; Huang, X. R.; Sun, H. B., Band-Gap-Controllable Photonic Crystals Consisting of Magnetic Nanocrystal Clusters in a Solidified Polymer Matrix. *Journal of Physical Chemistry C* **2009**, *113* (43), 18542-18545.
- [27] Chong, W. H.; Chin, L. K.; Tan, R. L. S.; Wang, H.; Liu, A. Q.; Chen, H. Y., Stirring in Suspension: Nanometer-Sized Magnetic Stir Bars. *Angewandte Chemie-International Edition* **2013**, *52* (33), 8570-8573.
- [28] Kralj, S.; Makovec, D., Magnetic Assembly of Superparamagnetic Iron Oxide Nanoparticle Clusters into Nano chains and Nanobundles. *Acs Nano* **2015**, *9* (10), 9700-9707.
- [29] Xiong, Q. R.; Lim, C. Y.; Ren, J. H.; Zhou, J. J.; Pu, K. Y.; Chan-Park, M. B.; Mao, H.; Lam, Y. C.; Duan, H. W., Magnetic nanochain integrated microfluidic

- biochips. *Nature Communications* **2018**, *9*.
- [30] Ye, M. M.; Zorba, S.; He, L.; Hu, Y. X.; Maxwell, R. T.; Farah, C.; Zhang, Q.; Yin, Y. D., Self-assembly of superparamagnetic magnetite particles into peapod-like structures and their application in optical modulation. *Journal of Materials Chemistry* **2010**, *20* (37), 7965-7969.
- [31] Zhang, T.; Huang, B. T.; Elzatahry, A. A.; Alghamdi, A.; Yue, Q.; Deng, Y. H., Synthesis of Podlike Magnetic Mesoporous Silica Nanochains for Use as Enzyme Support and Nanostirrer in Biocatalysis. *Acs Applied Materials & Interfaces* **2020**, *12* (15), 17913-17920.
- [32] Zhou, J. J.; Wang, C. X.; Wang, P.; Messersmith, P. B.; Duan, H. W., Multifunctional Magnetic Nanochains: Exploiting Self-Polymerization and Versatile Reactivity of Mussel-Inspired Polydopamine. *Chemistry of Materials* **2015**, *27* (8), 3071-3076.
- [33] Kralj, S.; Marchesan, S., Bioinspired Magnetic Nanochains for Medicine. *Pharmaceutics* **2021**, *13* (8), 1262.
- [34] Reeves, D. B.; Weaver, J. B., Simulations of magnetic nanoparticle Brownian motion. *Journal of applied physics* **2012**, *112* (12), 124311.
- [35] Wu, Q.; Wang, Z.; Kong, X.; Gu, X.; Xue, G., A facile strategy for controlling the self-assembly of nanocomposite particles based on colloidal steric stabilization theory. *Langmuir* **2008**, *24* (15), 7778-7784.
- [36] Xiao, Z.; Zhang, Q.; Guo, X.; Villanova, J.; Hu, Y.; Kulaots, I.; Garcia-Rojas, D.; Guo, W.; Colvin, V. L., Libraries of Uniform Magnetic Multicore Nanoparticles with Tunable Dimensions for Biomedical and Photonic Applications. *ACS Applied Materials & Interfaces* **2020**, *12* (37), 41932-41941.
- [37] Das, G. K.; Bonifacio, C. S.; De Rojas, J.; Liu, K.; van Benthem, K.; Kennedy, I. M., Ultra-long magnetic nanochains for highly efficient arsenic removal from water. *Journal of Materials Chemistry A* **2014**, *2* (32), 12974-12981.
- [38] Nkurikiyimfura, I.; Wang, Y. M.; Pan, Z. D., Effect of chain-like magnetite nanoparticle aggregates on thermal conductivity of magnetic nanofluid in magnetic field. *Experimental Thermal and Fluid Science* **2013**, *44*, 607-612.
- [39] Wang, H.; Yu, Y.; Sun, Y.; Chen, Q., Magnetic nanochains: a review. *Nano* **2011**, *6* (01), 1-17.
- [40] Yuan, H. Y.; Zvonkina, I. J.; Al-Enizi, A. M.; Elzatahry, A. A.; Pyun, J.; Karim, A., Facile Assembly of Aligned Magnetic Nanoparticle Chains in Polymer Nanocomposite Films by Magnetic Flow Coating. *Acs Applied Materials & Interfaces* **2017**, *9* (12), 11290-11298.
- [41] Zhao, Z.; Rinaldi, C., Computational predictions of enhanced magnetic particle imaging performance by magnetic nanoparticle chains. *Physics in Medicine & Biology* **2020**, *65* (18), 185013.
- [42] Anand, M., Thermal and dipolar interaction effect on the relaxation in a linear chain of magnetic nanoparticles. *Journal of Magnetism and Magnetic Materials* **2021**, *522*, 167538.
- [43] Zhou, Z.; Shen, Z.; Chen, X., Tale of two magnets: An advanced magnetic targeting system. *ACS nano* **2019**, *14* (1), 7-11.
- [44] Krommenhoek, P. J.; Tracy, J. B., Magnetic Field-Directed Self-Assembly of Magnetic Nanoparticle Chains in Bulk Polymers. *Particle & Particle Systems*

- Characterization* **2013**, *30* (9), 759-763.
- [45] Corr, S. A.; Byrne, S. J.; Tekoriute, R.; Meledandri, C. J.; Brougham, D. F.; Lynch, M.; Kerskens, C.; O'Dwyer, L.; Gun'ko, Y. K., Linear assemblies of magnetic nanoparticles as MRI contrast agents. *Journal of the American Chemical Society* **2008**, *130* (13), 4214-+.
- [46] Stueber, D. D.; Villanova, J.; Aponte, I.; Xiao, Z.; Colvin, V. L., Magnetic Nanoparticles in Biology and Medicine: Past, Present, and Future Trends. *Pharmaceutics* **2021**, *13* (7), 943.
- [47] Tietze, R.; Lyer, S.; Dürr, S.; Alexiou, C., Nanoparticles for cancer therapy using magnetic forces. *Nanomedicine* **2012**, *7* (3), 447-457.
- [48] Yavuz, C. T.; Mayo, J.; Yu, W. W.; Prakash, A.; Falkner, J. C.; Yean, S.; Cong, L.; Shipley, H. J.; Kan, A.; Tomson, M., Low-field magnetic separation of monodisperse Fe₃O₄ nanocrystals. *science* **2006**, *314* (5801), 964-967.
- [49] Wu, K.; Su, D.; Liu, J.; Saha, R.; Wang, J.-P., Magnetic nanoparticles in nanomedicine: A review of recent advances. *Nanotechnology* **2019**, *30* (50), 502003.
- [50] Ni, D.; Bu, W.; Ehlerding, E. B.; Cai, W.; Shi, J., Engineering of inorganic nanoparticles as magnetic resonance imaging contrast agents. *Chem Soc Rev* **2017**, *46* (23), 7438-7468.
- [51] Granot, D.; Nkansah, M. K.; Bennewitz, M. F.; Tang, K. S.; Markakis, E. A.; Shapiro, E. M., Clinically viable magnetic poly(lactide-co-glycolide) particles for MRI-based cell tracking. *Magnetic Resonance in Medicine* **2014**, *71* (3), 1238-1250.
- [52] Hinds, A.; Hill, J.; Shapiro, E.; Laukkanen, M.; Silva, A.; Combs, C.; Varney, T.; Balaban, R.; Koretsky, A.; Dunbar, C., Highly efficient endosomal labeling of progenitor and stem cells with large magnetic particles allows magnetic resonance imaging of single cells. *Blood* **2003**, *102*, 867-72.
- [53] Xu, C.; Miranda-Nieves, D.; Ankrum, J. A.; Matthiesen, M. E.; Phillips, J. A.; Roes, I.; Wojtkiewicz, G. R.; Juneja, V.; Kultima, J. R.; Zhao, W.; Vemula, P. K.; Lin, C. P.; Nahrendorf, M.; Karp, J. M., Tracking mesenchymal stem cells with iron oxide nanoparticle loaded poly(lactide-co-glycolide) microparticles. *Nano Lett* **2012**, *12* (8), 4131-9.
- [54] Wahsner, J.; Gale, E. M.; Rodríguez-Rodríguez, A.; Caravan, P., Chemistry of MRI Contrast Agents: Current Challenges and New Frontiers. *Chemical Reviews* **2019**, *119* (2), 957-1057.
- [55] Singamaneni, S.; Bliznyuk, V. N.; Binek, C.; Tsymbal, E. Y., Magnetic nanoparticles: recent advances in synthesis, self-assembly and applications. *Journal of Materials Chemistry* **2011**, *21* (42), 16819-16845.
- [56] Henderson, J.; Shi, S.; Cakmaktepe, S.; Crawford, T. M., Pattern transfer nanomanufacturing using magnetic recording for programmed nanoparticle assembly. *Nanotechnology* **2012**, *23* (18).
- [57] Jiang, C. P.; Leung, C. W.; Pong, P. W. T., Magnetic-Field-Assisted Assembly of Anisotropic Superstructures by Iron Oxide Nanoparticles and Their Enhanced Magnetism. *Nanoscale Research Letters* **2016**, *11*.
- [58] Sahoo, Y.; Cheon, M.; Wang, S.; Luo, H.; Furlani, E. P.; Prasad, P. N., Field-directed self-assembly of magnetic nanoparticles. *Journal of Physical Chemistry B* **2004**, *108* (11), 3380-3383.

- [59] Smoukov, S. K.; Gangwal, S.; Marquez, M.; Velev, O. D., Reconfigurable responsive structures assembled from magnetic Janus particles. *Soft Matter* **2009**, *5* (6), 1285-1292.
- [60] Anand, M., Hysteresis in a linear chain of magnetic nanoparticles. *Journal of Applied Physics* **2020**, *128* (2), 023903.